University of Southampton Research Repository

Copyright © and Moral Rights for this thesis and, where applicable, any accompanying data are retained by the author and/or other copyright owners. A copy can be downloaded for personal non-commercial research or study, without prior permission or charge. This thesis and the accompanying data cannot be reproduced or quoted extensively from without first obtaining permission in writing from the copyright holder/s. The content of the thesis and accompanying research data (where applicable) must not be changed in any way or sold commercially in any format or medium without the formal permission of the copyright holder/s.

When referring to this thesis and any accompanying data, full bibliographic details must be given, e.g.

Thesis: Author (Year of Submission) "Full thesis title", University of Southampton, name of the University Faculty or School or Department, PhD Thesis, pagination.

Data: Author (Year) Title. URI [dataset]

University of Southampton

Faculty of Engineering and Physical Sciences

School of Electronics and Computer Science

Structure/Property Relations of Graphene Oxide/Epoxy Nanocomposites: Tailoring the Particle Surface Chemistry for Enhanced Electrical and Thermal Performance

DOI: http://doi.org/10.5258/SOTON/T0021

by

Orestis Vryonis

ORCID: 0000-0002-2862-4494

Thesis for the degree of Doctor of Philosophy

June 2019

University of Southampton

Abstract

Faculty of Engineering and Physical Sciences
School of Electronics and Computer Science

Thesis for the degree of Doctor of Philosophy

Structure/Property Relations of Graphene Oxide/Epoxy Nanocomposites: Tailoring the Particle Surface Chemistry for Enhanced Electrical and Thermal Performance

by
Orestis Vryonis

In this study, graphene oxide (GO) of various surface chemistry configurations were characterized and then utilized as epoxy fillers with a main objective of enhancing the electrical and thermal performance of the matrix, without compromising the mechanical properties.

The initial step of the study was to distinguish and establish the chemical pathways through which the surface chemistry of highly oxidized GO interacts with the crosslinking reactions of the matrix. For this, GO was produced with acidic oxidation, based upon potassium permanganate ($KMnO_4$) and then characterized via Raman, thermogravimetric analysis (TGA) and X-ray spectroscopy (XPS), which revealed increased graphitic disorder and oxygen-based functionalities decorating the lattice. Afterwards, the GO was dispersed within the epoxy matrix via a solvent-based method, to give nanocomposites containing up to 2 wt.% of GO, a filler content that is sufficient for filler/matrix chemical interactions. The excess of epoxide groups in the system, associated with the GO surface chemistry, was confirmed with Fourier transform infrared spectroscopy (FTIR). These additional moieties react with the hardener consequently, displacing the reaction stoichiometry away from the optimum. The result of this is a change in the macromolecular architecture, which was revealed through the dielectric secondary relaxations. Furthermore, during post-curing (> 100 ^{o}C), hydroxyl groups on the GO surface react with residual epoxide groups through etherification reactions, to give a marked increase in the glass transition temperature (T_g). These reactions lead to increased filler/matrix interfacial interactions and contribute to increased tensile performance. In addition, post-curing serves to partially reduce the defect content of the GO lattice which, in turn, slightly increases the electrical conductivity of the system.

After establishing the chemical pathways of the GO/epoxy reactions and demonstrating the inefficient features of GO in enhancing the electrical and thermal properties of epoxy, an alternative surface chemistry should be sought. Thus, the second step of this study was to introduce an single-step synthetic route for the production of moderately oxidized GO (mGO), which would: allow enhanced electrical and thermal properties; maintain epoxy compatibility; ensure no adverse influence on the epoxy curing reactions and require potentially simplified material processing

strategies. This route included replacement of the $KMnO_4$ with chromium trioxide (CrO_3) as the oxidizing agent. The mGO was then characterized and contrasted with the previously synthesized GO and a commercially available low-oxygen graphitic product (edge-oxidized GO, eGO). Raman spectroscopy, TGA and XPS demonstrated a moderate level of oxidation and a reduced carbon defect content, compared to the GO and the eGO. Subsequently, the eGO and mGO were incorporated into the epoxy via a scalable high-speed mixing method and the respective nanocomposites were contrasted. Transmission and scanning electron microscopy showed a fine dispersion/exfoliation for the mGO and poor compatibility for the eGO which drastically affected the aspect ratio of the respective platelets. It was revealed that the mGO/epoxy interactions include slight perturbation of the epoxy crosslinking, albeit only at high filler contents (> 12 wt.%), while the eGO did not react with the matrix at all. Ultimately, the mGO led to a low electrical percolation threshold (P_t) of ~1 wt.%; a maximum increase in electrical conductivity of about eight orders of magnitude and a maximum thermal conductivity increase of 200% compared to the unfilled epoxy, while the tensile performance of the system was not compromised. Conversely, the eGO/epoxy systems showed poor behaviour, with a P_t of ~10 wt.% and a maximum thermal conductivity increase of 150%, while the tensile performance was rapidly compromised. Those effects were attributed to the fact that mGO displays mildly oxygenated graphitic lattice - not only on the peripheral (as in the case of eGO) but also on the basal plane.

Upon the single-step production of moderately oxidized GO surface chemistry, the possibilities of further improvements in terms of electrical and/or thermal performance had to be explored. Thus, the final step of this study was to graft various amino-terminated moieties onto the surface of mGO in an attempt to modify, furtherly, the interfacial interactions with the epoxy matrix. For this, the mGO was functionalised with two bifunctional molecules: poly(propylene glycol) bis(2-aminopropyl ether) of different molar masses (termed d230 and d4000 accordingly) and a trifunctional trimethylolpropane tris[poly(propylene glycol), amine terminated] reagent, termed t440. The grafting process was revealed to be successful via Raman spectroscopy, TGA and XPS, and the resulting functionalised (fGO) systems were termed d230/fGO, d4000/fGO and t440/fGO. It was shown that the grafting included typical epoxide-amine reactions that potentially increase the disorder onto the graphitic lattice, while the elevated temperatures of the process served to slightly reduce the initial mGO oxygen content. Afterwards, the abovementioned three fGO systems were incorporated into the epoxy where it was demonstrated by differential scanning calorimetry (DSC) that the presence of the grafted moieties affected the local fGO/matrix interfacial interactions and slightly perturbed the epoxy curing reactions. X-ray diffraction (XRD) revealed reduced graphitic stacking with increased reagent molecular mass, which eventually led in reduced P_t (0.5 wt.% with the usage of the d4000 reagent). Furthermore, the maximum electrical conductivity of the respective nanocomposites appeared to be slightly increased with increasing reagent molecular weight, an effect also related to the limited platelet stacking. For the same, potentially, reasons the thermal conductivity of the fGO-containing systems was adversely affected at low filler contents.

Table of Contents

Table of Tables

Table of Figures

Table of Figures

Research Thesis: Declaration of Authorship

Print name:	Orestis Vryonis

Title of thesis:	Structure/Property Relations of Graphene Oxide/Epoxy Nanocomposites: Tailoring the Particle Surface Chemistry for Enhanced Electrical and Thermal Performance

I declare that this thesis and the work presented in it are my own and has been generated by me as the result of my own original research.

I confirm that:

1. This work was done wholly or mainly while in candidature for a research degree at this University;
2. Where any part of this thesis has previously been submitted for a degree or any other qualification at this University or any other institution, this has been clearly stated;
3. Where I have consulted the published work of others, this is always clearly attributed;
4. Where I have quoted from the work of others, the source is always given. With the exception of such quotations, this thesis is entirely my own work;
5. I have acknowledged all main sources of help;
6. Where the thesis is based on work done by myself jointly with others, I have made clear exactly what was done by others and what I have contributed myself;
7. Parts of this work have been published as:

- O. Vryonis, S. T. H. Virtanen, T. Andritsch, A. S. Vaughan, and P. L. Lewin, “Understanding the cross-linking reactions in highly oxidized graphene/epoxy nanocomposite systems,” *J. Mater. Sci.*, vol. 54, no. 4, pp. 3035–3051, 2019
- O. Vryonis, T. Andritsch, A. S. Vaughan, and P. L. Lewin, “An alternative synthesis route to graphene oxide: influence of surface chemistry on charge transport in epoxy-based composites,” *J. Mater. Sci.*, vol. 54, no. 11, pp. 8302–8318, 2019

Signature:		Date:	

Acknowledgements

This study was part of the "SPARCARB" project which was funded by the European Union's Horizon 2020 research and innovation programme under the Marie Sklodowska-Curie grant agreement [No 642771].

The author would like to express his gratitude to those who contributed to the successful completion of this PhD and specifically to:

- Professor Alun S. Vaughan for the substantial guidance and confidence he showed in me throughout my PhD study.
- Dr. Thomas Andritsch for his meaningful supervision, his support whenever it was needed and the friendly chats before our meetings.
- Professor Paul Lewin for assigning this funded project to me.
- Dr. Igor O. Golosnoy for his crucial role as my examiner (twice) and as an influential member of the project's consortium.
- The Tony Davies High Voltage Laboratory in the University of Southampton, for giving me the chance to work in their facilities. Special thanks to: Neil Palmer, Mike Smith, Ian Virtanen.
- Global Lightning Protection Services A/S in Copenhagen and Herning, Denmark for hosting me in their facilities during my relocation in Denmark. Special thanks to: Søren Find Madsen and Lisa Carloni.
- Zoltek Corporation in St. Louis, Missouri, US for offering a short industrial internship in their facilities. Special thanks to: Ric Baldini, Kamesh Narasimhan, David Corbin and Christina Adler.
- Nordex Energy GmbH in Rostock, Germany for my second short industrial internship. Special thanks to: Hendrik Klein.
- Garmor Inc. for kindly providing, without any charge, part of the edge oxidized graphene oxide powder used in this study.
- Dr. Suvi T. H. Virtanen and Dr. Matthew Praeger for the technical help they provided within the lab during the first few months of my experimental sessions.
- Dr. Marc Walker for the use of Warwick Photoemission Facility within the Departments of Physics and Chemistry, at the University of Warwick
- Istebreq A. H. Saeedi for the support within the lab and the spontaneous brain storms.
- Evangelos Senis, a collaborating early stage researcher (ESR) in the SPARCARB project and my closest colleague throughout the whole duration of this PhD.

- The rest of the project’s ESRs: Timothy M. Harrell and Andrea A. M. Laudani for the enjoyable collaboration and moments we spent together during our working and/or free time.
- My lab colleagues Allison V. Shaw and Xinyu Wang for the help with XRD imaging and SEM analysis, respectively.
- My partner M. Angelica Hernandez Colin for the huge support; she was always there for me.
- Friends, house-mates and drinking buddies that spent some of their time with me when I really needed it; to name a few: I. Katsivalis, I. Chatzopoulos, D. Chatzipetros, J. D. Toepfer, D. Manouseli, G. M. Piana, R. Čerňanský.
- My family.

Definitions and Abbreviations

(002)	Graphite lattice spacing
1D material	One-dimensional material
2D material	Two-dimensional material
3RM	Three roll-milling
$Al(OH)_3$	Aluminium hydroxide
APTES	Aminopropyltriethoxysilane
CB	Carbon black
CFRP	Carbon fibre reinforced polymer
$CHCl_3$	Chloroform
CNT	Carbon nanotube
CrO_3	Chromium trioxide
d230	Poly(propylene glycol) bis(2-aminopropyl ether) with average molecular weight of 230 g/mol
d4000	Poly(propylene glycol) bis(2-aminopropyl ether) with average molecular weight of 4000 g/mol
DMA	Dynamic mechanical analysis
DSC	Differential scanning calorimetry
DTG	Differential thermogravimetric
EG	Expanded graphite
eGO	Edge oxidized graphene oxide
fGNP	Functionalized graphene nanoplatelets
fGO	Functionalized graphene oxide
FTIR	Fourier-transform infrared spectroscopy

FWHM	Full width at half maximum
GFRP	Glass fibre reinforced polymer
GNP	Graphene nanoplatelets
GO	Graphene oxide
H_2O_2	Hydrogen peroxide
H_2SO_4	Sulphuric acid
H_3PO_4	Phosphoric acid
hBN	Hexagonal boron nitride
HNO_3	Nitric acid
$I_{(2D)}/_{(G)}$	Raman intensity peak ratio between 2D and G bands
$I_{(D)}/_{(G)}$	Raman intensity peak ratio between D and G bands
$KClO_3$	Potassium chlorate
$KMnO_4$	Potassium permanganate
MDI	Methylene diphenyl diisocyanate
mGO	Moderately oxidized graphene oxide
$NaNO_3$	Sodium nitrate
PE	Polyethylene
PS	Polystyrene
P_t	Percolation threshold
PVDF	Poly(vinylidene fluoride)
rGO	Reduced GO
SEM	Scanning electron microscopy
t	Critical exponent for electrical conductivity

t440	Trimethylolpropane tris[poly(propylene glycol), amine terminated] with average molecular weight of 440 g/mol
TEM	Transmission electron microscopy
T_g	Glass transition temperature
TGA	Thermogravimetric analysis
THF	Tetrahydrofuran
UV/O_3	Ultraviolet/Ozone
V_c	Critical volume fraction
V_f	Volume fraction
vol.%	Volume percentage
W_f	Weight fraction
wt.%	Weight percentage
XPS	X-ray photoelectron spectroscopy
XRD	X- ray diffraction
ΔT_g	Glass transition temperature difference of one sample before and after the post-curing process
ε’	Real part of the complex relative permittivity
ε’’	imaginary part of the complex relative permittivity
ρ_f	Filler density
ρ_m	Matrix density material
σ_c	Electrical conductivity of the composite
σ_f	Electrical conductivity of the filler
σ_m	Electrical conductivity of the unfilled matrix
σ_{max}	Maximum electrical conductivity reported

Chapter 1 Introduction

1.1 Retrospection

The capability of controlling material systems on the molecular scale provided by nanotechnology, despite being obscure and uncertain, renders it one of the key scientific concepts of the early years of the 21st century. A nanostructured material is one where some of its structural features are of the nanometric scale, meaning that at least one of their dimensions is less than 100 nm. Over the last 20 years, materials exhibiting nanometric dimensions have gained attractions to the scientific community and are usually accompanied with novel ideas for advanced applications [1, 2]. Despite the scientific interest in nanostructured materials emerging during the past decades, mankind was utilizing nanotechnology long time ago. An example of nanotechnology in ancient times is the Lycurgus cup, crafted during the late Roman period around the 4th century and has been described as “the most spectacular glass of the period fittingly decorated, which we know to have existed”. Its dichroic optical properties are ascribed to the small portions of gold and silver nanoparticles dispersed inside the glass material [3]. When viewed in reflected light it appears green but, through transmitting light, it appears red, as shown in Figure 1.1.1.

Figure 1.1.1 Lycurgus cup viewed from reflected (left) and from transmitting (right) light. Image reproduced from [1].

---

[1] https://www.smithsonianmag.com/history/this-1600-year-old-goblet-shows-that-the-romans-were-nanotechnology-pioneers-787224/
This 1,600-Year-Old Goblet Shows that the Romans Were Nanotechnology Pioneers
Zeeya Merali, Sep, 2013

Another example of the early usage of nanotechnology is the, so called, Damascus steel, used by the Saracens. The production of this kind of steel started in South India and it was termed “the finest steel in the world” [4]. It was produced as 2.3 kg cakes of steel known as “Wootz” and exported to Damascus, Syria, where the blade-smiths mastered the art of forging into swords with a very specific surface pattern (Figure 1.1.2). Although, the exact and original manufacturing method of Damascus steel blades might still be of a debate, it is known that it consisted of high-purity iron steel with ~1.5% carbon content [5] which resulted in the development of cementite nanowires and carbon nanotubes [6] inside the blade’s metallic matrix, giving it extraordinary mechanical properties.

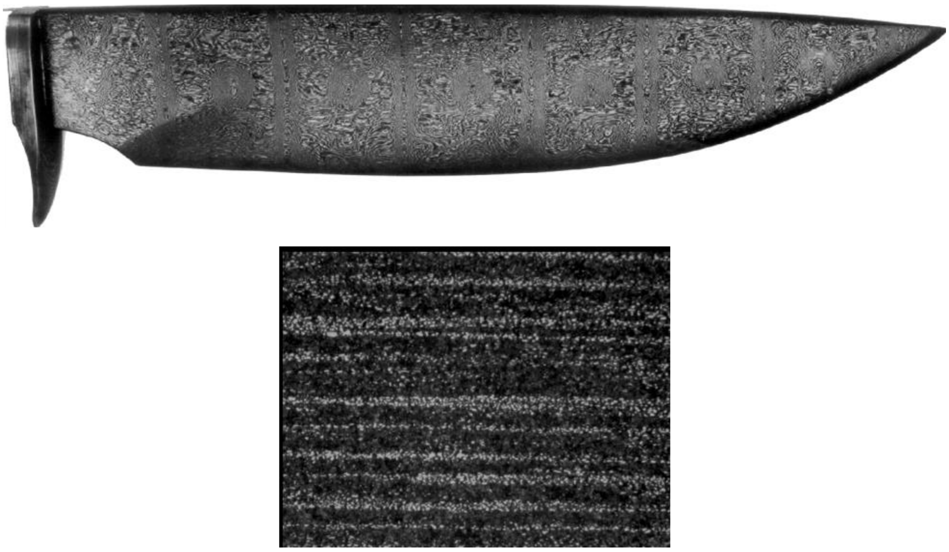

Figure 1.1.2 Up: “Wootz” Damascus blade showing the specific surface pattern.
Down: Longitudinal section of the same blade. Images reproduced from [5].

A more recent example is, the incorporation of nanoscale carbon black (CB) inside rubber compounds such as car tires since 1917. Carbon black is beneficial for improving the toughness and durability of the naturally white coloured rubber Figure 1.1.3a, b) and its addition makes car tires last even 5,000 miles more than the ones manufactured with unfilled rubber [7]. Another recent application of CB is as a polyethylene (PE) filler for the production of semi-conducting shields in power cables (Figure 1.1.3c) due to its good electrical and thermal conductivity (Figure 1.1.3d).

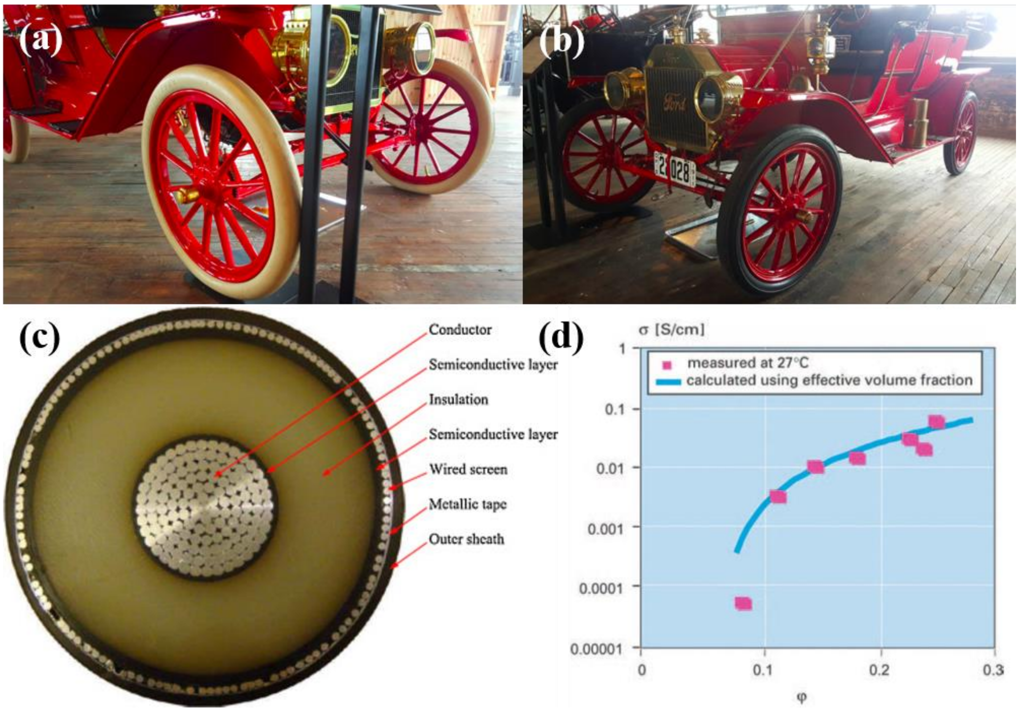

Figure 1.1.3 Carbon black industrial applications: (a) Car tires without and (b) with CB particles[2], (c) Cross section and layers of a typical power cable [8], Variation of the electrical conductivity of PE filled with different volume fractions of CB [9], with a critical fraction of ~0.07 (or ~7 vol. %). Images reproduced from the respective references.

In fact CB particles have been used for thousands of years as a pigment in paints and coatings [10]. The particle geometry of CB is spherical (as portrayed in Figure 1.1.4) and the main production method is by combustion of heavy aromatic oils [10]. Surface oxidation of CB has also been used to tailor its dispersion stability [10].

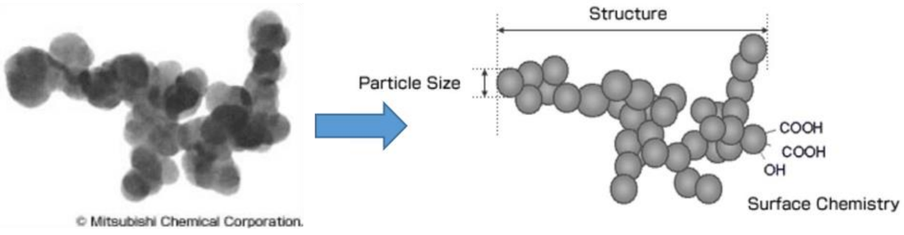

Figure 1.1.4 Left: Electron microscope image of CB and Right: visual representation of CB structure. Images reproduced from [3].

---

[2] https://jalopnik.com/heres-why-tires-are-black-1828925177
“Here’s Why Tires Are Black”, David Tracy, 11/15/18
[3] http://www.carbonblack.jp/en/cb/tokusei.html
“Three Main Properties of Carbon Black” Mitsubishi Chemical

1.2 Research motivation

An emerging sector where nanoparticles, such as the CB that was described above, could find application is renewable energy. Especially by considering the depletion of fossil fuels, as well as the continuously increasing energy requirements, it is deduced that the demand for improved and more efficient renewable energy sources is unavoidable.

Wind energy is one of the fastest-growing sources of electricity worldwide as can be seen in Figure 1.2.1. The global renewable power capacity at the end of 2018 reached 2,471 GW, while it was around 0,840 GW by 2000. Hydropower still has the highest share in the renewable energy total capacity, however between 2000 and 2018 its share has dropped from 93% to 50% as wind and solar power display rapid growth[4] reaching 24% and 20%, respectively at the end of 2018.

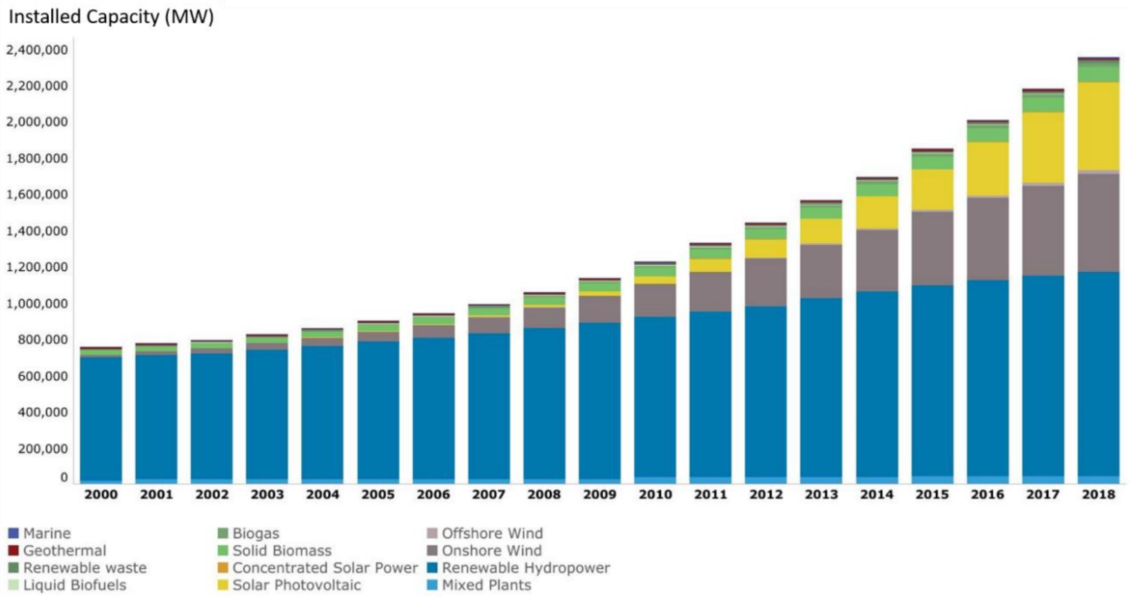

Figure 1.2.1 Cumulative installed renewable power capacity from 2000 to 2018. Image adapted from [5].

In order to meet the energy needs, wind turbine generators and blades are becoming larger to reach high enough standards in terms of production capacity. The upscaling of wind turbines mainly concerns longer blade lengths which is associated with increased mass, thus, structural issues. Those issues are being approached by the industry with the utilization of the lightweight carbon

---

[4] https://www.irena.org/Statistics/View-Data-by-Topic/Capacity-and-Generation/Statistics-Time-Series
International Renewable Energy Agency

fibre reinforced polymers (CFRP)[5,6] instead of the conventional glass fibre reinforced polymers (GFRP) and epoxy resins instead of polyester resins [11]. Besides the light weight, the CFRPs also exhibit relatively high electrical conductivity, contrarily to the insulating GFRPs, a fact that needs to be considered carefully during the design of the lightning protection coordination. The wind turbine blades are the most vulnerable parts to lightning, with each one of them being expected to experience a considerable number of strikes during their service life [12]. According to the international standard requirements[7], in the case of additional conductive components being present within the blade, these parts should be designed to conduct their share of lightning current and thus be connected to the lightning protection system. The blade components mostly considered shifting from GFRP to CFRP, are the spars (Figure 1.2.2).

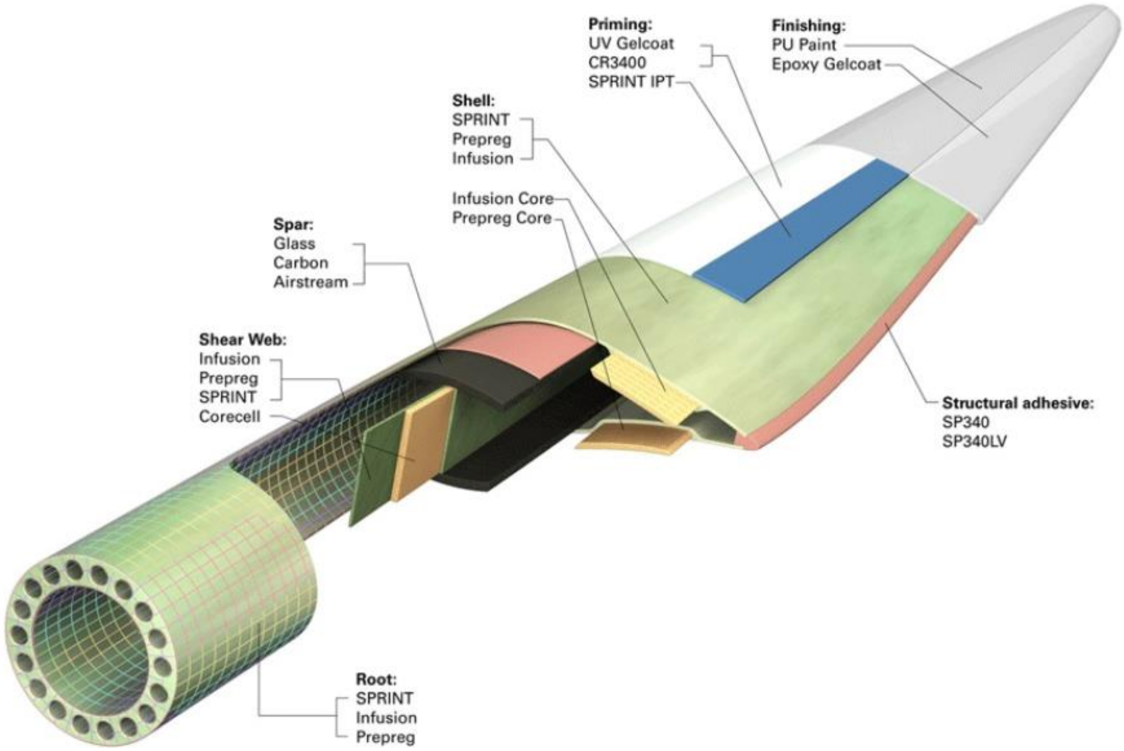

Figure 1.2.2 Typical illustration of a wind turbine blade's structural components. Image reproduced from [8].

---

[5] http://www.compositesworld.com/articles/wind-turbine-blades-glass-vs-carbon-fiber
"Wind turbine blades: Glass vs. carbon fiber", K. Wood, 31 Dec 2012

[6] http://www.windsystemsmag.com/article/detail/149/composite-materials-for-wind-blades
"Composite Materials for Wind Blades", J. C. Watson & J. C. Serrano, 22 Mar 2017

[7] IEC 61400: Wind turbines – Part 24 Lightning protection

[8] http://www.windpowerengineering.com/design/mechanical/blades/building-a-better-turbine-blade/
"Building a better turbine blade, P. Dvorak" , 5 May, 2010

The most common method of production of such components is resin transfer moulding, assisted by vacuum [11], which can be used on dry carbon fabric or on smaller pre-constructed CFRP components placed adjacent to each other. Typically, there are several bonds between the spar and the cable or metallic braid (down-conductor) that is designed to drive the lightning current from the (metallic) tip across the length of the blade to the ground. As a general rule, unidirectional CFRP (Figure 1.2.3) are used for spar components. The electrical and thermal anisotropic characteristics of the unidirectional CFRP [13], as well as the insulating characteristics of the epoxy adhesives in the interfaces are introducing the main challenges in terms of lightning protection coordination. The high currents generated during lightning strikes can be critical especially for the low conductivity directions (transverse and through-thickness) and/or on the epoxy interfaces, due to resistive heating [14]. Consequently, epoxy resins with enhanced electrical and thermal conductivity could serve to mitigate those effects.

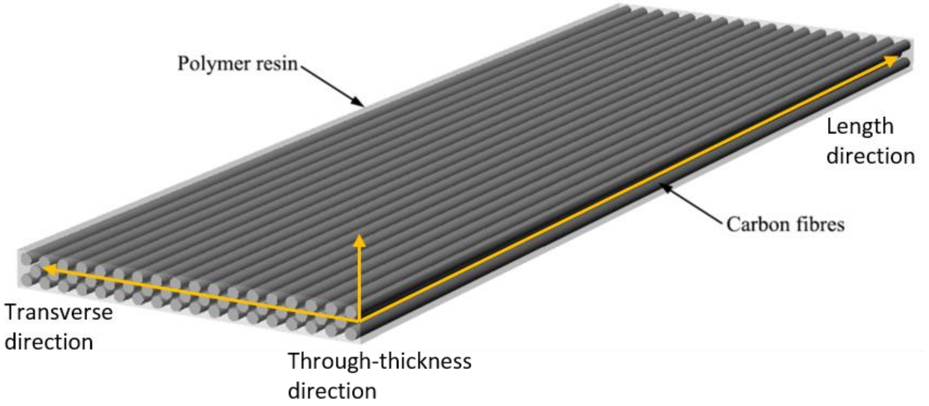

Figure 1.2.3 Schematic representation of unidirectional CFRP. Fibre diameter not in scale. Image adapted from [15].

1.3 Research aims and objectives

The main aim of this PhD project was to modify commercially available epoxy resin specifically used in wind turbine applications and more specifically to:

- Increase its electrical conductivity, above the antistatic limit (10^{-8} S/cm) [16],
- Enhance its thermal conductivity above 0.7 W/mK to match the values of the respective CFRP components in the transverse and through-thickness directions [17]
- Not compromise the mechanical properties of the epoxy system, at least at the filler contents where electrical percolation is achieved.

These aims will act as a means of mitigating the electrical/thermal issues mentioned in the previous section, without putting at risk the main purpose of such components (mechanical support). This was sought to be accomplished with the usage of nanometric particles that allow compliance with industrial requirements. Thus, nanoparticles that display:

- Appropriate filler geometry, to enhance the nanofiller efficiency in terms of mechanical [18], electrical [19] and thermal [20] performance
- Optimised surface chemistry to avoid unwanted epoxy stoichiometry perturbation [21]
- High yield/low cost of filler production [22], and
- Capability of being processed with scalable devices

were synthesised, characterised and incorporated into the epoxy matrix.

1.4 Research Questions & Novelty

Upon discussion on the literature regarding graphene-based materials (Chapter 2), it will be apparent that one of the dominant aspects in tailoring nanocomposite performance is the surface chemistry of GO. Nevertheless, a number of questions will emerge that have to be addressed. Thus, the answers to those questions represent the novelty of the present study.

It will be shown that GO can considerably disrupt the epoxy stoichiometry if used at relatively high filler contents. Such effects have been mentioned in the relative literature but are not yet fully understood. Therefore, the first set of questions is related to such effects:

1. It is assumed that the thermo-mechanical behaviour of GO/epoxy systems might be affected by the temperatures used to cure the epoxy. Is this true, and in which way?
2. Is it possible to trigger crosslinking (thus bonding) reactions in GO/epoxy systems separately?

Upon establishing that the usage of GO for electrical/thermal enhancements is problematical, the second set of questions focuses on tailoring the amount of oxygenated species on the GO surface without adding multiple processing steps.

3. Can we directly synthesize a moderately oxidised GO (mGO) by modifying the existing (efficient and scalable) acidic oxidation processes?
4. If the latter is possible, is the mGO oxygenation degree appropriate to achieve electrical and thermal conductivity enhancements, without compromising the mechanical properties or the stoichiometry of the epoxy?
5. Does the mGO-filled epoxy show improved performance compared to epoxy filled with commercially available EG derivatives?

After the questions on the alternative oxidation route will be addressed, the third and final set of questions focuses on the functionalization of GO.

6. Can we functionalize the previously synthesized mGO product, in order to achieve further electrical and/or thermal improvements?
7. If the latter is possible, which is the optimal surfactant structure, and why?

As such, Chapter 4 will be dedicated to give answers to questions 1 and 2, Chapter 5 will address questions 3, 4 and 5, while Chapter 6 will answer to questions 6 and 7.

1.5 Thesis Structure

An introduction regarding nanocomposites and potential applications is presented in Chapter 1, in order to define the general purpose and main research objectives of this study. Furthermore, questions related to the literature were raised, which will establish the guidelines for the following experimental Chapters.

Chapter 2 is divided in three sections. The first section (2.1) introduces several crucial aspects regarding the particle geometry and its effect on the nanocomposite performance (mechanical, electrical and thermal), as well as the industrial challenges emerging from the usage of such systems. In the second section (2.2) a review over graphene-based materials will be presented, which will mainly focus on production methods, especially for graphene oxide, as well as characterization strategies of such systems. The third section (2.3) includes a state of-the-art review of the recent advances regarding graphene-filled epoxy nanocomposites and discussion on the achieved mechanical, electrical and thermal performance as well as chemical considerations regarding the epoxy stoichiometry. At the end of Chapter 2 a summary on the related literature is presented.

Chapter 3 presents the experimental methods used for the purposes of this study, including the materials utilised and the characterization they underwent.

The results of the material characterization, as well as the interpretation, discussion and comparison with the literature will be presented in Chapters 4, 5 and 6. The main topic of Chapter 4 is the characterization of GO/epoxy nanocomposites with focus on the crosslinking reactions; how they are affected by the processing temperatures and the impact on the physical properties of the respective nanocomposites. Chapter 5 is dedicated on demonstrating the benefits of an alternative, single-step synthesis route in which CrO_3, is used instead of $KMnO_4$, in an attempt to reduce the extent of graphite oxidation in a moderate degree and minimise perturbation with the epoxy crosslinking while maintaining sufficient matrix compatibility. The resulted moderately oxidized graphene (mGO) is compared to the commonly used commercially available, low-oxygen content graphitic products by characterizing the respective epoxy nanocomposites. Chapter 6 considers functionalisation of the synthesized mGO by grafting various molecules on the surface in order to achieve furtherly improved performance of the respective nanocomposites.

Finally, Chapter 7 presents a general conclusion on the achievements of this work, with respect to the questions raised upon the literature and suggests possible future work derived from the impact of this study.

Chapter 2 Polymer Nanocomposites & Graphene-Based Nanomaterials

2.1 Theoretical Background on Polymer Nanocomposites and the Benefits of Non-Spherical Nanoparticles

The usage of any filler in polymers serves either to reduce the cost or to modify the properties of the system [23]. Polymers containing fillers with at least one nanometric dimension (<100nm) have attracted a significant amount of scientific interest the past decades and are known as polymer nanocomposites [2]. The major characteristic of nanometric fillers (or nano-fillers) is that, as a result of their significantly small size the interfacial area between them and the host matrix is dramatically increased compared to traditional micrometric fillers.

2.1.1 Particle geometry

One of the most crucial parameters that affects the optimum filler content is the particle geometry. The filler shapes can be typically categorized in: spherical particulates (like the CB mentioned in Chapter 1) with nanometric characteristics in three dimensions, tubes/rods with two nano-dimensions (also called 1D materials) and platelets/layered structures with one nano-dimension (also called 2D materials) [24]. Each geometry (Figure 2.1.1) displays different surface/volume relations depending mainly on the nanometric dimension.

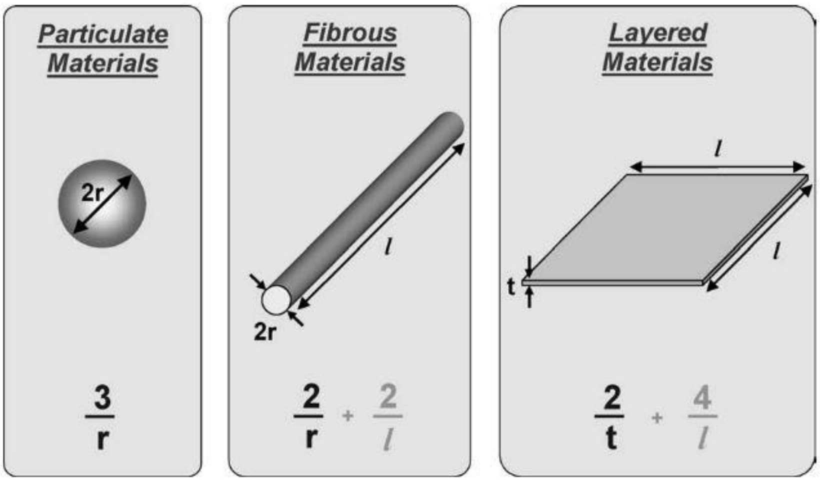

Figure 2.1.1 Representation of different particle geometries and their respective surface/volume relation. Image reproduced from [1].

If dispersed properly, non-spherical particles can display nano-dimensions (diameter for 1D and thickness for 2D materials) noticeably smaller when compared to the diameter of spherical nanoparticles. Therefore, the surface/volume ratios of tubes and platelets are sufficiently larger, which facilitates the interactions with the matrix.

Another important factor dictating the nanoparticle's interaction surface can be quantified by the, so called, *aspect ratio*, i.e., the ratio of the longest to the shortest dimension. While spherical inclusions display low aspect ratios (~1), the other two geometrical configurations can show higher values. Particles with platelet-like geometry like clays and layered silicates, can exhibit aspect ratios of up to a few hundreds. Tubular particles such as carbon nanotubes, can display aspect ratios up to a few thousands [16]. As a generic rule the shape/aspect ratio relation is as follows:

Spherical
Platelets (or Layered)
Tubes (or Rods)
↓ Increasing Particle Aspect Ratio

Both parameters described above, (i.e. increased surface/volume and aspect ratio) underline the significance of well dispersed non-spherical particles which have been repeatedly reported in the literature and represent the most crucial parameters towards nanocomposites with advanced mechanical, electrical and thermal performance. As such, the importance of such parameters will be discussed below.

2.1.2 Mechanical Reinforcements

As mentioned earlier, one of the main considerations in the case of nanocomposites has been the mechanical reinforcement. As such, a few examples of mechanical improvements are presented in Figure 2.1.2. The enhanced surface characteristics of nanoparticles, mentioned earlier, enable effective mechanical reinforcement, through stress-transfer from the relatively soft matrix to the rigid fillers [18]. More specifically, the polymer adjacent to the filler's surface becomes highly constrained and therefore mechanically reinforced, as depicted in Figure 2.1.2a. Assuming that the interface, or bonding, between filler and matrix allows it, the filler might carry a considerable portion of the applied stress. This mechanism applies both for 1D and 2D materials, with the latter geometry showing larger surfaces, thus greater reinforcing effect. An example of the effect of clay on the elastic modulus of nylon-6-based nanocomposites (mentioned earlier) is presented in Figure 2.1.2b. Similar effects have been observed in the case of tensile strength performance, albeit at relatively smaller filler contents, since this property is very sensitive to agglomeration [18]. Furthermore, surface modification might lead to altered or even furtherly enhanced performance via improved filler/matrix interfaces, as shown in Figure 2.1.2c. However, exceptions to this mechanism might occur depending on various parameters. An example is presented in Figure

2.1.2d, where the clay particles impair the crosslinking of polyester resin resulting in decreased elastic modulus.

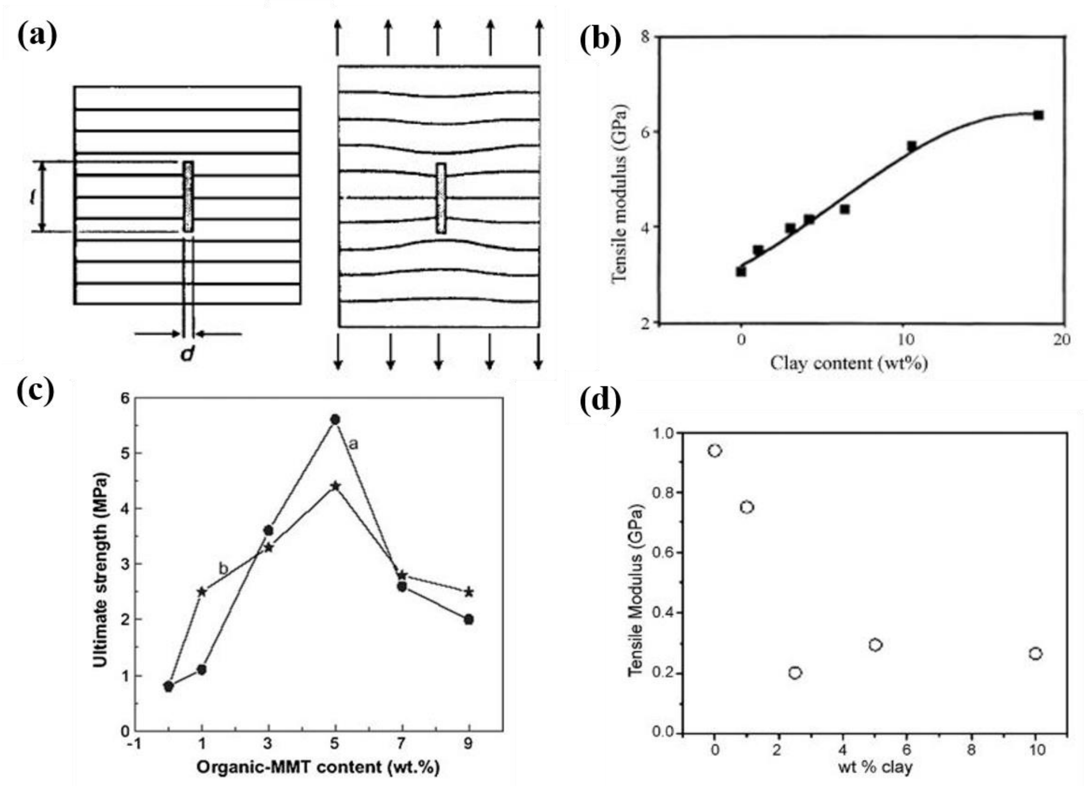

Figure 2.1.2 Mechanical reinforcement mechanism in composite materials filled with 1D or 2D particles of length *l* and diameter or thickness *d* [18]. (b) Effect of clay content on the elastic modulus of nylon-6-based nanocomposite [25]. (c) Tensile strength of polyurethane filled with clays modified in two different ways [26]. Elastic modulus of crosslinked polyester/clay nanocomposites [27]. Images reproduced from the respective references.

Moreover, platelet-like particles like graphene have been shown to effectively inhibit the crack propagation occurring within polymer matrices, resulting in increased strength values [28]. However, as stated above, this would only be achieved when the particles are finely dispersed and distributed within the host polymer. A poor dispersion/distribution and the subsequent agglomeration phenomena are detrimental for the mechanical performance of composites and regardless the size (micro or nano) of the filler, agglomeration reduces the strength and produces weaker materials [29], as stated earlier.

2.1.3 Electrical Conductivity Improvements

The enhancement of the electrical conductivity of polymers is another common objective addressed with the usage of various electrically conductive particles. Filler geometry represents a crucial parameter for this, as well. Traditionally, composite materials consisting of conductive fillers receive considerable research attention due to the diversity of applications they can find in electronics and antistatic devices, thermistors, etc. [30], as well as the applications mentioned in Chapter 1. In general, the conductivity of an insulating matrix containing an electrically conductive phase follows the percolation power law [31–33] and varies according to:

$$\sigma_c = \sigma_f (V_f - V_c)^t \qquad \text{(Equation 1)}$$

where σ_c and σ_f are the electrical conductivity of the composite and the filler respectively, t is a constant representing a critical exponent of the electrical conductivity and V_c is the critical fraction for which the composite exhibits a sharp conductivity increase. That is, V_c represents the so called *percolation threshold* (P_t). Definitions of P_t may vary with different studies defining it as: the volume fraction at which the particles form contiguous paths through physical contact, sharply increasing the electrical conductivity [34]; when the conductivity surpasses the antistatic limit (10^{-8} S/cm) [16]; or even when the system starts behaving non-linearly [35]. The most common interpretation is the first one, which usually converges well with the linear fitting into Equation 1. Theoretically, a system containing randomly dispersed spherical, conductive particles would be expected to be characterized by a percolation threshold at about 15 vol.% and a value of $t \approx 2$ but, in practice, significant divergences occur [35]. Lower percolation thresholds are expected from fillers with high aspect ratios [19] as illustrated in Figure 2.1.3a. Additionally, the values of the constant t are calculated from Equation 1 (usually mentioned as log-log plot) can also vary [36–38], depending on the, geometry and intrinsic properties of the filler. Figure 2.1.3b, shows conductivity values of poly(vinylidene fluoride) (PVDF) filled with CNT, where the P_t (mentioned as m_c) and the constant t show dependency on the aspect ratio as well as the intrinsic filler properties. More specifically, a ball-milling process decreased the CNT aspect ratio (blue) while acid treatment reduced the intrinsic CNT conductivity (green).

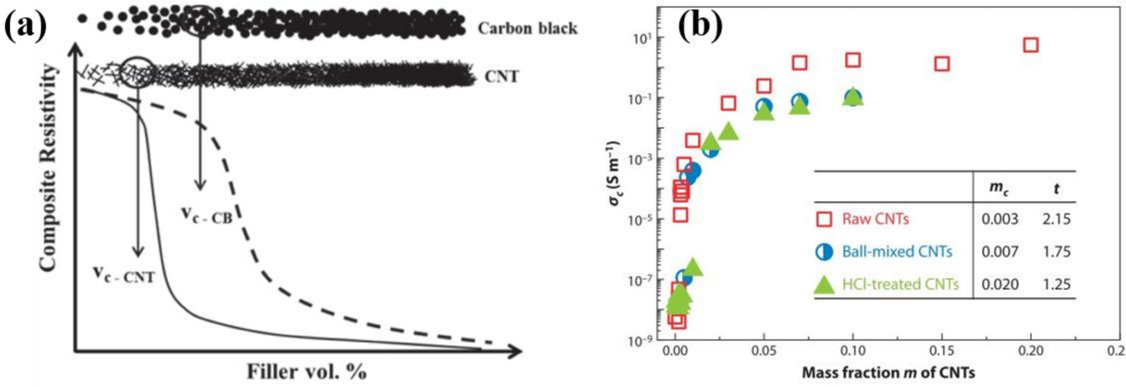

	m_c	t
□ Raw CNTs	0.003	2.15
◐ Ball-mixed CNTs	0.007	1.75
▲ HCl-treated CNTs	0.020	1.25

Figure 2.1.3 (a) Qualitative illustration of the dependence of the percolation behaviour on the filler geometry considering spherical and 1D particles [39], (b) Dependence of the σ_c as well as the percolation parameters of PVDF/CNT systems and the effect of different treatments on CNT [38]. Images reproduced from the respective references.

Taking into account the relations between aspect ratio and filler geometry, CNT are expected to result in the nanocomposites with the lowest P_t. Indeed, the related literature usually considers 1D materials as superior to 2D materials in terms of percolation performance. Figure 2.1.4 shows two seminal studies of polystyrene (PS) filled either with graphene or CNT, where the two fillers result in similar conductivity values albeit CNT displaying considerably lower P_t. More specifically, graphene resulted in a P_t of 0.1 vol.% (which would correspond to ~0.2 wt.%) while in the case of CNT-filled PS the respective value was 0.045 wt.%. Nevertheless, both fillers show lower P_t compared to the PE/CB systems (spherical geometry) shown in Chapter 1 (Figure 1.1.3d).

Ideally, the percolation threshold should be low enough to maintain satisfactory mechanical properties of the system. As in the case of mechanical reinforcements, a surface modification could also be deployed to improve the filler/matrix compatibility and further decrease P_t. However, as shown in Figure 2.1.3b chemical treatment could introduce parameters that might affect the system's intrinsic properties, thus, electrical behaviour. As such, these parameters need to be taken into consideration carefully.

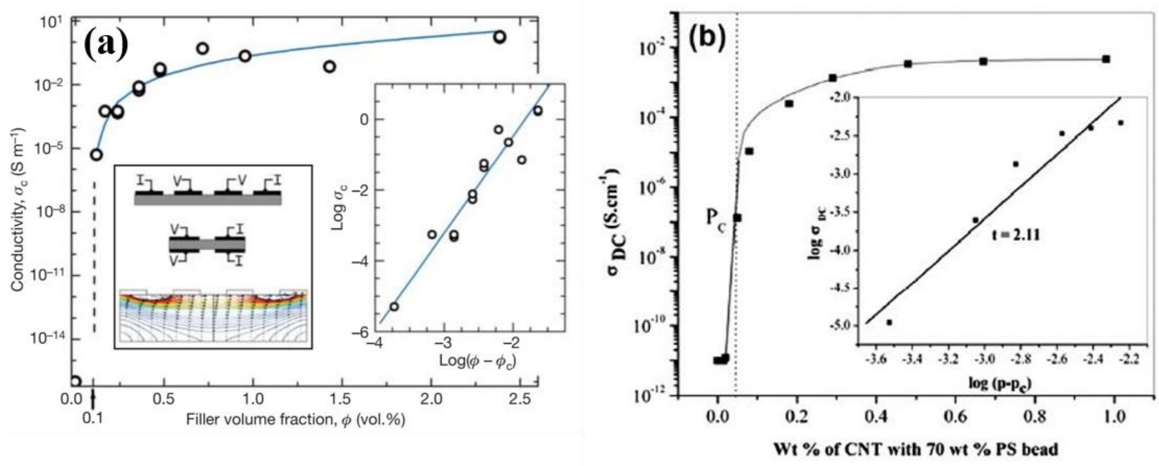

Figure 2.1.4 Polystyrene-based composites filled with (a) graphene [34] and (b) CNT [40], as well as the respective log-log plots included in the respective insets. P_t values are 0.1 vol% and 0.045 wt%, respectively. Images reproduced from the respective references.

2.1.4 Thermal Conductivity Enhancements

Another material property that is commonly enhanced with the usage of nanoparticles is thermal conductivity. In general, heat transfer in solids occurs due to thermal conduction and/or irradiation. The former is the main mechanism concerning our scope, which fundamentally corresponds to transfer of vibrational energy (phonons) through particle collisions. Thermal conduction is facilitated in crystalline (thus highly ordered) materials (Figure 2.1.5a) due to the tightly packed structure. Contrarily, amorphous materials, such as polymers, inhibit heat transfer due to the absence of a compact lattice. Thus, heat diffusion occurs through transmission of disordered vibrations/rotations of monomers/atoms towards the adjacent ones (Figure 2.1.5b). Incorporation of small amounts of crystalline nano-fillers into polymer matrices creates “thermal interfaces” or phonon/interface scattering due to the subsequent alteration of the heat transport mechanism (Figure 2.1.5c) which may be responsible for further inhibition of heat transport and reduction of the system’s thermal conductivity.

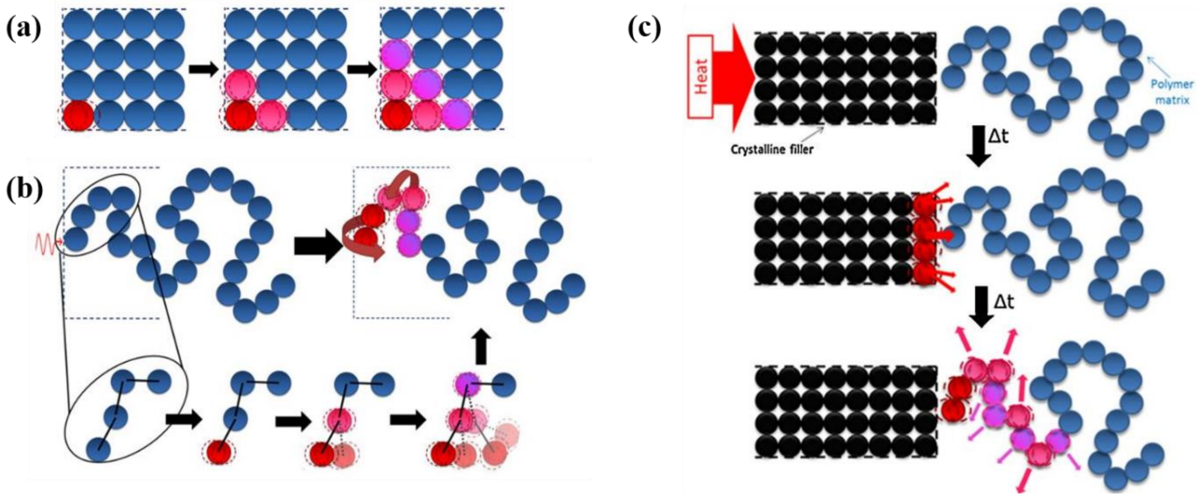

Figure 2.1.5 Thermal conduction mechanism in: (a) crystalline (b) amorphous (c) composite (combination of the two) materials. Images reproduced from [20].

Furthermore, the thermal conduction mechanism is very “sensitive” to defects compared to electron conduction. Small lattice defects can cause significant thermal resistance, an effect called “Kapitza resistance” or phonon/defect scattering as depicted in Figure 2.1.6. Finally, phonons can be scattered even while transmitting through the same medium due to anharmonicity and vibrations at different frequencies; an effect usually called “umklapp” or phonon/phonon scattering [20].

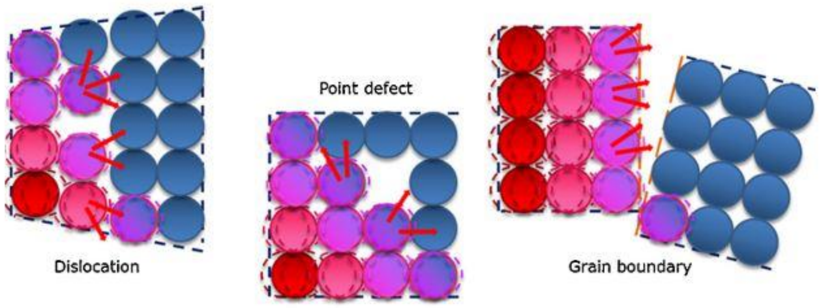

Figure 2.1.6 Phonon/defect scattering in crystalline materials. Image reproduced from [20].

These three effects (phonon/interface, phonon/defect and phonon/phonon scattering) separate the thermal conductivity of materials from the electrical in several aspects: Typically, electrical percolation is not followed by sharp thermal conductivity increase rather by a gradual and linear increase, as shown in Figure 2.1.7, thus substantial thermal conductivity enhancements are expected at rather larger filler contents.

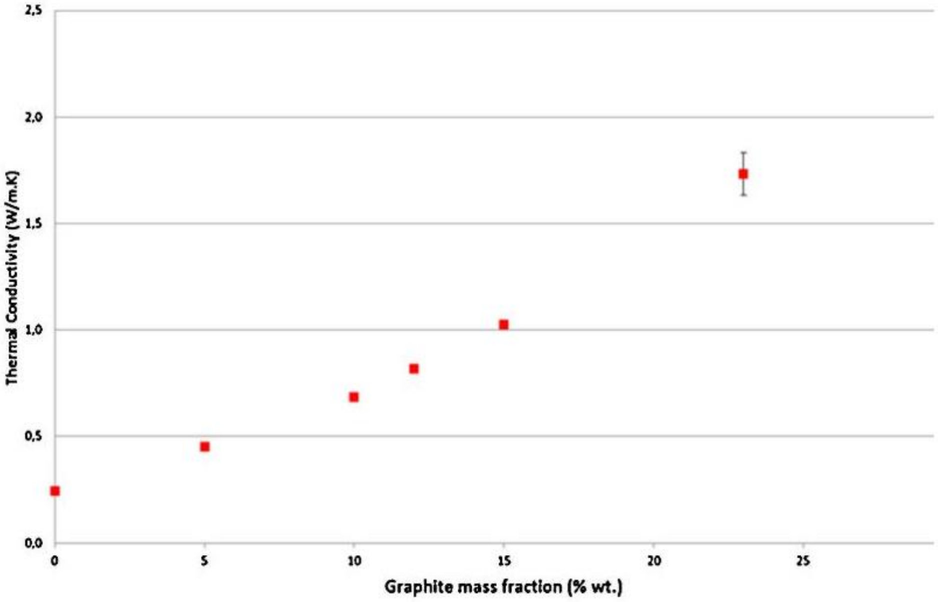

Figure 2.1.7 Typical thermal conductivity enhancement of epoxy resin filled with various contents of graphite. Image reproduced from [20].

Furthermore, it is impossible to fully benefit from the filler's intrinsic properties since its effective thermal conductivity will be drastically decreased when incorporated in polymers [41], due to the phonon scattering phenomena explained above. Also, fine dispersion within the matrix does not necessarily lead to enhanced thermal conductivity, as depicted in Figure 2.1.8. From the above it is implied that replacement of microparticles with nanoparticles would not necessarily result in improved thermal conduction, due to the increased interface resistances, hence strategies such as impairing the particle dispersion method [28] or increasing the particle size [42] appear to be more effective. However, these methods do not comply with the general scope of nanoparticle utilization, or with the mechanical/electrical aspects that were mentioned earlier to require fine dispersions.

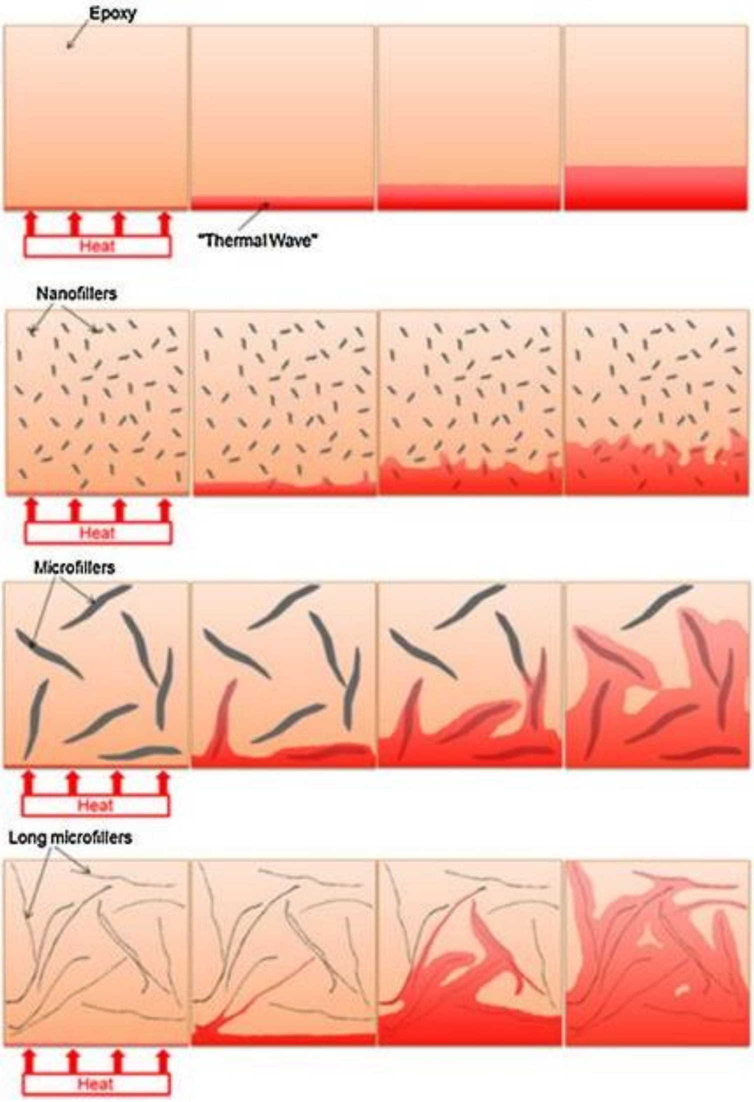

Figure 2.1.8 Heat transfer dependency on the filler's geometry. Image adapted from [20].

As far as nanometric particles are concerned, improvements can be sought through increased aspect ratios [43–46], or through improved filler/matrix bonding [16, 47, 48], achieved by particle surface treatment. Typical non-spherical fillers for thermal conductivity enhancements are the 1D CNT and the 2D graphene or hexagonal boron nitride (hBN), the structures of which are illustrated in Figure 2.1.9. Particle geometry has been shown to be of great importance when mechanical, electrical and thermal performance enhancements are required. However, it was claimed that in order to show the preferred performance, the particles need to be efficiently dispersed into the respective polymer matrices. As such, characterization of the dispersion level will be discussed in the next section.

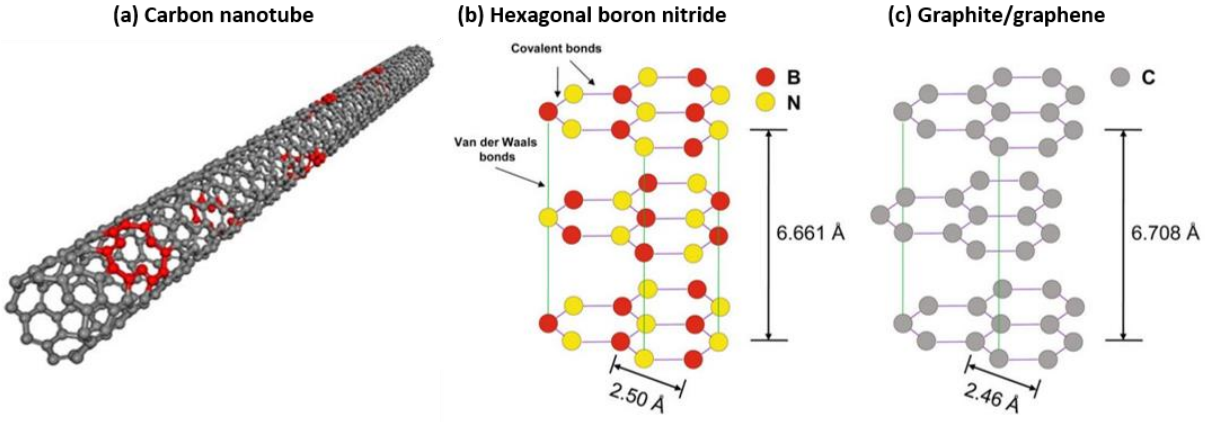

Figure 2.1.9 Structure of: (a) CNT (defects denoted red) [20], (b) hBN [49] and (c) graphite/graphene [49]. Images reproduced from the respective references.

2.1.5 Morphology

The aspects of particle dispersion and distribution are different and should not be confused with each other. The distribution of nanoparticles throughout the entire matrix may appear fine, displaying no matrix-rich areas, although particle agglomeration at a nanometric level (thus poor dispersion) might still exist, as shown in Figure 2.1.10b. Similarly, fine nano-dispersion (particle disaggregation) might occur without the particles being finely distributed, thus forming particle clusters, as illustrated in Figure 2.1.10c.

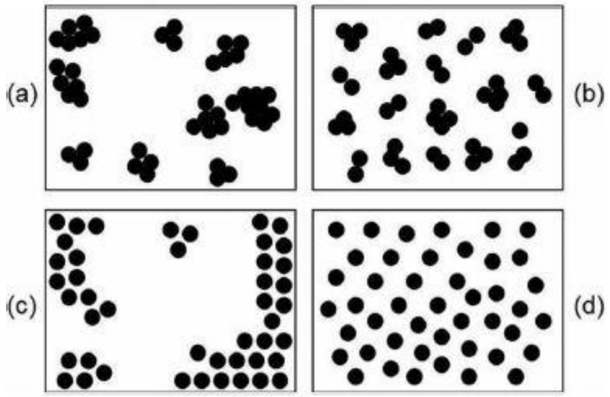

Figure 2.1.10 Qualitative representations of (spherical) particle distribution and dispersion, showing combinations of: (a) poor distribution with poor dispersion; (b) fine distribution with poor dispersion; (c) poor distribution with fine dispersion; (d) fine distribution with fine dispersion. Image reproduced from [50].

While it was discussed earlier that the usage of non-spherical nanoparticles can be beneficial in many ways, the downside of such structures, and especially layered nanoparticles, is that they tend to agglomerate and self-assemble more intensely when compared to spherical geometries [51]. Figure 2.1.11 illustrates the aggregation tendency, and thus, the difficulty of separation/dispersion, depending on the geometry of the nanomaterial.

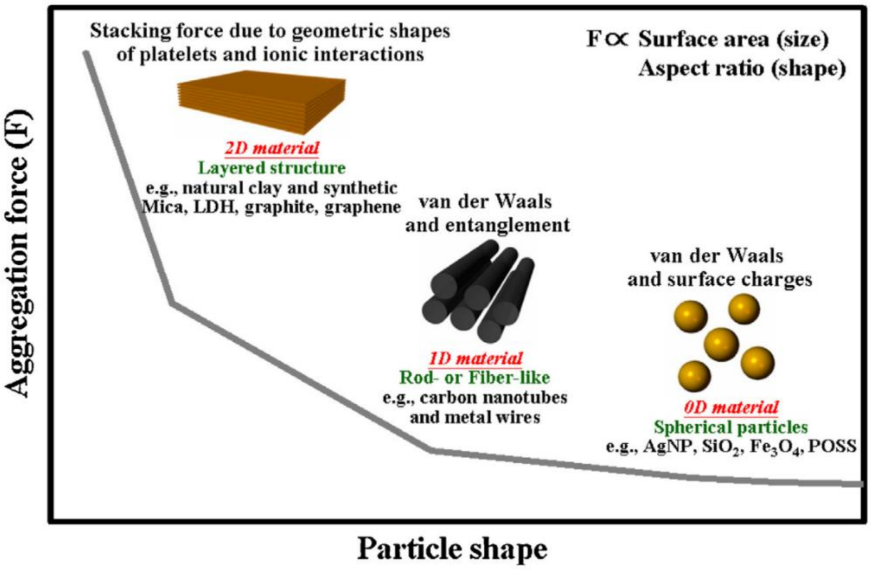

Figure 2.1.11 Dependence of the nanoparticle tendency to re-aggregate on their geometry features. Image reproduced from [51].

When introduced into polymer matrices, due to their lamellar nature, 2D materials display three dispersion levels, namely: phase separated, intercalated and exfoliated [52], as displayed in Figure 2.1.12. The first level is a phase separated state, which is caused by immiscibility of the constituents. The second stage is an intercalated phase in which the platelets remain partially stacked with polymer chains infiltrating in between. In the third, and most desired, stage the platelets display a randomly oriented (exfoliated) configuration with no stacking sequence between them. This third stage results in the highest surface/volume and aspect ratio values, as well as filler/matrix interactions.

Since phase separation represents poor dispersion and formation of relatively large clusters it is considered deleterious for composite performance; an intercalated configuration, or ideally exfoliated, would be preferable. Therefore, evaluation of the dispersion level is crucial in order to deliver the desirable properties of nanocomposites materials. For nanocomposites filled with 2D nano-fillers the most widely used techniques in terms of morphological characterization are: transmission electron microscopy (TEM), scanning electron microscopy (SEM) and X-ray diffraction (XRD) [18, 24, 52, 53].

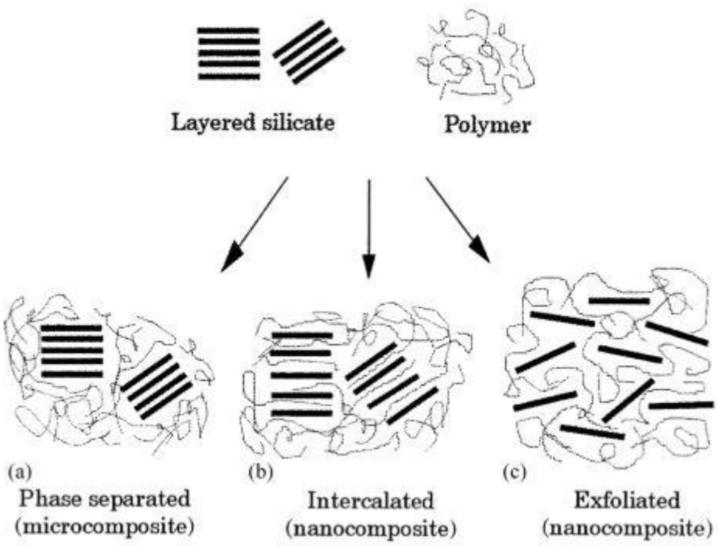

Figure 2.1.12 Dispersion levels for layered materials. (a) Phase separated, (b) intercalated and (c) exfoliated. Image reproduced from [54].

Combination of the abovementioned microscopy techniques and connection of the examined morphology to the examined properties results in fundamental understanding of the nanocomposite behaviour. An example is given in Figure 2.1.13 where both SEM and TEM imaging were used to characterize the morphology of epoxy/CNT nanocomposites and correlate it to the percolation behaviour of those systems. More specifically, four different preparation methods were used to incorporate CNT into the epoxy matrix, as shown in Figure 2.1.13a, namely conditions A, B, C and D, aligning with the complexity of each method. As such, condition D was the most complex, including multiple steps of surface treatment, solvent mixing and sonication. It can be seen in the TEM images that the disaggregation/disentanglement of the CNT is aligning with the complexity of the preparation method, with condition A showing the highest packing density or degree of entanglement. Accordingly, SEM imaging suggested that by adding more parameters to the preparation method the distribution of CNT is improved from big clusters (A) to uniformly distributed particles (D) with coexistence of the two stages being found in conditions B and C. Despite these improvements, the electrical behaviour of the respective nanocomposites is not complying with the characteristics described above, with condition D showing no percolation threshold at all due to impaired aspect ratio and reduced intrinsic CNT electrical conductivity, caused by the excessive treatment. The system with the highest degree of performance was sample B, which showed coexistence of poor and fine distribution and dispersion. It is implied that the sonication method that was followed in (B) is more effective than the shear mixing that was followed in (A). Furthermore, surface treatment (C) served to improve the P_t compared to (A) however the achieved electrical conductivity upon percolation was relatively lower compared to the rest of the samples, due to reduced intrinsic properties.

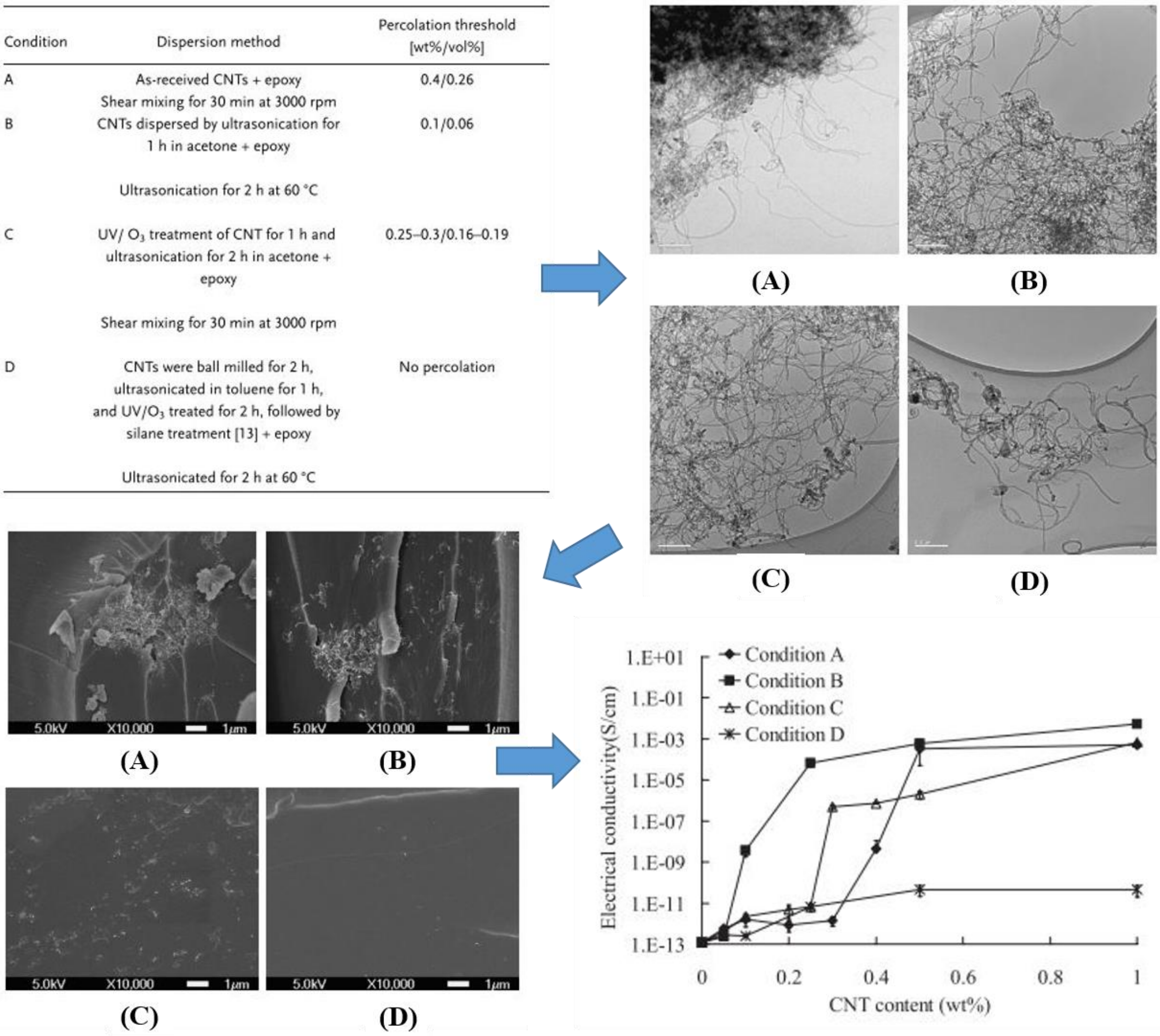

Condition	Dispersion method	Percolation threshold [wt%/vol%]
A	As-received CNTs + epoxy Shear mixing for 30 min at 3000 rpm	0.4/0.26
B	CNTs dispersed by ultrasonication for 1 h in acetone + epoxy Ultrasonication for 2 h at 60 °C	0.1/0.06
C	UV/ O_3 treatment of CNT for 1 h and ultrasonication for 2 h in acetone + epoxy Shear mixing for 30 min at 3000 rpm	0.25–0.3/0.16–0.19
D	CNTs were ball milled for 2 h, ultrasonicated in toluene for 1 h, and UV/O_3 treated for 2 h, followed by silane treatment [13] + epoxy Ultrasonicated for 2 h at 60 °C	No percolation

Figure 2.1.13 (Upper left) Processing methods followed to disperse CNT into epoxy. (Upper right) TEM images, (Lower left) SEM images, and (Lower right) percolation behaviour of the respective epoxy/CNT composites. Images reproduced from [46].

Therefore, it is claimed that excessive treatment/preparation could result in detrimental effects on the filler geometry and/or intrinsic properties while at the same time the dispersion/distribution is improved. Therefore, the preparation method should be carefully taken into consideration. Details on the manufacturing methods of polymer nanocomposites can be found in Appendix A.

2.1.6 Industrial Challenges – Health and Safety

While the research interest in nanocomposite materials has grown over the last decades, their entrance into the market, is somewhat delayed and the respective products are relatively rare. Apart from the lack of total understanding and prediction of the behaviour of nanoparticles in some cases, it is worth mentioning that safety and environmental issues represent drawbacks and difficulties in material processing.

Several handling guidelines should be taken into consideration, such as personal protection equipment, ventilated environment, disposal system, monitoring of the amounts of chemicals used, etc. Even though these rules are easily applied to the small-scale experiments that academia carries out, this is not the case for large-scale production in industry. Some of the precautions for nanomaterial handling are: new regulations and toxicology studies, new production processes and tools, minimization of people working with nanoparticles, personal protective equipment as well as minimization of time spent in the environment for the ones who do [55]. All of the abovementioned render “nanotechnology” costly, time consuming and discouraging for the industry.

The field of science associated with health and safety issues of nanoparticle handling is called “Nanotoxicology” investigating the hazards of nanoparticles while inside the body, such as oxidation [55], or the potential environmental hazards, such as the inhibition of root growth in plants [56]. Generally, nanoparticles can penetrate the human body in three ways: skin penetration, inhalation and digestion. The former is the least likely because of the thickness of the skin [57], but there are still possibilities, when wounded or cut skin are involved. Inhalation is more likely to occur and more dangerous considering the large surface area of human lungs [55]. Digestion starts from incomplete inhalation as some of the particles are accumulated in the mouth and end up in the digestion system along with the food. From there, the nanoparticles can end up in the liver and spleen [58]. As discussed above, the aspect ratio can be very crucial in the final outcome of the nanocomposite final properties. However, fibrous materials like CNTs or asbestos are well known to cause health issues. In the case of asbestos, it has been reported as the cause of mesothelioma, a type of cancer on the tissue of internal organs [59]. CNT exposure can lead to cytotoxicity, inflammatory cell influx, interstitial fibrosis in the lung, lung tumorigenesis and various other systemic effects [60]. Hence, the usage and the exposure of 1D materials are limited and therefore, their industrial applicability is limited. Since 2D nanomaterials display less toxicity concerns than 1D materials, their usage would be preferable compared to particulate shaped fillers due to their aspect ratio, as stated above. Health concerns related to graphitic-based nanoinclusions are presented in the extensive review by Ou et al. [61] where GO is claimed to be one of the least hazardous due to its surface functionality, rendering it even biocompatible in some cases.

2.2 Graphene-based Materials

In the previous section parameters concerning polymer nanocomposites such as the nanoparticle geometry, surface and aspect ratio, as well as the particle dispersion/distribution were discussed. Also, the health and safety challenges and how they are affected by the nanoparticle geometry were addressed. Therefore, the choice of the filler used in this study should comply with all the above-mentioned parameters.

Carbon has several allotropes (Figure 2.2.1) of different geometries and properties, while more of them are still being discovered and synthesized [62, 63]. These allotropes exist or can be reduced to nanometric dimensions and used as nanofillers.

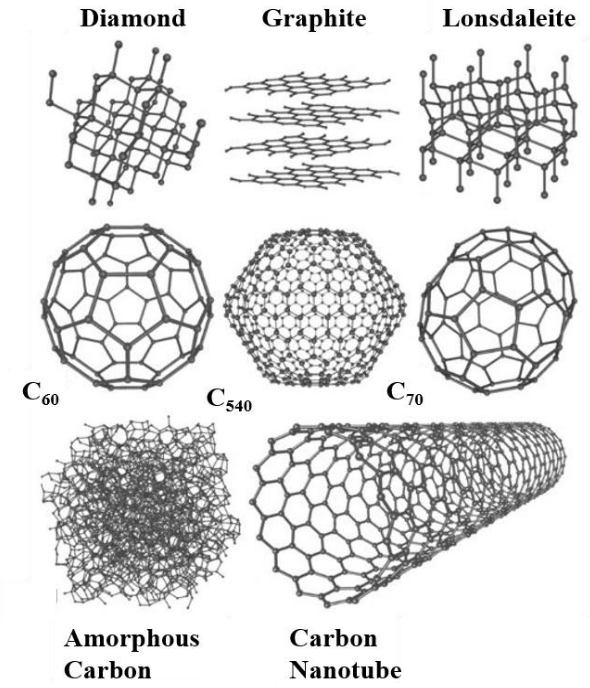

Figure 2.2.1 Various carbon allotropes. C_{60}, C_{540} and C_{70} represent fullerenes with the associated number of carbon atoms. Image adapted from [9].

Apart from mechanical reinforcements, many studies have been undertaken with a view of enhancing the electrical and thermal performance of the polymeric matrices, and this is commonly addressed with the incorporation of carbonaceous fillers, such as carbon black [64], graphite (EG) [42] carbon nanotubes [16], or even a combination of such systems [65, 66].

---

[9] https://courses.lumenlearning.com/boundless-chemistry/chapter/carbon/
Lumen, Boundless Chemistry, Nonmetallic Elements, Carbon

The nanometric equivalent of graphite is the 2D graphene which complies with all the above mentioned characteristics and, thus, is the material of interest in the current study. Therefore, a literature review on graphene-based materials, methods of production and/or functionalization, as well as their utilization in epoxy matrices, will be discussed below.

2.2.1 Production of Graphene-based Materials

Graphite is a natural layered material, the crystal lattice of which consists of an assembly of two-dimensional sp^2 hybridized graphene sheets stacked together. The key prerequisite for the exploitation of graphite's properties as a polymer filler [54, 67] is, for reasons explained earlier, layer separation and intercalation/exfoliation within the host matrix. Production of graphene especially for large scale industrial purposes such as the ones mentioned in Chapter 1 will require large scalability and yields combined with a relatively low cost. Among the existing methods (see Figure 2.2.2) the reduction of graphene oxide and the liquid-phase exfoliation offer the highest scalability accompanied by a relatively low cost, however the latter one has the drawback of very low yields.

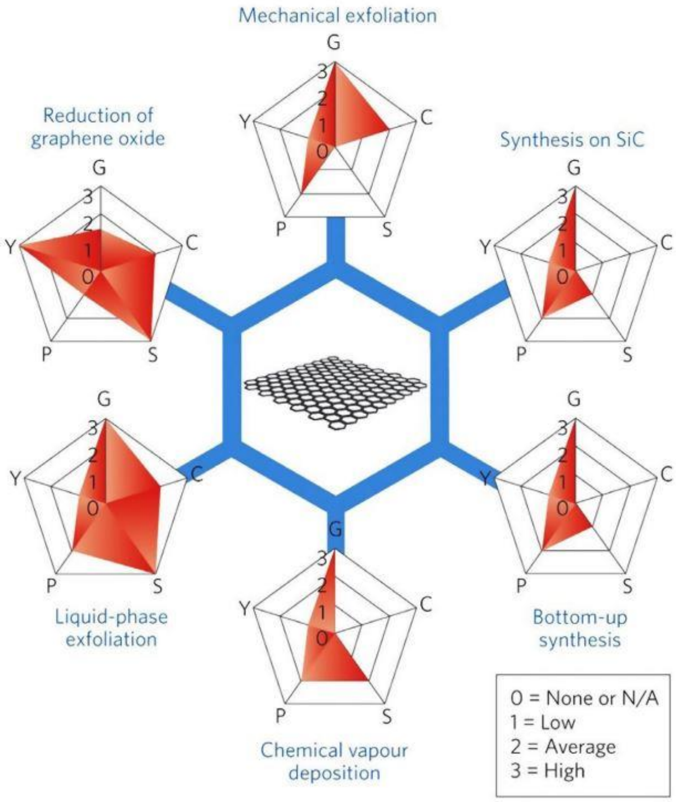

Figure 2.2.2 Common methods for graphene production. Evaluation is shown in terms of: (G) graphene quality, (C) cost of production (low values represent high costs), (S) scalability, (P) purity and (Y) yield. Image reproduced from [22].

One strategy stemming from the two methods described above is the production of the so-called expanded graphite (EG), which is commonly produced by acidic intercalation of graphite, followed by exposure to elevated temperatures (typically > 600 ^{o}C [68]) and thermal shock [69]. The latter process leaves residual carboxylic groups attached on the graphitic layer edges, resulting in slight edge oxidation [70]. Alternatively, the graphite can be directly exfoliated via sonication inside liquid solutions [71]. The isolation of graphene in 2004 [72] has subsequently generated vast global interest regarding its extraordinary properties [73, 74] and the technological utilization of graphene nanoplatelets or else edge-oxidised graphene oxide (GNP and eGO respectively) has, over the last decade or so, been extensively explored [54, 75]. These layered structures can be produced by various routes, as reviewed by Jang et al. [76], which typically include a further step after the production of EG in order to reduce the size to the nanometric scale. The downside for this method is that EG-based products are considered poorly compatible and/or exfoliated [75], thus optimization of the processing method is necessary [68].

An alternative route to layer exfoliation is through acidic oxidation and synthesis of oxidized graphite, consisting of graphene oxide (very often termed GO) layers [77]. GO exhibits a loosely packed layered structure in which the surfaces are decorated with a range of oxygen-based functionalities, resulting in a mixed configuration composed of both sp^2 and sp^3 hybridized carbon atoms [78]. Despite debate concerning the precise chemical structure of graphene oxide, the most widely adopted configuration (Lerf-Klinowski model) [79] involves basal planes decorated with epoxide (-O-) and hydroxyl (-OH) groups, while the peripheral planes contain carboxyl groups as can be seen in Figure 2.2.3.

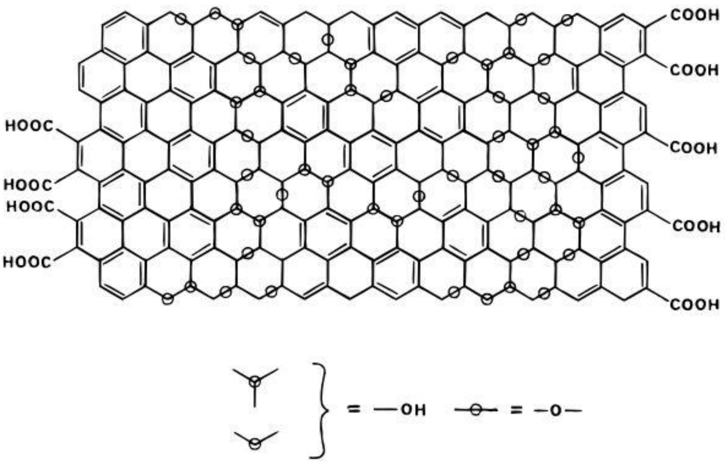

Figure 2.2.3 Structure of GO according to the Lerf-Klinowski model, reproduced from [79].

The existence of these groups beneficially increase hydrophilicity [78], inter-layer distance [80], organic solvent solubility [81] and compatibility with polymer matrices [82]. All of these factors enhance exfoliation within polar solvents/polymers [83, 84] and can ease the production of polymer-based nanocomposites. The downside for this method is that GO exhibits inferior mechanical [54], electrical [85] and thermal [86] properties, compared with the pristine graphene, due to the functional groups on its surface acting as defects. Therefore, additional, thermal or chemical procedures should be used to reduce the amount of impurities/functionalities and obtain reduced GO (rGO) with structure/properties more similar to that of graphene [85, 87].

Alternatively, the presence of functional groups can be exploited as reactive sites for further surface functionalization [88], either for GNP or GO. Since both GNP and GO display limited or extended oxygen functionality on the respective surfaces [79, 89] covalent bonding is facilitated. This is exploited by furtherly tailoring the surface chemistry of these components with the attachment of preferable chemical groups [90], resulting in the so-called functionalised GO or GNP (fGO and fGNP respectively). A schematic summary of the abovementioned production methods is presented in Figure 2.2.4.

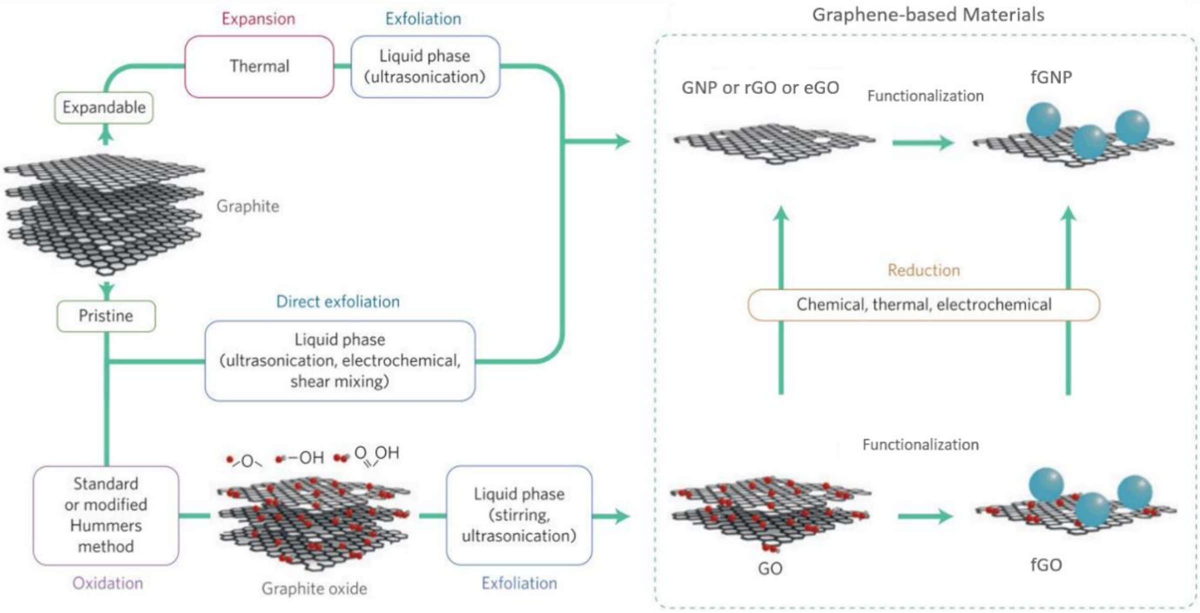

Figure 2.2.4 Summary of the most efficient routes of producing graphene-based materials used as polymer fillers. Image adapted from [22].

2.2.2 Synthesis of Graphene-Oxide

While many methods for the oxidation of graphite have been described, these can broadly be divided into five main categories [91], as seen in Table 2-1. The basic principle of these processes involves the intercalation of graphite in an acidic medium, combined with reaction with an oxidant. The earliest recorded method was reported by Brodie in 1859 [92], utilizing potassium chlorate ($KClO_3$) as an oxidant and fuming nitric acid (HNO_3) as the reaction medium. Later, the reaction medium was modified, first by Staudenmaier [93] by the addition of sulfuric acid (H_2SO_4) and then by Hofmann [94] by the usage of non-fuming HNO_3. All of these methods were hazardous ($KClO_3$ can be explosive and HNO_3 can produce acidic fog) and protracted (about four days). The most commonly used method was developed by Hummers in 1958 [95] and involves the use of potassium permanganate ($KMnO_4$) and sodium nitrate ($NaNO_3$) as oxidants in sulphuric acid (H_2SO_4) and, in this way, the duration of the process was reduced to just a few hours. Recently, it was shown that omission of the highly toxic $NaNO_3$ results in the same quality of product [96], while larger precursor (graphite) flake sizes will result in lower degrees of oxidation, compared with the usage of smaller precursor flakes [97]. Other modifications of the Hummer's method have been reported with varying concentrations of $KMnO_4$ [98], or varying both $KMnO_4$ and $NaNO_3$, as well as duration and temperature of the process [99], resulting in slight alterations of the respective oxygen contents. Finally, further refinement was reported by Tour in 2010 [100] with the usage of only $KMnO_4$ (albeit double amount compared to Hummers method) as oxidant and a mixture of H_2SO_4 and phosphoric acid (H_3PO_4) as the acidic reaction medium. The latter method was developed based on the findings of a previous study [101] showing that the addition of a weaker acid (H_3PO_4) into the H_2SO_4 medium promotes selectivity of the oxidative process, resulting in more intact undecorated graphitic basal planes thus, more regular structure [100]. However, the amount of oxygen groups on the respective GO was higher compared to GO synthesised with the previous methods.

Table 2-1 Summary of the main graphite oxidation processes. Table reproduced from [77].

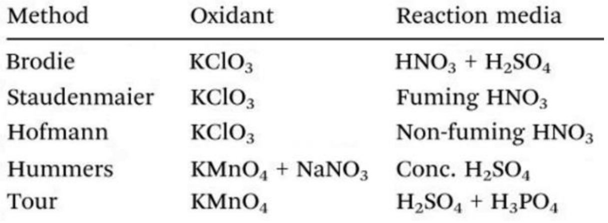

Method	Oxidant	Reaction media
Brodie	$KClO_3$	$HNO_3 + H_2SO_4$
Staudenmaier	$KClO_3$	Fuming HNO_3
Hofmann	$KClO_3$	Non-fuming HNO_3
Hummers	$KMnO_4 + NaNO_3$	Conc. H_2SO_4
Tour	$KMnO_4$	$H_2SO_4 + H_3PO_4$

Alternative methods such as the electrochemical exfoliation [102, 103] could be used, where graphite can be employed as an electrode to produce graphene. Typically, the method includes a liquid solution (electrolyte) in which two electrodes (one being the graphite) are submerged. Once DC bias is applied, the graphite dissociates into small pieces spread into the electrolyte solution. Modification of the acidity of the electrolyte could be used to tailor the oxygen content [104, 105]. The method is illustrated in Figure 2.2.5.

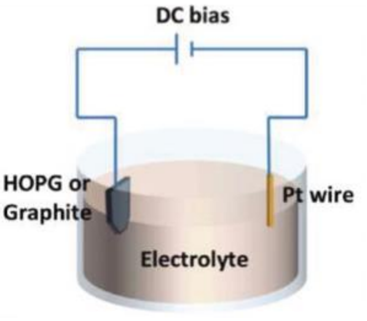

Figure 2.2.5 Schematic of the electrochemical exfoliation method, reproduced from [103].

The latter method was developed to achieve, a single-step-preparation, of low or mild defect content graphite, underlining the importance of such methods instead of the multistep oxidation/reduction procedures. Despite its advantages, this method is characterized by relatively high costs, complexity and reduced yields [106], compared to the well-established traditional methods described above.

2.3 Recent Advances in Epoxy/Graphene Systems

Numerous studies of epoxy resins filled with graphene-based fillers can be found in the literature [28]. In general, GO-derived systems are preferred over EG derivatives (GNP/eGO), due to the surface functionality, which leads to nanocomposites with high levels of dispersion and enhanced mechanical performance. However, since the usage of oxidants, and especially $KMnO_4$, in acidic solutions produces highly oxidising species [77, 96], GO produced using the associated methods displays poor properties and can disrupt considerably the epoxy crosslinking. Therefore, where high filler loading levels are required, for example, to enhance electrical or thermal conduction, the direct usage of GO in epoxy nanocomposites is problematical. Consequently, EG derivatives, rGO, or fGO, are necessarily utilised to avoid sub-optimal system properties. From the above account, it is evident that optimisation of the overall property envelope of graphene-based composite systems requires careful tailoring of both structural and chemical factors. The following sections will therefore discuss recent studies concerning epoxy/graphene systems and more specifically: (i) stoichiometric considerations, (ii) mechanical, (iii) electrical and (iv) thermal properties.

2.3.1 Epoxy Stoichiometry Considerations

The incorporation of low filler contents of GO into epoxy, has been reported to enhance the T_g of the system, an effect that has been ascribed to strong filler/matrix interactions [107, 108] or the wrinkled GO morphology [109]. Wang et al. [107] used GO of three different flake sizes, all of which resulted in the same T_g increase of ~10 °C (Figure 2.3.1a). Park et al. [108] used low contents of GNP and GO and observed a T_g increase of ~6 °C only with the usage of GO, while GNP resulted in minor increases (Figure 2.3.1b). In another study, Wan et al. [109] utilized GO which resulted only in minor T_g increment of 1.6 °C (Figure 2.3.1c). Silva et al. [110] used both GO and rGO at slightly higher filler contents (Figure 2.3.1d); the former resulted in a sharp T_g increase (14 °C) at low contents (< 1wt.%) followed by a T_g decrease to the same value shown by the unfilled epoxy, while the rGO resulted in a similar behavior albeit with slighter T_g increases (4 °C), underlining the fact that GO is much more reactive with the epoxy compared with the rGO. In the same study it was also claimed that higher filler contents than the ones presented in Figure 2.3.1d might not follow similar trends due to agglomeration phenomena, however the mixing method that was followed was relatively poor, mainly including mild stirring [110]. In the case of GNP, only higher contents (> 1wt.%) resulted in a considerable T_g increase (8 °C), as demonstrated by Zaman et al. [111] (Figure 2.3.1e).

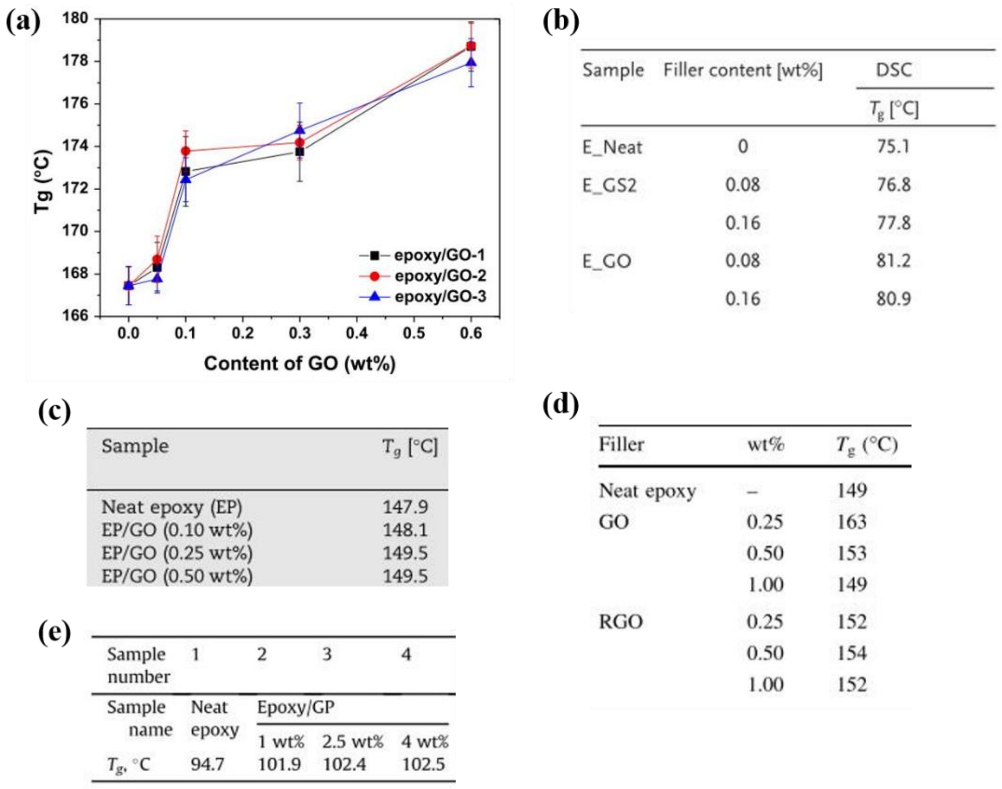

Sample	Filler content [wt%]	DSC T_g [°C]
E_Neat	0	75.1
E_GS2	0.08	76.8
	0.16	77.8
E_GO	0.08	81.2
	0.16	80.9

Sample	T_g [°C]
Neat epoxy (EP)	147.9
EP/GO (0.10 wt%)	148.1
EP/GO (0.25 wt%)	149.5
EP/GO (0.50 wt%)	149.5

Filler	wt%	T_g (°C)
Neat epoxy	–	149
GO	0.25	163
	0.50	153
	1.00	149
RGO	0.25	152
	0.50	154
	1.00	152

Sample number	1	2	3	4
Sample name	Neat epoxy	Epoxy/GP		
		1 wt%	2.5 wt%	4 wt%
T_g, °C	94.7	101.9	102.4	102.5

Figure 2.3.1 Increasing trend of T_g of epoxies filled with: (a) GO of three different flake sizes (GO-1: <20μm, GO-2: < 4μm, GO-3: <3μm) [107], (b) GNP (denoted as GS2) and GO [108], (c) GO [109], (d) GO and rGO [110] and (e) GNP [111]. Images adapted from the respective references.

Nevertheless, the similarities between the surface chemistry of GO and the epoxy are expected to result in stoichiometric imbalances. More specifically, the addition of GO equates to additional epoxide groups being introduced into the system, an effect that is typically dominant at filler contents higher than 0.5 wt.%, and results in reduced T_g values. Tang et al. [112] observed a T_g

decrease of ~12 °C compared with the unfilled epoxy, with the addition of 1 wt.% of GO (Figure 2.3.2a). An identical T_g decrease was observed by Wang et al. [113] (Figure 2.3.2b). Furthermore, the study of Zhou [114] reported that the presence of the excessive 3 wt.% of GO drastically reduced the T_g values by almost 39 °C (Figure 2.3.2c).

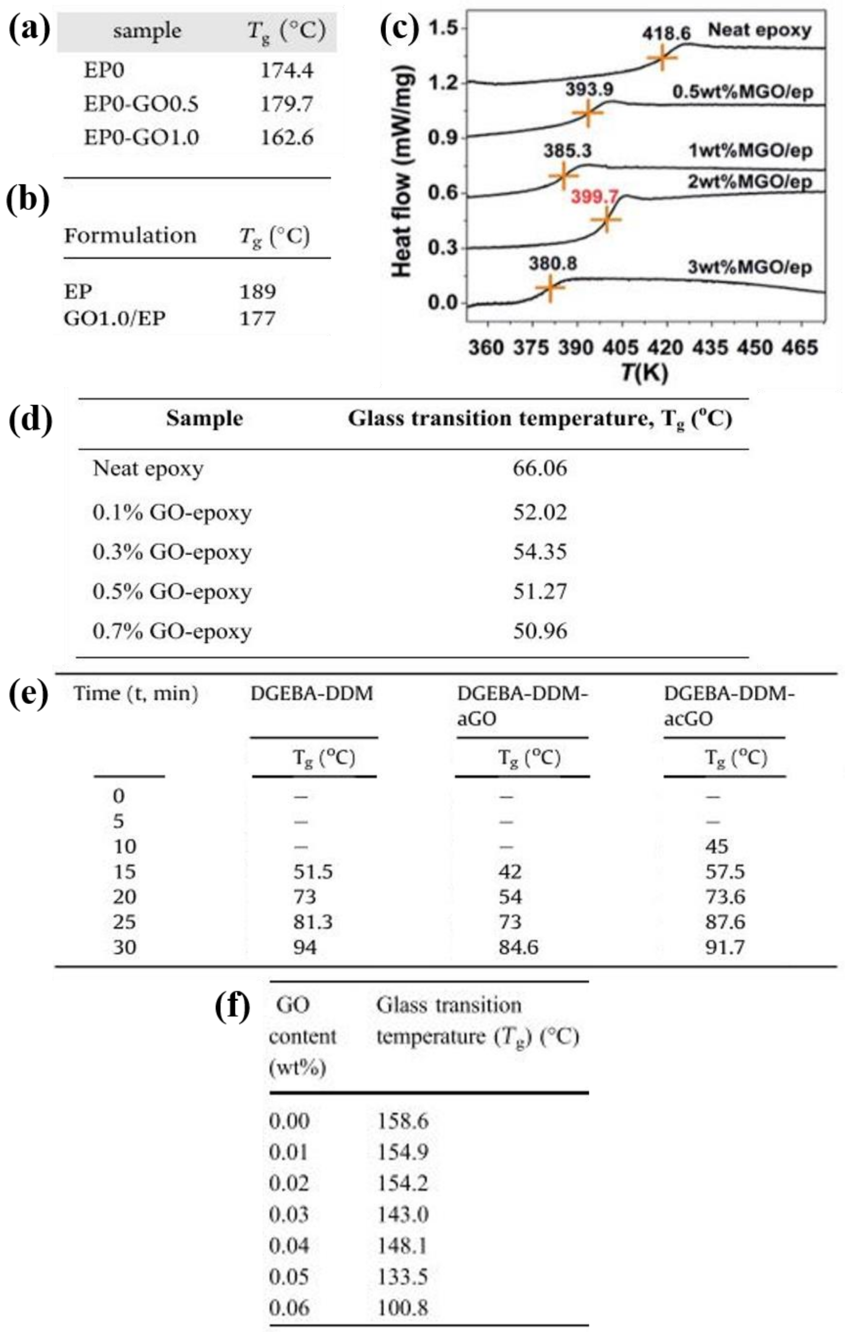

(a)

sample	T_g (°C)
EP0	174.4
EP0-GO0.5	179.7
EP0-GO1.0	162.6

(b)

Formulation	T_g (°C)
EP	189
GO1.0/EP	177

(d)

Sample	Glass transition temperature, T_g (°C)
Neat epoxy	66.06
0.1% GO-epoxy	52.02
0.3% GO-epoxy	54.35
0.5% GO-epoxy	51.27
0.7% GO-epoxy	50.96

(e)

Time (t, min)	DGEBA-DDM	DGEBA-DDM-aGO	DGEBA-DDM-acGO
	T_g (°C)	T_g (°C)	T_g (°C)
0	–	–	–
5	–	–	–
10	–	–	45
15	51.5	42	57.5
20	73	54	73.6
25	81.3	73	87.6
30	94	84.6	91.7

(f)

GO content (wt%)	Glass transition temperature (T_g) (°C)
0.00	158.6
0.01	154.9
0.02	154.2
0.03	143.0
0.04	148.1
0.05	133.5
0.06	100.8

Figure 2.3.2 Decreasing trend of T_g of epoxies filled with GO up to: (a, b) 1 wt% [112, 113], (c) 3 wt% [114], and (d) 0.7 wt% [115]. (e) T_g over time in unfilled epoxy (DGEBA-DDM), epoxy/GO (DGEBA-DDM-aGO) and epoxy/rGO (DGEBA-DDM-acGO) systems [21]. T_g of anhydride cured epoxy filled with various contents of GO [116]. Images adapted from the respective references.

Galpaya et al. [115] reported a T_g decrease of 15 °C in epoxy/GO systems containing up to 0.7 wt.% indicating perturbed resin stoichiometry starting from only 0.1 wt.% (Figure 2.3.2d). While these filler contents were shown above to result in increased T_g, here the opposite happened. This could be attributed to the quite low curing temperatures of the epoxy resin used in that study (95 °C), while in the above-mentioned studies the curing temperatures were considerably higher (in some cases up to 250 °C [107]), which might have triggered additional crosslinking reactions and/or thermally reduced the GO eliminating epoxide functionalities. As such, further investigation needs to be done. The same group [21] studied the effect of the oxygenated surface of GO on the curing of an epoxy. It was shown that, while curing, the propagation of crosslinking over time was considerably delayed in the epoxy/GO systems (Figure 2.3.2e), while at the same time, epoxy/rGO samples showed slighter effects. It was also claimed that, apart from epoxide/amine reactions, GO could facilitate etherification reactions with the epoxy via its hydroxyl groups. However, only one moderate curing temperature (100 °C) was employed, thus those effects were not clearly distinguished between each other. It is noteworthy that the incorporation of GO into epoxy resin cured with anhydride-based hardener [116] resulted in significantly reduced T_g values (58 °C) at very low filler contents (0.06 wt.%) underlining the fact that in such systems, the crosslinking reactions involve also hydroxyls and carboxyls, apart from epoxides, rendering GO drastically more reactive (Figure 2.3.2f).

Some of the studies mentioned above utilised functionalisation of the GO with surface chemistries based upon epoxy [109] or amine [108] functionalities, which demonstrated variations in T_g that were dependent on the respective end-groups. Specifically, grafting of epoxy molecules onto the GO surface resulted in slightly higher T_g values (< 2 °C) than those achieved with GO (presented in Figure 2.3.1c), while grafting amine-terminated groups resulted in slightly lower values than the ones achieved with GNP or GO (presented in Figure 2.3.1d). We attribute this effect to the differences in reactivity between epoxide (one reactive oxygen) and amines (two reactive hydrogens). The associated functionalisation reactions are portrayed in Figure 2.3.3a, b. Bao et al. [117] functionalized GO with reagents terminated with multiple glycidol groups (each one containing one epoxide ring), as illustrated in Figure 2.3.3c. The usage of such system at relatively high filler contents (5 wt.%) resulted in much lower T_g values (~40 °C) than in the unfilled epoxy, due to the presence of multiple reactive groups. The effect was denoted as "*cross-linking density reduction*".

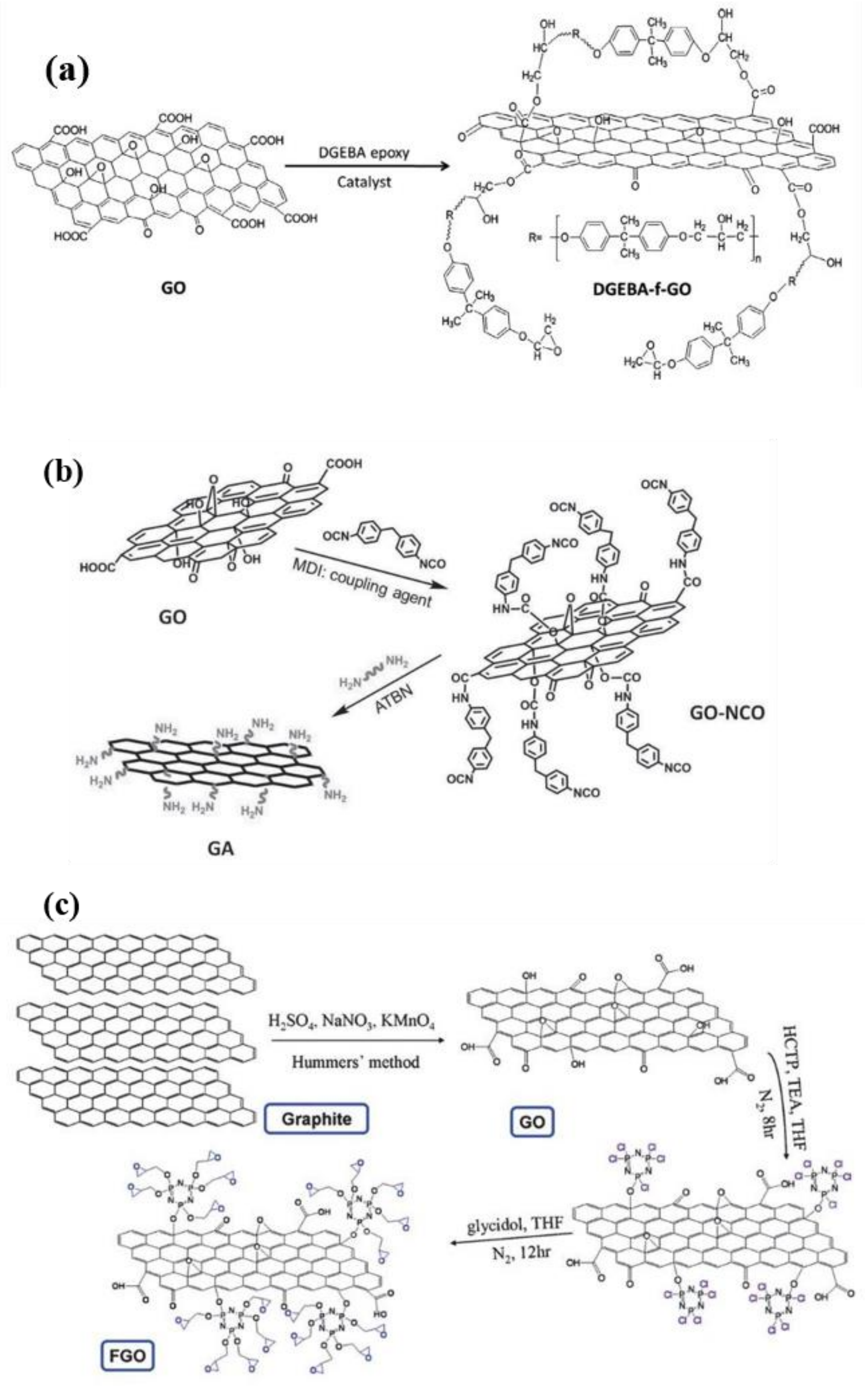

Figure 2.3.3 Functionalization of GO with: (a) epoxy molecules (DGEBA-f-GO) [109] and (b) amine terminated molecules (GA) [108], (c) multiple glycidol groups [117]. Images reproduced from the respective references.

Finally, epoxy filled with fGO decorated with different sizes of (amine terminated) reagents showed T_g variations dependent not only on stoichiometric imbalances but also on the structure of the respective molecule grafted onto the GO surface [118]. More specifically, the crosslinking density was shown to be noticeably perturbed (decreased T_g) only with the usage of a "short" functionaliser, whilst a “longer” molecule might have reached other adjacent reactive spots on the same or different GO flake (as shown in Figure 2.3.4), prior to incorporation in the epoxy, therefore providing limited reactivity.

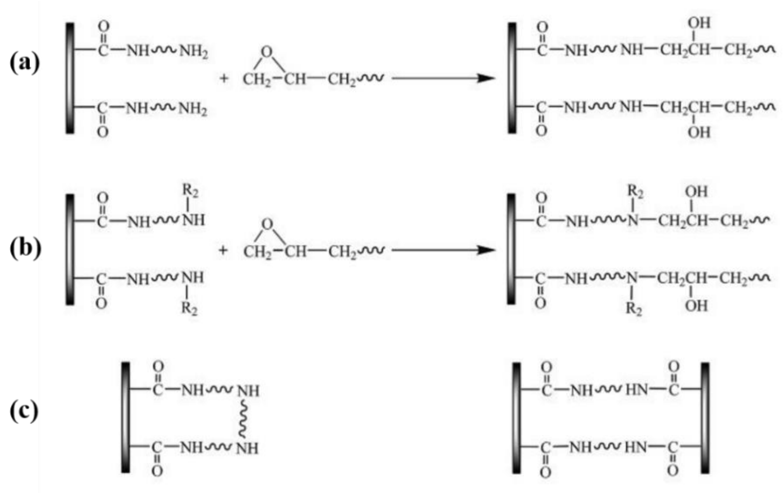

Figure 2.3.4 Possible reactions between amine functionalized GO and epoxy resin. (a) Primary amine with epoxide, (b) secondary amine with epoxide. The “long” reagent might react with adjacent spots prior to incorporation into the epoxy (c) and display limited reactivity with only secondary amines available. Image reproduced from [118].

2.3.2 Mechanical Properties

The effect of GO on the mechanical response of polymer matrices has been intensively studied over the last few years [28, 67]. The presence of functional groups serves to increase the mechanical response of the epoxy matrix as shown by Li et al. [83] by incorporating GO and rGO into an epoxy. It was claimed that the GO displayed improved compatibility and stress transfer with the matrix, thus this system’s tensile performance is enhanced compared with the rGO-filled systems (Figure 2.3.5).

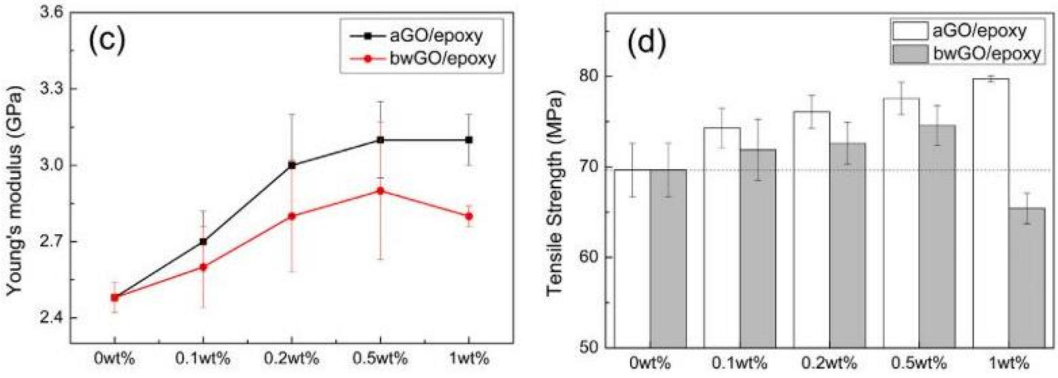

Figure 2.3.5 (a) Elastic modulus and (b) tensile strength of unfilled epoxy and epoxy filled with GO (denoted aGO) and rGO (denoted bwGO). Images reproduced from [83].

It has to be noted that, in the latter study, the epoxy stoichiometry began to degrade at the largest filler content used (1 wt.%). As shown earlier, GO functionality can considerably disrupt the epoxy stoichiometry at such contents. Similar effects have been reported even in the case of rGO [119], where slight mechanical degradation occurred alongside T_g reduction. Conversely, GNP may be used at relatively higher filler contents, as shown above. For example, Zaman et al. [111] observed that the stiffening effect of GNP on epoxy was diminishing at filler contents higher than 2.5 wt.% (Figure 2.3.6a). This is attributed to the poor filler/matrix interface and agglomeration, as such, the critical filler content is much higher than typical GO contents. Further functionalization with Methylene diphenyl diisocyanate (MDI) extended the abovementioned critical filler content, up to 4 wt.% (Figure 2.3.6a). On the contrary, another study used GO and rGO both functionalized with the same reagent (MDI) where the critical filler content was shown to be only 0.25 wt.%, indicating that the reactivity of functionalised systems is highly dependent on the reactivity of the precursor. Nevertheless, it is noteworthy that in the case of GNP the tensile strength (Figure 2.3.6b) is only degraded, when compared to the unfilled epoxy, underlining the poor matrix compatibility, an effect that has been observed in other cases as well [88].

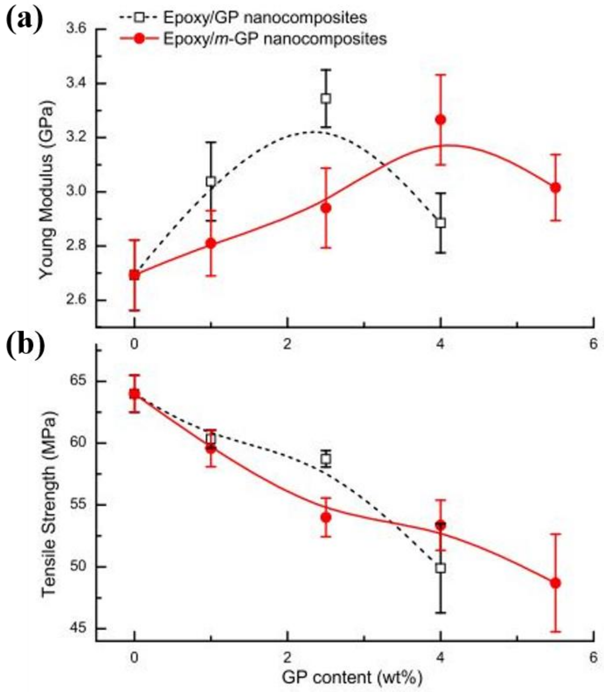

Figure 2.3.6 (a) Elastic modulus and (b) tensile strength of epoxy filled with GNP (denoted as GP) and fGNP (denoted as m-GP). The surface functionalization was done with MDI. Image reproduced from [111].

Surface functionalization of GO such as the grafting of epoxy molecules mentioned earlier, might be beneficial for even further enhancements, as shown in Figure 2.3.7, where the effects shown here are attributed to improved exfoliation as well as bonding with the matrix [109].

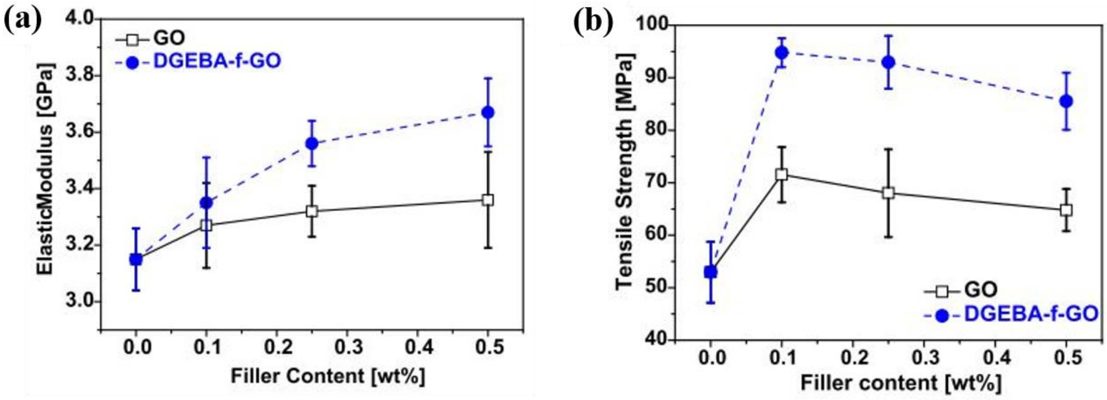

Figure 2.3.7 (a) Elastic modulus and (b) tensile strength of epoxy unfilled and filled with GO and fGO with epoxy molecules grafted on its surface. Image reproduced from [109].

However, in the case of the glycidol functionalization [117] that mentioned earlier, considerable mechanical degradation was observed. The multiple reactive endgroups that served to reduce the T_g also reduced the storage modulus of the epoxy composite at contents higher than 2 wt.%, as shown in Figure 2.3.8.

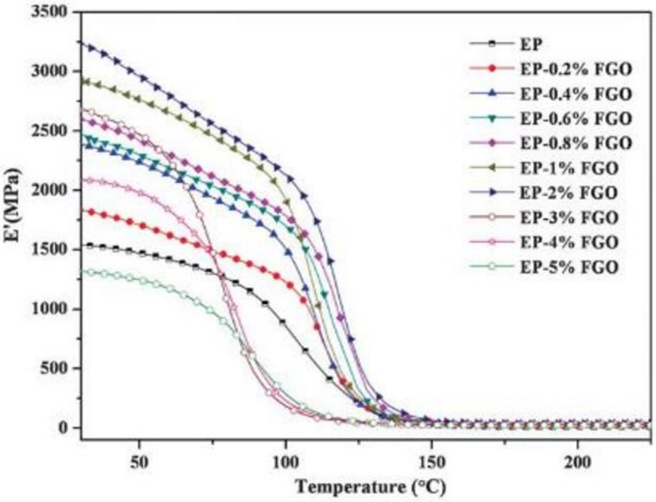

Figure 2.3.8 Storage modulus curve (taken from DMA) of unfilled epoxy as well as epoxy filled with fGO. The surface functionalization was done with multiple glycidol groups as shown in Figure 2.3.3c. Image reproduced from [117].

Finally, the impact of the molecular chain length of amino-reagents grafted onto fGO on the mechanical properties of epoxy, was investigated by Guan et al. [120] and Liu et al. [118]. It was shown that the epoxy systems filled with fGO functionalized with both reagents exhibited increased elastic modulus and tensile strength compared with the precursor GO, due to an enhanced filler/matrix interface. Comparison between the two amino-reagents showed lower tensile strength in the case of the longer functionaliser, due to its increased flexibility (Figure 2.3.9a). A schematic representation of the associated interfaces is presented in Figure 2.3.9b.

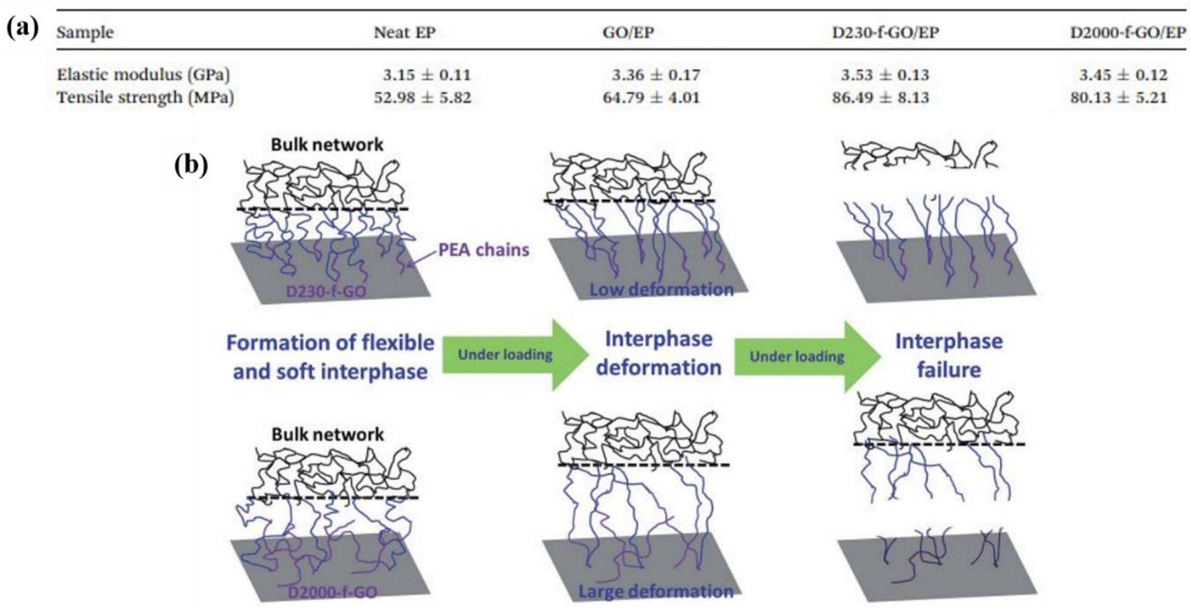

(a)

Sample	Neat EP	GO/EP	D230-f-GO/EP	D2000-f-GO/EP
Elastic modulus (GPa)	3.15 ± 0.11	3.36 ± 0.17	3.53 ± 0.13	3.45 ± 0.12
Tensile strength (MPa)	52.98 ± 5.82	64.79 ± 4.01	86.49 ± 8.13	80.13 ± 5.21

Figure 2.3.9 (a) Tensile properties of unfilled epoxy (Neat EP) and epoxy filled with 0.50 wt% of GO (GO/EP), and fGO functionalized with short (D230-f-GO/EP) and long (D2000-f-GO/EP) amino-reagents. (b) Illustration of the associated interfaces under mechanical stress. Image adapted from [120].

2.3.3 Electrical Properties

As mentioned earlier, most of the studies concerning epoxy/GO nanocomposites focus on the mechanical and not the electrical performance of such systems. This could be attributed to the poor electrical properties of GO. Thus, the usage of EG-based systems is expected to be dominant in this section. Studies concerning electrical conductivity enhancements of epoxy, either with GO- or EG-based fillers will be discussed below.

2.3.3.1 Electrical Enhancements in Epoxy/GO Nanocomposites

Direct usage of GO as a means of tailoring the electrical conductivity of epoxy-based nanocomposites has, to our knowledge, only previously been considered in the following three studies.

Mancinelli et al. [121] achieved an increase of almost 2 orders of magnitude (filler content up to 0.5 wt.%) only by thermally treating (post-curing at 130 °C) the nanocomposite partially to reduce the GO; before thermal treatment, no increase in electrical conductivity was observed, compared with the unfilled epoxy matrix. Kim et al. [122] did not achieve any significant conductivity increase with the usage of up to 3 wt.% GO. Only the study presented by Tang et al. [123] achieved a modest conductivity enhancement of 6 orders of magnitude (up to ~10^{-10} S/cm) with a P_t of 6 vol.%, as presented later in Figure 2.3.12b. It is of considerable significance to note that the GO contents mentioned above were reported earlier to affect negatively the epoxy curing reactions. A summary of the abovementioned review is presented in Table 2-2. Since, in some cases the achieved conductivity values were relatively low, the respective data are presented as a σ_c/σ_m ratio, where σ_m is the electrical conductivity of the unfilled matrix.

Table 2-2 Electrical conductivity parameters related to Epoxy/GO nanocomposites found in the literature.

P_t	σ_{max} (S/cm)	Comments	Ref.
-	-	Filler contents up to 0.5 wt.% $\sigma_c/\sigma_m = 2.4$ After thermal treatment at 130 °C $\sigma_c/\sigma_m = 78$	[121]
-	-	Filler content up to 3 wt.% $\sigma_c/\sigma_m \sim 2.2$	[122]
6 vol. %	~10^{-10}	At the same filler contents of GO epoxy stoichiometry is disrupted.	[123]

Thus, studies of systems based upon GO in epoxy indicate, at best, percolation onsets at high volume fractions and relatively small improvements in electrical conductivity followed by adversely perturbed epoxy stoichiometry.

2.3.3.2 Electrical Enhancements in epoxy/rGO and Epoxy/fGO Nanocomposites

In view of the ineffective nature of GO as a means of increasing electrical conduction in epoxy-based composites, reduction or functionalization procedures are typically used to address the limitations of directly using GO. For example, Thachil et al. [119] used microwave exposure to reduce GO and, consequently, achieved a percolation threshold of 0.27 vol.%; the maximum conductivity value reported (σ_{max}) was ~10^{-10} S/cm (Figure 2.3.10a). A similar behaviour was observed by Hsiao et al. [124] who employed, among other things, thermal reduction of GO at 700 °C in an argon atmosphere; in this study, the σ_{max} reached 10^{-8} S/cm (Figure 2.3.10b).

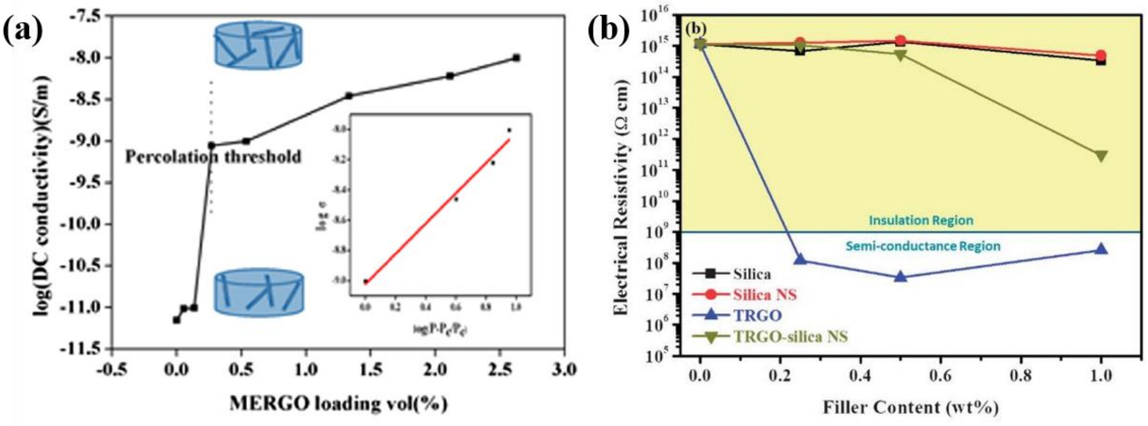

Figure 2.3.10(a) Variation of electrical conductivity of epoxy filled with microwave reduced GO (denoted as MERGO) content. Insets show schematics of dispersion and log-log plot [119]. (b) Electrical resistivity of epoxy containing silica-based and GO-based fillers. (where NS is nanosheet and TRGO is thermally reduced GO) [124]. Images reproduced from the respective references.

A much greater conductivity increase was achieved by the extensively reduced GO system, mentioned earlier, including chemical reaction with hydrazine hydrate, followed by subsequent annealing at 250 °C under N_2 [125]. The composite systems of the latter study exhibited an σ_{max} of 10^{-1} S/cm and a P_t of < 1 vol.% (Figure 2.3.11).

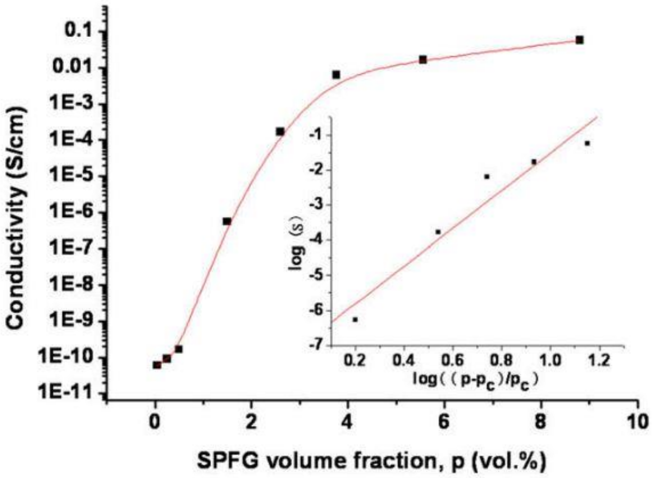

Figure 2.3.11 Electrical conductivity of epoxy filled with rGO (denoted as SPFG, meaning solution processable functionalized graphene) reduced with a two-step method, including chemical reaction with hydrazine hydrate, followed by annealing at 250 °C under N_2. Inset shows the log-log plot. Image reproduced from [125].

In the case of functionalized GO, the GO functionalised via attachment glycidol groups, mentioned earlier [117], resulted in composites with a σ_{max} of 10^{-11} S/cm with a P_t of 2 wt.% (Figure 2.3.12a).

On the contrary, surface functionalization of GO with polyetheramines [123] resulted in a much greater increase in conductivity, up to ~10^{-2} S/cm (Figure 2.3.12b).

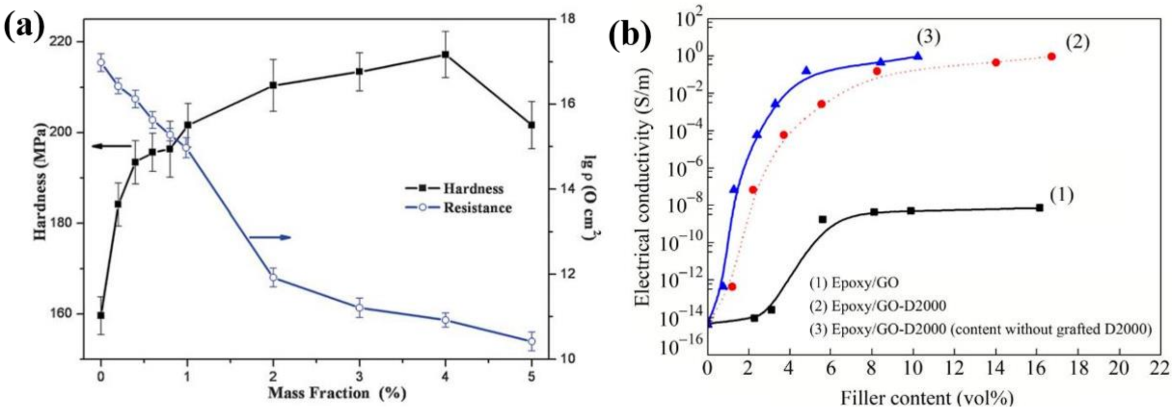

Figure 2.3.12 (a) Volume resistivity (blue curve corresponding to axis on the right side) of epoxy resin filled with glycidol fGO. (Black curve shows hardness of the respective samples) [117]. (b) Electrical conductivity of epoxy filled with (1) GO and (2) amine-functionalised GO. The red dotted line indicates the equivalent volume of GO excluding the amount of amine reagent [123]. Images reproduced from the respective references.

A more detailed summary of the abovementioned review, along with comments on the treatment each filler was subjected to, as well as specific details on the nanocomposite behaviour, is presented in Table 2-3.

Table 2-3 Electrical conductivity parameters related to epoxy/rGO & epoxy/fGO nanocomposites found in the literature.

Filler	P_t	σ_{max} **(S/cm)**	**Comments**	**Ref.**
rGO	0.27 vol.%	~10^{-10}	Microwave treatment	[119]
	~0.25 wt.%	~10^{-8}	Thermal treatment; Argon atmosphere	[124]
	0.52 vol.%	~10^{-1}	Chemical reduction with hydrazine hydrate, followed by thermal treatment at 250 °C under N_2 for 2 h	[125]
fGO	2 wt.%	~10^{-11}	Glycidol groups attached on the GO surface	[117]
	~2 vol.%	~10^{-2}	Amine Functionalization Gradual percolation	[123]

Comparing the results presented above, it is evident that the usage of rGO- and fGO- filled epoxy systems results in improved properties compared to the poor electrical performance of GO-filled epoxy resins. Most of the studies report comparable electrical behaviour with each other, with electrical conductivity values between 10^{-11} and 10^{-8} S/cm, while the percolation thresholds reported are always smaller than the one reported for GO earlier (6 vol.%). In two of the cases mentioned above [123, 125] the σ_{max} values were exceptionally high; 0.1 and 0.01 S/cm, respectively. Despite the two-step reduction method [125] leading in higher σ_{max} values, the amine functionalisation is considered more efficient due to the easy steps and handling it includes. It has to be mentioned that in all of the cases described above, the rGO/fGO was introduced into the epoxy resin in a liquid solvent.

2.3.3.3 Electrical Enhancements in Epoxy/EG Composite Systems

Studies considering systems based upon EG derivative fillers are summarised have been reported to lead in percolation thresholds of: 2 wt.% [126]; >2 vol.% [127]; 0.5 vol.% [128] and 1 phr [129]. The σ_{max} values reported in those studies were: 10^{-3} S/cm; 10^{-5} S/cm; 10^{-6} S/cm; 10^{-3} S/cm, respectively, as shown in Figure 2.3.13 (a-d). Surface functionalisation of EG via UV/O_3 exposure, attempted by Li et al. [130] resulted in epoxy composites with relatively higher conductivity values at intermediate filler contents compared with the untreated EG. However, the σ_{max} and P_t values were identical (Figure 2.3.13e). An attempt of direct disaggregation of graphite via prolonged sonication in solvent, was shown to lead in a P_t of > 8 wt.% [71], however the respective σ_{max} value was rather high, approaching 10^{-2} S/cm (Figure 2.3.13f).

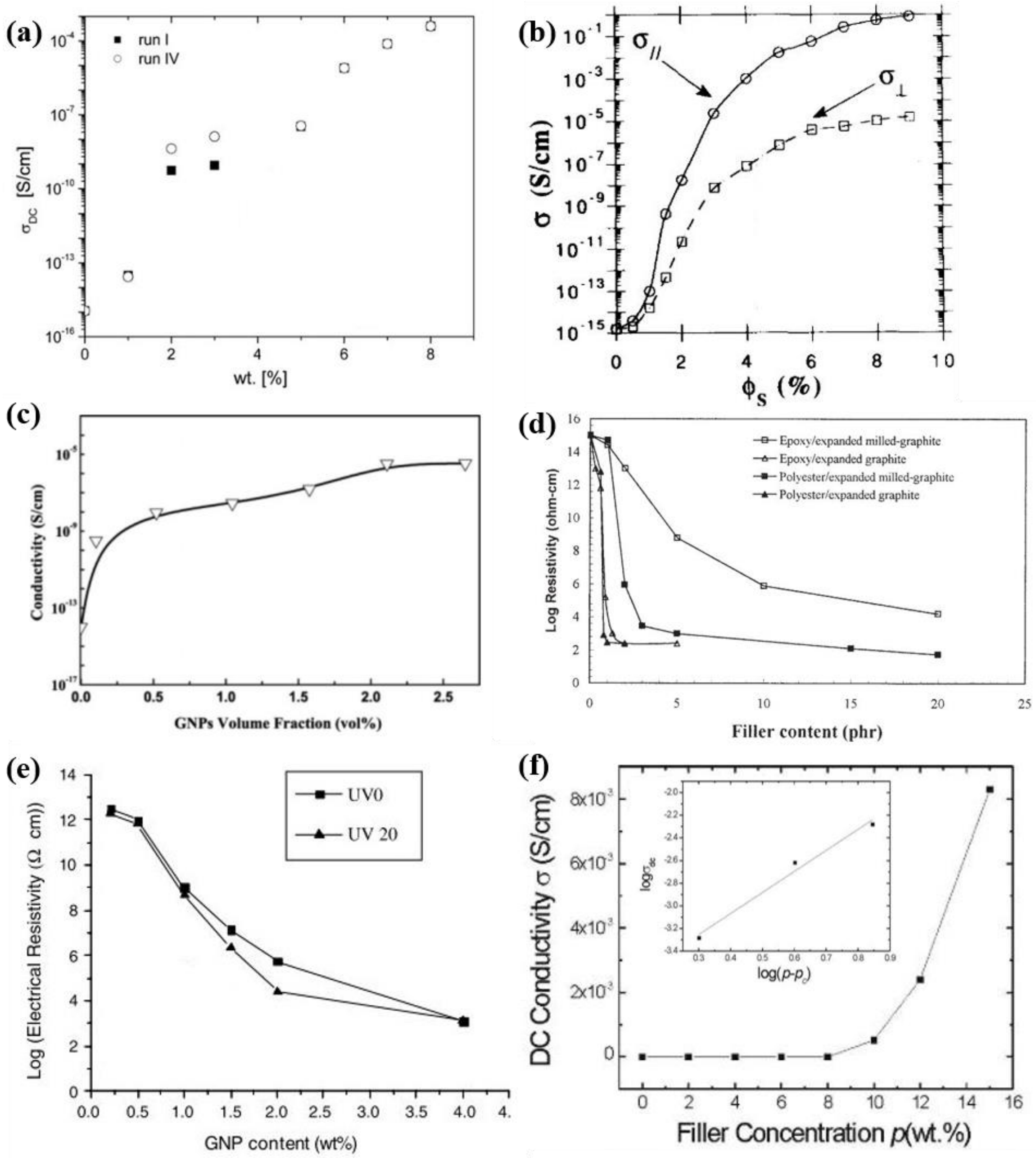

Figure 2.3.13 Electrical conductivity of epoxy filled with EG. (a) Measured after the first and fourth run [126], (b) Measured in-plane and perpendicularly [127], (c) After extensive sonication of EG inside acetone (denoted as GNP) [128]. (d) Comparison of EG and milled EG in polyester and epoxy resins [129], (e) Before and after UV/O_3 treatment (UV0 and UV20 respectively) and (f) after extensive sonication of graphite inside ethanol. Inset shows the log-log plot [71]. Images adapted from the respective references.

A more detailed summary of the abovementioned review, along with comments on the treatment each filler was subjected to, as well as specific details on the composite behaviour, is presented in Table 2-4.

Table 2-4 Electrical conductivity parameters related to epoxy/EG composites.

Filler	P_t	σ_{max} (S/cm)	Comments	Ref.
EG	~3 wt.%	$\sim 10^{-3}$	Acetone suspension ultra-sonicated for 10 h	[126]
	~1.3 vol.%	$\sigma_{\perp} \sim 10^{-5}$ $\sigma_{//} \sim 10^{0}$	Cyclohexane suspension grinded and ultra-sonicated Anisotropic composites	[127]
	0.5 vol.%	$\sim 10^{-6}$	Acetone suspension ultra-sonicated for 20 h	[128]
	1 phr	$\sim 10^{-3}$	Epoxy-ethanol suspension & ultrasound bath at elevated temperatures for 3 h Incorporation of milled EG resulted in P_t ~5 phr	[129]
	~ 1 wt.%	$\sim 10^{-4}$	Acetone suspension ultra-sonicated for 8 h UV/O_3 treatment for 25 min	[130]
	8 wt.%	10^{-2}	Ethanol suspension ultra-sonicated for 3 h	[71]

The results presented above show σ_{max} values relatively higher than the ones achieved with rGO/fGO, underlining the fact that the EG systems display less disrupted lattice, due to their limited oxygen content. The relatively large deviations on the σ_{max} values is possibly attributed to different grades of the respective commercial EG products. The attempt of surface functionalisation did not display drastic alterations on the electric performance while the attempt of direct exfoliation of graphite resulted in poor P_t, an effect possibly associated with low compatibility with the solvent, limited disaggregation and poor dispersion.

2.3.3.4 Electrical Enhancements in Epoxy/GNP Nanocomposites

In the case of studies on GNP/epoxy systems, direct dispersion within a solvent prior to introduction of the GNP into the resin has been reported [131] to result in a percolation threshold >1 wt.% and an σ_{max} of 10^{-6} S/cm (Figure 2.3.14a).

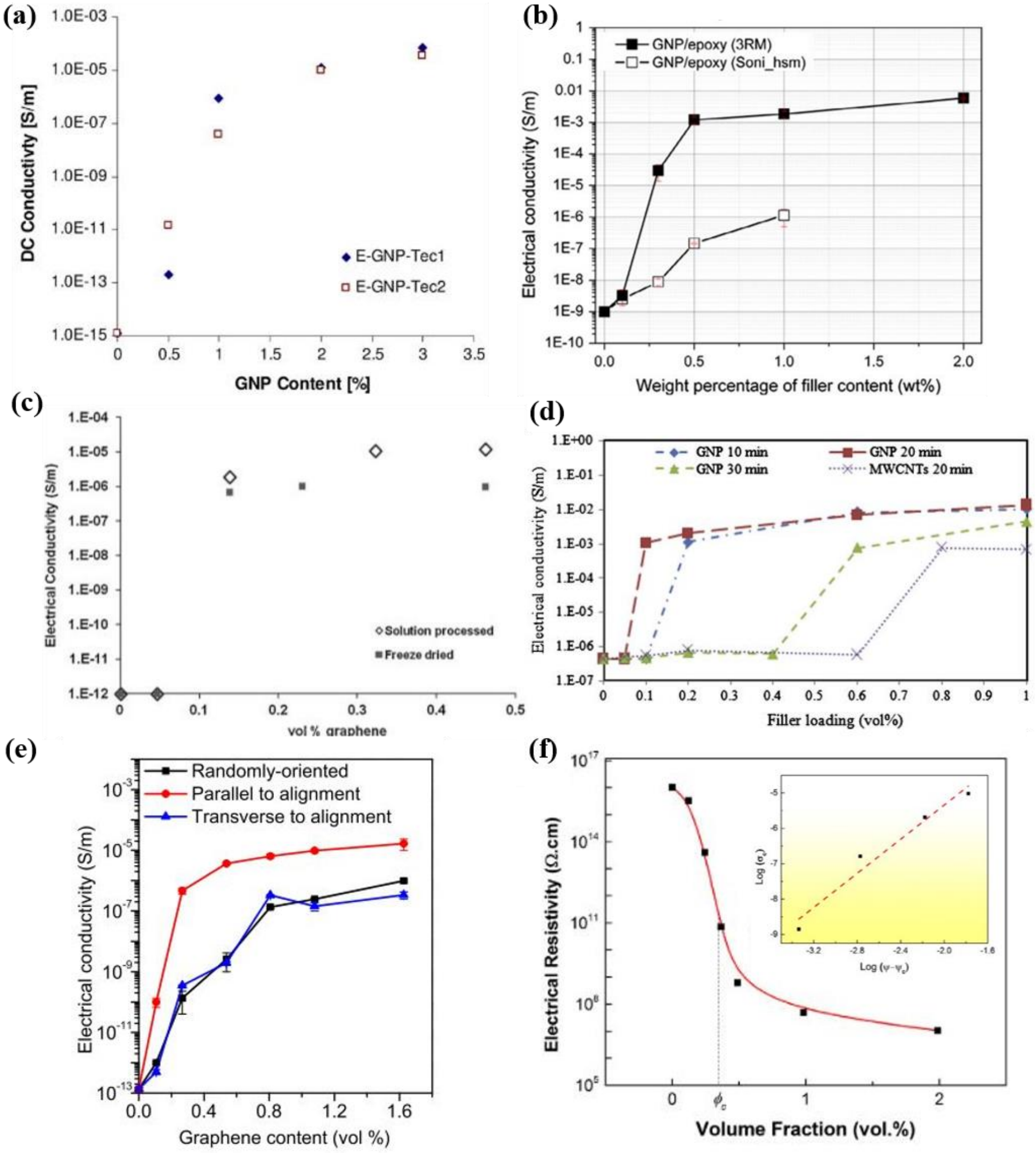

Figure 2.3.14 Electrical conductivity of epoxy filled with GNP (a) After disaggregation in $CHCl_3$ or THF suspensions (Tech1 and Tech2 respectively, GNP content is wt.%) [131]. (b) Prepared with 3RM or combination of sonication and high-speed mixing at elevated temperatures [132]. (c) Prepared via solvent mixing and freeze drying [133]. (d) After sonication over various periods of time [134]. (e) After Ac-electric field orientation and comparison with randomly oriented GNP [135], (f) functionalised with amine groups. Inset shows the log-log plot, φ_c indicates the percolation threshold which is 0.32 vol.% [88]. Images adapted from the respective references.

More complex dispersion strategies have been reported for GNP, the results of which can be found in Figure 2.3.14b-e. These include three-roll milling [132], encapsulation with poly(vinyl pyrrolidone) combined with freeze-drying [133], spin coating (up to 12,000 rpm) [134] and AC-field induced alignment [135]; the resulting data vary widely, with σ_{max} values ranging from 10^{-9} S/cm to 10^{-4} S/cm. Finally, fGNP functionalised with amine groups was prepared by Ma et al. [88], the usage of which resulted in epoxy nanocomposites displaying a P_t of 0.32 vol.% with $\sigma_{max} = 10^{-8}$ S/cm (Figure 2.3.14f). The usage of the untreated GNP was reported to result in P_t values more than four times larger (1.33 vol.%), however the σ_{max} value was of the same order of magnitude [136]. A detailed summary of the abovementioned review, with comments on the treatment each filler was subjected to, as well as specific details on the nanocomposite behaviour is presented in Table 2-5.

Table 2-5 Electrical conductivity parameters related to epoxy/GNP nanocomposites.

Filler	**P_t**	**σ_{max} (S/cm)**	**Comments**	**Ref.**
GNP	~1 wt.%	~10^{-6}	$CHCl_3$ or THF suspension ultra-sonicated for 2 h	[131]
	0.3 wt.%	~10^{-4}	Three-roll milling process	[132]
	0.088 vol.%	~10^{-7}	Freeze-drying of polymer-stabilized graphene suspensions	[133]
	0.1 vol.%	~10^{-4}	Epoxy suspension ultra-sonicated for 20 min. Films obtained via spin coating with speeds 900 – 12,000 rpm	[134]
	0.22 vol.%	$\sigma_\perp$ ~10^{-9} $\sigma_{//}$ ~10^{-7}	Epoxy suspension ultra-sonicated for 30 min, then three roll milling followed by AC-field induced alignment P_t without alignment was 0.52 vol.%	[135]
	0.32 vol.%	~10^{-8}	Amine functionalization Suspension in THF followed by mechanical stirring and sonication The untreated filler resulted in P_t = 1.33 vol.%	[88]

From the abovementioned review, it is indicated that the usage of GNP results in relatively lower P_t values than the ones achieved with EG. However, it was shown that in some of the cases the preparation method involved advanced or multiple-step processes which might have affected the achieved P_t values, while the previously presented EG studies included simple preparation methods. The σ_{max} values appear to be relatively scattered again, for the same reasons explained for EG.

Regarding surface treatment, the amine functionalization was shown to be crucial also for GNP by improving the P_t, however the σ_{max} was not improved in this case. Nevertheless, despite their improved electrical performance, it was shown earlier that GNP systems quickly deteriorate the mechanical properties of the respective epoxy nanocomposites, while the GNP production method is characterized by reduced yields compared to GO derivatives.

2.3.4 Thermal Properties

The incorporation of GO has been reported in a few studies to increase the thermal conductivity of epoxy-based systems. Nevertheless, for reasons similar to the ones explained for the electrical properties above, the discussion will also expand to rGO/fGO as well as EG-based systems.

2.3.4.1 Thermal Enhancements in Epoxy/GO Nanocomposites

Two studies by Zhou et al. [114] and Kim et al. [137] utilized GO into epoxy up to 3 wt.% and resulted in similar thermal conductivity values; close to 0.4 W/mK which was a twofold increase compared to the unfilled epoxy. The former prepared the GO/epoxy samples via a combination of solvent and high speed mixing and claimed that filler contents higher than 2 wt% suffered from agglomeration phenomena, which they linked to the reduced the thermal conductivity values they observed at those filler contents (Figure 2.3.15a). The latter prepared the GO/epoxy samples via solvent method and demonstrated that functionalization with aluminium hydroxide ($Al(OH)_3$) resulted in decreased thermal conductivity values (see Figure 2.3.15b) due to the lower thermal conductivity of $Al(OH)_3$ compared to GO [137]. In another study [116] the usage of only 0.06 wt% of GO resulted in a thermal conductivity increased by 50% compared with the unfilled epoxy (anhydride based system), however, this was achieved via in-situ thermal reduction of the GO through annealing of the GO-filled epoxy at 200 ^{o}C. Nevertheless, the latter method might not be applicable to specific epoxy formulations or applications. It is also worth mentioning that these achievements were at the expense of lowered T_g values (by ~38 ^{o} [114] and ~58 ^{o}C [116]) due to GO-induced disrupted crosslinking phenomena. Despite the fact that the abovementioned studies associate the thermal conductivity behaviour with factors like intrinsic properties of the filler [116, 137], it is indicated that the bonding of GO with the epoxy (see decreased T_g values) could be the main reason for those thermal conductivity enhancements; as suggested earlier that enhanced filler/matrix bonding results in facilitated heat transport. On the contrary, the study by Wang et al. [113] utilized GO via solvent method, up to 1 wt.% and despite showing decreased T_g values (see Figure 2.3.2b) there was no alteration of the thermal conductivity of the epoxy system and had to be extensively functionalized (with silica and amino-groups) in order to do so (Figure 2.3.15d).

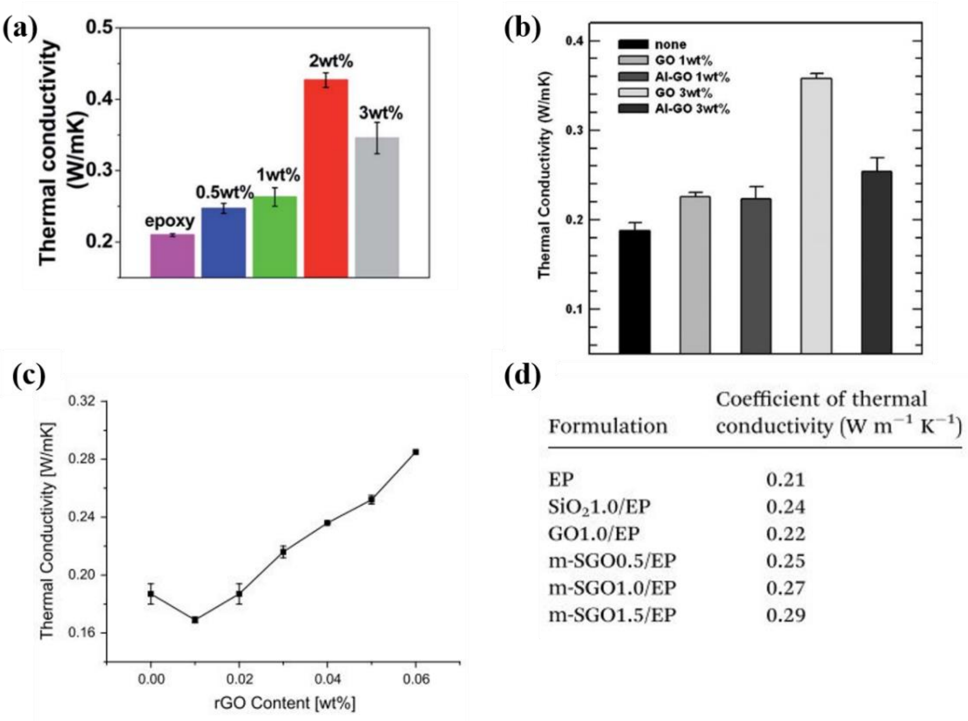

Formulation	Coefficient of thermal conductivity (W m^{-1} K^{-1})
EP	0.21
$SiO_2$1.0/EP	0.24
GO1.0/EP	0.22
m-SGO0.5/EP	0.25
m-SGO1.0/EP	0.27
m-SGO1.5/EP	0.29

Figure 2.3.15 Thermal conductivity of epoxy filled with GO. (a) Agglomeration caused reduced values at contents >2wt% [114]. (b) Functionalization with $Al(OH)_3$ reduced the thermal conductivity [137]. (c) In-situ thermal reduction resulted in significant increment related to the filler content [116]. (d) GO usage was not efficient, without functionalization [113]. Images adapted from the respective references.

It is, therefore, indicated that the GO usage might be beneficial for purposes such as thermal conductivity enhancements due to promoted bonding with the epoxy. However, one of the abovementioned studies indicates that GO significantly agglomerates at high filler contents, deteriorating the composite's performance, which might be the reason why GO shows quite large electrical P_t as shown earlier. Furthermore, the fact that another study contradicts the abovementioned by introducing GO via a similar method (solvent) into similar epoxy formulation (amine-based hardener) and not resulting in any thermal conductivity alteration, suggests that the heat transport in GO-filled epoxy systems is attributed to various factors and should be furtherly investigated.

2.3.4.2 Thermal Enhancements in Epoxy/rGO and Epoxy/fGO Nanocomposites

Hsiao et al. [124] used up to 1 wt.% of rGO and rGO that was subsequently coated with silica, with the latter resulting in epoxy composites with considerably higher thermal conductivity values (Figure 2.3.16a). Pu et al. [90] used rGO, amino-functionalized GO (A-graphene) and silica coated GO (S-graphene) with the latter resulting in epoxy composites with the highest thermal conductivity values (Figure 2.3.16b), an effect that was evident above 1 wt.%. The moderate enhancements achieved with the rGO are attributed to phonon scattering, while amino-functionalisation resulted in systems with slightly lower thermal conductivity values than the ones displayed by the rGO-filled epoxy, possibly due to the same reasons.

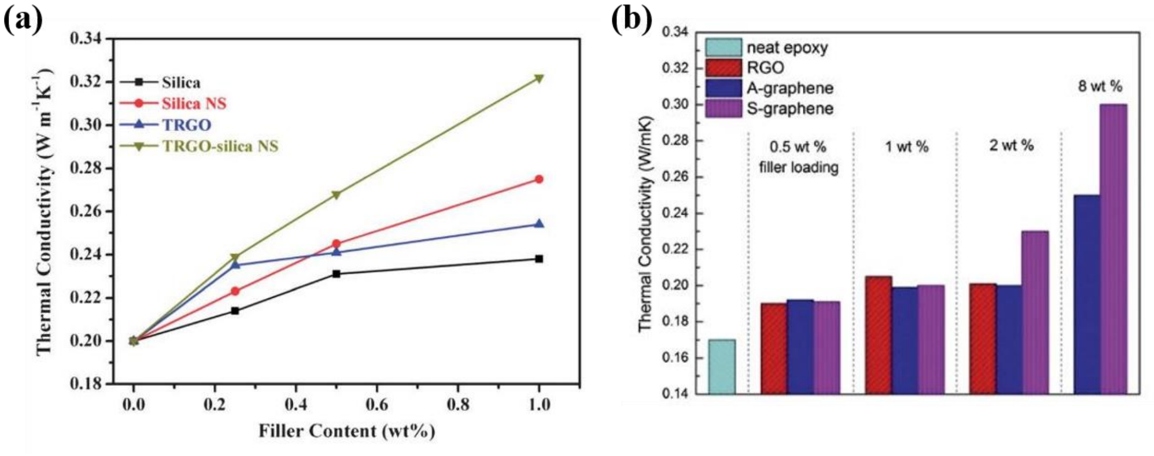

Figure 2.3.16 Thermal conductivity of epoxy containing rGO- and fGO- based fillers, where: (a) NS is nanosheet and TRGO is thermally reduced graphene oxide [124] (b) where RGO is chemically reduced GO, A-graphene is GO functionalized with aminopropyltriethoxysilane (APTES), S-graphene is GO coated with silica [90]. Images reproduced from the respective references.

From the above, it is apparent that the usage of rGO results in moderate thermal conductivity enhancements that align with each other. Coating with silica was shown to be the most efficient method, in both cases. However, this approach was shown earlier to impair the electrical performance of the system (Figure 2.3.10b).

2.3.4.3 Thermal Enhancements in Epoxy/EG and Epoxy/GNP Systems

The incorporation of graphitic flakes is usually done up to considerably larger filler contents [20, 71], achieving considerably higher thermal conductivity values, as indicated in Figure 2.3.17a and Figure 2.1.7 (shown in Section 2.1). The usage of amine functionalized EG was reported by Chatterjee et al. [138] to result in a ~34% increase with 2 wt.% content (Figure 2.3.17b), while the same filler content of EG was reported to show ~25% increase at the same filler content (Figure 2.3.17a), indicating that functionalisation might be beneficial also in the case of EG.

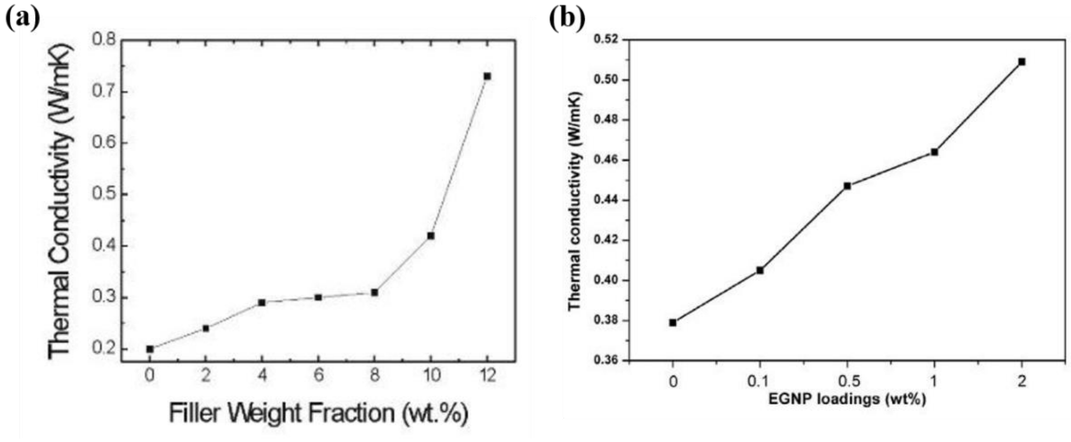

Figure 2.3.17 Thermal conductivity of epoxy containing EG- based fillers. (a) After extensive sonication of graphite inside ethanol [71]. (b) Amine functionalized EG (denoted as EGNPs) [138]. Images reproduced from the respective references.

Studies including GNP for thermal conductivity enhancements can also be found in the literature. The system prepared by the three-roll milling process mentioned earlier [132], exhibited an increase of ~16% using 2 wt.% of GNP, as shown in Figure 2.3.18a. This enhancement is considerably lower compared with both EG-filled systems described above, possibly due to the fact that GNP might exhibit reduced aspect ratios caused by the size-reduction processing it undergoes. It was also shown that the smallest filler content (0.3 wt.%) resulted in significantly reduced thermal conductivity values, which was ascribed to phonon scattering. Finally, Gu et al. [139] reported a linear thermal conductivity increase with the usage of up to 30 wt% of GNP and fGNP (Figure 2.3.18b). Functionalization with a silane coupling agent resulted in improvements only at high filler contents (>20 wt.%). The effect was ascribed to improved interfacial compatibility with the matrix as well as lower interfacial thermal resistance.

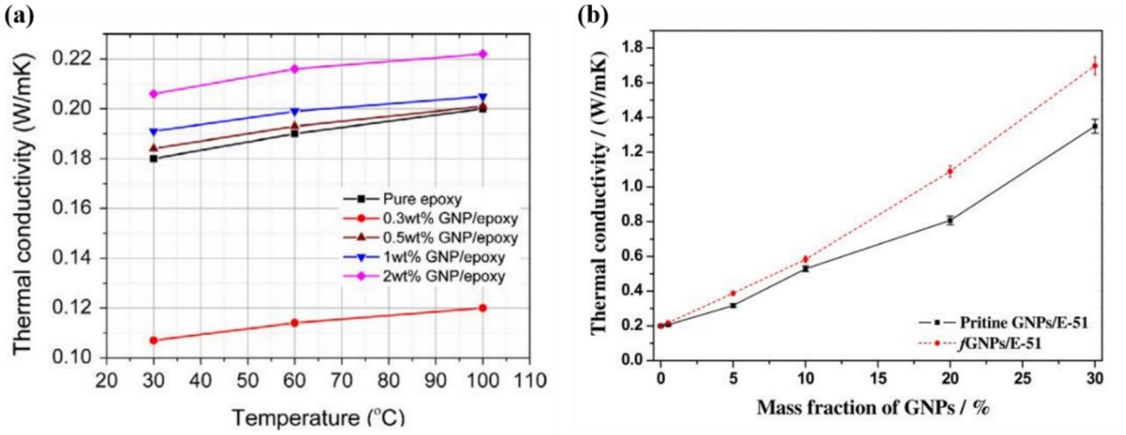

Figure 2.3.18 Thermal conductivity of epoxy containing GNP [132]. (a) As a function of temperature. (b) Before and after the functionalization with silane coupling agent [139]. Images reproduced from the respective references.

2.4 Summary

It was shown in Chapter 2 that the filler geometry is a crucial parameter since utilisation of non-spherical nanofillers results in improved mechanical performance as well as electrical and thermal conductivity values, at lower filler contents. It was stated that the highest improvements can be obtained from particles with tube-like geometry, however these characteristics are considered challenging because of the health hazards (such as oxidation and cancer) in case they are found inside the human body. Another non-spherical geometry that offers considerable performance improvements without including any health hazards is the platelet shape. As such, graphene-based particles are a materials of particular interest.

The first step towards utilisation of such material is an efficient (high yield) and scalable nanoparticle production method, which was shown to be via the synthesis of graphene oxide (GO). Although, such systems display relatively poor properties compared to the pristine graphene, it was shown that the compatibility and bonding with the epoxy matrices they display renders them preferable over the traditional, low functionality, expanded graphite (EG) products and the respective nanometric derivatives. Nevertheless, the densely decorated surface of GO and the subsequent bonding with the epoxy also sets limitations on the filler content of such systems, due to disruption of the epoxy resin chemistry and reduction of the glass transition temperature. These effects are still not clear enough.

Since the conventional synthesis methods produce GO that displays the abovementioned problematic characteristics, GO is only used sparingly. It was be shown that when relatively higher filler loading levels are required (e.g. to enhance electrical or thermal conduction), further GO processing should be done (reduction) or else EG-based fillers have to be used. To avoid using such systems with poor compatibility or multi-step processing and low production yields certain GO synthesis parameters can be modified in order to result in products displaying various chemical characteristics. It was shown in Chapter 2 that a few approaches consider modifications on the existing synthesis methods but only result in slight alterations of the high GO surface chemistry, while other methods (electrochemical exfoliation), despite resulting in preferable moderate surface chemistry, they cannot be scaled up sufficiently for mass production. Therefore, the production of a moderately oxidized GO (mGO) should be sought by single-step processes based upon the modifications of the conventional methods for GO. Furthermore, the performance of such products should be compared to the commercially available EG-based products.

Finally, it was shown that the surface oxidation displayed by the rGO, or even EG products, results in composites with relatively mediocre electrical conductivity values compared to the ones expected by the respective graphite precursors. After reviewing the surface functionalisation processes, it was revealed that only two powder treatment methods have resulted in noticeably high σ_{max} values, of which the amine-functionalisation is the most efficient. In fact, amino-functionalisation was shown to be beneficial in a series of other cases including EG and GNP systems. While the effect of the structure of the amino-functionaliser on the mechanical performance of the respective fGO/epoxy systems has been investigated, such effects on the electrical performance (σ_{max} and P_t) are still unclear.

Chapter 3 Materials, Processing & Characterization

3.1 Materials

The epoxy resin used was an amine-cured, Bisphenol A-based system, namely EPILOX™ Infusion System 5300, produced and supplied by LEUNA-Harze GmbH. This resin was chosen for this study because its low viscosity (~275 mPas/25 °C) makes it appropriate for structural fibre reinforced composites in wind energy applications, the application of interest. The two parts used are ER 5300 as epoxy monomer (epoxy equivalent weight: 170 g/eq) and EC 5310 as hardener (amine value: 520 mg KOH/g) components respectively. The system was formerly produced and supplied by BASF, The Chemical Company under the name "Baxxodur® system 5300" with the two components named "Baxxores® ER 5300" and "Baxxodur® EC 5310".

The graphite precursor for every GO powder that was synthesized for this study is the same, and was supplied by Sigma Aldrich (product no. 496596). The oxidation method used for the production of GO was done using commercially available phosphoric acid (H_3PO_4, 79620 Sigma Aldrich), sulfuric acid (H_2SO_4, 435589 Sigma Aldrich), potassium permanganate ($KMnO_4$, 26910 VWR International) and a hydrogen peroxide solution (349887 Sigma Aldrich). The mild oxidation method used for the production of mGO was done using commercially available Chromium (VI) trioxide (CrO_3, 11390939 Fischer Scientific). Edge oxidized graphene (eGO) powder is a commercially available product described by 5 – 10% oxidation degree, 15-20 layers thick and a mean particle size of 500 nm, with 90% of them being smaller than 800 nm. The eGO was kindly supplied by Garmor Inc.

The functionalization of mGO was done with amino-groups namely:

- Poly(propylene glycol) bis(2-aminopropyl ether) with average molecular masses of:
    1. ~230 g/mol and
    2. ~4000 g/mol (both display the same general structure, illustrated in Figure 3.1.1a)
- trimethylolpropane tris[poly(propylene glycol), amine terminated] ether, with average molecular mass of:
    3. ~440 g/mol (Figure 3.1.1b)

The two former represent diamine systems and will be denoted as d230 and d4000, while the latter is a triamine system and will be termed t440. The d230, d4000 and t440 reagents were supplied by Sigma Aldrich (406651, 406694 and 406708, respectively).

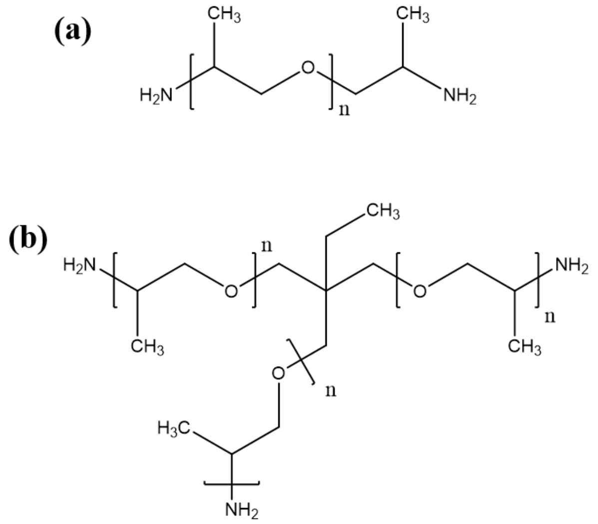

Figure 3.1.1 Molecular structure of (a): d230 (n~2), d4000 (n~68) and (b): t440 (n~2).

3.2 Processing

After listing the materials used for the purposes of this study, the next section presents the processes followed to synthesize the GO and mGO systems as well as the functionalisation of mGO to produce various fGO powders. Furthermore, comments on the powder processability are presented.

3.2.1 Synthesis of Graphene Oxide

A modified Tour method was used to synthesize GO. Initially, the H_3PO_4 was dried on a hot plate by heating to a boiling point of 260 ^oC; the acid was stirred slowly throughout this process and the temperature was monitored every 10 min. When dried, the H_3PO_4 was left at ambient conditions to cool down for several hours. Afterwards, 40 ml of a H_2SO_4/H_3PO_4 mixture (5:2 per volume) was mixed with 1.8 g of $KMnO_4$ and stirred at 50 ^oC to give a homogeneous solution. Afterwards, 300 mg of graphite were added to the solution and left for 4 h under mild shaking. Another batch was prepared and left for 30 min to demonstrate the effect of the process duration. The system was neutralized by transferring into 100 ml of cool distilled water, to which, 10 ml of the H_2O_2 solution was added. Centrifugation (Heraeus™ Megafuge™ 8) at 8872g for 10 min was used to retrieve the GO and remove the supernatant acid. The sediment was re-dispersed and washed in distilled water (three times), ethanol (once) and acetone (twice); after each step, the GO was recovered from the suspension using centrifugation. A final GO/acetone solution was obtained and probe sonicated (UP 200S) for 30 min with a 7 mm diameter tip. The resulting GO was incorporated into the epoxy within this solvent, since subsequent drying led to a material that was too agglomerated to be utilised. The process steps are illustrated in Figure 3.2.1. Henceforth, the resulting oxidised graphite will be referred to as GO.

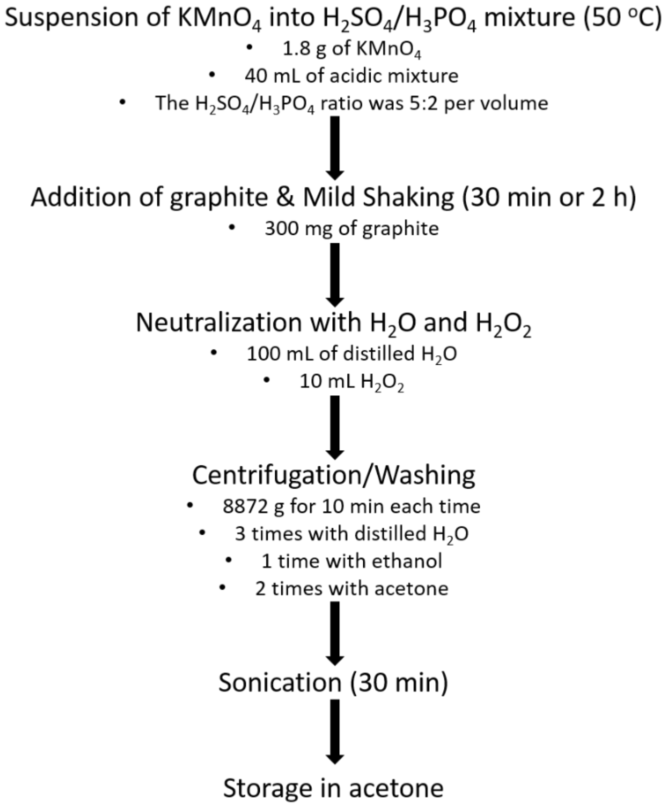

Figure 3.2.1 synthesis route for the production of GO.

3.2.2 Synthesis of Moderately Oxidized Graphene Oxide

As stated earlier the effectiveness of graphite oxidation in a medium where the traditionally used potassium permanganate ($KMnO_4$) oxidant is replaced by chromium trioxide (CrO_3) is investigated. The latter is known as an effective intercalant [140, 141] and has previously been reported only weakly to react with graphite [142].

For this synthesis, the graphite:acid ratio was the same as in the previous method. It was stated in Chapter 2 that by diluting the H_2SO_4 with the weaker H_3PO_4, the selectivity of the acidic solution is promoted, an effect that is unnecessary when the dominating $KMnO_4$ oxidant is replaced by the relatively weakly reacting CrO_3. As such, only H_2SO_4 was used as a reaction medium. A saturated solution was produced by adding ~20 mg of CrO_3 per ml of H_2SO_4 under continuous magnetic stirring at 50 °C; to assist dissolution of the CrO_3, the as-received crystals were first ground to a fine powder using mortar and pestle. The resulting orange-coloured solution was poured into a glass flask containing the appropriate amount of graphite and was placed on a shaker for 30 min for the oxidation to proceed. After this time, the system was neutralized, centrifuged, washed and sonicated using the same conditions described above. Finally, the mGO was dried at 100 °C overnight since, in this case, this procedure did not lead to a highly agglomerated product. The process steps are illustrated in Figure 3.2.2.

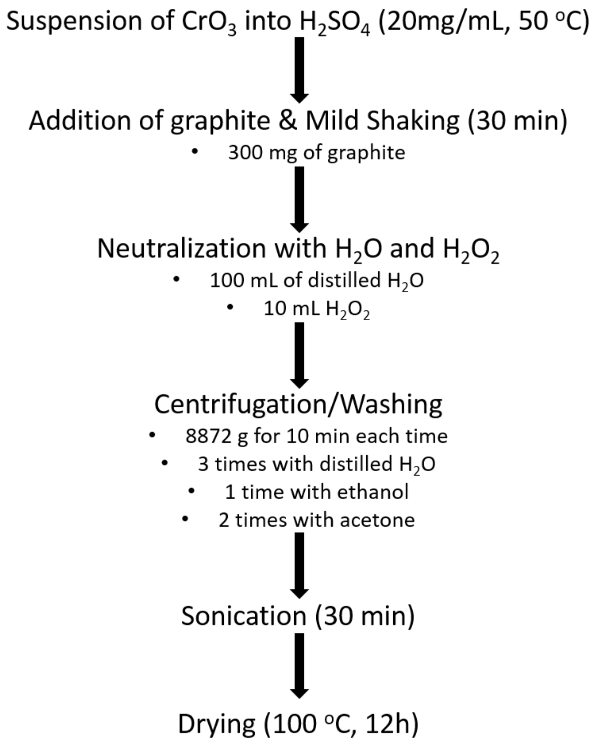

Figure 3.2.2 Synthesis route for the production of mGO.

Visual comparison of suspensions in acetone of GO (yellowish suspension to the left in Figure 3.2.3) and mGO (greyish suspension to the right in Figure 3.2.3) reveals a marked difference in colour. GO colloidal suspensions typically display yellow-brown colour as opposed to the well-known greyish-black coloured graphite or other oxygenated systems with relatively low oxygen content such as rGO [87]. Generally, systems not displaying dark colours are most likely to be characterized by highly oxygenated surfaces. Since the visual observation represents the most direct way (however not quantitative) to determine the degree of oxidation, we interpret the marked colour difference between GO and mGO in terms of differences in the functional group density.

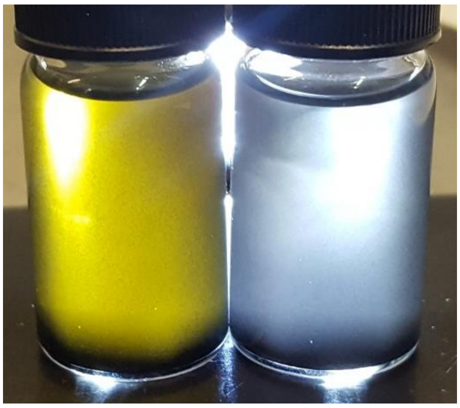

Figure 3.2.3 Suspensions in acetone of GO (yellowish suspension to the left) and mGO (greyish suspension to the right).

3.2.3 Powder Processability

To our knowledge a suspension can be proven considerably more expensive compared to the respective dry product. Furthermore, industrial implementation is limited as far as suspensions, and especially organic solvents, are related due to environmental risks, time-consuming manufacturing steps etc. Small amounts of the synthesized acetone suspensions were dried under ambient temperature inside fume extractor in order to assess the possibility of utilization of the respective powders in dry form. Figure 3.2.4 shows the powders synthesized with the two methods, after being dried. It can be seen that the GO powder (either of the two oxidizing durations) formed a pellet-like compound upon drying which was not suitable for usage as a filler, thus requiring further processing. This effect could be attributed to the highly oxygenated surface of the system, possibly leading to pronounced hydrogen bonding and re-agglomeration of the graphitic sheets. On the other hand, mGO, displayed powder form after the drying process, able to be used in a solvent-free manufacturing process. The same behavior was achieved upon drying at 100 ^{o}C, which was eventually used for the fGO systems (mentioned below) as well. The eGO powder was supplied in dry form.

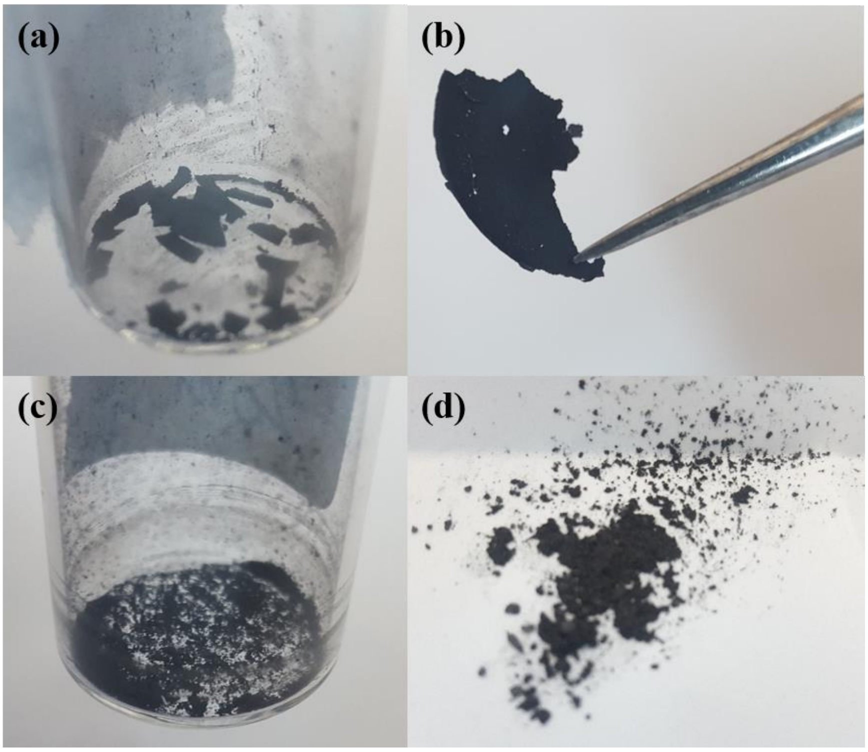

Figure 3.2.4 GO (a, b) and mGO (c, d) powders upon drying.

3.2.4 Amino-Functionalization of Moderately Oxidized Graphene Oxide

A suspension (5 mg/mL) of mGO in the required organic solvent was first prepared and sonicated for 15 min, before the appropriate amine reagent was added in a 1:10 (GO: amine) weight ratio. This formulation was chosen based upon published work; excessive reagent/GO ratios have been shown to result in extensive flake restacking [143]. The above system was then refluxed at 90 ^{o}C under mild stirring for 2h. Since aqueous suspensions are more stable and promote GO exfoliation [81], distilled water was initially preferred to disperse GO and act as medium for the amine surface treatment. However, the d4000 reagent is not compatible with water and reagent t440 was found to phase separate from water at elevated temperatures (> 70 ^{o}C). Therefore, functionalization with t440 and d4000 was conducted in 1-propanol, which is compatible with both the GO and the amine reagents and provides a sufficiently high boiling point (97 ^{o}C) for the functionalization to occur. The functionalisation process continued with a secondary thermal treatment at higher temperatures, which has been reported to be beneficial [123] in terms of residual oxygen removal as well as propagation of the covalent bonding. This process was conducted for 3 h in a rotary evaporator (IKA RV 10 digital V) under continuous mild rotation, at a constant temperature of 125 ^{o}C (heating bath, IKA HB 10) and under an applied vacuum. This process maintained dispersion through continuous agitation, as well as leading to rapid solvent removal while the reaction kept propagating. Upon completion of the process, the resulting fGO systems were retrieved by centrifugation followed by ethanol washing (4 times) and subsequent centrifugation. Finally, the fGO were dried at 100 °C overnight. The process steps are illustrated in Figure 3.2.5. Henceforth, the respective powders will be termed d230/fGO, t440/fGO, d4000/fGO, depending on the amine reagent used to functionalise them.

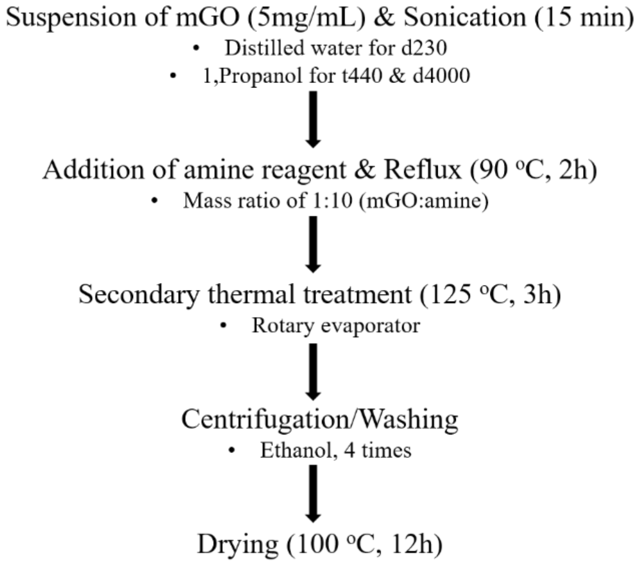

Figure 3.2.5 Amino-functionalization process of mGO.

3.3 Preparation of Epoxy Nanocomposites

This section describes the manufacturing methods followed for the preparation of epoxy samples filled with GO, mGO, eGO and fGO systems. Since the abovementioned systems exhibit different structural/chemical characteristics, the preparation of the respective nanocomposites had to be adjusted accordingly. Therefore the section is divided in three sub-sections.

3.3.1 Epoxy/GO Nanocomposites

As already mentioned the GO/acetone solution retrieved from the GO synthesis was directly used to incorporate it into the epoxy monomer via a simple solvent method. Although it has been reported before [81] that GO/aqueous suspensions are more stable than those based upon organic solvents, the usage of organic solvents is more beneficial in terms of (a) compatibility with the polymer matrix and (b) more efficient subsequent removal. Furthermore, non-polar organic solvents have been found to be non-compatible with GO and failed to disperse it [81], which is attributed to the high polarity of the oxygen-groups decorating the GO surface, a phenomenon that also characterizes the epoxy monomer, since the latter is also polar. In terms of solvent usage, acetone is the most commonly used one for GO/epoxy systems [83, 89, 107]. Therefore acetone, which offers compatibility with both epoxy and GO (at least in the short-term [81]), was employed as the solvent medium. Usually solutions of small contents (0.5mg/mL [83], 1mg/mL [107, 115]) are found to be used in the literature. Typically, sonication durations would be expected to be affected by the solution concentration used, and were found to span between 30 min [107], 1 h [115] and 3 h[108], however studies have used up to 4 h sonication [83] times even though the solution concentration was pretty low (0.5 mg/mL) [83]. In other cases, sonication was done directly in the epoxy/GO mixture for 4 h [89], or inside the hardener for 3 h under elevated temperatures (70 ^{o}C) [108]. Especially the latter would accelerate the reaction between the hardener and the GO prior to addition of the epoxy, thus adding a lot of complexity to our study. Since this study is examining samples up to relatively higher filler contents than the studies mentioned above, the usage of small solution concentrations (thus large amounts of acetone) was found to be impractical. Furthermore, the same amount of solution concentration was preferred to be used in every filler content for consistency, thus, a GO/acetone solution of 5 mg/mL was utilised, while the sonication time was chosen to be 3 h in accordance to the solution concentration. The epoxy monomer was also added to the acetone/GO solution and probe sonicated (UP 200S), with a 7 mm diameter tip. The nanofiller contents used were 0.5, 1 and 2 wt.% of GO, along with the unfilled epoxy sample. Solvent removal was done with a hot plate at 80 ^{o}C, while slowly stirring. The procedure continued with vacuum degassing to remove any residual solvent trapped inside the system. For consistency reasons, the epoxy sample, despite being unfilled, was nevertheless prepared using the same solvent procedure described above, meaning that it was diluted with acetone, probe sonicated and then dried. The reason for this was to create a reference sample that excludes any effects due to traces of residual acetone. Afterwards, the hardener was added in a weight ratio of 10:2 (epoxy:hardener), as suggested by the supplier. The final mixture was vacuum degassed to remove trapped air, cast into appropriately shaped moulds and cured in a fan oven at 70 ^{o}C for 6 h, in accordance with the supplier's instructions. After testing, samples were additionally post-cured in a fan oven at 130 ^{o}C for 6 h and tested again. In the case of destructive characterization methods, such as tensile testing new samples were prepared, cured and post-cured accordingly. It is worth mentioning, that there was a considerable sample colour change from brown to black after the post-curing (Figure 3.3.1), something that has been observed elsewhere [144] and is associated with reduction of the GO.

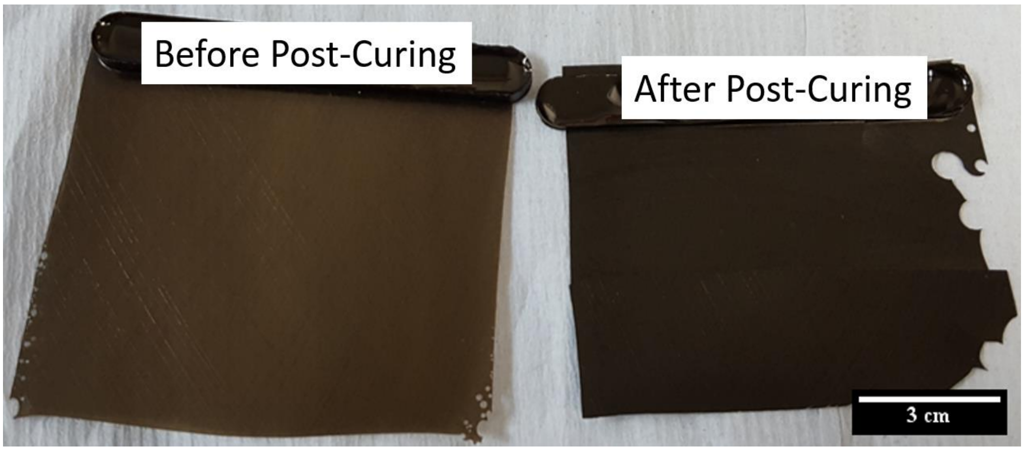

Figure 3.3.1 Epoxy/GO samples before and after the post-curing process.

3.3.2 Epoxy/mGO and Epoxy/eGO Nanocomposites

Although, it is common initially to distribute GO in a solvent to aid dispersion, this was found to be unnecessary in the case of mGO and eGO, since both obviate the need for subsequent solvent removal. From a technological perspective, direct dispersion without the need for the involvement of additional processing steps may be advantageous [108, 112], since solvent usage adds complexity, as explained earlier, increased preparation cost, environmental issues, etc. Furthermore, in order to prove that a material is compatible with the examined matrix and can be used in large scale applications, automated scalable mixing devices should be preferred. Therefore, both epoxy/mGO and epoxy/eoGO nanocomposites were prepared via a planetary mixer (Speedmixer™ DAC 150.1 FV) method, as follows: the epoxy was first mixed for 5 min with the appropriate amount of dry filler, using a planetary mixer operating at 3,000 rpm. Subsequently, the hardener was added in the stoichiometric weight ratio and the mixture was vacuum degassed, cast into moulds, and cured as mentioned above.

3.3.3 Epoxy/fGO Nanocomposites

In accordance, the planetary mixer was utilised here as well. Apart from the challenges of the solvent method mentioned above, utilisation of the widely used acetone [118, 145] should be discouraged in conjunction with amino-functionalisation, since primary amines can react with this solvent at elevated temperatures (required for solvent removal) producing imine-terminated groups, thereby altering the system's chemistry.

3.4 Characterization Methods

This section is divided in two subsections. The first one describes the methods used to characterise the structure and chemistry of the graphitic powders considered here. The second one describes the methods used to characterise the respective epoxy nanocomposites.

3.4.1 Powder Characterization

The powder systems utilised in this study were characterized with three complementary methods: Raman spectroscopy, XPS analysis and TGA. Details on the sample preparation and/or treatment as well as the exact experimental process used can be found in the next paragraphs.

Raman

Raman spectroscopy is useful for evaluating the structural characteristics of graphitic- based materials [146]. Details on the characterization of graphitic systems via Raman spectroscopy can be found in Appendix C.

The dry graphite, GO, eGO and mGO powders were characterized by Raman spectroscopy, to evaluate the structural characteristics induced by the imposed processing each sample was undergone. For this, a Renishaw RM1000 confocal microprobe system was employed, using a 780 nm excitation wavelength and operating at 2.5 mW power. The device was calibrated, prior to every measurement, with a reference silicon sample (Raman shift: 520 cm^{-1}). The peak analysis, regarding the tested samples, was done via OriginLab, assuming Lorentzian peak shapes. Specifically, for the case of D’ band, deconvolution was undertaken only when the peak was observable in the obtained spectra. For the $I_{(D)}/I_{(G)}$ and $I_{(2D)}/I_{(G)}$ ratios, peak heights were considered.

XPS

X-ray photoelectron spectroscopy (XPS) is a method based on the photoemission principle according to which X-ray bombardment on a sample can cause enough excitation to some electrons making them able to escape from the respective atoms. Those signals’ energy and intensity correspond to different elements and bonds between elements and are used for determining the elemental concentration of the examined sample. From the above it is apparent that XPS represents a more straightforward method, than Raman, to determine the oxidation degree of GO. Details on the characterization of graphitic systems via XPS can be found in Appendix C.

The XPS data were recorded and collected in the Warwick Photoemission Facility, University of Warwick. The samples were attached to electrically-conductive carbon tape, mounted onto a sample bar and loaded into a Kratos Axis Ultra DLD spectrometer. The measurements were performed in the main analysis chamber, at room temperature, with the sample being illuminated by a monochromatic Al Kα X-ray source, at a 90° angle. The core level spectra were recorded using a pass energy of 20 eV, from an analysis area of 300 x 700 μm. The spectrometer work function and binding energy scale of the spectrometer were calibrated using a polycrystalline Ag sample prior to the commencement of the experiments. In order to prevent surface charging the surface was flooded with a beam of low energy electrons throughout the experiment and this necessitated recalibration of the binding energy scale. To achieve this, the graphitic sp^2 component of the C1s spectrum was referenced to 284.4 eV. The data were analysed in the CasaXPS package, using Shirley backgrounds and Voigt peak shapes.

TGA

Thermogravimetric analysis (TGA) is a characterization method which monitors mass loss as a function of temperature [147] and is commonly used to quantify the concentration of oxygen-based functionalities grafted onto GO [148]. Details on the characterization of graphitic systems via TGA can be found in Appendix C.

A Perkin-Elmer Pyris 1, TGA analyser was used to assess the extent of the oxidation of the GO, eGO, mGO and fGO samples, as well as the possibilities of impurities in the case of the graphite powder. The platinum pan used in this study was first held at 900 ^{o}C, in air environment, for 30 min to remove possible impurities or residual material. Afterwards, the device was calibrated by scaling the platinum pan at 70 ^{o}C. Subsequently, the air flow was changed to nitrogen flow and the samples were mounted, weighed and held at 70 ^{o}C for 10 min before being heated up to 600 ^{o}C at 10 ^{o}C/min.

3.4.2 Epoxy Nanocomposites Characterization

The epoxy nanocomposite systems filled with GO, mGO, eGO and the three fGO powders were subjected to a series of characterization techniques that varied according to each system's attributes. Details on the sample preparation/treatment as well as the exact experimental process that was followed for each of them can be found in the next paragraphs.

TEM

Morphological characterization was done via TEM imaging. TEM allows the direct observation of the dispersed nano-structures, representatively illustrating the dispersion level and despite being a quite local characterization method, it can be found in the literature quite often [2, 24]. This method is based on electron density and diffraction contrast differences between different structures. The layered nano-fillers in a polymer nanocomposite, can be observed with different contrast tones in the TEM images, depending on the degree of exfoliation. If the structures are sufficiently thick (immiscible configuration) they can be observed easily independently of the orientation of the layers. While the degree of dispersion becomes finer, the contrast tone of the layered structure can be very light.

For the GO- and eGO- filled nanocomposites a Hitachi H 7000, device was employed, following ultramicrotomy using an RMC MT-7 system and a Diatome 35° diamond knife. For the mGO- filled samples an FEI Tecnai T12, instrument was used following ultramicrotomy using a Leica Ultracut E ultramicrotome together with a Diatome 45° diamond knife. Section thickness was ~80 nm in both cases. The image analysis was done with the software ImageJ.

Tensile

Tensile testing was conducted on the unfilled, GO-, mGO- and eGO- filled epoxy samples using a Tinius Olsen H25KS Tensometer. For this, dumbbell-shaped samples of 4 mm in thickness were used. The displacement rate was 1 mm/min, until sample failure. A total of three measurements per batch were used to determine standard deviation errors.

SEM

Scanning electron microscopy (SEM) represents a useful tool on the morphological characterization of nanocomposites since it can give direct information on the surface characteristics of the respective samples as well as the particle distribution within the matrix.

As such, the fractured areas of the tensile tested samples were examined via an EVO LS25, Zeiss, scanning electron microscope. The specimens were gold coated (K550X Sputter Coater) for 3 min. The image analysis was done with the software ImageJ.

FTIR

Utilization of Fourier-transform infrared spectroscopy (FTIR) has been proven useful to monitor the curing kinetics of epoxy resins, since it is sensitive to the formation or consumption of the crosslinking-related groups [149–151]. Related information can be found in Appendix B.

An iD7 attenuated total reflectance Fourier transform infrared spectrometer (ATR-FTIR – Nicolet iS5, Thermo-Scientific) was used to obtain the FT-IR spectra of the unfilled and GO-filled epoxy samples. The respective data were normalized using a standard normal variate correction [152] with the software irAnalyze, before plotting.

XRD

XRD is a method based on the diffraction of X-rays and can detect and separate immiscible, intercalated and exfoliated configurations due to interlaminar distance variations. Generally, layered fillers show peaks at certain angles representing their specific interlayer spacing. When incorporated into polymer matrices, the peak might shift to lower angles (larger interlayer spacing) reflecting an intercalated structure, or it could appear to be weaker in intensity, due to exfoliation and lack of layered structure.

X-Ray diffraction (XRD) patterns of the mGO- filled and all the fGO-filled epoxy were acquired using a Rigaku Smart Lab instrument (Cu K-α radiation, λ=1.54 Å), in the geometrical range of 2ϑ=10-30^o, with increments of 0.02^o. For the peak analysis OriginLab was used, assuming Voigt peak shapes, while for the diffraction intensities peak areas were considered.

DSC

Differential scanning calorimetry (DSC) is the most widely used method for determining the T_g of epoxy resins [153]. As such, the glass transition temperature (T_g) of all the epoxy-based systems (unfilled resin as well as epoxy filled with GO, eGO, mGO and all fGO powders) was determined by using a Perkin-Elmer DSC7, differential scanning calorimeter. For this, the device was calibrated with reference to pure indium's melting point (156.6 ^{o}C) by heating at 10 ^{o}C/min. The epoxy-based samples were measured via heating, cooling and re-heating scans, from 25 ^{o}C to 120 ^{o}C all at the same heating/cooling rate of 10 ^{o}C/min, in order to erase the thermal history of the epoxy-based samples [154]. Each sample's T_g was determined from the second heating programme by using the point of inflection of the step-like transition in the heat flow curve. A total of three measurements were considered per batch to calculate average and standard deviation values for the T_g of the epoxy-based systems.

Electrical Conductivity

The electrical conductivity of the epoxy-based samples was determined by means of two-probe methods. The samples filled with GO were tested with a Keithley 6487 picoammeter. The samples filled with mGO and fGO were tested with a Keithley 6517B electrometer/high resistance meter fitted with an 8009-resistivity. Applied voltage was kept at 100V. The conductivity was determined using the formula:

$$\sigma = \frac{1}{R}\frac{l}{A} \qquad \text{(Equation 2)}$$

where σ is the conductivity, R the resistance, l the sample's thickness and A the cross-sectional area of the sample. The samples were rectangular shaped, ~200 μm in thickness, while their surfaces were polished with abrasive paper (grade 1,000) and treated either with gold coating (K550X Sputter Coater, 3 min each side) or silver paint. The percolation plots were analysed with OriginLab, where the percolation threshold was considered as the lowest filler volume converging with the percolation power law (Equation 1, page 13).

Thermal Conductivity

A steady-state technique was deployed to determine thermal conductivity at ambient temperature. The in-house built apparatus is a guarded hot plate configuration, including a "heating" and a "cooling" blocks, which promote one dimensional heat flow through the tested sample. Heat was extracted with a Huber Minichiller 280 cold bath/circulator, while the heat flux was monitored with an HFS-4 OMEGA Engineering, thin film flux sensor (sensitivity: 1.6 μV/(W/m^2)). The device was calibrated with fused silica and polytetrafluoroethylene (PTFE). More details about the apparatus can be found in [17]. The thermal conductivity was determined using the formula:

$$q = -k \frac{\Delta T}{\Delta x} \qquad \text{(Equation 3)}$$

Where q is the heat flux, k is the thermal conductivity, ΔT is the temperature difference between the heating and cooling blocks and Δx is the sample's thickness. The disk-shaped samples had a thickness of 3 mm and a diameter of 50 mm. The samples surfaces were treated by abrasive paper to reduce roughness and then by applying thermal grease, to ensure fine thermal contact. Interface resistance effects between the apparatus and the samples were erased by measuring three epoxy samples of different thicknesses and using:

$$\frac{\Delta x}{k_{meas}} = \frac{\Delta x}{k_{true}} + \frac{1}{h} \qquad \text{(Equation 4)}$$

where k_{meas} is the measured thermal conductivity, k_{true} is the thermal conductivity of the sample and $1/h$ is the thermal interface resistance, as described in [17]. The achieved measurement uncertainty was 0.12%.

Dielectric Spectroscopy

Dielectric spectroscopy [155] is widely recognised as one of the most sensitive methods to investigate the epoxy curing kinetics, since the polar bonds derived by the crosslinking, such as C-O-C, C-OH, and N-H are affected by the electric stimulus. The complex relative dielectric permittivity (ε^*) is defined as:

$$\varepsilon^* = \varepsilon' - i\varepsilon'' \qquad \text{(Equation 5)}$$

where ε' the real and ε'' the imaginary parts of the relative dielectric permittivity, which are dependent on the capacitance and the conductance of the material, respectively. Reorientation of dipoles (relaxations), derived from polar groups, under applied AC electric field results in alterations of the ε' and ε'' spectra of the polymer and can be readily detected during phase transitions (e.g., glass transition) and secondary transitions (e.g., localized phenomena). The dielectric relaxations of a polymer are labelled with the Greek letters, α-, β- and γ- as observed from low to high frequencies or high to low temperatures, respectively. Usually the α process is associated with the random segmental motions of the glass transition, while the β- and γ- relaxations are associated with local motions or re-orientations that are dependent on the chemical structure of the system [155–157]. More specifically, the secondary relaxations in the case of amine crosslinked epoxy resins are attributed to:

- localized motions involving unreacted end-groups (γ- relaxation) and
- motions of the hydroxyl - ether groups that are formed during cross-linking (β- relaxation) [155].

As such, the samples of this study were characterized using a Solartron 1260A Impedance/Phase Gain Analyser with the 1296A Dielectric Interface System attached. The test cell was a Janis Research STVP-200-XG system cryostat and the temperature was controlled with a Lake Shore 332 Cryogenic Temperature Controller. Liquid nitrogen was used as a cooling fluid while the examined temperature range varied from -160 ^{o}C to 20 ^{o}C with 10 ^{o}C steps. The tested samples were kept under helium atmosphere throughout the whole series of tests. The applied AC voltage was kept constant at 1 V and the examined frequency range was from 10^{-1} Hz to 10^{5} Hz. The obtained values are averaged from measurements taken at an integration time of: 10 s in the frequency range of 100 kHz to 1 Hz, and 10 cycles' values from 1 to 0.1 Hz. The disk shaped specimens (25 mm wide, ~0.2 mm thick) were gold coated (K550X Sputter Coater) for 3 min on each side to ensure the quality of ohmic contact.

Chapter 4 Understanding the Cross-linking Reactions on Highly Oxidized Graphene/Epoxy Nanocomposites

In this Chapter, the synthesized GO was characterized to assess the degree of oxygenation. Afterwards, a number of characterization methods were employed on the respective GO/nanocomposites, to monitor the chemical and physical properties, as well as to determine whether the observed behavior was attributed to the disturbed epoxy crosslinking phenomena, that were mentioned in the relative literature. As such, this Chapter will serve to answer the first two questions that were raised in Chapter 1:

1. It is assumed that the thermo-mechanical behaviour of GO/epoxy systems might be affected by the temperatures used to cure the epoxy. Is this true, and in which way?
2. Is it possible to trigger crosslinking (thus bonding) reactions in GO/epoxy systems separately?

Part of the results presented below are published in Journal of Materials Science as a full-length article:

O. Vryonis, S. T. H. Virtanen, T. Andritsch, A. S. Vaughan, and P. L. Lewin, "Understanding the cross-linking reactions in highly oxidized graphene/epoxy nanocomposite systems," *J. Mater. Sci.*, vol. 54, no. 4, pp. 3035–3051, 2019.

4.1 GO Characterization

The results of the graphite and GO characterization via Raman, XPS and TGA, as well as the respective data analyses and discussion are presented in the next subsections.

4.1.1 Raman spectroscopy

Figure 4.1.1a shows Raman spectra obtained from the graphite and the GO powder, while Figure 4.1.1b shows the deconvoluted Raman spectra, obtained from peak analysis fitting.

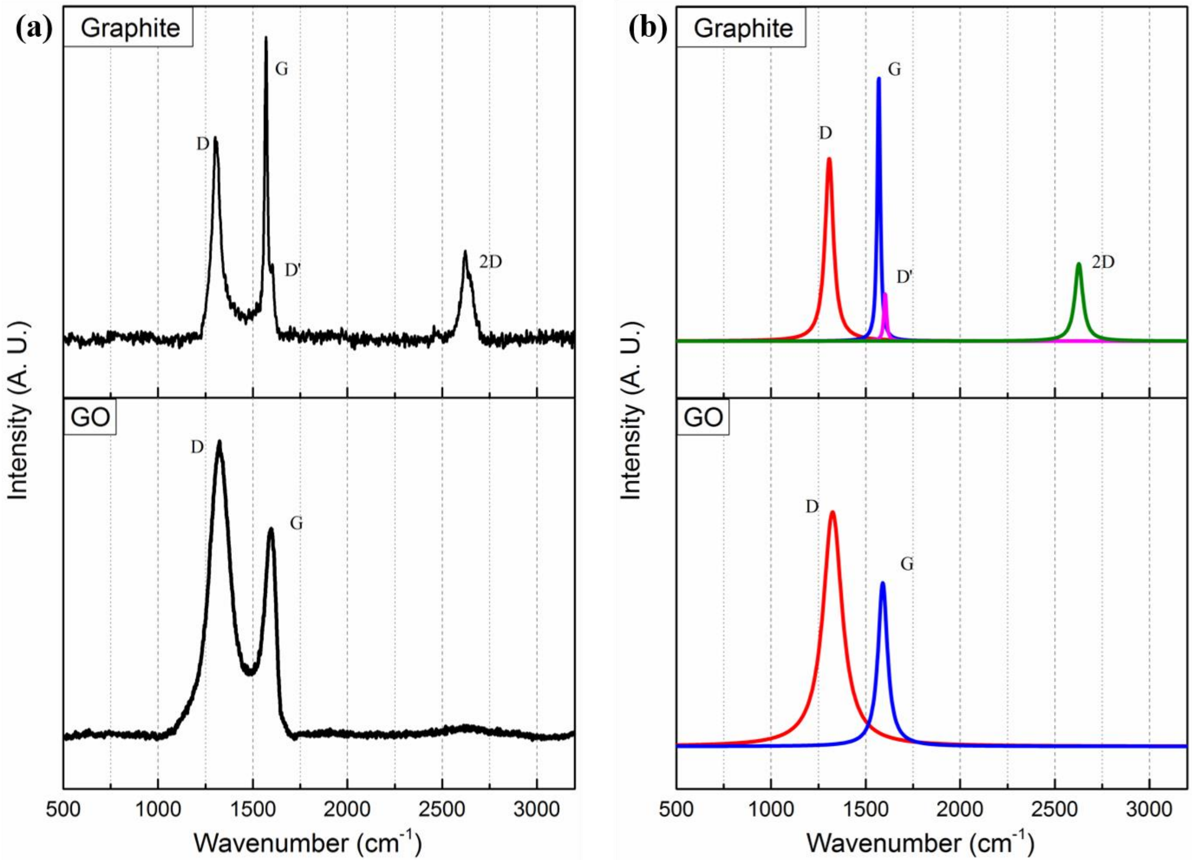

Figure 4.1.1 (a) Raman spectra of the precursor graphite and the synthesized GO and (b) deconvoluted Raman spectra.

In the case of graphite, a total of four characteristic peaks can be observed at 1307, 1569, 1603, and 2627 cm^{-1}, that represent the D, G, D′ and 2D bands, respectively, as explained in Appendix C. As expected, the Raman response of the precursor graphite is dominated by vibrations of the carbon atoms, as well as the highly ordered stacking sequence, which manifest themselves as sharp and intense G and 2D bands. However, the D and D′ bands indicate the presence of defects. Conversely, the GO specimen exhibits the opposite form of behaviour, which is characterized by the broadened and less intense G band, the pronounced D band, as well as the absence of the 2D band. Furthermore, the G band for the GO sample has shifted to *higher* wavenumbers, compared with that of graphite, and is located at 1590 cm^{-1}. As such, the D’ band is not visible for the GO sample and peak deconvolution is not considered. As shown in the graph insets, the $I_{(D)}/I_{(G)}$ ratio of the GO is considerably higher than that of graphite, while the same behaviour is displayed with the FWHM values. Moreover, since the GO does not display any 2D band, due to the absence of stacking order, the $I_{(2D)}/I_{(G)}$ ratio could not be calculated. The respective Raman data can be found in Table 4-1.

Table 4-1 Raman data for the precursor graphite and the GO.

	Band	**Position**	**FWHM**
Graphite $I_{(D)}/I_{(G)} = 0.67$ $I_{(2D)}/I_{(G)} = 0.29$	D	1307.78 ± 0.34	53.01 ± 0.98
	G	1569.53 ± 0.14	18.73 ± 0.44
	D’	1603.37 ± 0.71	16.25 ± 2.24
	2D	2627.32 ± 0.68	50.50 ± 1.99
GO $I_{(D)}/I_{(G)} = 1.42$	D	1325.49 ± 0.27	121.54 ± 0.82
	G	1590.69 ± 0.26	62.86 ± 0.78
	D’	--	--
	2D	--	--

These results, therefore, confirm that the imposed oxidation process has resulted in disruption of the graphite lattice via the attachment of various oxygen-based functional groups.

4.1.2 XPS

Figure 4.1.2 shows XPS survey data obtained from the precursor graphite and the GO powders. Derived elemental ratios are presented in the insets. It can be seen that the precursor graphite displays an oxygen content of 3.2%, resulting in a C/O ratio of ~30, which is consistent with the Raman data presented above, indicating minor impurities. The synthesized GO shows a much lower C/O ratio of ~2.8 and an oxygen content of ~26%. These values are typical for GO, as explained in Appendix C. It should be noted that the small S (sulphur) content displayed by the GO is consistent with published data, where the effect has been attributed to covalently bonded sulphates or adsorbed sulfuric acid [97].

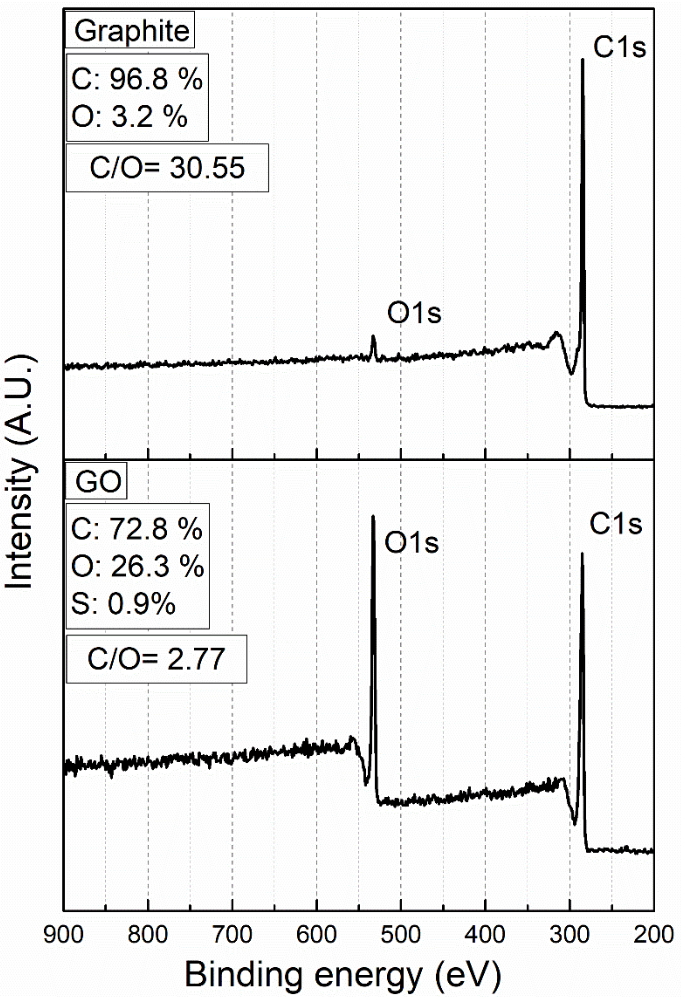

Figure 4.1.2 XPS survey plots on the precursor graphite and the GO.

Figure 4.1.3 shows the deconvolution of the C1s core-level spectra into the 5 peaks attributed to: sp^2 hybridized carbon (284.4 eV), sp^3 hybridized carbon (285.04 eV), C-O bonds from hydroxyls or epoxides (286.72 eV), C=O bonds (288 eV) and O=C-O bonds (289.06 eV) from carboxyls, as explained earlier. Two more (weak) peaks appear at 290.85 eV and 293.9 eV both attributed to $\pi \rightarrow \pi^*$ transitions (also called $\pi \rightarrow \pi^*$ shakeup) an effect that is characteristic to the carbon aromatic structure [158]. Despite the latter not giving direct indications on the elemental composition, it represents a measure of the intact graphitic characteristics of the material [159]. The GO shows pronounced presence of epoxides and hydrogens which, as discussed earlier, exists on the graphitic basal plane and can participate in the epoxy crosslinking reactions. It has been shown in the article introducing Tour's method [100] that the amount of epoxides is dominant compared to hydroxyls when graphite is processed with this method. The carboxyl group presence is also confirmed, which was discussed earlier to be attached on the graphitic peripheral plane. It was discussed earlier that the Lerf - Klinowski model [79] considers only carboxylic groups in the GO edges, thus a number of studies only deconvolute one contribution ascribed to O=C-O, while some other studies identify the carbonyl (C=O) contribution as a separate moiety [158]. In this study we present the contributions of both C=O and O=C-O bonds by acknowledging that a carbonyl bond is included in a carboxyl group. Thus, one could only assume the sum of both C=O and O=C-O peaks as a single contribution from carboxylic functionalities or alternatively as different contributions from carbonyls and carboxyls. Furthermore, the significant amount of sp^3 hybridized carbon atoms compared to the intact sp^2 ones, indicates the severe oxidation by $KMnO_4$. Conversely, the graphite shows a significant sp^2 carbon hybridization peak and a diminished amount of oxygen functional groups compared to the GO. The extent of disorder on the GO graphitic lattice compared to the graphite is also confirmed by the decreased π → π* shakeup values this sample displays.

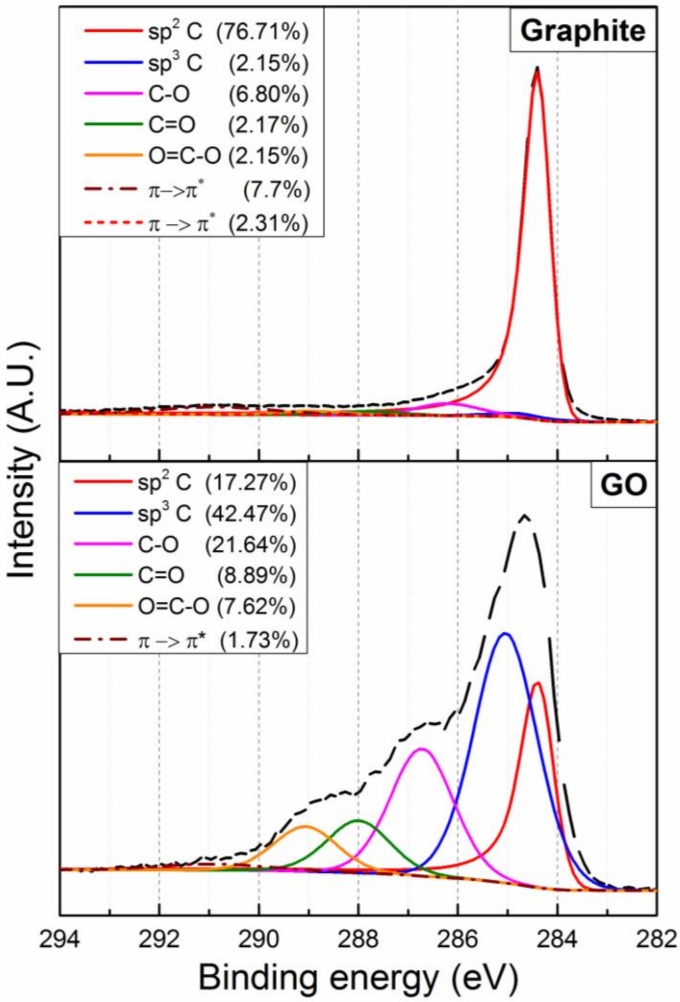

Figure 4.1.3 Deconvolution of the C1s spectra of the graphite and the GO.

From the above, it is confirmed that the graphite was successfully decorated with various oxygen-based groups, aligning with the Raman spectra shown above.

4.1.3 TGA

The successful graphite oxidation is also demonstrated by the TGA data shown in Figure 4.1.4. The graphite shows a minimal mass loss of ~1.5% at 700 °C (see inset in Figure 4.1.4), which confirms the existence of minor impurities, aligning with the Raman and XPS data. On the other hand, the GO specimen shows a significant variation in mass with temperature, similar to the ones described in Appendix C. The pronounced mass loss (~40%) between 200 °C and 350 °C is associated with the removal of labile oxygen–based groups, while the further monotonic mass decrease until the end of the measurement is attributed to the removal of stable oxygen-based groups. It is also indicated that adsorbed water exists within the GO specimen, since a mass loss of ~5 % is displayed up to ~150 °C.

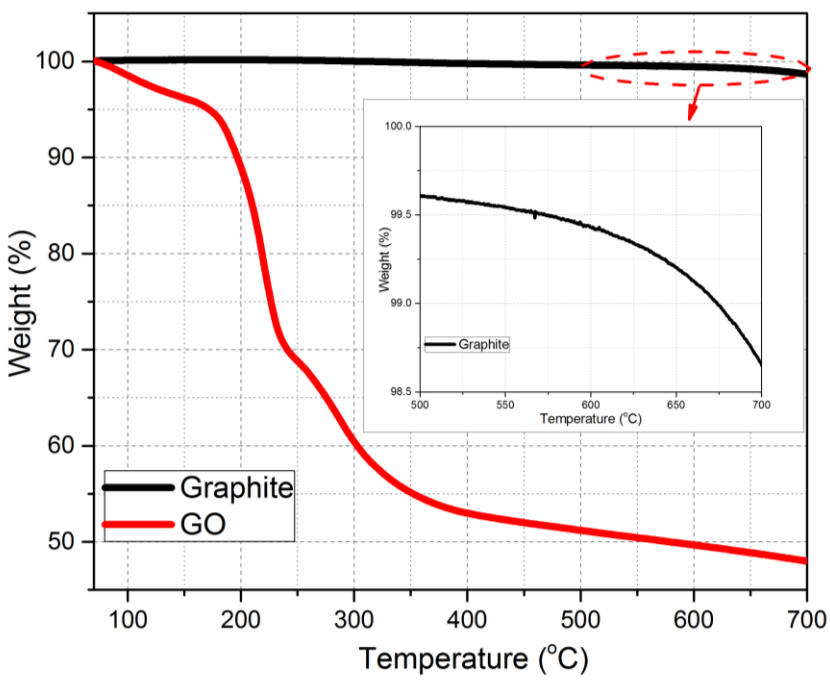

Figure 4.1.4 TGA plots for graphite and GO. Inset: magnified view of the graphite's high temperature regime.

All three methods described above align with each other and prove the fact that the synthesis of GO was successful with the attachment of epoxide and hydrogen groups on the basal plane while carboxylic groups are also present and attached on the peripheral plane. Since the first step of this study was achieved with the oxidation of graphite the next one, characterization of the respective epoxy nanocomposites, will be described below.

4.2 Chemistry of Epoxy/GO Nanocomposites

This section presents the characterization results of the epoxy/GO nanocomposites via DSC, FT-IR and dielectric spectroscopy as obtained before and after the post-curing process. These techniques give an insight on the chemistry and more specifically the stoichiometry of the GO-filled systems.

4.2.1 DSC

Table 4-2 presents the T_g temperatures, of the unfilled and GO- filled epoxy samples as obtained before and after the post-curing, as well as the T_g difference that resulted from the post-curing (ΔT_g). In this, both weight fraction (W_f) and volume fraction (V_f) values are presented, the latter being derived from the former using Equation 6 [84]:

$$V_f = \frac{W_f \rho_m}{W_f \rho_m + (1 - W_f)\rho_f} \qquad \text{(Equation 6)}$$

where ρ_m is the matrix density (1.16 g/cm^3) and ρ_f is the filler density, which according to [84, 85] is 2.2 g/cm^3. From this, it is evident that incorporation of 0.5 wt.% of GO results in a T_g increase of ~1 °C, compared with the unfilled epoxy, however such variations fall within the measured standard deviation errors. The incorporation of 1 wt.% of GO or larger, reduces the T_g of the system, similarly to what was presented earlier in Chapter 2. It is apparent that the effect is markedly more pronounced in the sample containing 2 wt.% of GO, with a T_g decrease of almost 11°C, compared to the unfilled epoxy. Thus, the associated filler content leads in a dominant presence of GO.

Table 4-2 T_g values of the unfilled and GO- filled epoxy samples before and after the post-curing. The difference between those values is indicated as ΔT_g.

GO content (wt.%)	GO content (vol.%)	T_g (°C) before post-curing	T_g (°C) after post-curing	ΔT_g (°C)
Unfilled	--	77.33 ± 0.75	85.87 ± 0.88	8.5
0.5	0.26	78.20 ± 0.77	85.84 ± 0.53	7.6
1	0.53	74.87 ± 0.59	79.37 ± 0.69	4.5
2	1.06	66.5 ± 0.83	78.37 ± 0.71	11.8

After post-curing, the unfilled sample displays a ΔT_g of 8.5 °C, due to the propagation of crosslinking. The samples filled with 0.5 and 1 wt.% GO display a monotonically decreasing pattern of the associated ΔT_g value after post-curing. However, the 2 wt.% GO-filled sample displays a ΔT_g of almost 12 °C, which is noticeably larger compared to the other samples, including the unfilled epoxy. This effect confirms the significance of the associated GO content in the curing reactions. It is strongly implied that during post-curing the GO-dominated sample (filled with 2 wt.% of GO) undergoes a considerably accelerated/alternated crosslinking reaction, which manifests itself as an increased ΔT_g.

4.2.2 FT-IR Spectroscopy

The FT-IR spectra of the unfilled epoxy and the epoxy filled with 2 wt.% of GO, as obtained before and after the post-curing process, are presented in Figure 4.2.1. Since the main focus here concerns the disruption of the epoxy stoichiometry, the hydroxyl, ether and epoxide (oxirane) related wavelength regions, (~3400 cm^{-1}, 1180-1010 cm^{-1} and 915-830 cm^{-1}, respectively), will be monitored as explained in Appendix B. The related band regions are pointed out with arrows by indicative illustrations of the relative chemical groups.

It can be seen in Figure 4.2.1a that the post-curing process triggered the etherification reactions in the unfilled epoxy since the related system displays increased absorbance in the ether-group region. This effect resulted in the ΔT_g of 8.5°C, that was presented above. The introduction of GO into the system, prior to post-curing, results in pronounced oxirane-group bands, (Figure 4.2.1b), which aligns with the T_g reduction of ~12 °C observed by this sample. Both the unfilled and GO-filled samples display similar hydroxyl group band intensity, which is attributed to the reason that not enough crosslinks are formed yet in the GO-filled sample. If the two samples were at the same crosslinking stage the GO-filled epoxy would have displayed increased hydroxyl concentration due to the incorporated hydroxyls from the GO surface. Therefore, it is implied that the crosslinking reactions of the GO-filled epoxy are delayed, as stated elsewhere [21].

Figure 4.2.1c shows the IR spectra of the GO-filled sample as obtained before and after the post-curing process. From this, it appears that after the thermal process the system displays significantly increased hydroxyl and significantly decreased epoxide group regions, while the observed ether group bands are also increased. This indicates that the epoxide consumption is considerably accelerated during post-curing via both reactions with hardener, and etherification reactions. This aligns well with the fact that the post-cured GO-filled sample displayed a significant ΔT_g.

Finally, comparing the unfilled and GO- filled samples, both after being post-cured (Figure 4.2.1d), it can be seen that the difference in the respective epoxide group regions is minimal. Considering that the GO-filled sample should be epoxide-rich compared to the unfilled sample, it is confirmed that during post-curing, the residual oxiranes are massively consumed via hardener and etherification reactions, in the nanocomposite system. Additionally, thermal reduction could occur during the post-curing, which aligns with the colour change of the epoxy samples shown earlier. This would readily trigger oxirane removal since they are the most volatile and thermally unstable functionalities on the GO surface [158], resulting in a partially-thermally-reduced GO. Systems such as rGO were shown in Chapter 2 to result in increased T_g values for various reasons, which might represent an additional factor for the increased ΔT_g of the associated sample. The latter effect might be the reason why some studies, mentioned in Chapter 2, display only increased T_g values, when using considerably higher curing temperatures than the ones used in this study.

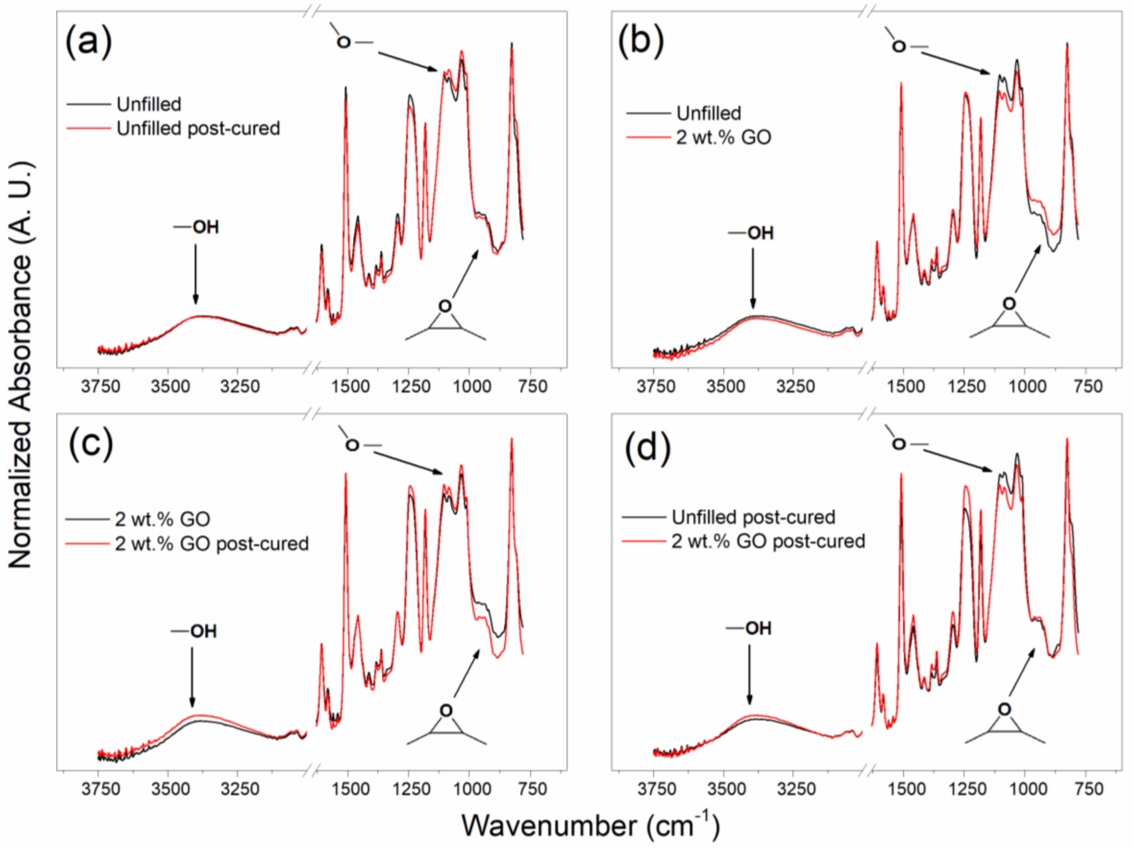

Figure 4.2.1 FT-IR spectra of the unfilled and 2 wt.% GO filled samples, prior and after the post-curing, in the 3750 – 750 cm^{-1} regions.

4.2.3 Dielectric Spectroscopy

Figure 4.2.2a, b depict the real part of the complex relative permittivity (ε'), and its variation with frequency, at 20 °C, before and after the post-curing, respectively. Since charges can accumulate around nanoparticles [160], ε' would be expected to increase with filler content. Moreover, an increased population of polar groups (existing on the GO surface) should also contribute to the dielectric response of the medium [155]. Hence, for both these reasons, a monotonic increase in ε' value with increasing GO loading level could reasonably be expected. However, as shown in Figure 4.2.2a, the sample filled with 0.5 wt.% GO is characterized by reduced ε' values compared to the unfilled sample. Nanocomposite systems exhibiting a lower ε' than that of the unfilled matrix material have been reported and discussed elsewhere [161, 162] and this phenomenon has been ascribed to local interactions leading to molecular immobilization on interfacial regions. Thus, the relatively low ε' values of the 0.5 wt.% sample before post-curing reveal a strong interfacial region which is attributed to the GO surface chemistry. It was shown earlier that specifically this sample did not show any T_g decrease due to the fact that the associated bonding was not sufficient to alter the epoxy stoichiometry. Therefore, dielectric spectroscopy is proved to be more sensitive in distinguishing such effects, compared to DSC. After post-curing (Figure 4.2.2b), ε' is slightly increased for the unfilled sample and considerably increased for all GO-filled samples, with the system containing 0.5 wt.% GO now exhibiting higher values of ε' than the unfilled epoxy. As such, this effect is attributed to the GO and not the matrix. It was claimed earlier that the post-curing thermal process resulted in partial thermal reduction of the GO, an effect that has been reported elsewhere [144, 163] to increase the ε' values of the respective composite. In theory, however, reduction of GO, which involves removal of polar groups, should have caused a decreased ε' value. Therefore, it is suggested the dominant consequence of the post-curing is the relative increase in the electrical conductivity of the partially reduced GO [121]. As a result this sample exhibits enhanced electrical heterogeneity [157], which leads to higher ε' values [36, 162].

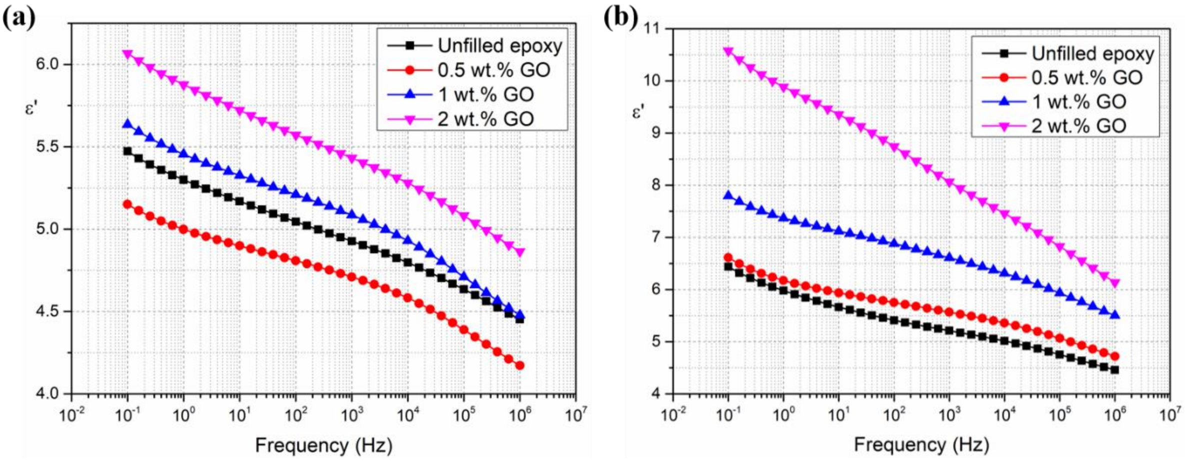

Figure 4.2.2 Real part of the relative complex permittivity at 20 °C, before (a) and after (b) the post-curing.

Figure 4.2.3 presents the variation of the imaginary part of the relative permittivity (ε'') with frequency, obtained from the unfilled epoxy and the epoxy filled with 2 wt.% of GO, before the post-curing. The examined temperatures are between -150 °C and -50 °C so as to reveal variations in the γ and β relaxation processes. Considering first, the data obtained at -150 °C and -130 °C (Figure 4.2.3a, b). The γ relaxation, prior to post-curing, is relatively weak for the unfilled system but broader and more pronounced for the system containing 2 wt.% of GO. Furthermore, the γ relaxation peak maximum of the unfilled sample is located at lower frequency than for the system containing the GO. This phenomenon is ascribed to the fact that the γ relaxation, generally, arises from a range of different polar end-groups, depending on the matrix chemistry. As such, the unfilled epoxy being at the optimum stoichiometry, displays a γ relaxation that contains contributions from equal numbers of unreacted epoxides and amines. In contrast, the system containing GO, displays a spectrum, strongly influenced by the excess of epoxide groups. This assertion is consistent with the FT-IR data discussed previously. As such, we suggest that for both systems, the observed γ relaxation originates from the motion of terminal epoxide and amine groups (i.e. two different species with different dynamics and dipole moments) and that the observed differences can be explained by variations in the concentration of each.

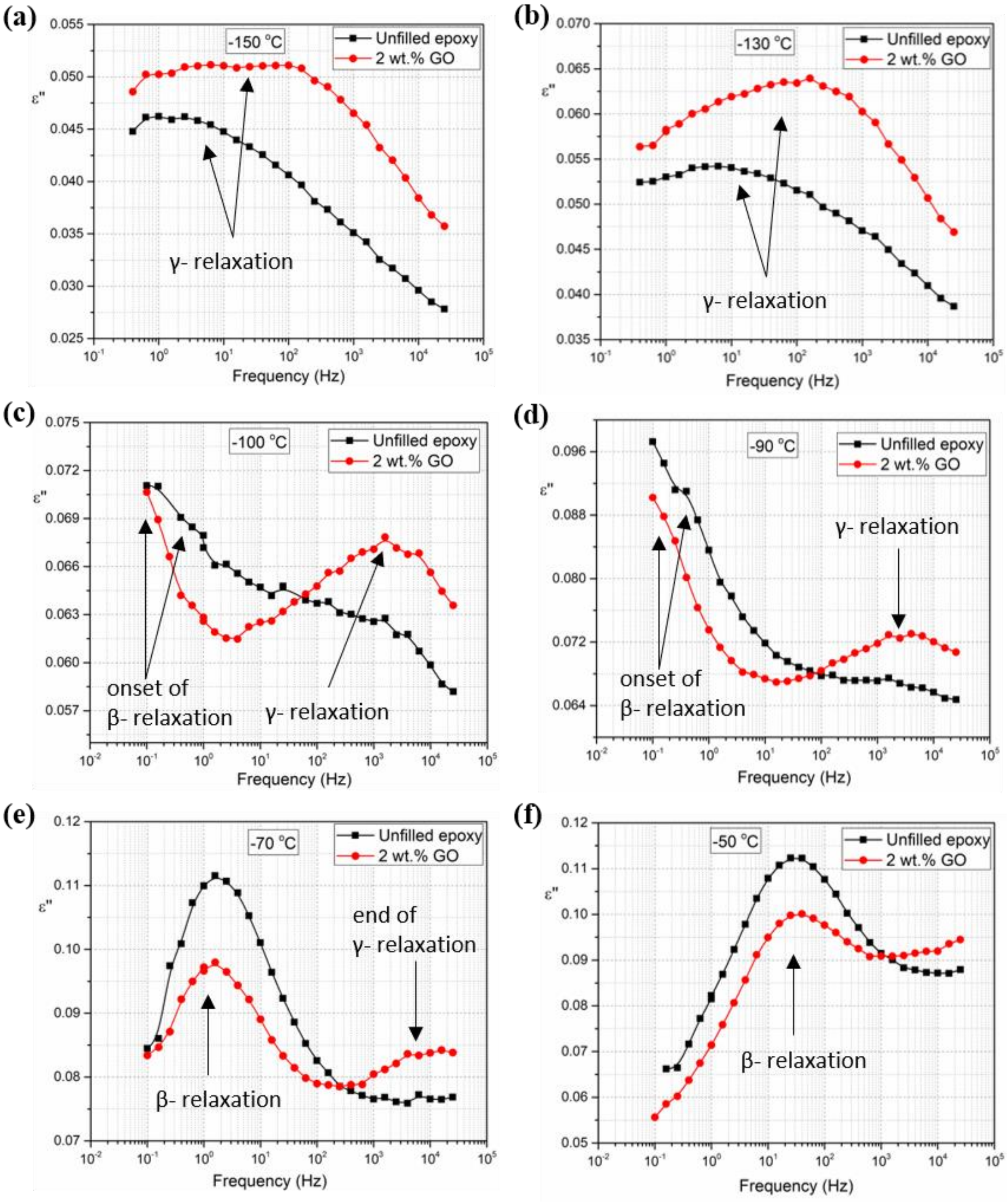

Figure 4.2.3 Imaginary part of the relative complex permittivity at: (a) -150 °C, (b) -130 °C, (c) -100 °C, (d) -90 °C, (e) -70 °C and (f) -50 °C, as obtained prior to post curing.

As the temperature increases (Figure 4.2.3c, d) the *ε′′* spectra reveal the β relaxation “entering” the low frequency regime, while the γ-relaxation is shifting towards higher frequencies for the GO-filled sample. However, the latter relaxation has disappeared in the case of the unfilled epoxy, underlining the weak characteristics of the related dipoles when the system exhibits absolute stoichiometric balance. Upon complete appearance of the β- relaxation (Figure 4.2.3e, f), it is revealed that both samples display this relaxation peak at the same frequency.

Figure 4.2.4 presents the variation of *ε″* with frequency, obtained from the unfilled epoxy and the epoxy filled with 2 wt.% of GO, after the post-curing. The presented temperatures span between -150 °C and 0 °C in order to monitor the γ and β relaxations, as well as the newly appeared interfacial/charge transport phenomena.

Considering, first, Figure 4.2.4a, b it appears that the shape of the γ relaxation of the unfilled sample is comparable to that seen before thermal treatment (see Figure 4.2.4a, b), suggesting the existence of residual unreacted epoxides/amines. Conversely, post-curing of the GO-filled sample results in a dramatic change in the dielectric spectrum, with significantly increased losses being evident over the complete frequency regime. Especially the slope that appears in the low frequency regime, and possibly swamps the γ relaxation (Figure 4.2.4a, b, c) is attributed to charge transport as well as interfacial phenomena. This behaviour aligns well with the *ε′* spectra of the post-cured samples, presented above (Figure 4.2.3b) attributing the effect to the thermal reduction and enhanced electrical conductivity of the GO which, in turn, increases charge transport losses and/or interfacial polarization phenomena [157].

Furthermore, post-curing results in a considerable modification of the β relaxation which, from Figure 4.2.4d-h appears to be broader and detected at higher temperatures which aligns with the related literature [155], as explained in Appendix B. More specifically, the β relaxation now forms a peak maximum between 10 Hz and 100 Hz at -30 °C – for both samples, while before the post-curing this occurred at -50 °C (see Figure 4.2.3f). By comparing the β relaxation peaks of the two post-cured samples, it can be seen that the one displayed by the GO- filled epoxy is much more pronounced and shifted towards slightly lower frequencies. This is attributed to the limited mobility of the hydroxyl-ether dipoles formed in the epoxy/GO interface, confirming the promoted bonding between them which occurred during the thermal process. Furthermore, after the β relaxation has shifted to the high frequency regime (Figure 4.2.4g, h), the charge transport-related slope, that was observed before (Figure 4.2.4a, b, c) appears again at the low frequency, implying that it was previously covered by the strong presence of the β relaxation.

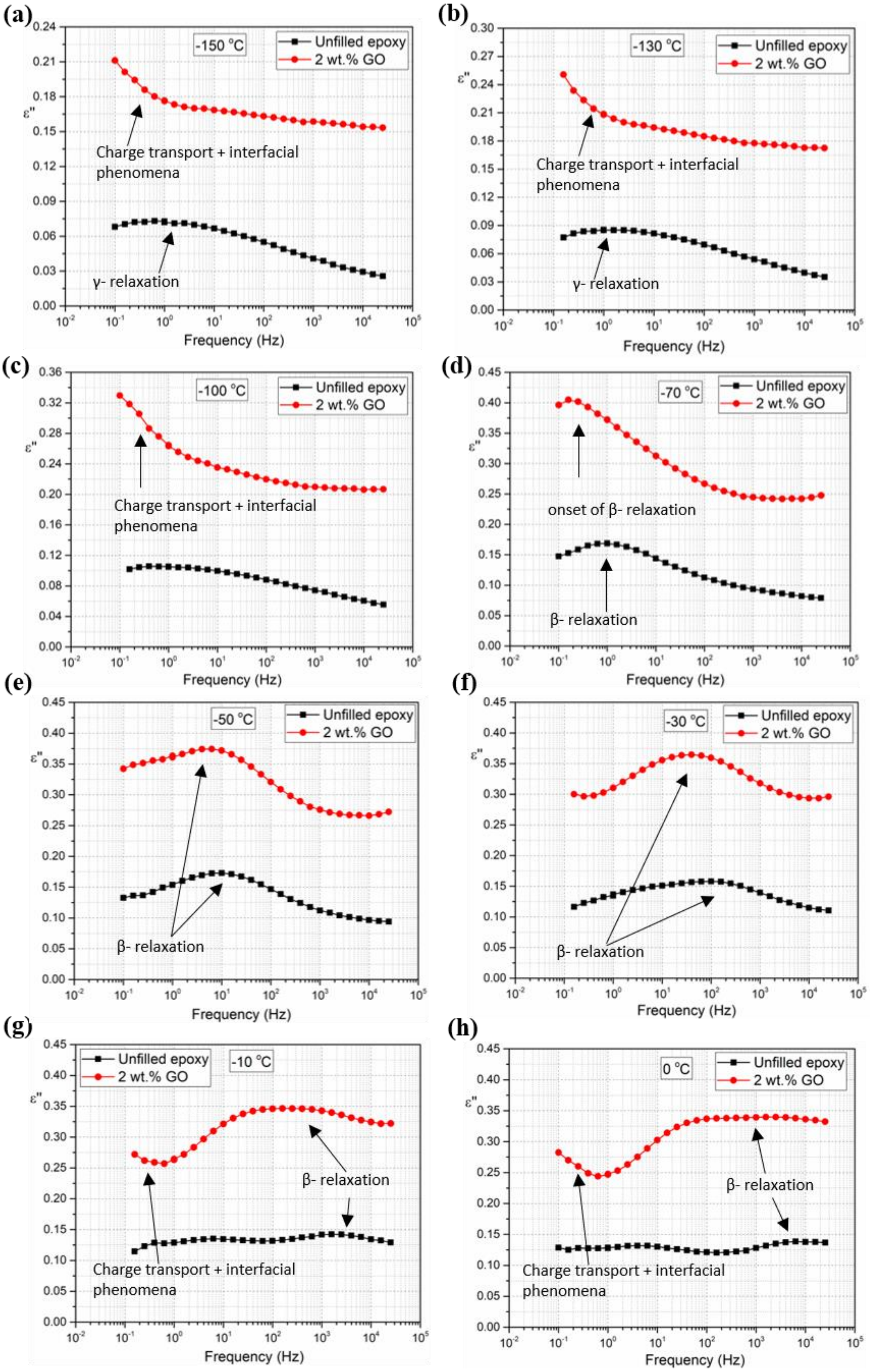

Figure 4.2.4 Imaginary part of the relative complex permittivity at: (a) -150 °C, (b) -130 °C, (c) -100 °C, (d) -70 °C, (e) -50 °C, (f) -30 °C, (g) -10 °C and (h) 0 °C, as obtained after post curing.

4.3 Structure and Properties of Epoxy/GO Nanocomposites

This section presents SEM, TEM, tensile, electrical and thermal conductivity characterization of the epoxy/GO systems as obtained before and after the post-curing process.

4.3.1 SEM

SEM images of the fractured tensile samples are presented in Figure 4.3.1. From this, it is evident that the fracture surface of the neat epoxy system (Figure 4.3.1a, b) is relatively smooth. The addition of GO results in rougher fracture surfaces (Figure 4.3.1c-f), which is caused by the presence of the GO resulting in crack inhibition [83]. These results align with previous studies and have been reported to be independent of the GO functional group density [83].

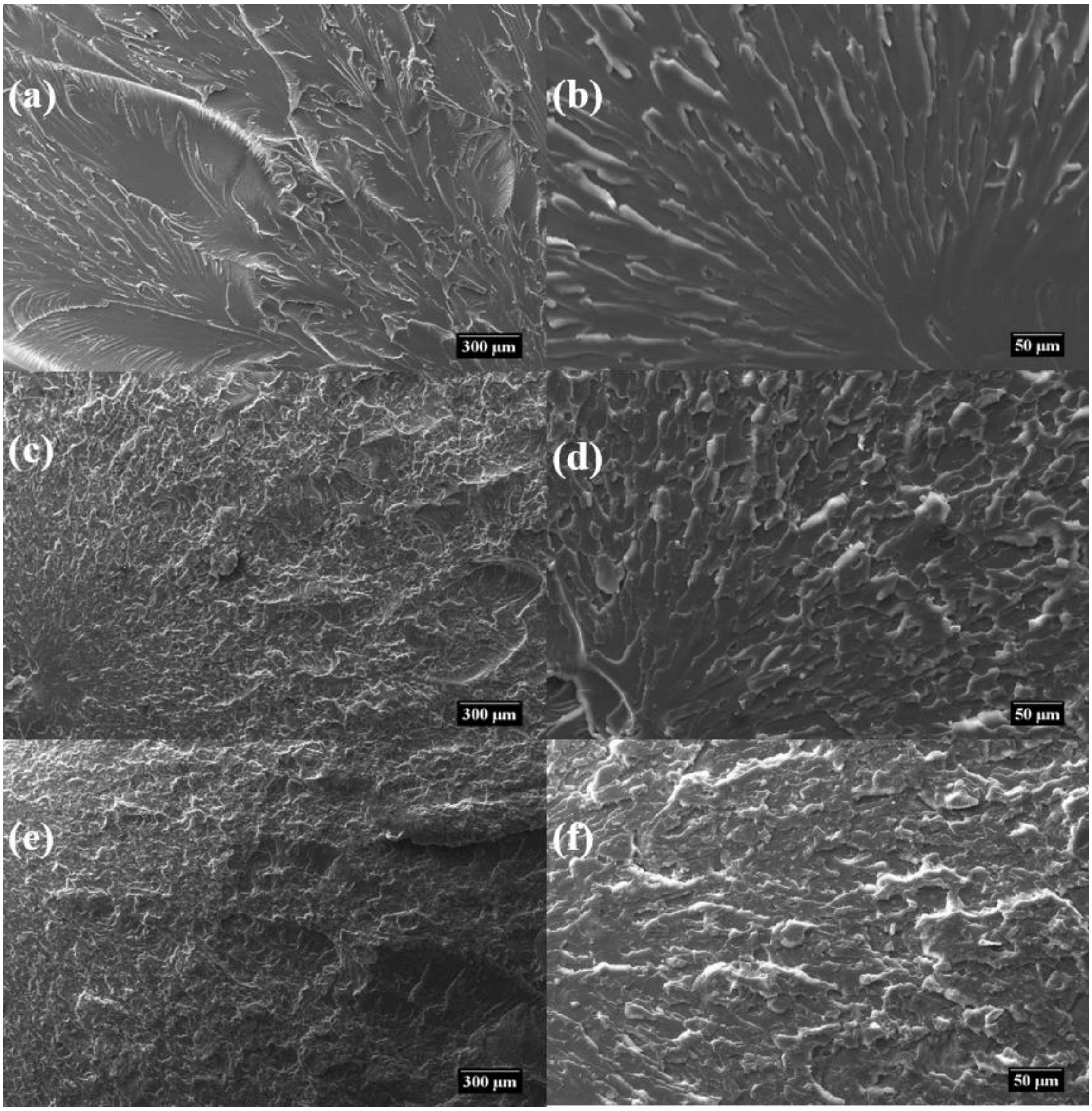

Figure 4.3.1 SEM images of the fractured areas of epoxy: (a, b) unfilled; (c, d) filled with 0.5 wt.% of GO; (e, f) filled with 2 wt.% GO. All images are taken from samples prior to post-curing.

Fractured areas of the post-cured, samples are displayed in Figure 4.3.2. Comparing the images presented here with the respective ones prior to post-curing (Figure 4.3.1), it can be seen that very similar surface features are displayed. This implies that the same reinforcement mechanism, described above, applies here. Therefore, the post-curing does not affect the crack patterns even though the epoxy/GO bonding was shown to have been promoted by the thermal process.

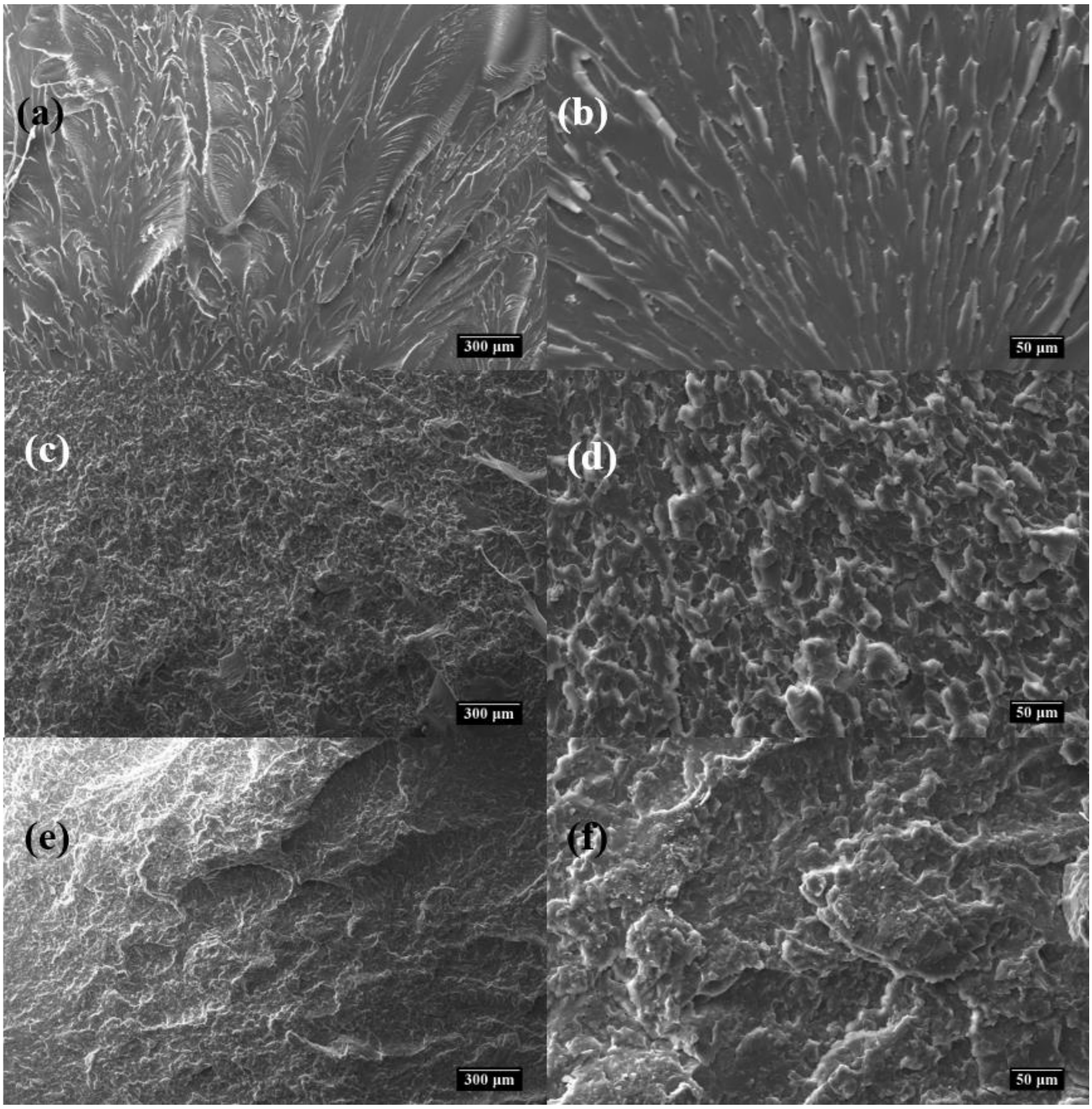

Figure 4.3.2 SEM images of the fractured areas of epoxy: (a, b) unfilled; (c, d) filled with 0.5 wt.% of GO; (e, f) filled with 2 wt.% GO. All images are taken from samples after post-curing.

As expected, the presence of GO flakes was more evident in the 2 wt.% content, (Figure 4.3.3) and their respective sizes were found to vary from a few micrometres (> 3 μm) to less than 1 μm as indicated with the red arrows in Figure 4.3.3a, b. Some degree of extended agglomeration or poorly distributed flakes were evident, as shown in the red circles. The sizes of such agglomerated structures were found to be larger than 3 μm (Figure 4.3.3b) or even close to 10 μm (Figure 4.3.3a).

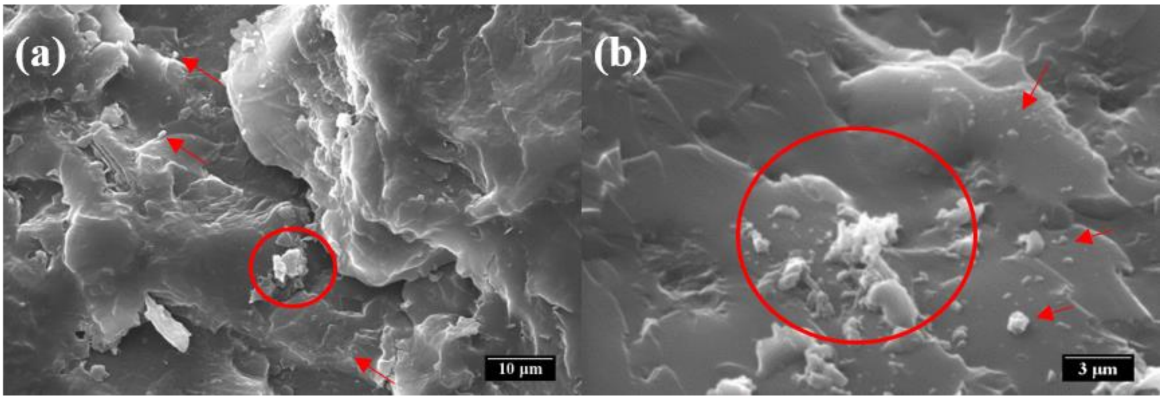

Figure 4.3.3 SEM images of the fractured areas of post-cured 2wt.% GO-filled samples.

4.3.2 TEM

The TEM images of the GO- filled samples, at different contents, are shown in Figure 4.3.4.

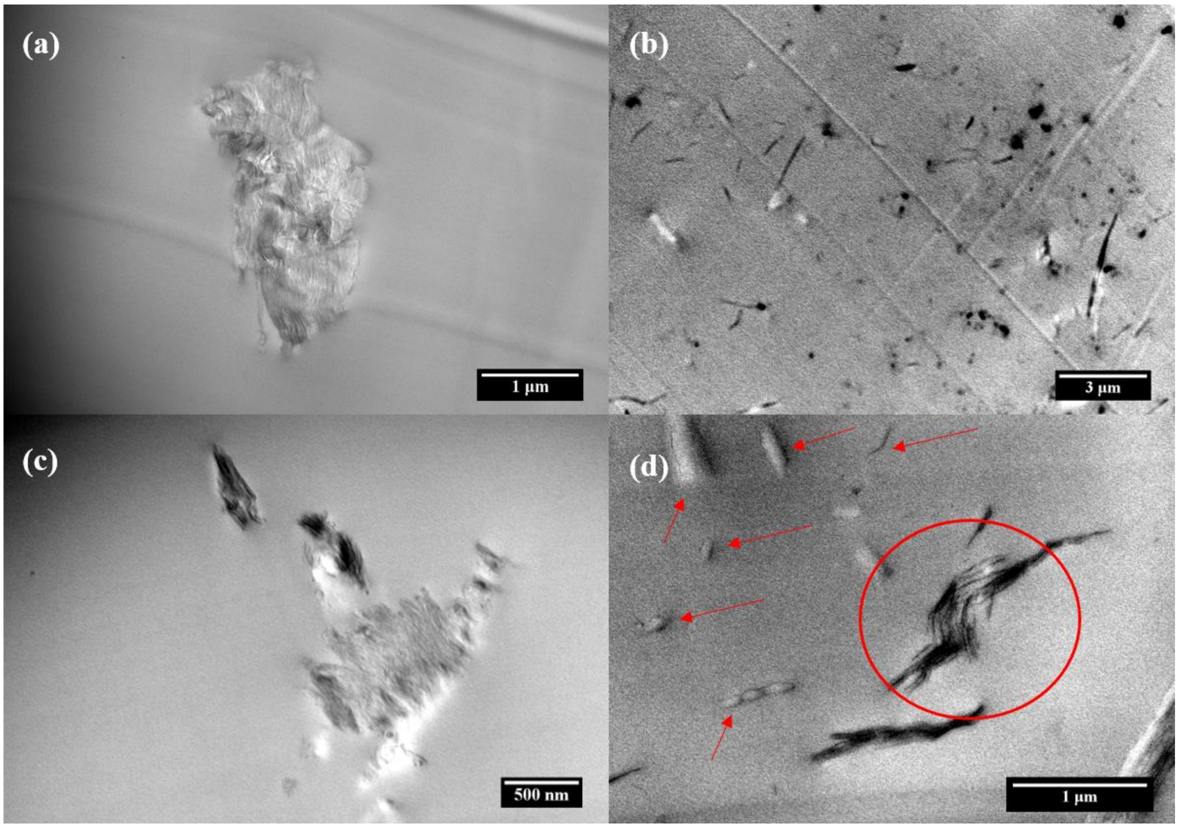

Figure 4.3.4 TEM images of the GO/epoxy nanocomposites with: (a) 0.5 wt.% and (b, c, d) 2 wt.% filler contents.

Wide ellipsoidal shaped inclusions were observed, randomly oriented, with micrometric in-plane sheet dimensions aligning with the dimensions shown by the SEM imaging above. In bright field microscopy of this type, contrast can arise from a number of processes, including variations in the local thickness, therefore, we associate the contrast variations seen here, with such effects.

Therefore, as seen in Figure 4.3.4b, agglomerated structures (darker colour) coexist with exfoliated ones. Intercalated structures were also observed as shown in the red circle in Figure 4.3.4d, while the arrows indicate various randomly sized tactoids.

4.3.3 Tensile Testing

Figure 4.3.5 contains elastic modulus and the tensile strength data of the unfilled and GO- filled epoxy samples, as obtained before and after the post-curing process.

Considering the behaviour prior to post-curing initially, it can be seen that the addition of a small percentage of GO (0.5 wt.%) increases both the modulus and strength of the epoxy system. The GO interfacial adhesion with the epoxy as well as its 2D structure result in enhanced modulus and reduced crack propagation [83]. This also aligns with the rough fractured surfaces seen above in the relevant SEM images. However, further addition of GO seems adversely to affect the system's performance. As explained in Chapter 2, high filler contents have as a generic consequence the impairment of the composite's mechanical performance and especially tensile strength due to increased agglomeration, which is consistent with the SEM images shown above. Nevertheless, the observed decreased modulus might have been affected by another factor and not agglomeration. Since the epoxy stoichiometry was found to be adversely affected by the GO surface chemistry at higher than 0.5 wt.% contents, we suggest that this phenomenon might represent another reason for the decreased modulus. It was shown in Chapter 2 that Bao et al. [117] referred to the GO-induced cross-linking reduction, as the main reason for impaired storage modulus.

After post-curing, it can be seen that the tensile performance (both modulus and strength) of the unfilled system deteriorates. This effect is ascribed to the excessively high crosslinking densities achieved by the post-curing process, that detrimentally affect the mechanical properties of polymers, as stated elsewhere [28, 107]. Indeed, the epoxy suppliers do not suggest any post-curing regime for the specific resin system used here. This phenomenon is also apparent for the 0.5 wt.% filled system, underlying again the fact that at this GO content, the behaviour is dominated by the matrix. On the contrary, as the filler percentage shifts to higher values, the tensile performance starts increasing after the nanofilled samples are post-cured. In particular, the 2 wt.% filled sample exhibits elastic modulus and tensile strength values that are noticeably higher after post-curing, a result that is counter to the behavior of the matrix-dominated samples. As mentioned earlier, apart from the filler dispersion effects, modifications to the matrix stoichiometry should also be considered as a deteriorating factor, in the case of elastic modulus. However, it is confirmed here that this applies also in the case of tensile strength. As such, we suggest that the observed enhancements in mechanical performance seen at higher GO loading levels are stoichiometry related, since the GO dispersion within the matrix would not improve during post-curing.

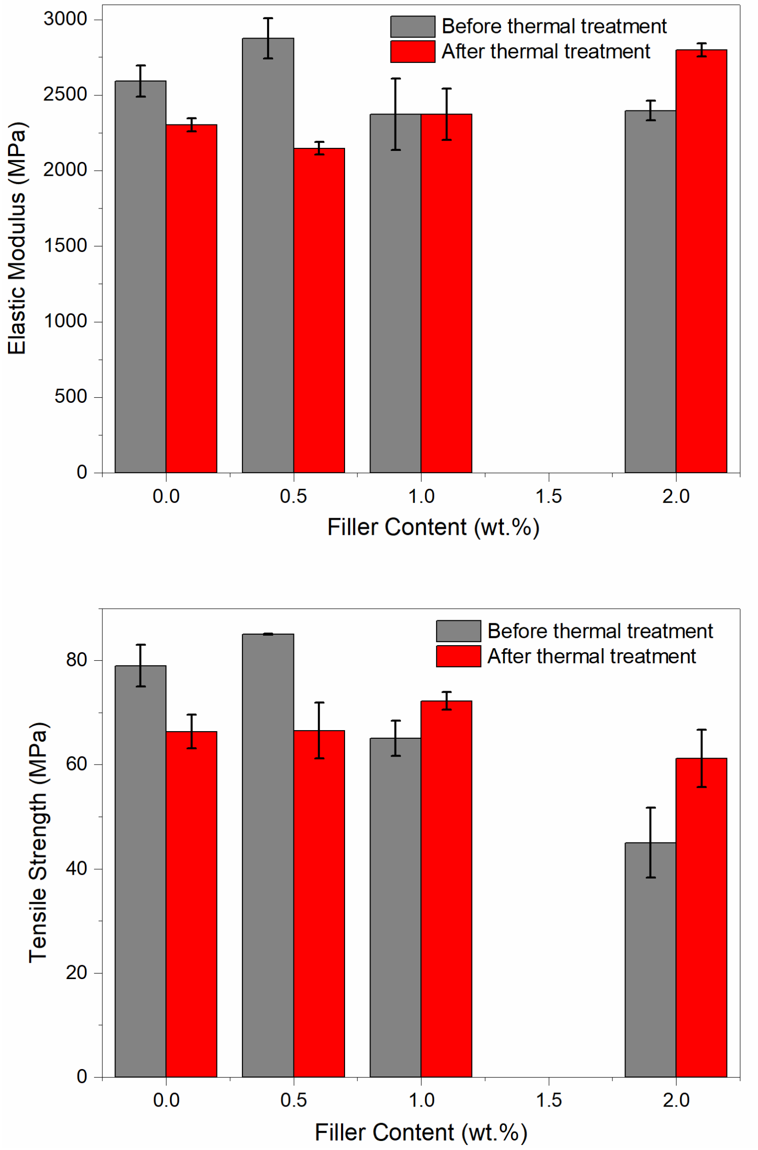

Figure 4.3.5 Elastic modulus (upper) and tensile strength (lower) of the unfilled and GO filled samples, prior to and after post-curing.

Therefore, it is shown that the promoted, by the post-curing, GO/epoxy bonding that was observed earlier resulted in increased tensile performance of the GO-dominated sample (2 wt.%). These reactions are confirmed to be accelerated by the high temperatures of the post-curing process, while the opposite happens for the matrix dominated samples that show thermally deteriorated tensile performance. It has to be noted though, that since the latter effect is dependent on the epoxy matrix used in the present study (with low temperature curing temperature), it might not be observed in other epoxy matrices with considerably higher curing/post-curing temperatures.

4.3.4 Electrical Conductivity

Figure 4.3.6 compares electrical conductivity data obtained from the unfilled and GO-filled samples, before and after post-curing. It can be seen that initially, prior to post-curing, the incorporation of GO does not alter the conductivity of the system while, after the post-curing, all samples exhibit increased electrical conductivity values. However, the GO-filled systems show a much more pronounced increase compared to the unfilled system, suggesting that this uplift is not determined by changes in the matrix polymer. Rather, we suggest that, for the nanofilled systems, thermal reduction of the GO is the dominant explanation for the increased electrical conductivity values that are seen [121], perfectly aligning with the dielectric data presented above.

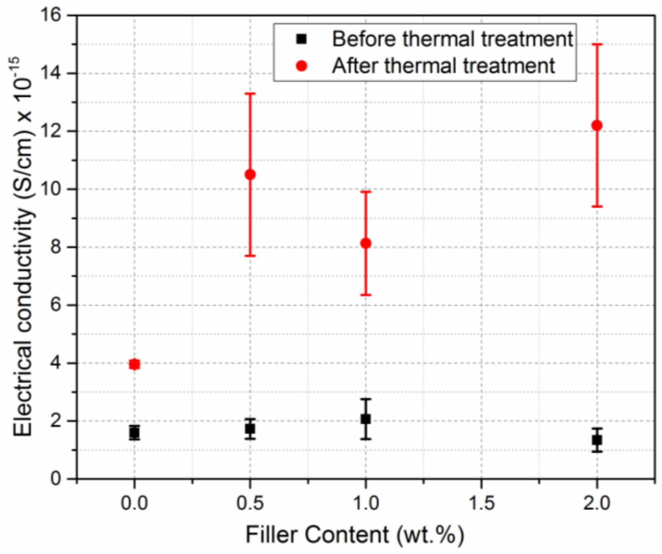

Figure 4.3.6 Electrical conductivity of the unfilled and GO filled samples, prior and after the post-curing.

4.3.5 Thermal Conductivity

Figure 4.3.7 presents the thermal conductivity data for the unfilled and GO-filled systems before and after the post-curing. From this, it would appear that the unfilled epoxy resin displays a slight thermal conductivity increase after the post-curing process. The addition of GO does not result in any considerable alterations implying that the effect of GO on the system's thermal conductivity is independent from the thermal processing in this case. As explained in Chapter 2 heat transport in GO-filled epoxy systems might be affected by several competing factors, thus the related literature presents diverging thermal behaviour of such systems. Here, it is suggested that heat transport in GO/epoxy systems is not affected by the specific parameters/materials considered.

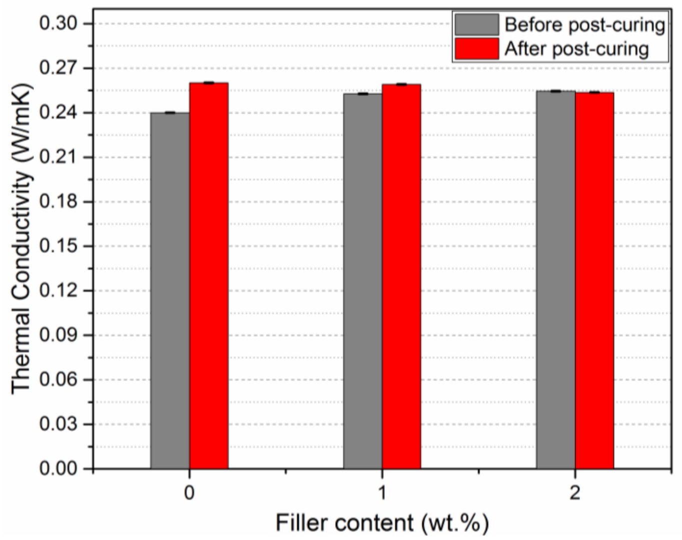

Figure 4.3.7 Thermal conductivity of the unfilled and GO filled samples, prior and after the post-curing.

4.4 Summary

Graphene oxide was successfully synthesized using acidic graphite oxidation, since TGA and Raman characterization conducted on the resulting GO both indicate attachment of a large amount of oxygen-containing groups. Epoxy-based nanocomposites were prepared, with GO filler contents of up to 2 wt.%. The examination of these samples was done after a curing thermal processing at 70 ^{o}C and then, after a post-curing process at 130 ^{o}C in order to demonstrate whether the temperature represents any significance on the performance of the system.

Before post-curing the FT-IR spectroscopy revealed an excess of epoxide ring groups in the GO-filled system, which is associated with the filler's surface chemistry. The presence of these additional reactive moieties has important consequences, in that they consume hardener amine groups (acting as excess epoxy monomer) and, consequently, displace the overall reaction stoichiometry away from the optimum. The result of this is a change in the network architecture and, in particular, the introduction of epoxy terminated branches; this change was observed in decreased T_g, and tensile performance and was confirmed by the γ relaxation of the dielectric spectrum.

During post-curing, the epoxide/hardener reactions are accelerated in the GO-dominated samples, however the hydroxyl groups existing on the GO surface also react with residual epoxide groups through etherification reactions. Furthermore, post-curing also serves for partial thermal reduction of the GO, as demonstrated by the increased electrical conductivity, dielectric permittivity and losses at low frequencies of the system. In this way, post-curing consumes excess epoxide groups and, in respect, can be considered to compensate for the initial stoichiometry imbalance within systems containing GO. This leads to a large increase in T_g for the GO filled system compared with the unfilled epoxy and to increased interfacial interactions at GO surfaces, which contributes to the observed enhancement in tensile performance seen in the GO systems after post-curing. We therefore infer that high temperature processes such as the post-curing process used in this study serve: (a) to promote the propagation of crosslinking through two different reaction routes and (b) to reduce partially the GO. The associated chemical pathways are proposed in Figure 4.4.1.

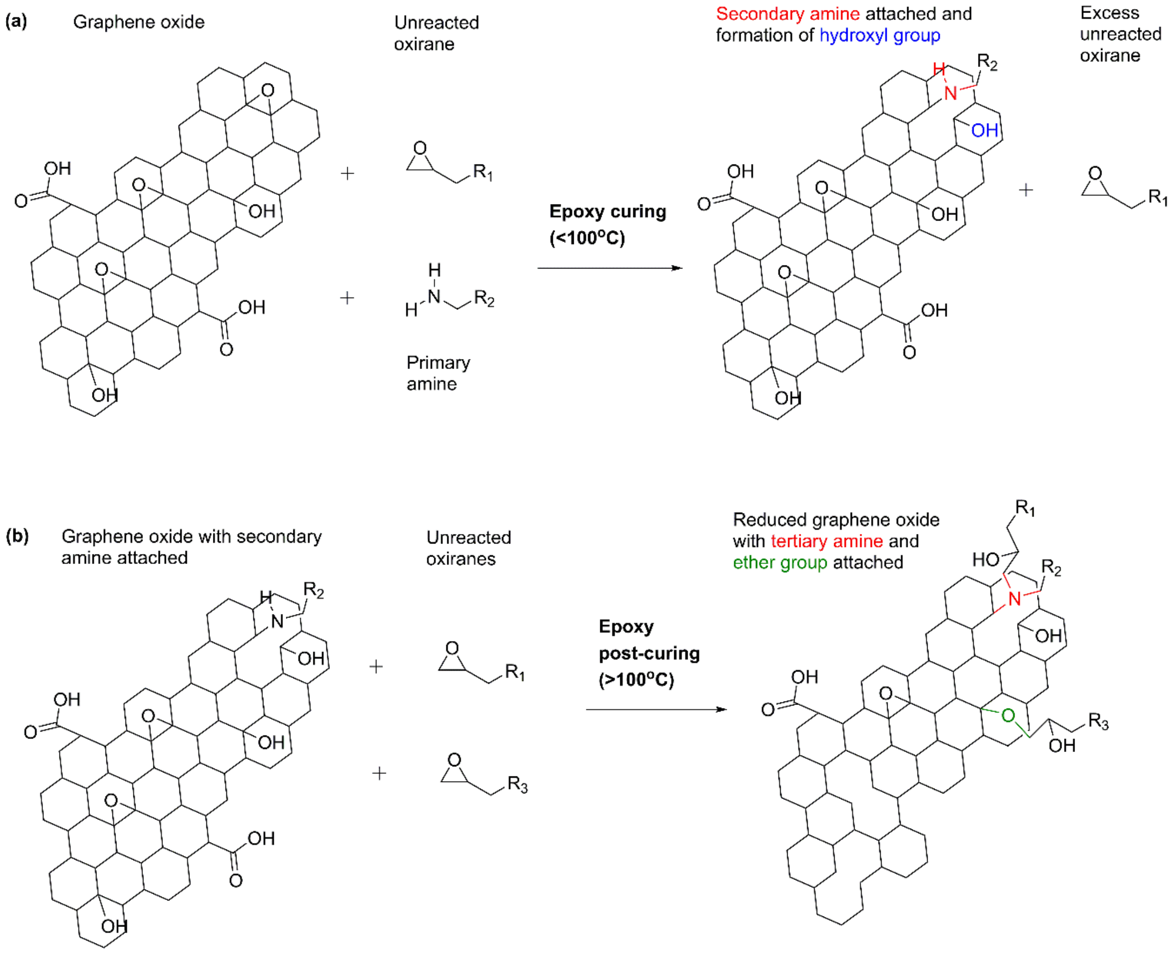

Figure 4.4.1 Crosslinking reactions between epoxy and GO. During curing (a) GO surface epoxide groups react with hardener molecules forming a hydroxyl and a secondary amine on the reaction site. During post-curing (b) the epoxide terminated groups can react either with secondary amines, or with hydroxyl groups through etherification. GO is also being partially reduced.

As such, the first two research questions that were raised in Chapter 1 were answered: (1) by identifying the benefits of high processing temperatures in GO/epoxy systems and (2) by triggering epoxide/amine reactions at curing temperatures below 100 °C and etherification temperatures at post-curing above 100 °C.

Chapter 5 Alternative Synthesis Route to Graphene Oxide: Optimized Surface Chemistry for Epoxy-based Composites

In this chapter, the mGO that was produced via the acidic oxidation utilizing CrO_3 instead of $KMnO_4$ was characterized and compared with the conventional GO that was presented in the previous chapter, as well as with a commercially available eGO. The purpose is to evaluate the oxygenation degree, as well as the structural characteristics of mGO by contrasting with the two widely used products that were mentioned. Afterwards, the structure and properties of the GO-, mGO- and eGO- epoxy composites will be contrasted in order to demonstrate the effect of the chromium-based oxidation as well as determine the optimum attainable surface chemistry of such fillers. Therefore, this Chapter will serve to answer three of the questions that were raised in Chapter 1:

3. Can we directly synthesize a moderately oxidised GO (mGO) by modifying the existing (efficient and scalable) acidic oxidation processes?
4. If the latter is possible, is the mGO oxygenation degree appropriate to achieve electrical and thermal conductivity enhancements, without compromising the mechanical properties or the stoichiometry of the epoxy?
5. Does the mGO-filled epoxy show improved performance compared to epoxy filled with commercially available EG derivatives?

Part of the results presented below are published in Journal of Materials Science as a full-length article:
O. Vryonis, T. Andritsch, A. S. Vaughan, and P. L. Lewin, “An alternative synthesis route to graphene oxide: influence of surface chemistry on charge transport in epoxy-based composites,” *J. Mater. Sci.*, vol. 54, no. 11, pp. 8302–8318, 2019

Another part of the results presented in this chapter is submitted in SN Apllied Sciences as a short communication paper with the title:
“Structural & Chemical Comparison between Moderately Oxygenated and Edge Oxygenated Graphene: Mechanical, Electrical and Thermal Performance of the Epoxy Nanocomposites”

5.1 GO/mGO/eGO Characterization

The results of the mGO and eGO characterization via Raman, XPS and TGA, as well as the respective data analyses and discussion are presented in the next subsections. For comparison, the graphite and GO characterization that were presented in Chapter 4 are shown here again.

5.1.1 Raman Spectroscopy

The Raman spectra of graphite, GO oxidized for 4 h or 30 min, as well as the mGO and eGO are presented in Figure 5.1.1a. Figure 5.1.1b shows the deconvoluted Raman spectra. The respective Raman data are presented in Table 5-1.

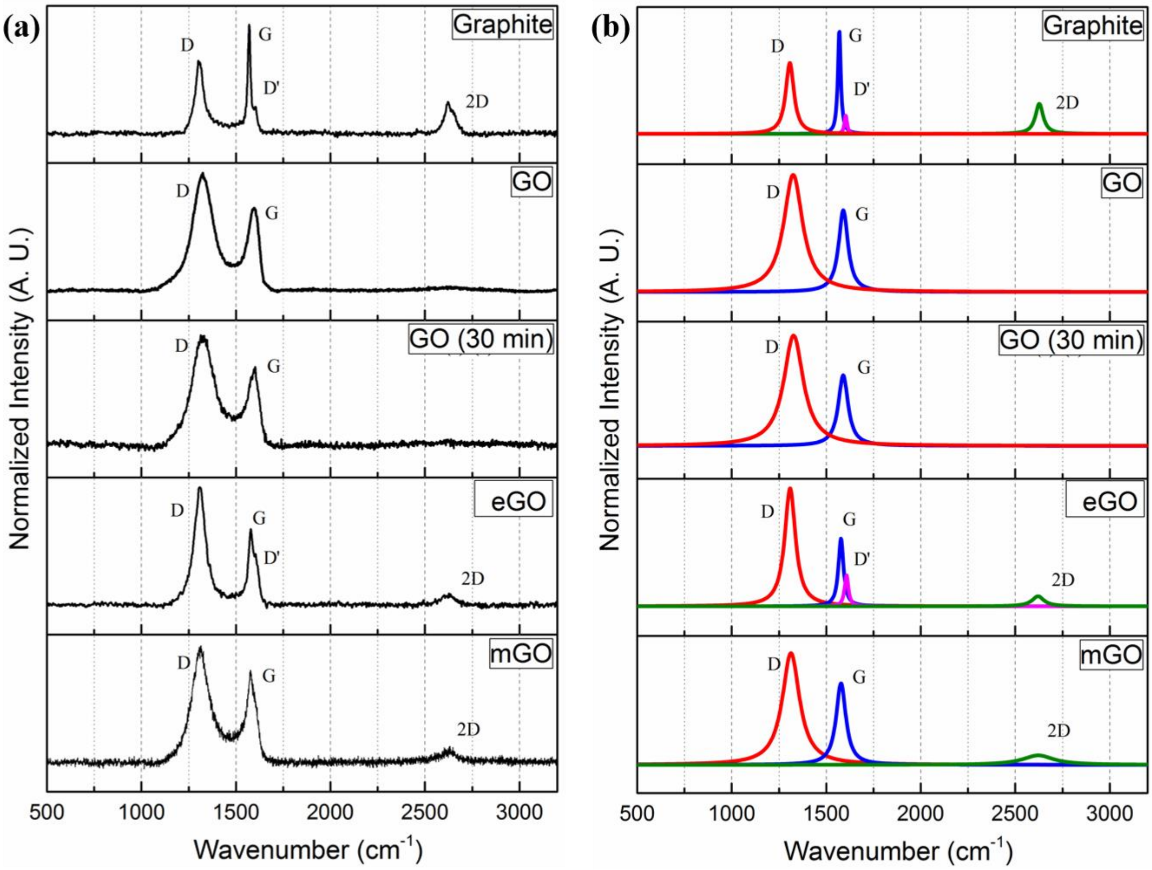

Figure 5.1.1 Raman spectra of the precursor graphite, GO obtained by 4 h and 30 min oxidation duration, eGO and mGO and (b) deconvoluted Raman spectra.

The GO that was oxidized for 30 min displays a G peak at 1590 cm^{-1}, similarly to the GO oxidized for 4 h. This effect indicates that the changes in oxidation time do not extend lattice disruption. Both GO samples exhibit similar D band characteristics, and eliminated 2D bands, for reasons explained earlier. On the other hand, the eGO shows a G band located at 1578 cm^{-1}, which is lower than in GO samples and higher than graphite. The D band of eGO appears quite intense, however narrower than these of GO samples, indicating limited extend of disorder. The D’ band is observable, similarly to graphite, albeit more pronounced, aligning with the (slight) oxygenated degree of eGO over graphite. The weak presence of the 2D band indicates some stacking order being preserved.

Table 5-1 Raman data for the precursor graphite, the two GO systems, the eGO as well as the mGO.

	Band	**Position**	**FWHM**
Graphite $I_{(D)}/I_{(G)} = 0.67$ $I_{(2D)}/I_{(G)} = 0.29$	D	1307.78 ± 0.34	53.01 ± 0.98
	G	1569.53 ± 0.14	18.73 ± 0.44
	D’	1603.37 ± 0.71	16.25 ± 2.24
	2D	2627.32 ± 0.68	50.50 ± 1.99
GO $I_{(D)}/I_{(G)} = 1.42$	D	1325.49 ± 0.27	121.54 ± 0.82
	G	1590.69 ± 0.26	62.86 ± 0.78
	D’	--	--
	2D	--	--
GO (30 min) $I_{(D)}/I_{(G)} = 1.40$	D	1327.52 ± 0.47	125.86 ± 1.45
	G	1590.13 ± 0.50	62.58 ± 1.50
	D’	--	--
	2D	--	--
eGO $I_{(D)}/I_{(G)} = 1.55$ $I_{(2D)}/I_{(G)} = 0.21$	D	1309.27 ± 0.13	68.90 ± 0.13
	G	1578.26 ± 0.24	32.41 ± 0.67
	D’	1607.57 ± 0.39	24.20 ± 1.26
	2D	2620.60 ± 1.40	76.99 ± 4.16
mGO $I_{(D)}/I_{(G)} = 1.26$ $I_{(2D)}/I_{(G)} = 0.16$	D	1313.71 ± 0.26	111.37 ± 0.80
	G	1578.56 ± 0.26	62.54 ± 0.77
	D’	--	--
	2D	2621.85 ± 3.55	200.87 ± 11.53

In the case of mGO, the G band is also located at 1578 cm^{-1}, implying that its graphitic structure is equivalent to eGO. Nevertheless, the G band is broadened similarly to the GO specimens, thereby, D’ band is not observable. Despite the attempts of deconvolution of the associated band, in order to exclude possible effects on the G band shape, the obtained fitting results were not consistent and therefore were not considered. Furthermore, the G band of mGO appears less intense compared to the system’s D band and, in this respect, the mGO mirrors the Raman behaviour of the GO and eGO. The presence of the 2D band in the mGO Raman spectrum suggests that, also here, some stacking order is preserved after the oxidation process, similarly to eGO but contrarily to both GO samples. The $I_{(D)}/I_{(G)}$ intensity ratios for the precursor graphite, GO (4 h oxidation), GO (30 min oxidation), eGO and mGO were: 0.67, 1.42, 1.40, 1.55, and 1.26, respectively, as shown in Table 5-1. The acquired results clearly indicate that the induced disorder of mGO is limited compared to both GO samples, by showing smaller $I_{(D)}/I_{(G)}$ values compared to the latter samples. Nevertheless, eGO that was not synthesized in our lab shows a considerably larger ratio compared to every other synthesized sample, suggesting that the different precursors and/or processes used for its production are of considerable significance. It has been shown elsewhere [164] that the $I_{(D)}/I_{(G)}$ ratio might keep increasing up to 1,000 ^{o}C or even 1,600 ^{o}C, due to arising carbon-based defects. Furthermore, it has been claimed [165] that increased $I_{(D)}/I_{(G)}$ values after GO reduction might be attributed to smaller domains of sp^2 carbon atoms and/or larger fractions of graphitic edges. The fact that eGO has been produced by processes, possibly, including thermal shock at temperatures similar to the abovementioned, might be the reason of the increased $I_{(D)}/I_{(G)}$ ratio it displays. Finally, since both eGO and mGO display 2D band, the $I_{(2D)}/I_{(G)}$ ratios were calculated. A comparison of these ratios with the ones displayed by the graphite reveal that the mGO is the one with the highest disorder, while graphite displays the lowest degree of disorder, as expected.

These results, therefore, confirm that the chromic acid oxidation process has resulted in a mild disruption of the graphitic lattice, which is reduced compared to the manganese-based GO. Comparison between the mGO and eGO systems via Raman is not clearly straightforward, thus further indications will be sought by the TGA and XPS analysis presented below.

5.1.2 TGA

Figure 5.1.2 compares TGA data obtained from the precursor graphite, the eGO, the mGO and the GO samples prepared using the two different oxidation times. From this it appears that all the systems that were subjected to oxidation with the presence of an oxidant (either $KMnO_4$ or CrO_3) show three weight loss processes, as depicted in Figure 5.1.2. These processes will be called Regions I, II and III here, and are ascribed to removal of (I) water, (II) labile oxygen-based groups and (III) stable oxygen-based groups, as explained in Chapter 4 and Appendix C. The two GO systems display minor differences, underlying the fact that varying the oxidation time within the range considered here does not lead to considerable changes, albeit that the mass loss appears to be slightly larger in the case of the system oxidized for longer time. This implies that the graphite surface chemistry is rapidly disrupted by the manganese-based oxidizing agent, since reducing the duration of the process by 8-fold results in only a minor change in the product. On the other hand, the usage of CrO_3 in place of $KMnO_4$ leads to a significantly limited mass loss, of ~10% in region II, implying that the mGO structure contains proportionally fewer labile oxygen groups compared to GO, that displays a mass loss of ~30% in the same region. Indeed, the mGO that was synthesized without being subjected to any subsequent reduction process, displays a smaller related mass loss than either chemically reduced GO (via reaction with hydrazine hydrate, as shown in Appendix C, (Figure C.4a) [125] or microwave reduced GO [119]. Furthermore, mGO appears to be more oxygenated compared to the eGO. The latter displays minimal mass loss in regions I and II, similarly to GNP (shown in Appendix C, Figure C.4b) indicating absence of water and reduced amount of labile functionalities. The latter oxygen-based groups have been previously linked [158] to those that decorate the basal plane, aligning with the fact that eGO is mostly peripherally oxygenated and indicating that mGO is also decorated on the basal plane. All fillers show a similar progressive mass loss in region III, which has been related to the peripheral stable C=O bonds and aligns with the fact that every sample is edge oxygenated, with the detail that eGO shows only this characteristic. This process is genuinely connected to the presence of antagonistic processes related to C=O groups, such as release of oxygenated by-products and subsequent trapping and/or loss of the C=O bonds and subsequent conversion of other C-O bonds to C=O, as stated elsewhere [158]. It is worth mentioning that region III is also associated with the formation of alternative aromatic hydrocarbon structures such as phenols or aromatic diols [158]. The fact that eGO might already display such structures would be associated to the thermal shock process used for its production, as stated above.

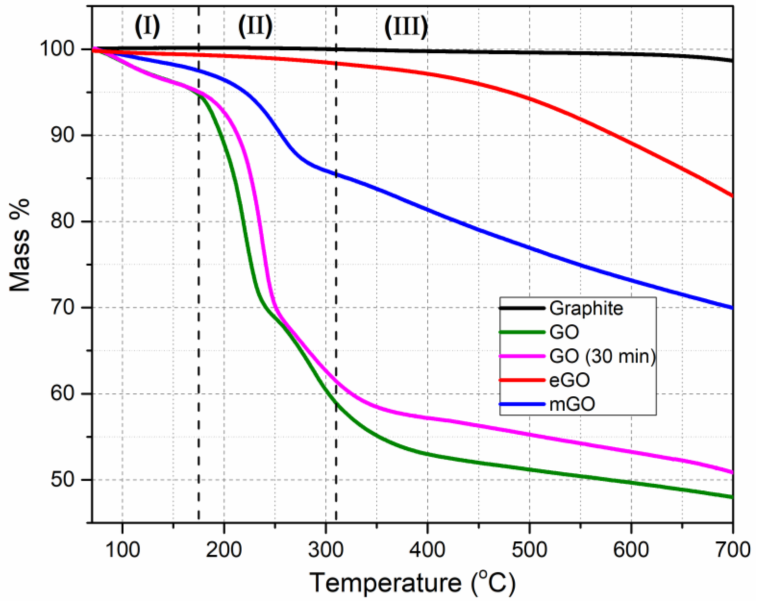

Figure 5.1.2 TGA plots for precursor graphite (black), mGO (blue), eGO (red) and GO obtained by 4h (green) and 30 min (pink) oxidation duration.

5.1.3 XPS

Table 5-2 shows the elemental ratios as obtained from the XPS spectra of the precursor graphite, the GO, the eGO and the mGO powders. From this it appears that mGO displays a moderate oxygen content that lies between the oxygen contents of GO and eGO, aligning with the TGA data described above. It can also be seen that the eGO does not display any sulphur content, indicating that the thermal shock served to evaporate the entirety of the sulfuric content.

Table 5-2 Percentage elemental contents calculated from the XPS analysis.

Sample	C (%)	O (%)	S (%)
Graphite	96.8	3.2	0.00
GO	72.8	26.3	0.9
eGO	91.2	8.8	--
mGO	83.3	16.3	0.4

Figure 5.1.3 shows the respective XPS survey scans, as well as the derived C/O ratios in the insets. It can be seen that the C/O ratio for the mGO is ~5.1, in comparison, eGO typically shows a C/O value of ~10.4. The electrochemical exfoliation approach mentioned in Chapter 2 has shown, under specific circumstances, similar oxygen contents to mGO, albeit with more complex production [105].

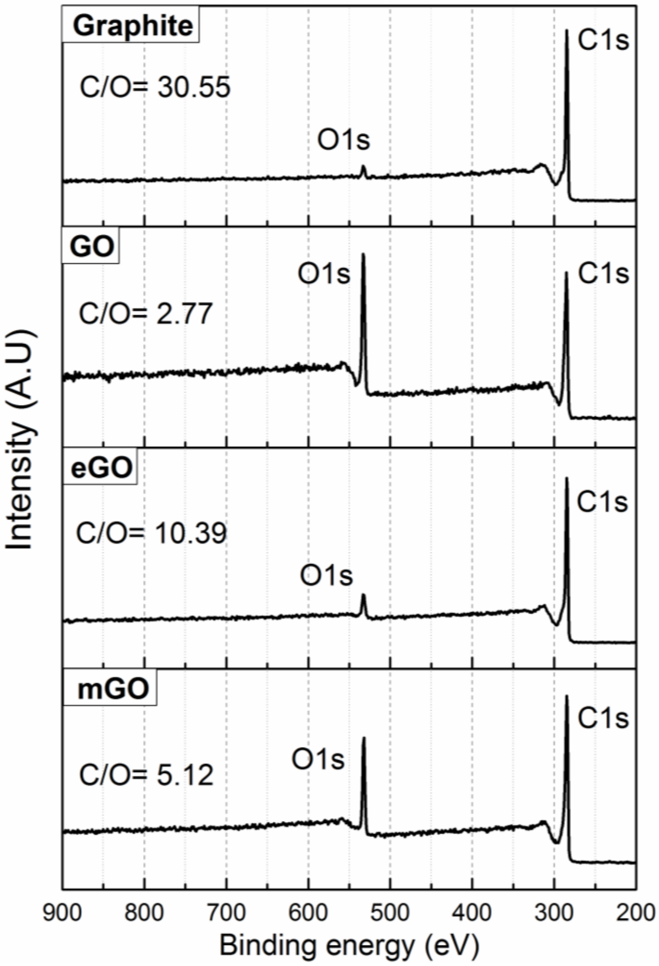

Figure 5.1.3 XPS survey plots on precursor graphite, GO, eGO and mGO powders.

Figure 5.1.4 shows the deconvolution of the respective C1s spectra, together with the assigned carbon bonding in the insets. From this it appears that, as expected, the GO shows the most significant sp^3 hybridized carbon atoms and carbon-to-oxygen bonding, as well as the weakest π → π* peaks.

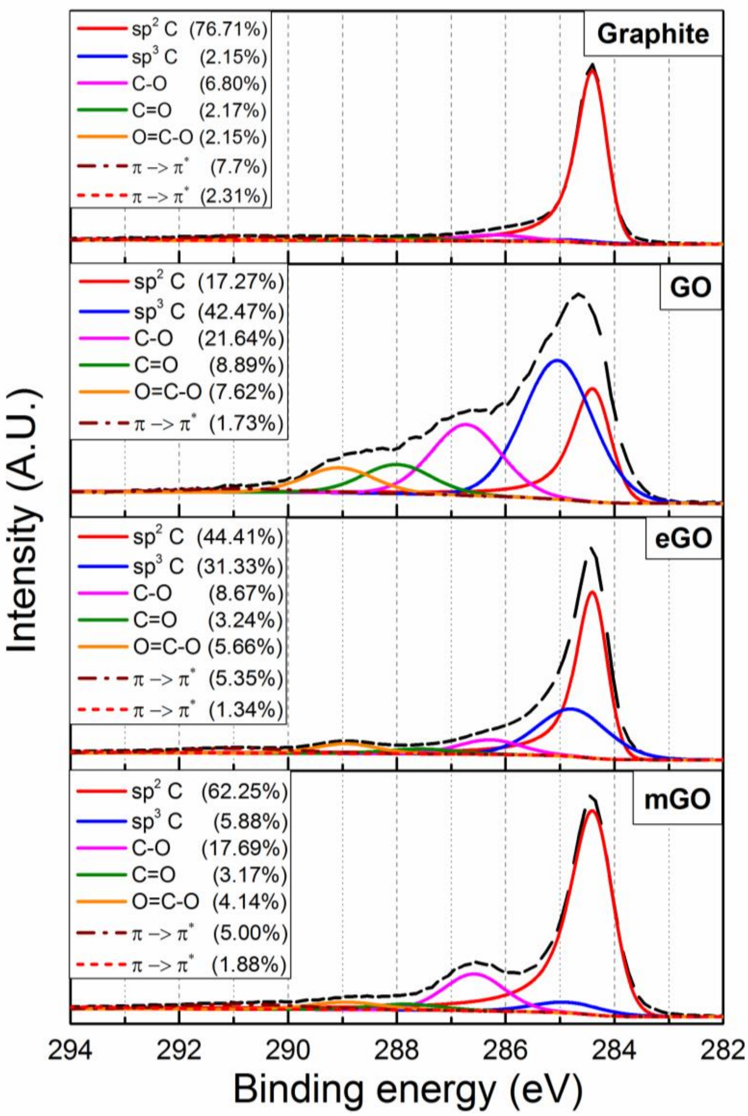

Figure 5.1.4 Deconvolution of the C1s spectra of the graphite, GO, eGO and mGO powders.

The eGO shows relatively large ratio of carboxylic groups (C=O and O=C-O bonds) compared to the rest of the carbon bonding, aligning with the Lerf-Klinowski model [79]. Furthermore, the sp^3 carbon-related peak is quite strong in the case of eGO, despite its low oxygen content. This is associated with the presence of hydrocarbon-based defects such as anthracene [166], or the aromatic compounds mentioned above, which were shown in Appendix C to be present even after oxygen removal through thermal reduction [70]. The latter aligns well with the assumption made above, claiming that eGO displays carbon-based defects, which strongly indicates that they were generated due to the thermal shock processing. Alternatively, these defects pre-existed in the (presumably not fully graphitized) precursor used for eGO. This effect represents the main reason for the increased $I_{(D)}/I_{(G)}$ ratio in the Raman spectra of eGO, indicating that the disorder of this system is mainly attributed to the presence of carbon defects and not oxygen. Conversely, mGO displays a considerably limited extent of sp^3 carbon hybridization compared to GO and eGO specimens, as well as a decreased amount of oxygen-based functionalities compared to the GO, aligning with the Raman and TGA characterisation presented above. Nevertheless, both mGO and eGO display equivalent $\pi \rightarrow \pi^*$ transition values that are lower than these of graphite and higher than these of GO. It is noteworthy that the dominant functionalities present on the mGO surface are stem from C-O bonds, underlining the fact that the mGO system displays a basal plane decorated with epoxides and hydroxyls. The presence of carboxylic groups is relatively weaker compared to the GO and eGO reflecting a slightly decorated peripheral plane. Overall, the chromic-based method resembles the chlorate methods, in terms of grafted functionalities [91] as described in Chapter 2 and Appendix C, but in a much lower amount.

Figure 5.1.5 shows the deconvoluted O1s peaks together with the assigned oxygen bonding, in order to further distinguish the eGO from the rest of the systems. All samples exhibit three main peaks attributed to: aromatic O=C (530 – 531 eV), aliphatic O-C (532 eV) and aromatic O-C (533 eV). Apart from eGO all the other samples display another peak at 535 eV, attributable to adsorbed water molecules [158]. From this it appears that the GO and mGO powders show a relatively similar pattern of oxygen bonding ratios with their precursor graphite, showing slightly increased intensity of the aliphatic bonds, which stems from the dominant oxygen-based functional groups. On the contrary, the eGO displays a considerably pronounced aromaticity which is attributed to the carbon-based defects mentioned above.

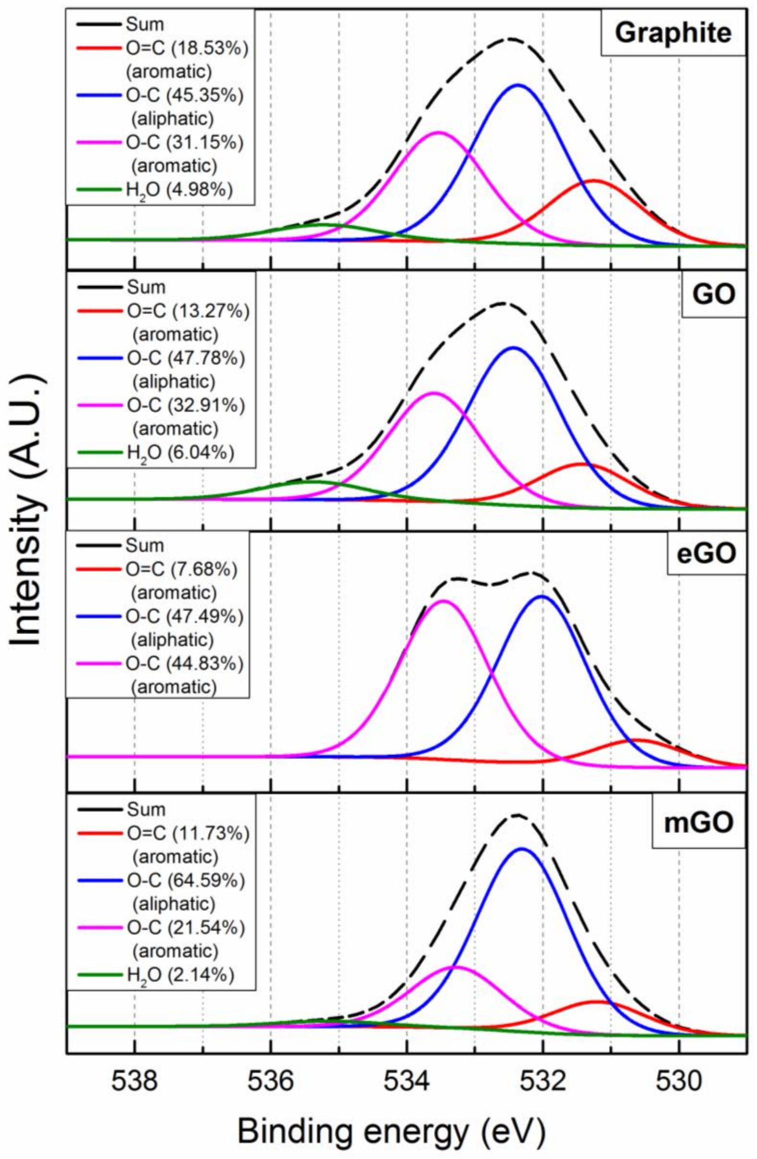

Figure 5.1.5 Deconvolution of the O1s spectra of the graphite, GO, eGO and mGO powders.

5.2 Structure and Properties of Epoxy/mGO and Epoxy/eGO Nanocomposites

The characterization presented above provides consistent evidence to conclude that the usage of chromic acid has led to a product that is characterized by reduced disorder and moderate level of oxidation, when compared with the GO and eGO products. As mentioned earlier, the purpose of synthesizing such a product is to effectively increase the electrical and thermal conductivity of epoxy resins without disrupting the thermo-mechanical performance. As such, in this section, the impact of mGO on the structure and physical properties of epoxy composite systems will be described and compared to the respective eGO/epoxy systems.

5.2.1 DSC

Figure 5.2.1 presents the effect of mGO and eGO content on the T_g of the respective nanocomposites. In this, both weight fraction, W_f, and volume fraction, V_f, values are presented.

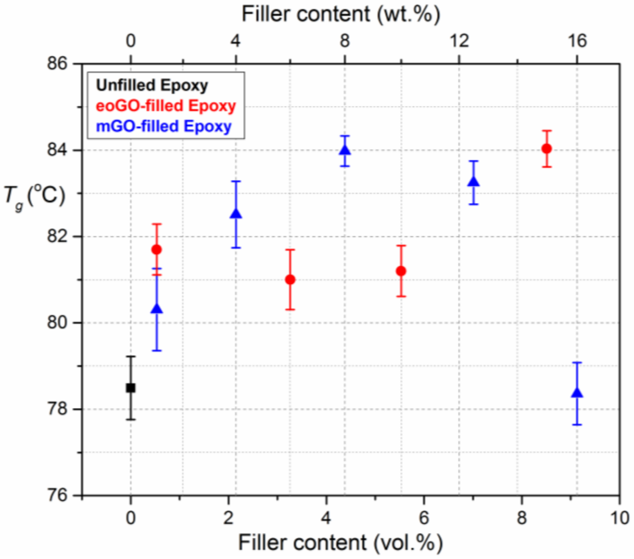

Figure 5.2.1 Weight and volume percentage of mGO- and eGO- filled epoxy samples and their respective T_g.

From the above, it can be seen that the glass transition temperature of the epoxy matrix is not detrimentally affected by the inclusion of mGO, albeit that a statistically significant increase in T_g is observed from 4 – 12.5 wt.%. The addition of eGO shows similar but slightly more gradual T_g enhancement trend. Increased T_g values have been reported at small GO filler contents (< 0.5 wt.%) and relatively larger GNP contents (~4 wt.%) due to constrained chain mobility, as shown in Chapter 2 (Figure 2.3.1). The addition of mGO and eGO into epoxy result in comparable to the aforementioned GNP effects, since the T_g is slightly increased at relatively high filler contents. This effect is expected for eGO (since technically represents GNP) but also underlines the reduced oxygen content of mGO. Ultimately, at the highest mGO content, the T_g value drops, which is ascribed to the relatively high concentration of reactive functional groups, as shown in Chapter 4 with the usage of GO, albeit at considerably higher filler contents. However, the addition of eGO did not result in a drop in T_g, even at the highest filler content, showing no reaction with the epoxy at all. Considering the latter interpretation, the T_g dependence presented in Figure 5.2.1 is consistent with the previous indications that the density of functional groups grafted onto the mGO surface is limited compared with conventional GO and higher compared with eGO. Evidently, mGO can be incorporated into epoxy matrices at much higher loading levels than conventional GO without adversely affecting the curing reaction of the matrix polymer.

5.2.2 SEM & TEM

SEM images as taken from fractured surfaces of the mGO- and eGO- filled samples are presented in Figure 5.2.2. It is evident that the inclusion of either of these two systems alters the crack propagation pattern, resulting in identical rough fractured surfaces, such as the ones shown earlier in the case of GO. This effect was claimed earlier to be independent from the functional density of GO and is shown here to also apply for systems with relatively lower (mGO) and significantly lower (eGO) functionality densities. Thus both fillers show similar, rough crack propagation patterns.

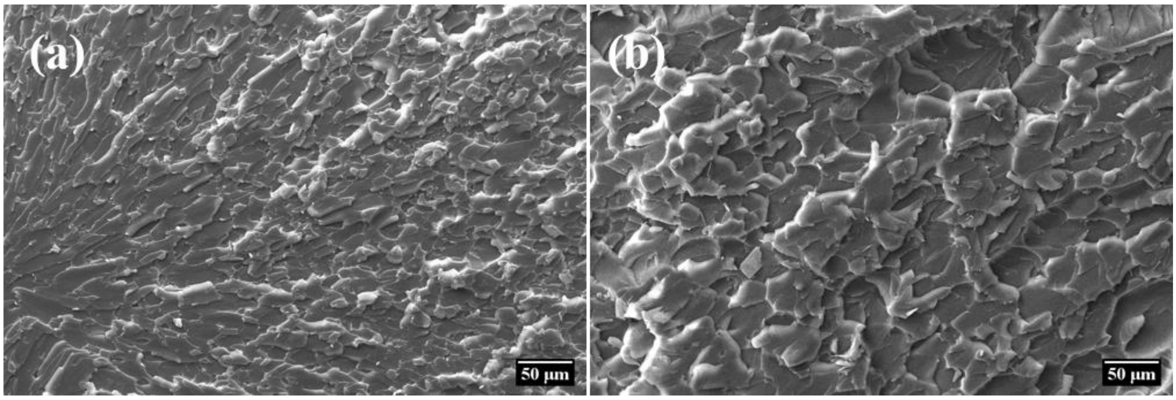

Figure 5.2.2 Crack propagation pattern as taken from SEM imaging of: (a) eGO-filled and (b) mGO-filled epoxy.

However, a closer look (Figure 5.2.3) reveals that the distribution of mGO within the matrix is different from that of eGO. More specifically, eGO is not distributed homogeneously resulting in “densely populated” spots that act as crack initiators (red indications in Figure 5.2.3a, c). On the other hand, mGO displays homogeneous distribution within the matrix (Figure 5.2.3b, d). It is indicated that the increased functionality of mGO over eGO considerably improves the matrix compatibility of the former and extended formation of clusters is avoided.

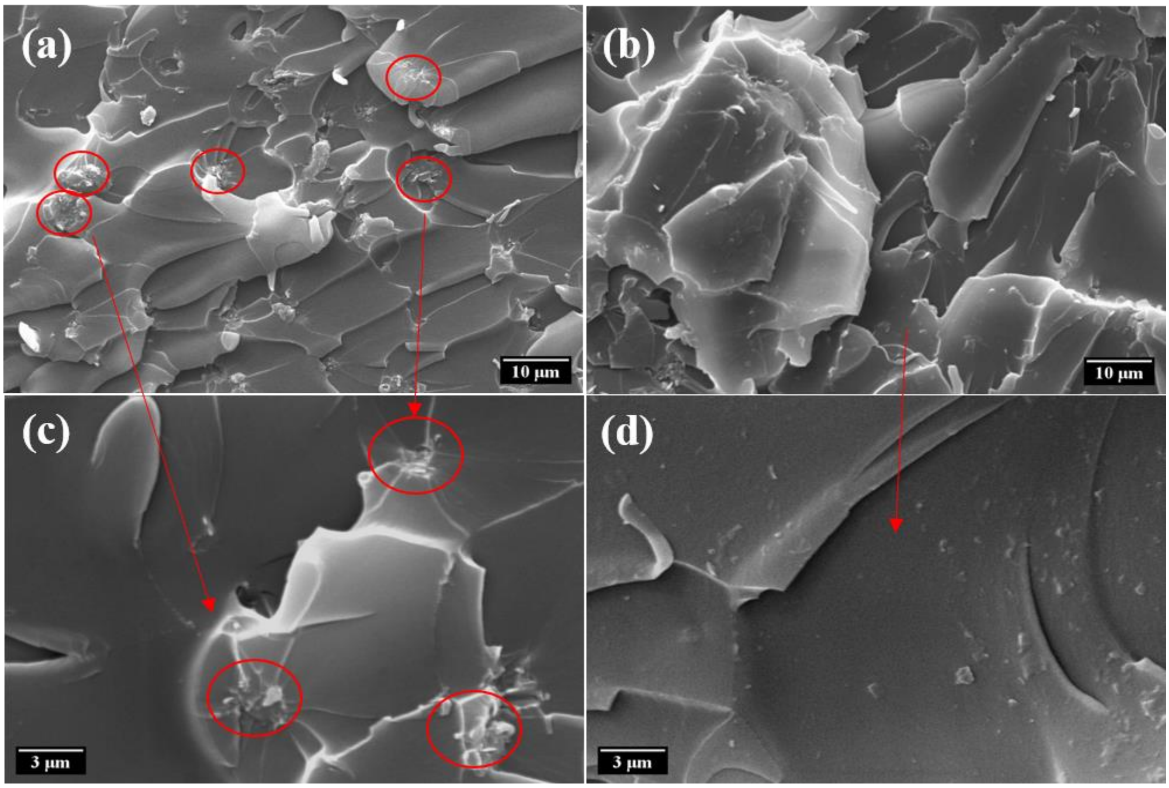

Figure 5.2.3 SEM images of epoxy filled with 0.5 wt.% of (a, c) eGO and (b, d) mGO.

While it is possible clearly to distinguish larger eGO clusters in the case of systems based upon this filler, the SEM images are less informative concerning the dispersion of mGO and, as such, complementary TEM data are presented in Figure 5.2.4.

These micrographs reveal a satisfactory dispersion of the mGO that contain a range of exfoliated entities and small regions of stacked platelets (circled in red) forming in this way a graphitic network within the matrix. From the variation in contrast from image to image, it is evident that some areas are characterized by well-exfoliated structures while, in others, the mGO retains a graphitic multi-layered configuration (red circles). This conforms to the Raman spectra presented above, which implies that some degree of stacking order has been preserved due to the relatively weak oxidation. In contrast, the eGO appears to, generally, be less well dispersed/distributed and form larger clusters that display significantly higher contrast. As such, eGO shows much more “resin-rich” areas than the mGO.

More SEM and TEM images, showing the same behaviour, can be found in the next section, since the two microscopy techniques were used to determine the size distribution of the mGO and eGO systems.

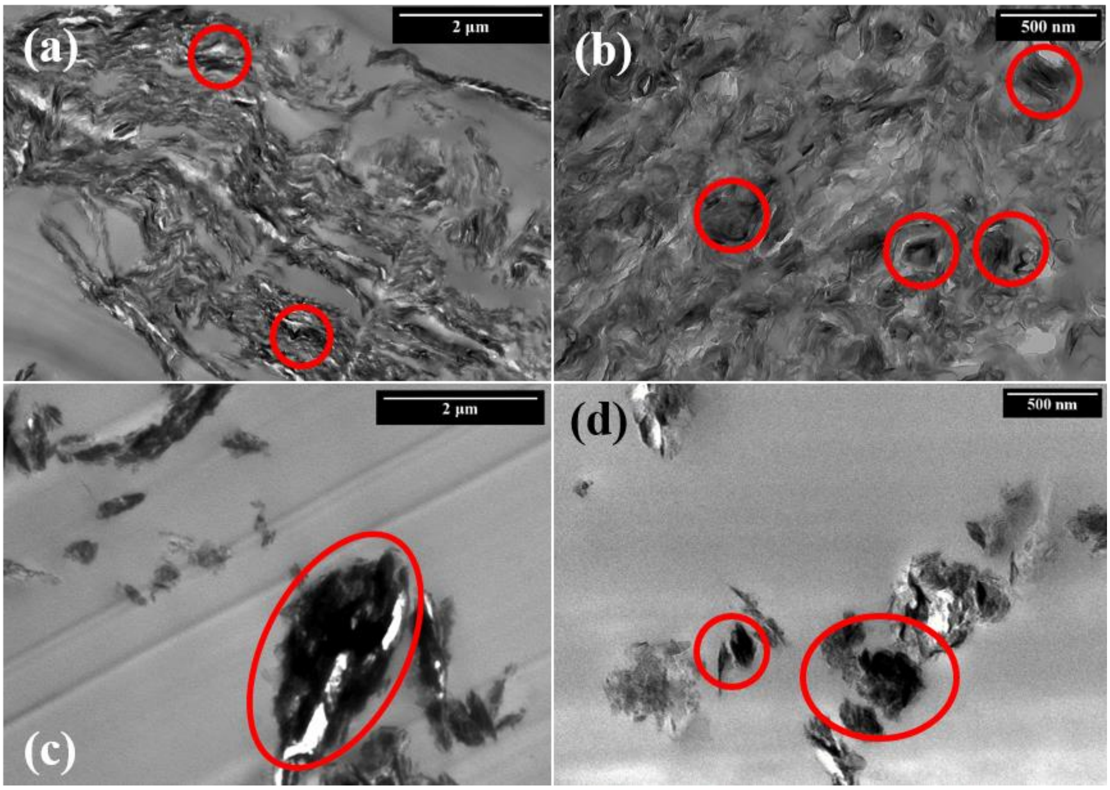

Figure 5.2.4 TEM images of epoxy filled with 4 wt.% of (a, b) mGO and (c, d) eGO.

5.2.3 Particle Size Distribution

SEM images of fracture surfaces of samples filled with mGO (Figure 5.2.5) and eGO (Figure 5.2.6) were also used to assess the respective particle size distribution. Image analysis undertaken for 64 individual mGO tactoids shows a size distribution between 0.75 - 1.1 µm for 45% of them, while 23% of the flakes exhibit a lateral size between 1.3 - 1.7 µm, as shown in Figure 5.2.5d. Figure 5.2.5e-f illustrate representative TEM images of isolated tactoids found in the 1 vol.% mGO-filled sample, with maximum lateral sizes ~1.6 µm and ~0.8 µm, respectively, aligning with the abovementioned size distribution.

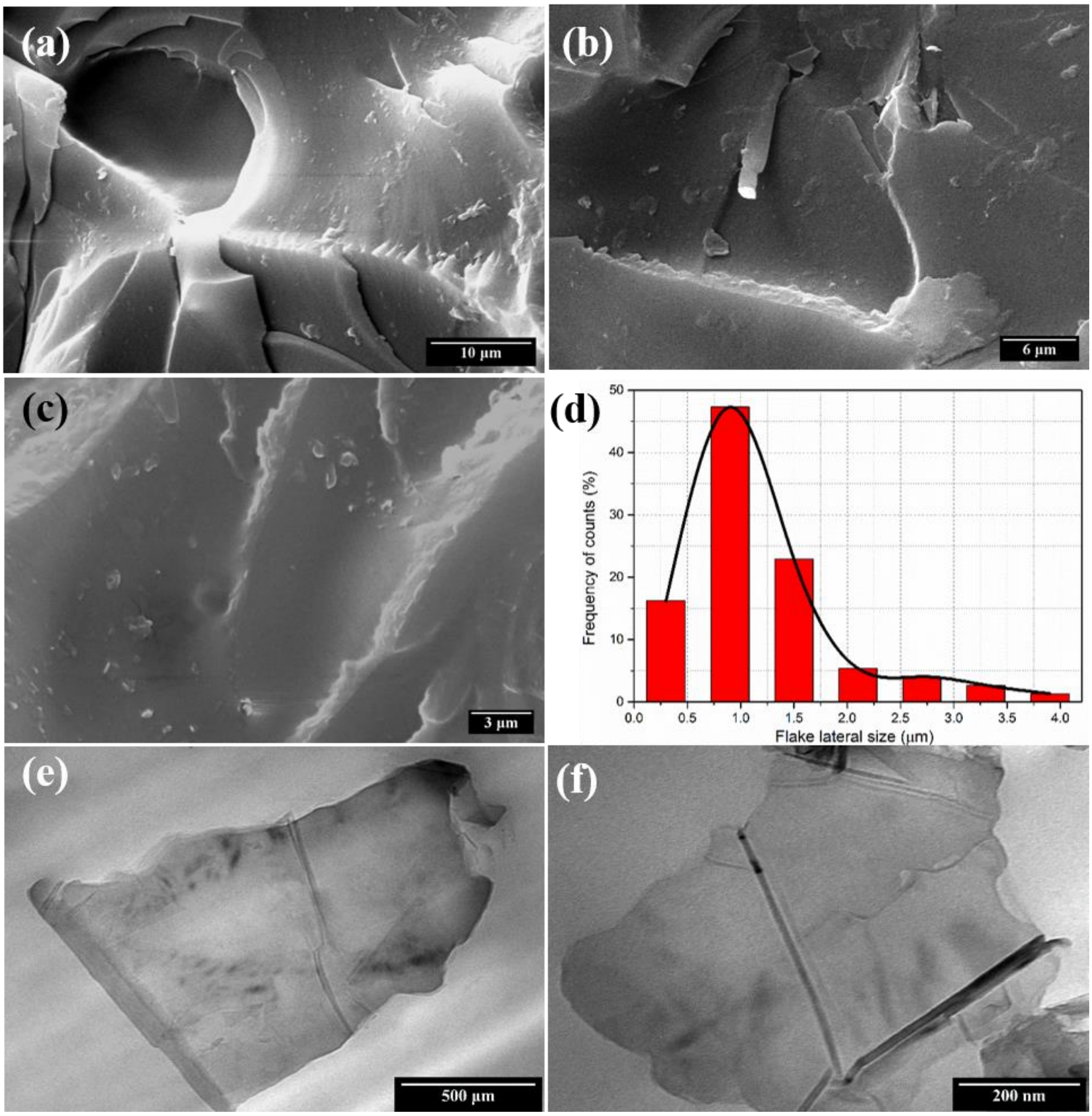

Figure 5.2.5 (a-c) SEM images taken from mGO-filled nanocomposites. (d) Lateral size distribution determined by analysing 64 different tactoids from the SEM images. (e, f) TEM images of isolated representative mGO platelets found at the 1 vol.% mGO-filled samples.

In the case of eGO- filled samples, the image analysis was conducted for 61 individual eGO tactoids revealing dominant lateral size of ~500nm for almost 65% of them, while 20% of the flakes displayed a size of 800nm, as shown in Figure 5.2.6d. The latter results are good accordance with the manufacturer's specifications (see Chapter 3). Contrarily to the mGO behaviour, eGO tactoids were proved difficult to distinguish in the TEM images, due to the significant existence of eGO clusters, as shown in red circles in Figure 5.2.6e. Nevertheless, some isolated structures were visible, such as the ones in Figure 5.2.6f

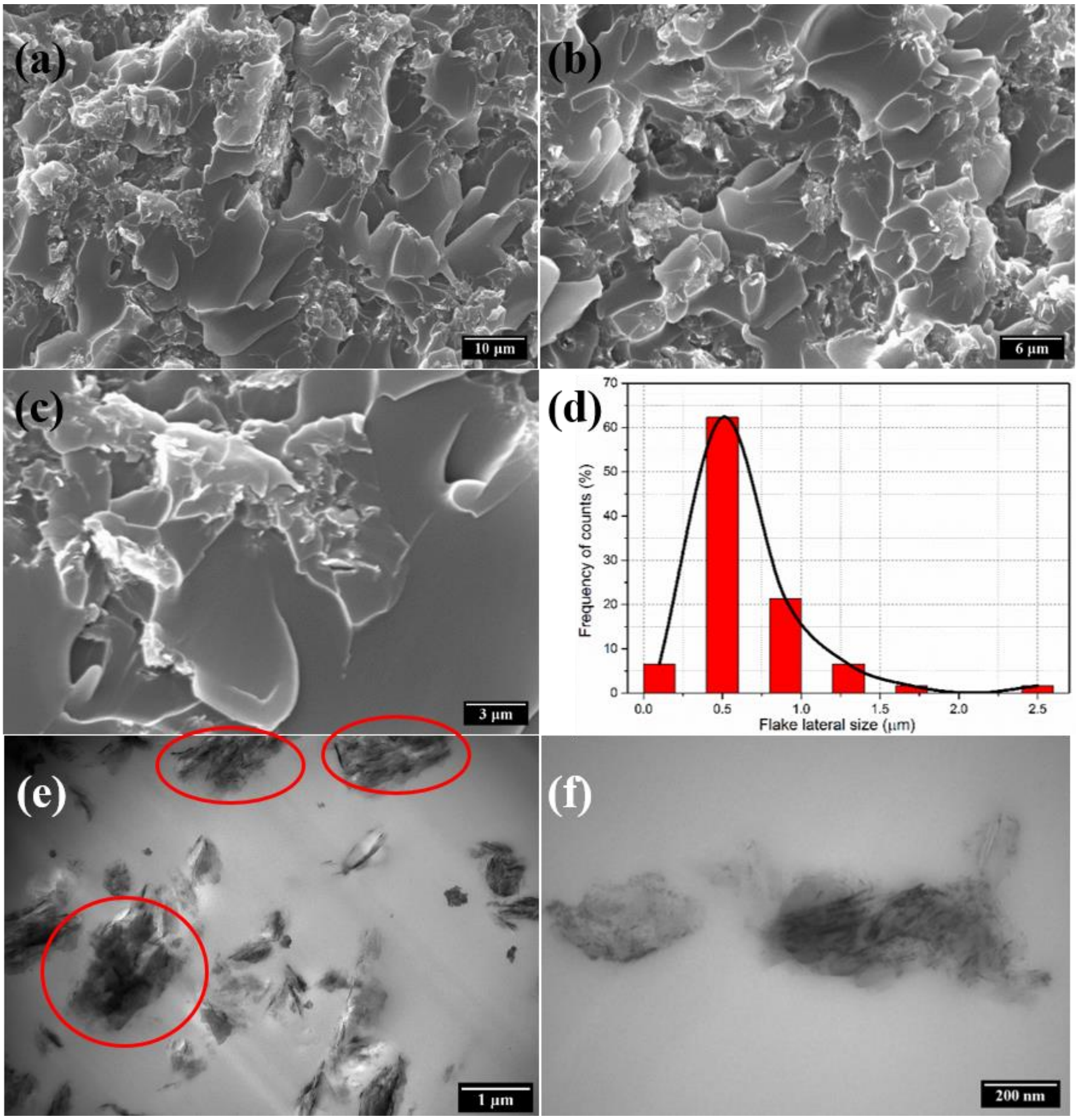

Figure 5.2.6 (a-c) SEM images taken from eGO-filled nanocomposites. (d) Lateral size distribution determined by analysing 61 different flakes from the SEM images. (e) TEM images of isolated eGO tactoids co-existing with clustered ones (in red circles) f) TEM image of a representative eGO tactoid found at the 0.56 vol.% eGO-filled sample.

TEM images of samples filled with mGO (Figure 5.2.7) and eGO (Figure 5.2.8) were also used to assess the respective platelet thickness distribution. Analysis of 17 mGO tactoid dimensions revealed a thickness distribution with the highest probability (> 40%) between 5 nm and 6 nm. Assuming a monolayer thickness of ~0.8 nm [54] for oxidized graphite, the majority of the examined structures contain less than 10 layers. The aggregated structures, such as that circled in red in Figure 5.2.7c, typically appeared to be ~60 nm in thickness.

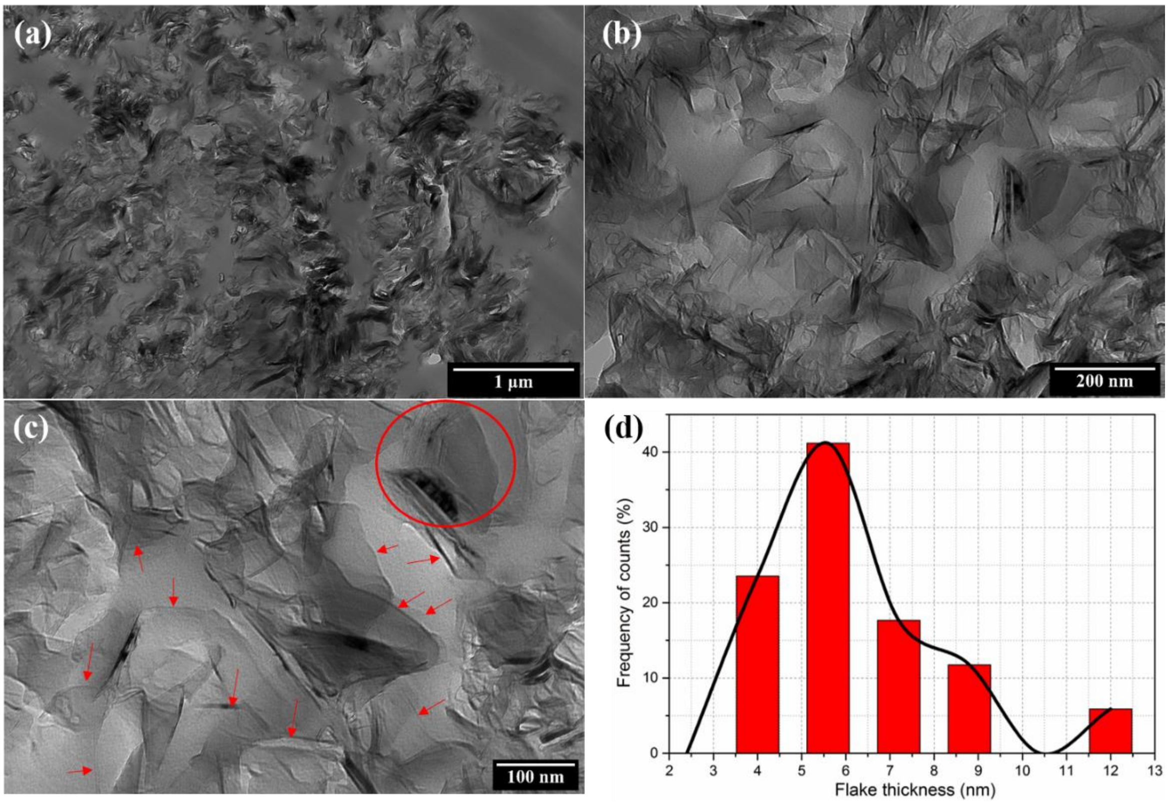

Figure 5.2.7 TEM images of the mGO-filled sample at different magnifications as well as thickness distribution determined by analysing 17 individual tactoids.

Analysis of 20 eGO tactoids revealed a thickness distribution with the highest probability (45%) of around 20 nm, which would correspond to 25 layers according to the previous layer thickness specification. In this case the clustered structures, such as the ones in red circles in Figure 5.2.8a, c, appeared to display various sizes spanning from ~100 nm to ~2 μm in thickness/diameter.

It has to be noted that in the case of high magnification TEM images concerning eGO (see Figure 5.2.6f and Figure 5.2.8c) small structures, that typically span between 10 – 20 nm exist surrounding or attached on the eGO tactoids. We attribute these entities to the carbon-based impurities, such as anthracene and other carbon fragments that were proved to exist for eGO, via Raman and XPS characterization.

Overall, the size distribution of mGO and eGO reflects the processes used for their production as well as the acquired surface chemistry. The mGO filler aside from showing fine distribution/dispersion compared with the eGO, it also displays considerably larger aspect ratio. By considering the peak size/thickness distributions mGO displays an average aspect ratio of ~163, while the same value for eGO is only ~25. In the case of the latter system the edge oxidation did not promote efficiently layer separation (thus larger thicknesses) while the lateral size is speculated to be reduced by the size reduction treatment (sonication or milling, etc.) that EG derivatives undergo as explained in Chapter 2. Therefore, the importance of a single-step, mild oxidation of graphite is underlined.

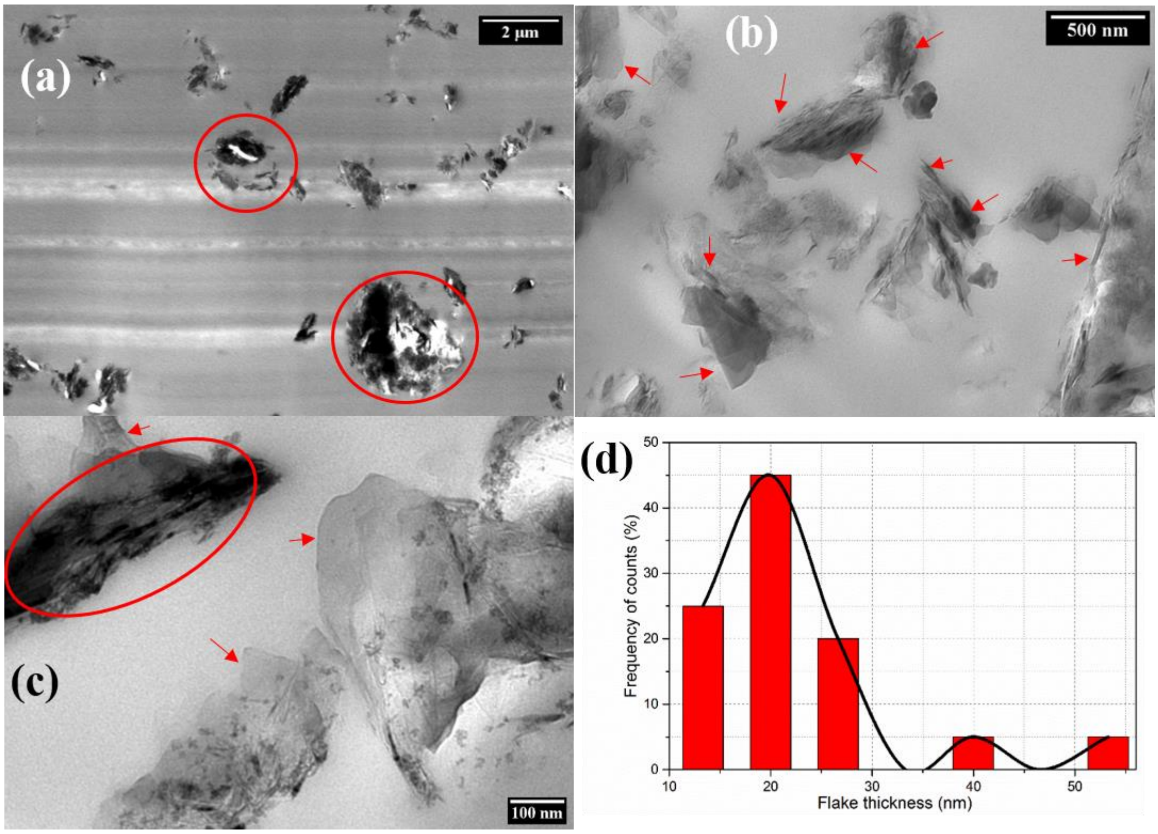

Figure 5.2.8 TEM images of the eGO-filled epoxy at different magnifications as well as thickness distribution determined by analysing 20 individual eGO tactoids.

5.2.4 Tensile Testing

Figure 5.2.9 illustrates the elastic modulus and tensile strength of the unfilled, mGO and eGO-filled samples. First it has to be noted that the slight alteration of the unfilled epoxy's tensile strength displayed here, compared to the one shown earlier in Chapter 4 (Figure 4.3.5) is possibly attributed to variations between batches. Furthermore, for the preparation of eGO- and mGO- filled samples the epoxy supplier (and also manufacturer) was different from the one that supplied the epoxy used for the previously presented GO- filled samples.

The addition of both mGO and eGO slightly increases the elastic modulus of the epoxy system, while the tensile strength appears only to decrease after a certain amount of filler is added. It was demonstrated in Chapter 4 that the GO increased both the elastic modulus and tensile strength of the epoxy at low filler contents, an effect attributed to the highly oxidized surface of GO. Both mGO and eGO display considerably lower oxygen content compared to GO, an effect that was discussed in Chapter 2 (Figure 2.3.5) to result in lesser mechanical enhancements [83]. Furthermore, no detrimental effects on the modulus values were seen, which was earlier attributed to altered stoichiometry, confirming that neither mGO nor eGO significantly perturb the epoxy crosslinking at the filler contents considered here. Comparing the tensile strength of mGO and eGO-filled samples it can be seen that the addition of the latter rapidly deteriorates the system's performance, while this is not the case with mGO, which maintains the strength at higher filler fractions. Since, here, there is no adverse effect on the epoxy stoichiometry, the tensile strength is only impaired by agglomeration or poor particle distribution. The latter effect aligns with the SEM images shown above and claiming that the eGO clusters can act as a crack initiators. Therefore, we suggest that the observed behaviour is directly linked to the surface chemistry of each powder, which results in either fine (mGO) or poor distribution (eGO) within the epoxy matrix.

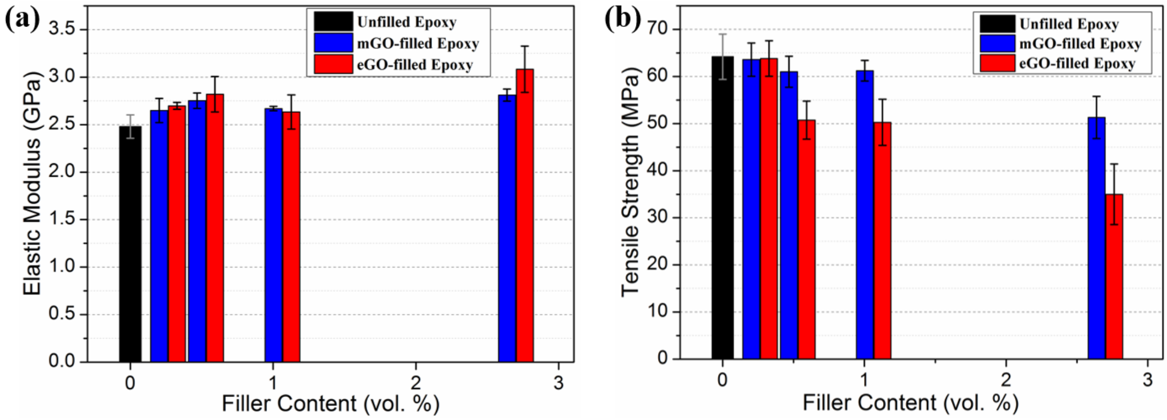

Figure 5.2.9 (a) Elastic modulus and (b) tensile strength of the unfilled, mGO- and eGO- filled samples.

5.2.5 Electrical Conductivity

Figure 5.2.10 shows the dependence of electrical conductivity on mGO and eGO volume fractions. At the lowest loading levels (0.1 – 0.4 vol.%), mGO- filled samples show an increase in conductivity of about two orders of magnitude progressively occurring while, between 0.40 vol.% and 0.53 wt.%, the conductivity sharply increases by a factor approaching eight orders of magnitude, compared to the unfilled epoxy. Nevertheless, the two highest mGO contents (7 vol.% and 9.1 vol.%) did not follow the pattern and resulted in slightly decreased values indicating that at these filler contents mGO slightly restacks. In contrast, the eGO-filled systems are characterized by markedly lower conductivity values at each corresponding filler content, compared to mGO. The variation with eGO composition is much more gradual showing a relatively steep increase up to ~7 vol. % and a mild increase at higher filler contents. The maximum observed conductivity for both systems is of a comparable order of magnitude, albeit achievable at significantly higher eGO contents.

Interestingly, eGO did not display the slight conductivity decrement, indicating that such effect might be a result of the extent of mGO oxidation. It was claimed in Chapter 2 that GO results in considerably large percolation thresholds, presumably, due to agglomeration at high filler contents. Since the mGO displays reduced oxidation degree compared to GO these effects appear at higher filler contents, similarly to the T_g variation, shown above.

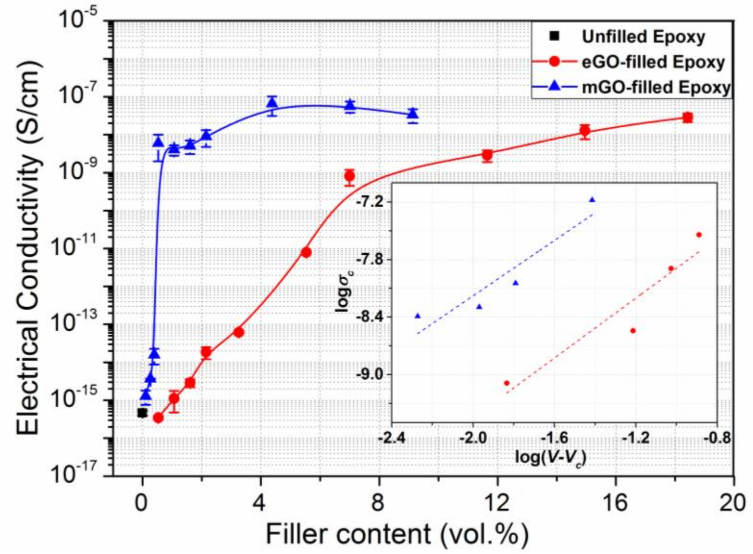

Figure 5.2.10 Variation of electrical conductivity with mGO and eGO content. Inset: log – log plot using percolation thresholds of 0.53 vol.% and 5.3 vol.%, respectively.

By linearly fitting the experimental results into the percolation power law (Equation 1) (log-log plot inset in Figure 5.2.10), the σ_f and V_C and t values presented in Table 5-3 were calculated. The data that did not follow the pattern due to stacking phenomena were excluded from the linear fit.

Table 5-3 Percolation parameters, as calculated from the electrical conductivity behaviour of mGO- and eGO- filled samples.

	Parameters		
Filler	**σ_f (S/cm)**	**V_c**	**t**
mGO	$10^{-(5.29 \pm 0.72)}$	0.0053	1.44 ± 0.38
eGO	$10^{-(6.33 \pm 0.48)}$	0.053	1.56 ± 0.37

Comparison of these results with published data reveals that the exponential factor t derived from the mGO and eGO-based systems considered here is in reasonable agreement with reported values [38], while the calculated conductivity of the mGO and eGO (σ_f) is, in reasonable agreement when compared to values obtained from systems based on GO and EG derivatives, as shown in

Chapter 2 (Tables 2-3, 2-4 and 2-5). Furthermore, the percolation threshold obtained by the usage of mGO is significantly lower (around 12 times smaller volume) than the one shown in Chapter 2 to have been achieved with the usage of GO [123] and more importantly it is not accompanied by adverse effects on the matrix curing.

Overall, the percolation behaviour shown here is in good accordance with the structural characterization, and size distributions presented above. The mGO, that was shown to display improved matrix compatibility and increased aspect ratio, results in a small percolation threshold. In the case of eGO, the minimal oxygen content and presumably the production processing it underwent, result in limited matrix compatibility, agglomeration, reduced aspect ratio and eventually a high percolation threshold.

5.2.6 Thermal Conductivity

Thermal conductivity values and their dependency on the mGO and eGO content are presented in Figure 5.2.11. From this it would appear that the incorporation of both fillers increases the thermal conductivity of the epoxy system with a linear pattern, albeit at a different rate. It can be seen that the incorporation of 4.38 vol.% (8 wt.%) mGO results in an almost twofold increase (from 0.24 W/mK for the unfilled epoxy to 0.46 W/mK for the mGO-filled system)), while a similar value (0.45 W/mK) was achieved with the addition of 11.65 vol.% (20 wt.%) of eGO. The maximum achieved value with the usage of mGO was a threefold increase (0.73 W/mK), at 9.13 vol.% (16 wt.%) while a value (of 0.60 W/mK) was achieved by adding the excessive 18.43 vol.% (30 wt.%) of eGO.

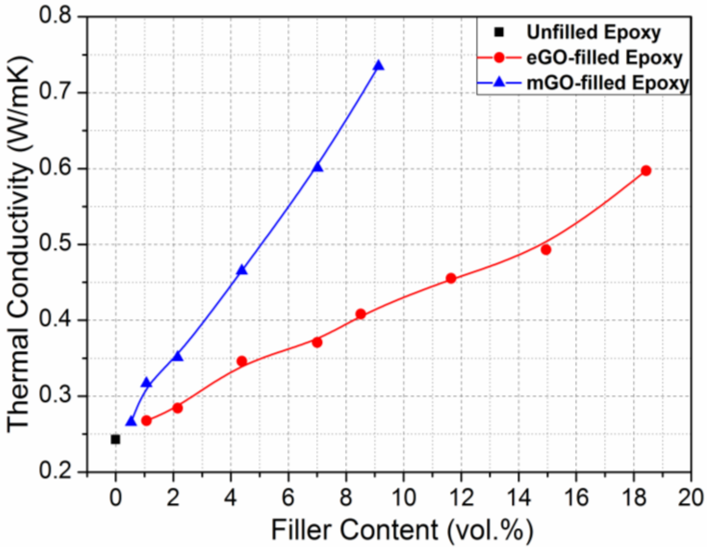

Figure 5.2.11 Variation of thermal conductivity with mGO and eGO filler content.

It was claimed earlier that mGO displays higher surface functionality density (oxygen impurities) compared with the eGO. This, according to the theory explained in Chapter 2 (Section 2.1.4), would result in reduced thermal conductivity values. However, the thermal behaviour of the mGO nanocomposites superficially appears contrary to this claim, since the obtained performance from these systems is drastically enhanced compared with the one obtained with eGO. This clearly aligns with the results shown earlier, indicating that mGO displays larger aspect ratio (demonstrated by the microscopy image analysis) and enhanced matrix bonding (evinced by DSC), both of which serve to increase the thermal conductivity of the respective nanocomposites. Furthermore, it was revealed that eGO, despite its significantly low oxygen content still displays lattice impurities that are based on hydrocarbon fragments, presumably caused by the thermal shock processing.

As such, graphite oxidation with chromic acid served to promote filler/matrix interactions via basal plane oxygenation (thus reactive epoxides on the filler surface), increased aspect ratio (via mild processing and/or improved matrix compatibility), both without furtherly damaging the undecorated graphitic lattice. For the reasons mentioned mGO displays optimal structural/chemical characteristics for thermal conductivity improvements.

5.3 Summary

Moderate oxidation of graphite was successfully achieved utilizing CrO_3 instead of $KMnO_4$ as oxidizing agent, in a reaction medium of H_2SO_4. The process is single-step using the same equipment and similar chemical components with the traditional, high yield, acidic routes and includes no further processing. Raman spectroscopy, TGA and XPS demonstrated that the chromic acid mildly oxidizes the graphite, compared to previous synthetic routes. Comparison of the synthesized mGO with commercially available eGO demonstrates extended basal-plane oxygenation for mGO. It is also revealed that the thermal processing used for the eGO production damages its undecorated graphitic lattice.

Epoxy-based nanocomposites filled with eGO and mGO were characterized and compared in terms of structural features, as well as, mechanical, electrical and thermal performance. It is revealed that the mGO shows moderately promoted bonding with the matrix, aligning with the displayed oxygen content and impairing the T_g values at high filler contents while, in the meantime, eGO remains unreactive with the epoxy resulting only in slightly increased T_g values. SEM and TEM images revealed good mGO distribution/dispersion, while the eGO showed poor distribution with formation of clusters, and poor dispersion with increased flake thickness. It is suggested that the mGO contains sufficiently larger amount of oxygen-based functional groups to render it compatible with the epoxy matrix. As such, mGO displays critically larger aspect ratio when incorporated into the matrix underlining the importance not of oxygen content *per se* but basal plane oxygenation, since only peripheral oxygenation (shown by eGO) appears relatively ineffective in promoting higher levels of matrix compatibility.

Both fillers serve to, similarly, increase the elastic modulus, however the eGO-filled epoxy shows rapidly deteriorating tensile strength when compared with mGO-filled samples due to the formed clusters and the subsequent crack initiation. Incorporation of mGO results in a sharp percolation threshold of 0.53 vol.%, while eGO leads to a gradual increase with calculated percolation threshold 10 times higher than that of mGO. Despite that, both systems resulted in similar electrical conductivity values, which was confirmed by the percolation fitting through similar intrinsic filler conductivities.

Finally, the thermal conductivity of eGO-filled samples is poorly enhanced when compared with the respective mGO-filled samples. This effect was attributed to two main reasons: (1) larger aspect ratio and (2) promoted matrix bonding for mGO.

Thus, the structural/chemical distinctiveness revealed by mGO and eGO, as well as the linkage to the respective nanocomposite properties creates a scope for optimized electrical and thermal performance, without compromised mechanical properties. Furthermore, comparison of the behaviour obtained by mGO with the range of other graphite-based filler systems presented in Chapter 2 reveals an attractive combination of properties, particularly when ease of synthesis and yield efficiency are taken into account. Therefore, it is believed that in the case of mGO, scope exists for future utilisation or further modification.

As such, research questions 3, 4 and 5, that were raised in Chapter 1 were, respectively, answered in this chapter by:

- the successful one-step synthesis of moderately oxidized graphene
- its potential of being used for electrical and thermal improvements without extensively perturbing the epoxy crosslinking and
- its improved performance in comparison with commercially available low-oxygen graphitic compounds (eGO).

Chapter 6 Amino-Functionalized mGO: Effect of Surfactant's Molecular Structure on the Electrical & Thermal Performance of the Epoxy Nanocomposites

In this chapter, the amine-functionalisation of mGO via grafting of two bifunctional (d230 and d4000) and one trifunctional (t440) reagents will be described. The respective d230/fGO, d4000/fGO and t440/fGO systems were characterized and compared with each other as well as with the mGO precursor in order to demonstrate the functionalization and the associated chemical and structural effects. Subsequently, each fGO system was incorporated into the epoxy resin in an attempt to investigate the impact of such modified surfaces on the maximum electrical conductivity, percolation threshold and thermal conductivity of the respective epoxy-based nanocomposites. Therefore, this Chapter will serve to answer two final questions that were raised in Chapter 1:

6. Can we functionalize the previously synthesized mGO product, in order to achieve further electrical and/or thermal improvements?
7. If the latter is possible, which is the optimal surfactant structure, and why?

Part of the results presented in this chapter is under review in Polymer Composites as a full length paper with the title:

"Effect of Surfactant Molecular Structure on the Electrical & Thermal Performance of Epoxy/Functionalised-Graphene Nanocomposites"

6.1 Characterization of fGO

Covalent bonding of the d230, t440 and d4000 reagents to the mGO surface includes the same epoxide-amine reactions that were demonstrated in Chapter 4 and which are illustrated in Figure 6.1.1. The chemical reactions that took place during the functionalisation process are expected to result in chemical and structural alterations to the precursor material and, therefore, this topic will be addressed in this section.

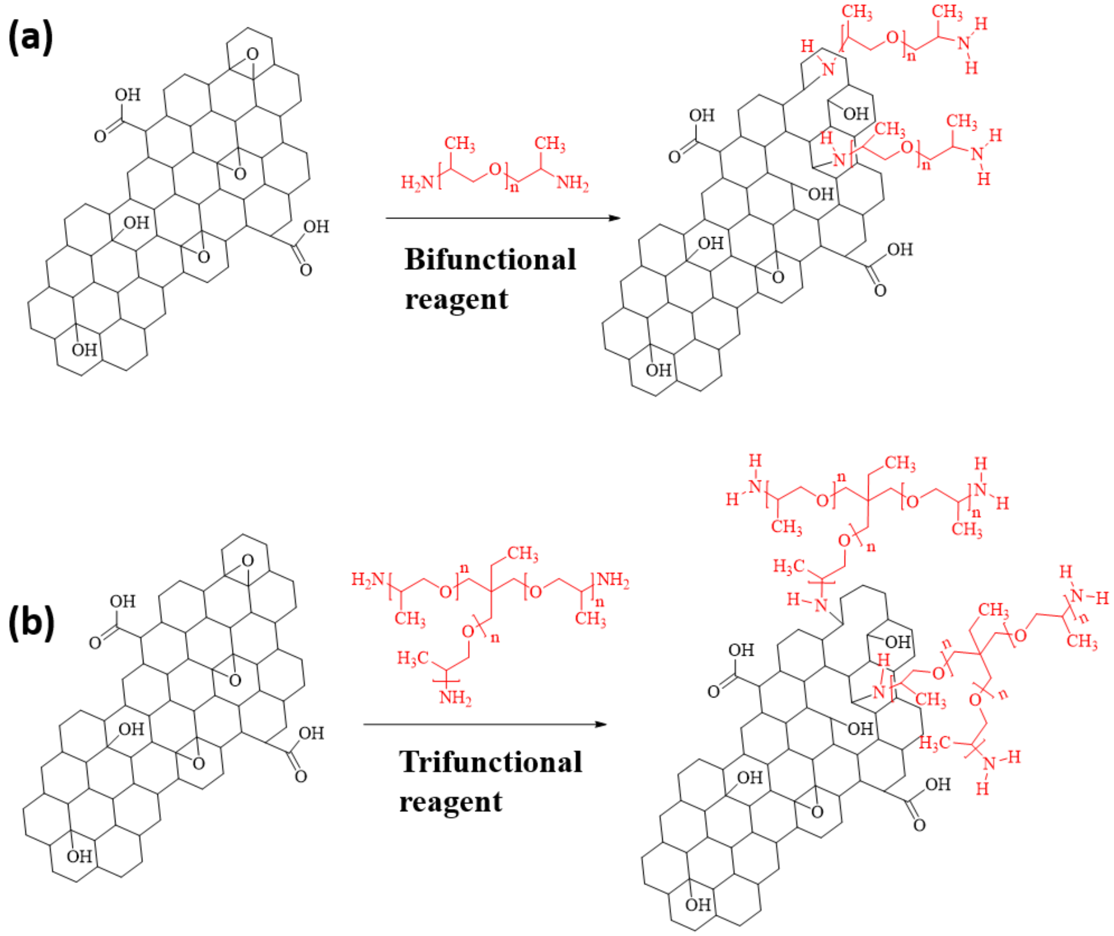

Figure 6.1.1 Covalent bonding of (a) bifunctional and (b) trifunctional amine reagents onto the surface of mGO.

6.1.1 TGA

Figure 6.1.2 shows the variation of sample mass with temperature, as determined by TGA (Figure 6.1.2a, c), together with the associated differential thermogravimetric (DTG) plots (Figure 6.1.2b, d) of the mGO, the three fGO and all three liquid amine reagents. In the case of the mGO, the principal mass loss process occurs between about 150 °C and 300 °C and gives rise to a DTG peak maximum at ~250 °C (Figure 6.1.2b). This process was discussed in Chapter 5. In contrast, all fGO systems, display diminished magnitude of the abovementioned mass loss process (DTG peak maximum at ~220 °C in those systems), and a new principal thermal decomposition process with a

DTG peak maximum at ~360 °C. For the reasons described above, it can be assumed that in the case of the fGO systems the mass loss up to 300 °C is associated with residual unreacted oxygen groups originating from the mGO surface. Contrarily, one could ascribe this effect to desorption of unreacted amine molecules. However, it is evident from the TGA and DTG plots of the liquid reagents (Figure 6.1.2c, d, respectively) that while d230 evaporates below 300 °C, the t440 and d4000 reagents evaporate above 300 °C. Since the minor decomposition that occurs around 220 °C appears to relate to an equivalent process in all three fGO systems, it is suggested that it is more reasonably related to the presence of unreacted oxygen groups, originating from the precursor mGO surface. Tang et al. [123] reported the associated mass loss up to 300 °C in their amine-functionalised GO, with values of ~4.5%. The respective values in the case of the fGO systems presented here, appear to vary between 1.4% and 2.3% of the sample mass and slightly increase with increasing functionaliser molecular mass. The decreased oxygen residue presented in this study compared to [123] is possibly a consequence of two factors: (i) the smaller oxygen content of the precursor mGO, compared with GO synthesized via Staudenmaier method [123]; (ii) the use of a different approach for the secondary thermal treatment step (see Chapter 3, Figure 3.2.5). Specifically, the use of a vacuum rotary evaporator in the present study in place of a fan oven [123] may have led to enhanced removal of unreacted oxygen-based groups from the system's surface.

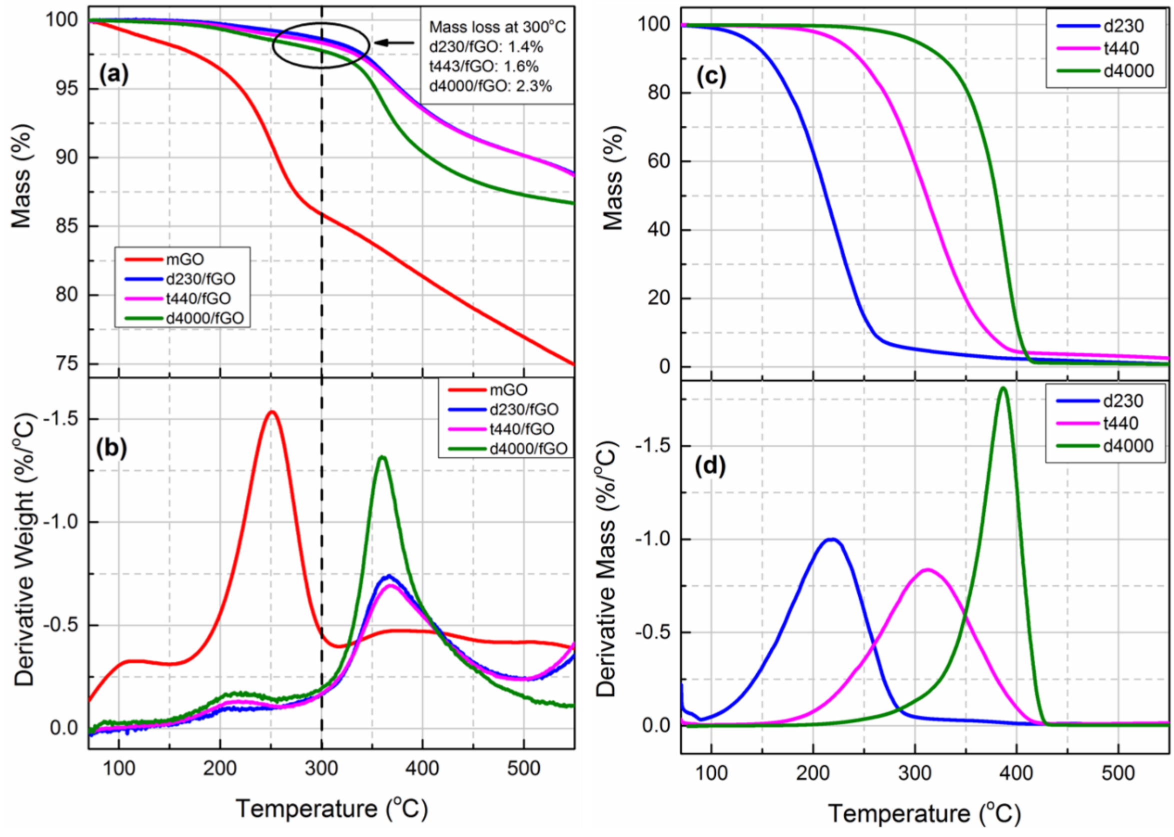

Figure 6.1.2 (a, b) TGA and DTG plots of the precursor mGO and the fGO systems. (c, d) TGA and DTG plots of the amine reagents.

Furthermore, the amino-modified surface chemistry has been reported to result in increased hydrophobicity [143], which aligns with the TGA data presented here and implying limited evidence of water desorption in any of the fGO systems. Finally, the presence of the high temperature (> 400 °C) degradation process in all fGO systems reveals the existence of the stable C=O groups [158], implying that the amine reagents did not react with the peripheral carboxyl groups. While reaction of amines with carboxylic groups is possible with subsequent formation of amide bonding, this reaction would not be favoured in the absence of a catalyst, as indicated elsewhere [167].

Therefore, the TGA/DTG plots presented in Figure 6.1.2 are readily interpreted in relation to relevant published literature and are consistent with the replacement of epoxide groups on the mGO surface with covalent bonds to the functionaliser molecules.

6.1.2 Raman Spectroscopy

Raman spectra obtained from the mGO and the three fGO powders are presented in Figure 6.1.3a. Figure 6.1.3b shows the deconvoluted Raman spectra as obtained peak analysis fitting. The respective Raman data can be found in Table 6-1.

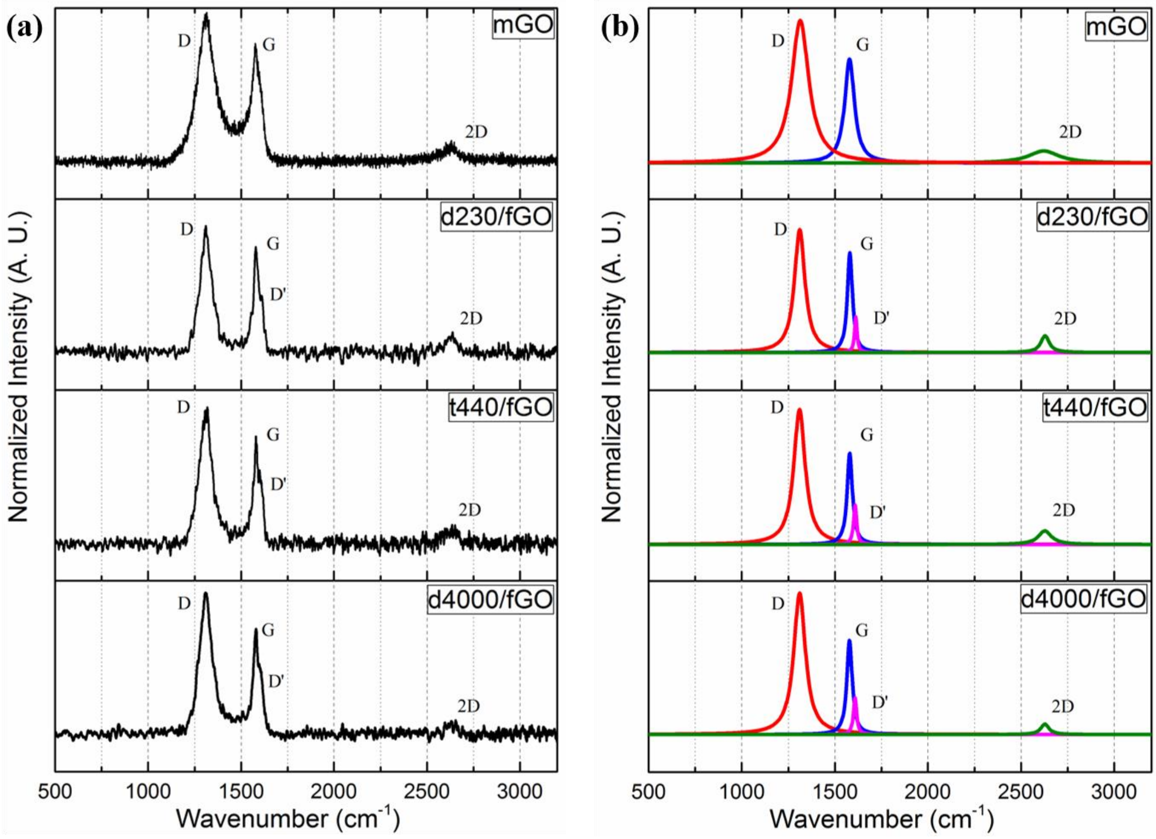

Figure 6.1.3 (a) Raman spectra of the precursor mGO and the respective fGO obtained by amine-functionalization and (b) deconvoluted Raman spectra.

The G band of every sample displays relatively weaker intensity than that of the D band which indicates disorder caused by oxidation in the case of mGO and/or functionalisation in the case of the fGO systems. The amine-functionalisation appears to shift the D band to *lower* wavenumbers than the one displayed by the precursor mGO (see Table 6-1), in line with results reported previously [118, 143]. In view of the Raman data reported in the previous Chapters (Table 4-1 and Table 5-1) it can be seen that the D band shift towards *lower* wavenumbers is opposite to the effect of oxidization on the graphite (D band moving towards *higher* wavenumbers), suggesting that the fGO systems were subjected to a relative reduction compared with the precursor mGO. Furthermore, the latter is evinced by the shape of the G and D bands, upon functionalisation. Specifically the FWHM values of both of these Raman bands drops considerably (see Table 6-1) after functionalisation with every amino-containing compound. This narrowing effect is ascribed to the removal of oxygen-based groups from the mGO surface through thermal reduction and resulted in the reappearance of the weak D’ band at slightly *higher* wavenumbers than the G band. Despite excluding the contribution of the D’ band signal, the location of the G band after the amine functionalisation, is still slightly displaced towards *higher* wavenumbers compared to that displayed by mGO (see Table 6-1), which indicates induced disorder. On the contrary, other studies have revealed slight shifts of the G band position towards *lower* wavenumbers [118, 143], which was associated with partial thermal reduction of the oxygen content of GO during functionalisation at elevated temperatures. Therefore, it is suggested that the divergent behaviour described here is a consequence of the low initial oxygen content of the mGO precursor used in this study, whereupon, removal of oxygen during functionalisation is of relatively minor significance to the position of the G band. Even so, the effect of partial reduction induced by the functionalisation seems to be of great significance for the position of the D band as shown above.

The $I_{(D)}/I_{(G)}$ ratio has also been affected by the amine functionalisation. Grafting of d230 molecules onto the mGO surface results in a decrease in this parameter from 1.26 (observed for the mGO) to 1.20, implying reduction of the associated lattice disorder, which aligns with the partial thermal reduction of mGO mentioned above. Therefore, functionalisation with this relatively short molecule is not sufficient to increase the $I_{(D)}/I_{(G)}$ ratio, which is mainly affected by the thermal removal of oxygen groups. In contrast, grafting of more complex (t440) or longer (d4000) molecules leads to markedly increased $I_{(D)}/I_{(G)}$ values of 1.28 and 1.35, respectively, indicating increasing disorder compared to the precursor mGO, which parallels published data [118]. As such, the Raman spectra, concerning the effect of grafting amino-containing moieties onto the surface of mGO, are again interpreted in terms of two antagonistic effects: the elevated processing temperatures used which partially eliminate defects in the mGO structure, slightly reducing the disorder; the grafted molecules reducing the overall ordering, a phenomenon that increases with molecular length.

Table 6-1 Raman data for the precursor mGO, as well as the d230/fGO, t440/fGO and d4000/fGO.

	Band	**Position**	**FWHM**
mGO $I_{(D)}/_{(G)}$ = 1.26 $I_{(2D)}/I_{(G)}$ = 0.16	D	1313.71 ± 0.26	111.37 ± 0.80
	G	1578.56 ± 0.26	62.54 ± 0.77
	D’	--	--
	2D	2621.85 ± 3.55	200.87 ± 11.53
d230/fGO $I_{(D)}/_{(G)}$ = 1.20 $I_{(2D)}/I_{(G)}$ = 0.19	D	1311.00 ± 0.27	68.30 ± 0.78
	G	1580.43 ± 0.28	32.51 ± 0.86
	D’	1611.89 ± 0.48	16.35 ± 1.67
	2D	2629.11 ± 1.54	55.26 ± 4.51
t440/fGO $I_{(D)}/_{(G)}$ = 1.28 $I_{(2D)}/I_{(G)}$ = 0.17	D	1309.83 ± 0.23	74.04 ± 0.68
	G	1579.72 ± 0.36	34.01 ± 0.98
	D’	1608.24 ± 0.50	19.99 ± 1.77
	2D	2628.41 ± 2.17	86.06 ± 6.50
d4000/fGO $I_{(D)}/_{(G)}$ = 1.35 $I_{(2D)}/I_{(G)}$ = 0.12	D	1310.56 ± 0.20	75.95 ± 0.59
	G	1578.44 ± 0.31	34.83 ± 0.86
	D’	1607.79 ± 0.49	20.71 ± 1.70
	2D	2628.28 ± 1.98	53.42 ± 5.82

The presence of the 2D band in every fGO Raman spectrum indicates that, similarly to mGO, some layered order is preserved. Functionalisation with the d230 reagent increases the $I_{(2D)}/I_{(G)}$ ratio compared to that displayed by mGO, implying increased stacking order. However, grafting of t440, leads to an $I_{(2D)}/I_{(G)}$ ratio value that is comparable to that of mGO, while functionalisation with d4000 results in a considerably lower $I_{(2D)}/I_{(G)}$ value (0.12), suggesting less ordered stacking. However, the intensities of the 2D bands shown here are rather weak for every sample, suggesting that analysis of those bands might be inaccurate, as indicated by the relatively large errors related to this peak (Table 6-1). Furthermore, while the trends of reduced stacking with increasing functionaliser molecular mass appears physically reasonable, analysis of $I_{(D)}/I_{(G)}$ and $I_{(2D)}/I_{(G)}$ intensity ratios is shown in Appendix C to result in inconsistencies regarding the physics and chemistry of GO systems and, as such, over-interpretation should be avoided.

6.1.3 XPS

Figure 6.1.4 shows XPS survey scans of the mGO and fGO powders, along with the derived elemental ratios in the insets. From this, it is evident that all powders display contributions from carbon and oxygen atoms (C1s and O1s peaks), while all fGO systems also display a minor contribution from N atoms (N1s peak), which confirms the existence of the amine reagents grafted onto the mGO surface. The d230/fGO and t440/fGO are characterised by lower oxygen contents than the mGO, however, the d4000/fGO system shows the highest oxygen content compared to all samples. While in the case of mGO, the oxygen atoms are related solely to the functional groups described in the previous Chapter; in the case of fGO systems, two oxygen sources exist: the residual oxygen-based groups of the precursor and the ether groups of the grafted molecules.

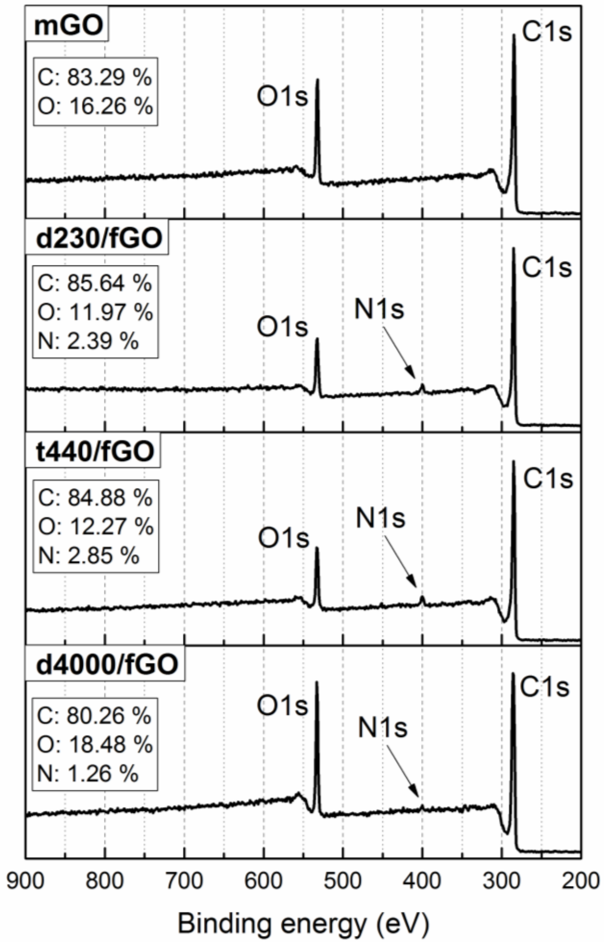

Figure 6.1.4 XPS survey plots of the mGO as well as all fGO powders.

As such, grafting of d230, t440 and d4000 molecules onto mGO replaces one epoxide with one hydroxyl (typical epoxide/amine reactions) and also multiple ethers (on the reagent backbone), which should either have little impact on the proportion of oxygen in the system (in d230 C:O:N ratio ~9:2:2) or high impact (in d4400 C:O:N ratio ~207:68:2). The fact that the d230/fGO and t440/fGO display lower oxygen contents than mGO provides further evidence of thermal reduction during functionalisation, as proposed above. The increased oxygen content of the d4000/fGO can then be ascribed to this functionaliser's ether groups (~68 per molecule), which dominates over the influence of thermal reduction. From Figure 6.1.4, the system with the highest nitrogen content is t440/fGO, which contains three terminal amine groups. The d4000/fGO appears to be characterised by a much smaller nitrogen content than the two other fGOs, which contain relatively short-chain functionaliser molecules. While this is qualitatively reasonable, numerical analysis of the implied elemental ratios were found to suffer from inconsistencies, which suggests that uncertainties in the nitrogen-related data are too large to permit quantitative interpretation.

Figure 6.1.5 presents the deconvoluted C1s peaks, as well as the assigned carbon bonding in the insets. Apart from the carbon bonding peaks described in the previous Chapters, the fGO systems display one additional peak at ~285.5 eV, which is ascribed to C-N bonds. This qualitatively confirms amino-group grafting, as does the increasing intensity of sp^3 C and C-O related peaks which, respectively, stem from the C-C bonding and the ether groups present within the grafted molecules.

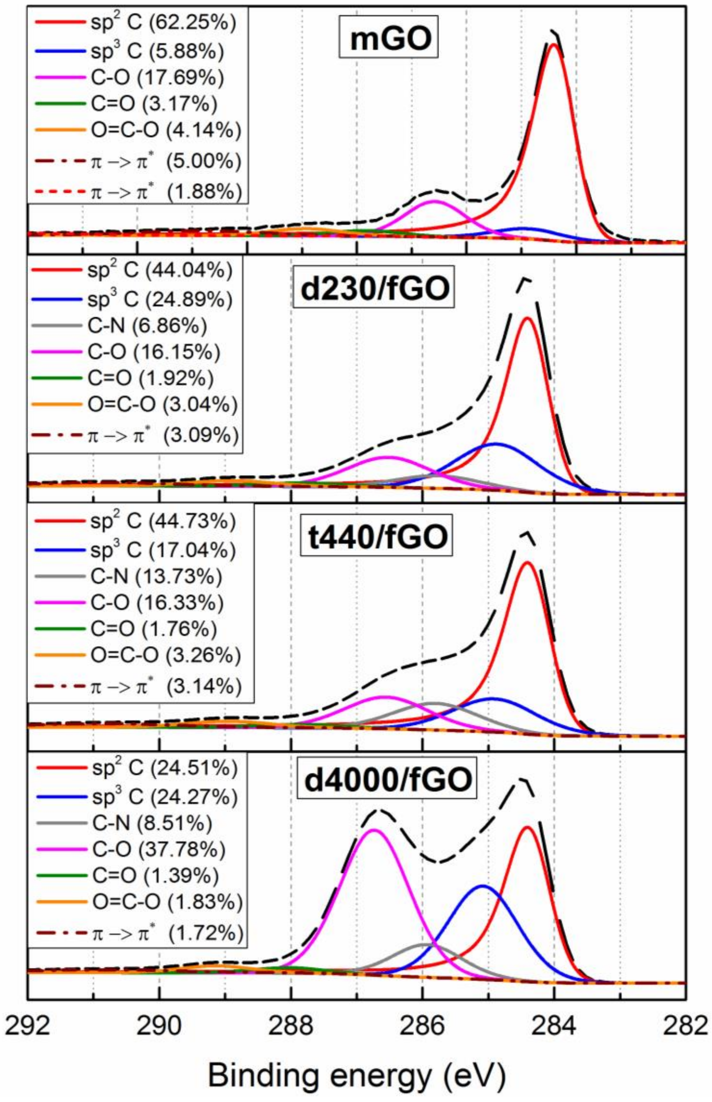

Figure 6.1.5 Deconvolution of the C1s spectra of the mGO as well as all fGO powders.

6.2 Characterization of Epoxy/fGO Nanocomposites

The next section presents and discusses the characterization results of the epoxy samples filled with different contents of the three fGO powders. The methods described here are: DSC, XRD, electrical and thermal conductivity.

6.2.1 DSC

The impact of the fGO volume fraction on the T_g of the respective epoxy composites is shown in Figure 6.2.1, where the respective behaviour of mGO-filled epoxy is depicted for comparison purposes. The addition of mGO has previously been shown to result in increased T_g values at low to intermediate filler loadings and decreased T_g values at high contents, a variation that stems from a combination of physical and chemical processes, respectively. In the case of all three fGO- filled systems, the measured T_g is reduced or comparable to values obtained from the unfilled epoxy, at every filler content. This implies that, in the case of fGO systems, chemical factors dominate, presumably, as a consequence of both the structure of grafted fGO surfaces and the presence of potentially reactive groups within the covalently bonded functionaliser molecules.

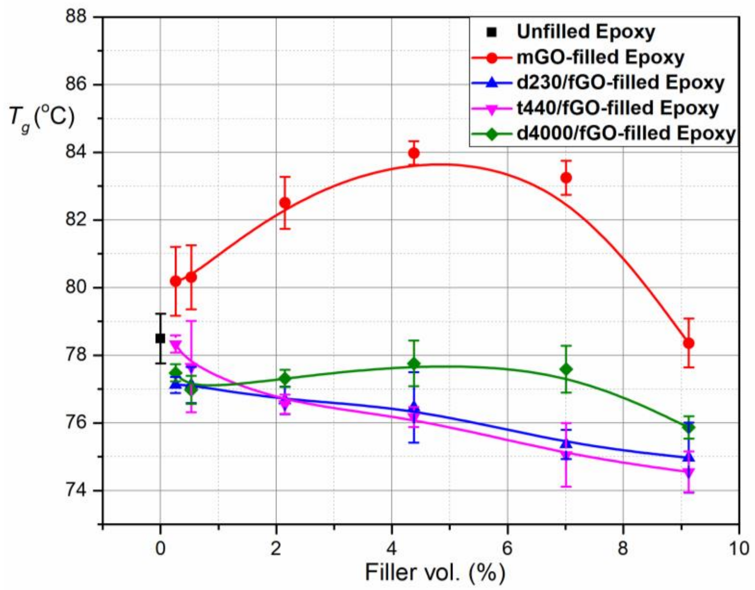

Figure 6.2.1 Filler volume fraction dependency of the glass transition temperature of the mGO- and fGO-filled epoxy samples.

Since the predominant reaction in grafting involves graphitic surface epoxide groups and functionaliser terminal amine hydrogens then, in the case of both diamine reagents, grafting will likely involve either the replacement of one active surface epoxide with one secondary and one primary amine (single end attachment – ciliated surfaces) or the replacement of two surface epoxide groups with two secondary amines (double end attachment – looped chain configurations or inter-platelet bonding). Similar arguments apply for the triamine system, albeit that, here, the maximum chemical impact would correspond to the replacement of one surface epoxide with five active amine hydrogens (single end attachment), while the minimum would correspond to triple attachment, however the latter configuration is not likely to happen considering the relatively short length of this reagent. An illustration of the abovementioned configurations can be found in Figure 6.2.2. While the above interpretation is qualitatively consistent with stoichiometric imbalances leading to reduced T_g values in fGO systems, the quantitative effects depend on how the precise functionaliser molecular structure affects surface grafting and matrix bonding, the consequent fGO surface structure and the residual number of unreacted amine hydrogens left to react with the matrix. From Figure 6.2.1, it is evident that the systems filled with the diamine functionalised d230/fGO and the triamine functionalised t440/fGO are both characterised by a continuous and equivalent decrease in T_g with increasing filler content. This suggests that, in both systems, matrix stoichiometry is being monotonically and equivalently affected by the presence of unreacted amino-groups, despite the additional potential reactivity of the triamine. This phenomenon could be attributed to various topological effects. A comparison of the epoxy filled with the diamine functionalised d230/fGO and d4000/fGO powders reveals a tendency for the latter system to exhibit somewhat higher T_g values. This effect is attributed to the increased probability of the long amine-terminated molecules reacting with both ends, to give looped configurations, as described in Chapter 2 (Figure 2.3.4). The consequence of this would be that fewer active hydrogens in general; primary amines in particular, would be introduced into the epoxy containing d4000/fGO than into the epoxy containing d230/fGO. However, this interpretation in terms of the residual number of unreacted amine hydrogens is inconsistent with the relative behaviour of the diamine d230/fGO and triamine t440/fGO systems discussed above, indicating that the observed T_g is affected not only by the number of amine groups present in the functionaliser, but also by the reagent's structure.

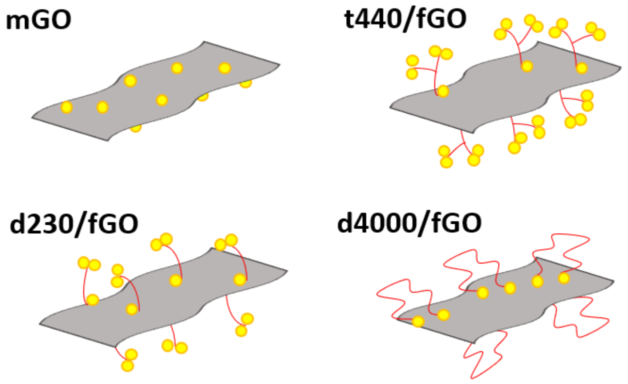

Figure 6.2.2 Illustration of reactive groups as yellow spheres: epoxide rings for mGO and primary/secondary amines for d230/fGO, t440/fGO and d4000/fGO.

6.2.2 XRD

Figure 6.2.3a presents normalized XRD spectra obtained from the mGO-filled and fGO-filled systems at different filler contents. The deconvoluted spectra, upon removal of the epoxy-related background, are presented in Figure 6.2.3b.

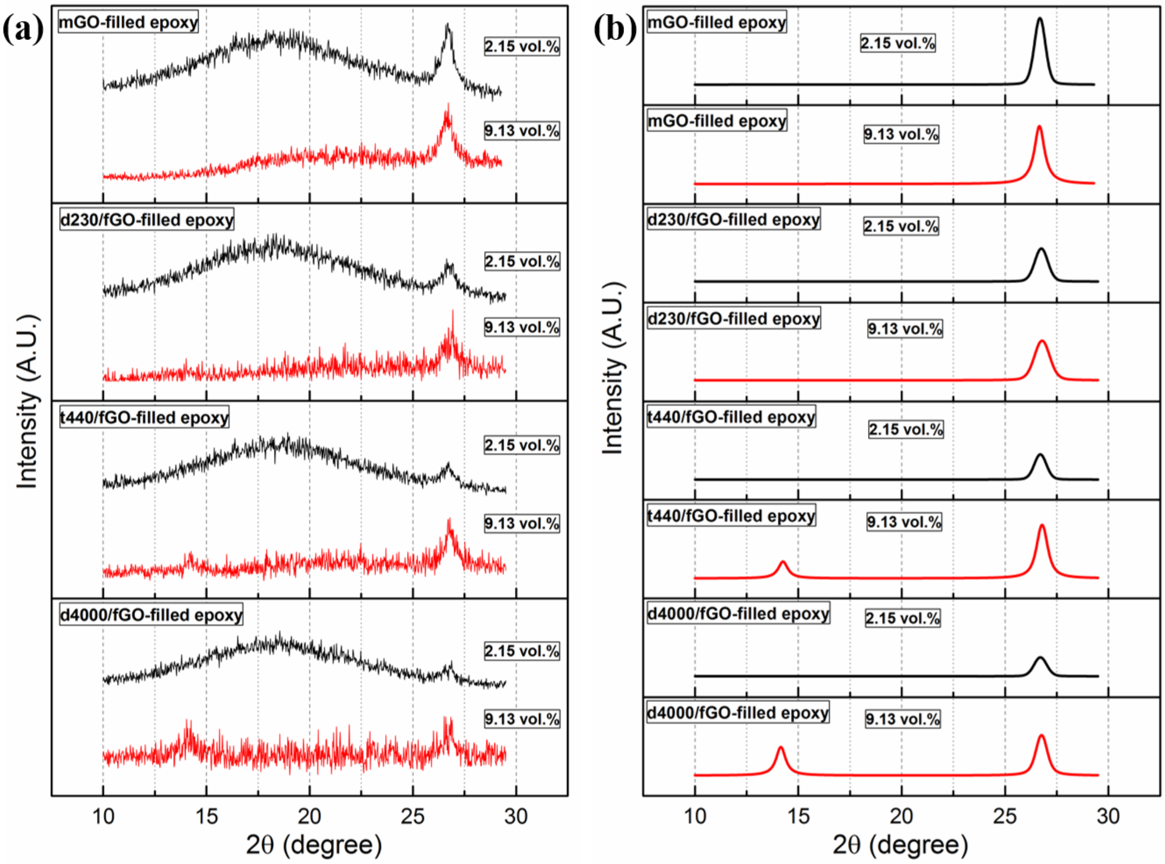

Figure 6.2.3 (a) XRD spectra of mGO- and fGO- filled samples at various filler contents and (b) deconvoluted XRD spectra.

Considering, first, the data obtained at the lower filler content (2.15 vol.%), the broad peak located between 15° – 20° is attributed to scattering caused by the epoxy matrix, while the relatively sharper peak centred at 26.7° corresponds to a periodicity of 0.33 nm associated with the graphitic (002) planes. Similar graphitic XRD features were shown in the study of Ma et al. [88]. The spectra presented here indicate the presence of a population of stacked graphitic layers. The observed variation in the intensity of the graphitic peak from system to system (see Table 6-2), is associated with changes in the degree of graphitic platelet stacking. The latter is mostly extensive in the mGO precursor and its intensity decreases with increasing reagent molecular weight, as can be seen in Table 6-2, aligning qualitatively with the discussion of the Raman data presented above, which implied reduced stacking in the t440/fGO and d4000/fGO systems. The fact that even the d230/fGO-filled epoxy displays weaker (002) peak, than the mGO-filled epoxy indicates, presumably, that the d230-functionalised surface promoted intercalation/exfoliation, compared to mGO, upon incorporation into the epoxy.

In the case of samples filled 9.13 vol.% of the relevant nanofiller the (002) peak intensity is increased compared to the epoxy-related peak due to the increased filler volume and, possibly, also as a consequence of restacking (i.e. increased agglomeration). Indeed the intensity of the 26.7^o peaks are increased for every 9.13 vol.% system, compared with the respective 26.7o peaks of each system (see Table 6-2). However, the systems containing t440/fGO and d4000/fGO display an additional peak at $2\vartheta = 14^o$, which corresponds to a structural motif characterised by an interlayer periodicity of 0.63 nm. Interestingly, the latter peak appears to increase in intensity relative to the 26.7^o peak with increasing reagent molecular mass. This feature, presumably, stems from stacks of fGO with an expanded, interlayer spacing. Such an interpretation is consistent with the notion that agglomeration fGO occurs at 9.13 vol.% but not at 2.15 vol.% and, quite reasonably, that the use of higher molecular mass reagents tends to inhibit the formation of periodic agglomerates.

Table 6-2 XRD peak intensities for the precursor mGO, as well as the d230/fGO, t440/fGO and d4000/fGO.

Filler	**Content (vol. %)**	**Intensity of $2\vartheta = 26.7^o$**	**Intensity of $2\vartheta = 14^o$**
mGO	2.15	0.45 ± 0.02	--
	9.13	0.50 ± 0.01	--
d230/fGO	2.15	0.26 ± 0.03	--
	9.13	0.38 ± 0.04	--
t440/fGO	2.15	0.18 ± 0.03	--
	9.13	0.46 ± 0.04	0.14 ± 0.03
d4000/fGO	2.15	0.15 ± 0.05	--
	9.13	0.33 ± 0.06	0.23 ± 0.05

6.2.3 Electrical Conductivity

The dependence of the nanocomposite electrical conductivity on the respective mGO and fGO contents is presented in Figure 6.2.4. Fitting the experimental data to the percolation power law (Equation 1) leads to the calculated parameters displayed in Table 6-3 and the log-log plots presented in the insets of Figure 6.2.4.

Table 6-3 Conductivity parameters as calculated from the percolation behaviour of mGO and fGO-filled epoxy.

Filler	**σ_f (S/cm)**	**V_c (vol.%)**	***t***
mGO	$10^{-(5.29 \pm 0.72)}$	0.53	1.44 ± 0.38
d230/fGO	$10^{-(6.17 \pm 0.19)}$	0.53	0.97 ± 0.12
t440/fGO	$10^{-(5.87 \pm 0.17)}$	0.53	1.08 ± 0.10
d4000/fGO	$10^{-(5.68 \pm 0.23)}$	0.26	1.13 ± 0.12

From this, it is evident that the addition of either d230/fGO or t440/fGO to the matrix results in a sharp percolation threshold at 0.53 vol.%, similarly to the behaviour that was observed with inclusion of the precursor mGO. Conversely, percolation threshold for the d4000/fGO-filled epoxy is markedly reduced to 0.26 vol.%. This reduction in V_c for the d4000/fGO-filled epoxy is consistent with the interpretation of the XRD data presented above, whereby, the higher molecular mass grafted reagent tends to reduce the periodicity and propensity for restacking. Therefore, it is confirmed that these phenomena are more pronounced with the usage of the reagent d4000 due to its high molecular length.

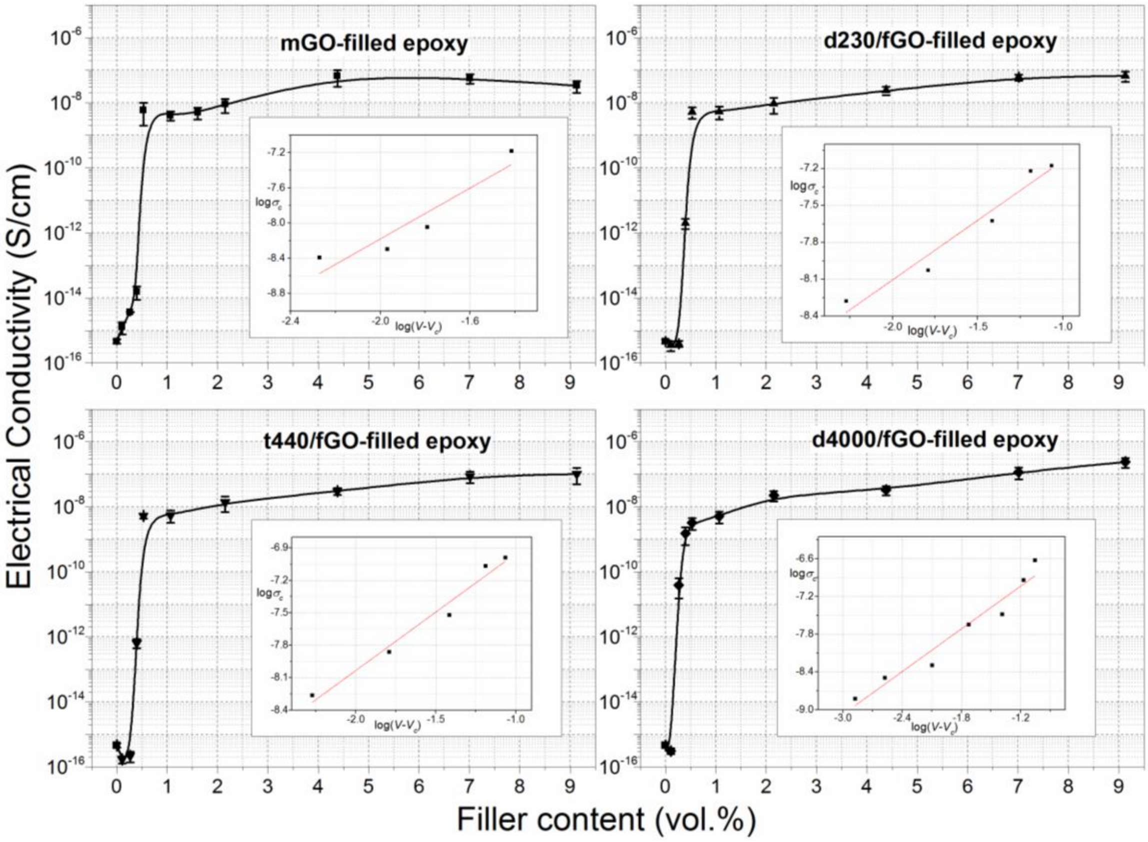

Figure 6.2.4 Variation of electrical conductivity with mGO and fGO filler content. Percolation thresholds indicated with black vertical dashed lines. Insets: log – log plots.

Beyond the percolation threshold, further modest increases in conductivity occur in all systems. It was shown in Chapter 5 that in the case of mGO, the electrical conductivity increases up to 6.6 x 10^{-8} S/cm at 4.4 vol.% and thereafter slightly decreases to 3.35 x 10^{-8} S/cm at 9.1 vol.%. This effect was ascribed to the restacking phenomena explained earlier. In contrast, all three of the amino-functionalised powders exhibit monotonic increases in conductivity with increasing filler content over the range of compositions considered above. Moreover, increasing the functionaliser molecular mass appears additionally beneficial in this respect, with the maximum measured electrical conductivity being 2.36 x 10^{-7} S/cm in the system containing 9.1 vol.% of d4000/fGO – nearly an order of magnitude higher than that seen with the same loading level of mGO. From the XRD data shown above, it is evident that the intensity of the (002) peak is greater in the mGO, implying a considerable degree of ordered stacking, while this effect is mitigated in the fGO-filled systems, due to their ciliated surface structure, which is a consequence of functionaliser grafting. Therefore, it is suggested that the inhibition of restacking that was interpreted earlier, especially at the high filler contents, in the fGO systems is the cause of the observed electrical conductivity behaviour of the respective nanocomposite epoxy systems. This effect appears to be stronger with increasing reagent molecular weight, underlying the importance of long molecules grafted on the graphitic surfaces. An illustration of the abovementioned effect is presented in Figure 6.2.5.

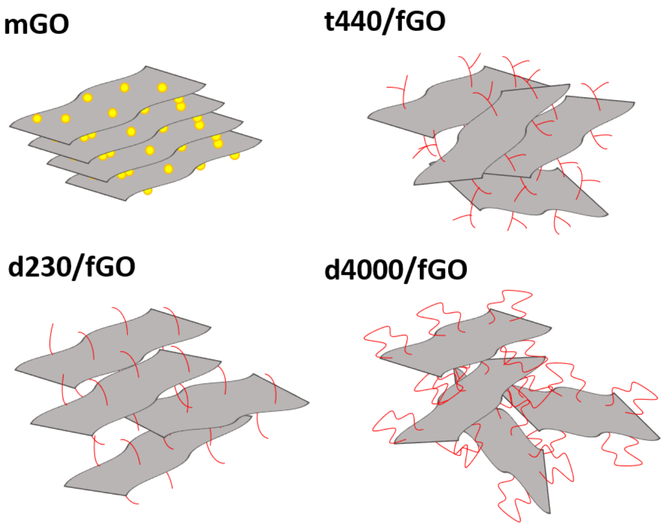

Figure 6.2.5 Illustration of mGO, d230/fGO, t440/fGO and d4000/fGO as well as their proposed orientations inside the epoxy matrix.

Furthermore, from the calculated data presented in Table 6-3, it appears that functionalisation with any of the amine reagents reduces the calculated σ_f compared with the respective value obtained from the precursor mGO. This effect reinforces the notion that the increased electrical conductivity seen at high nanofiller contents in the systems containing fGO is related to improved dispersion and prevention of platelet restacking, as discussed above. That is, the observed conductivity stems from a competition between enhanced filler dispersion and deteriorated intrinsic filler conductivity, as assumed elsewhere [88] for fGNP systems. The observation that functionalisation serves in our systems to reduce the measured electrical conductivity is, however, contrary to the work of Tang et al. [123], who reported that the thermal treatment using during amine functionalisation additionally serves to reduce GO surfaces and, thereby, drastically increase the intrinsic electrical conductivity of the nanofiller, and thus, the respective nanocomposites (see Chapter 2, Figure 2.3.12). As in the case of the TGA results presented above, this discrepancy is in terms of the differences in the precursor systems used for the two studies. While the precursor employed in the abovementioned study was a conventional, highly oxidised GO produced using a Staudenmaier method, here, the mGO system was used, which is characterised by a relatively lower oxygen content. Thereby, despite the innovations used here for the synthesis of the fGO systems (modified solvent; refined thermal reduction protocol) and the usage of three different reagents with different molecular geometries and molecular masses, the significance of the precursor's chemical structure was proven more crucial in enhancing the electrical conductivity via surface functionalisation.

6.2.4 Thermal Conductivity

The thermal conductivity dependence on the fGO volume contents are presented in Figure 6.2.6, where the performance of the respective mGO-filled samples is also displayed, for comparison. From the above, it can be seen that systems containing up to 4.4 vol. % of all three fGO powders exhibit almost identical thermal conductivity values. These values are slightly reduced compared with the respective values obtained from the equivalent mGO-filled systems. That is, it appears that functionalisation with any of the amino-groups considered here does not improve the thermal conductivity of the respective nanocomposites compared to the mGO-filled nanocomposites and, indeed, it even reduces it. This pattern slightly changes at higher than 4.4 vol.% contents, with the d230/fGO- and t440/fGO- filled samples showing almost equivalent behaviour with the mGO-filled epoxy. The samples filled with the d4000/fGO still display slightly reduced values compared to the mGO-filled ones. In general, amino-functionalisation constitutes a method of grafting molecules onto pre-existing "defects" and, from this perspective, it is not unreasonable that such a process should not markedly change the intrinsic properties of the nanofiller. However, it was shown in Chapter 2 that the filler's intrinsic properties are of relatively minor importance in determining thermal conductivity [41], where factors such as interfacial phonon scattering and filler/matrix bonding dominate. Considering the latter factor, it was shown earlier that including either d230/fGO or t440/fGO was interpreted in terms of perturbed matrix even at the lowest filler contents, an effect that involves the formation of covalent bonds between these two fillers and the matrix. However, such interactions did not serve to increase the thermal conductivity of the respective composites at those low contents. Furthermore, the fact that the precursor mGO can also bond with the matrix suggests that interfacial bonding *per se* is not the origin of the effects seen here. Therefore, the only factor that may have affected inversely the thermal conductivity of the fGO-filled samples is the interfacial phonon scattering that was discussed in Chapter 2 (section 2.1.4). Indeed, the data presented in this Chapter were interpreted as indications that amine functionalisation served to prevent stacking (thus improve dispersion) within the matrix, an effect that was stated in Chapter 2 to impair heat conduction due to the increased number of thermal interfaces.

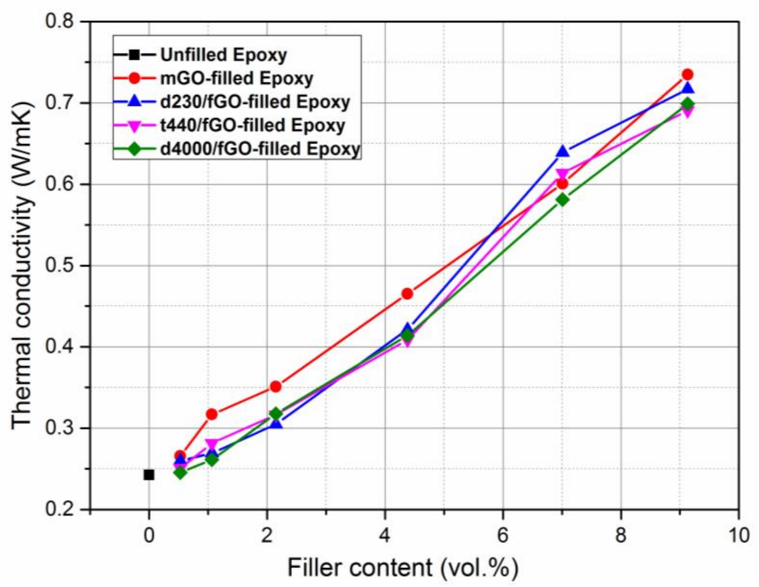

Figure 6.2.6 Variation of thermal conductivity with mGO and fGO filler content.

Comparison of the results presented here with the related literature presented in Chapter 2 (section 2.3.4) it can be seen that the amine functionalisation of mGO resulted in behaviour similar to the study of Pu et al. [90], where epoxy filled with amino-functionalised rGO showed slightly lower thermal conductivity values than the epoxy filled with the un-functionalised rGO powder (Chapter 2, Figure 2.3.16b). However, due to the number of competing factors that may influence heat transport through multiphase systems, comparison of the impact of different functionalisation strategies and different precursor systems, such as the study of Gu et al. [139] (Figure 2.3.18b, Chapter 2) is not straight forward and needs further investigation.

6.3 Summary

Amino-functionalised graphene was successfully prepared utilising the mGO as a precursor. The surface modification was done using three different amine reagents: two linear bifunctional and one trifunctional molecule, all with various molecular weights. TGA, Raman spectroscopy and XPS analysis demonstrated successful grafting of the abovementioned moieties onto the surface of mGO. All fGO samples showed indications of minor unreacted oxygen populations, as well as, partial thermal reduction due to the elevated temperatures of the functionalisation process. Epoxy-fGO composites were prepared and compared to the mGO-filled epoxy via via DSC, XRD, electrical and thermal conductivity characterisation. It was shown that the amine reagents result in composites with decreased T_g values, compared to the mGO-filled epoxy due to the displacement of the epoxy stoichiometry away from optimum. This effect was attributed to the ciliated fGO surfaces, dominating over physical interaction effects observed with mGO. Noticeably, the crosslinking perturbation is partially avoided with the usage of the long bifunctional reagent, due to increased probability of double end attachment (i.e. consumption of additional amine hydrogens) this molecular structure permits. XRD revealed the presence of structures with a periodicity characteristic of graphite, together with additional structural motifs of higher periodicity, an effect indicative of the presence of stacked mGO or fGO. The proportion of stacks reduced with increasing reagent chain length, implying improved dispersion in nanocomposites produced using d4000/fGO. Consequently, a reduced percolation threshold was seen in composites containing d4000/fGO, compared with every other powder. However, it is suggested that the ciliated surfaces that result from surface grafting serve to reduce the thermal conductivity at low filler contents, compared to the precursor-filled systems an effect arising from additional interfaces and increased thermal resistance caused by the surfactants. As such, research questions 6 and 7 that were raised in Chapter 1 were, respectively, answered in this chapter by:

- successfully functionalising the mGO by covalent bonding of amino-reagents to the epoxide groups of the precursor
- revealing that a long bifunctional reagent displays the optimal surfactant structure since it serves to decrease the percolation threshold and prevent restacking without extensively perturbing the epoxy crosslinking

However, it is evident that amino-functionalisation is not a universal panacea, since thermal diffusion was hindered, while the initially desirable effects of significantly increased electrical conduction were not achieved, underlying the importance of the usage of different precursors.

Chapter 7 Concluding Remarks

This Chapter summarizes the main findings of the study and suggests further investigations as future work.

7.1 Summary

In the study presented above, GO of different functionality degrees were synthesized (or purchased) and used as fillers in epoxy resin matrix in order to investigate the derived structure/property relations. More specifically, four types of GO were utilized, namely:

- GO; as-received via oxidation with $KMnO_4$ as an oxidant and a H_2SO_4/H_3PO_4 solution as the oxidation medium, resulting in high oxygen content on the GO surface
- mGO; received from oxidation with CrO_3 as an oxidant in a H_2SO_4 oxidation medium, resulting in moderate oxygen content
- eGO; commercially available graphitic powder, produced by means of acidic intercalation and thermal shock, resulting in low oxygen content
- fGO; by functionalization of mGO with three different amine-terminated molecules (named d230/fGO, t440/fGO and d4000/fGO)

The synthesis steps for the GO, mGO and fGO powders, the preparation of the respective epoxy nanocomposites (including the eGO nanocomposites) as well as the characterization methods employed for those systems, are presented in Chapter 3. It was shown that the GO forms pellet-like compounds upon drying, which was ascribed to the high oxygen content onto its surface. This effect does not allow direct usage of the as-received dry GO powder; thus, it has to be retained into a solvent after the synthesis. On the contrary, every other powder considered in this study could be utilized after drying, due to the relatively lower functionality density they displayed. Therefore, a solvent method (acetone) was employed in the case of GO, while high speed (planetary) mixing was used for the rest of the fillers. As such the importance of a moderate (or low) oxygenation degree on the manufacturing aspect is underlined, since solvent methods were discussed to be unattractive for the industry.

The utilization of the densely oxygenated GO powder into the epoxy was presented in Chapter 4. It was shown that such systems perturb the crosslinking of the matrix, upon curing, aligning with the related literature. A high temperature processing (above 100 °C) serves to accelerate the crosslinking reactions and trigger two reaction routes, namely, epoxy/hardener and homopolymerization reactions. In contrast, low temperature processing only triggered the former one. Consequently, the mechanical performance of such systems is deteriorated, compared to the unfilled system, after the low temperature processing (curing at 80 ^{o}C in this study) and improved after the high temperature processing (post-curing at 130 ^{o}C in this study), while the opposite happened for the unfilled epoxy (and the epoxy-dominated nanocomposites). It was also shown that the high temperature thermal process partially reduced the GO, slightly increasing the electrical conductivity of the respective nanocomposites and removing unreacted epoxide groups. Since the main objective of this study was to increase the electrical and thermal conductivity of the epoxy, the usage of GO was proved to be problematic, not only due to the stoichiometric considerations described above, but also due to the poor electrical conductivity that was achieved even after post-curing (increase of only about one order of magnitude).

The characterization of the mGO powder as well as the performance of the respective nanocomposites were presented in Chapter 5. In order to demonstrate the functionality of mGO towards enhanced electrical and thermal properties more clearly, it was compared with a standard commercial eGO powder that can be found in the market. It was shown that the mGO displays increased oxygenation compared to the eGO, which corresponds to a mild oxygen content (~16%) and C/O ratio (~5); such characteristics have previously been achieved in a single step process only through electrochemical methods [104]. The oxygenation of mGO occurs on both the basal and peripheral planes, in contrast to eGO which is only peripherally decorated. Furthermore, the undecorated graphitic lattice remains intact (sp^2 hybridization) in the case of mGO, while eGO exhibits superficially increased sp^3 hybridization, a fact ascribed to the processing used for its production. When incorporated into epoxy resin the mGO perturbs the crosslinking at high filler contents (~16 wt.%) compared to the GO, which offers the opportunity to be utilised at high filler grades. On the contrary, eGO does not react at all with the epoxy matrix. The poor matrix compatibility of eGO results in agglomeration, which tends to promote crack propagation and rapid deterioration of the system's tensile strength; on the contrary mGO is finely distributed and maintains the epoxy's tensile strength at higher filler contents. It was shown that mGO displays an average flake lateral size of ~1μm while in the case of eGO the lateral dimensions are ~500 nm, a phenomenon ascribed to the processing the eGO was subjected to. Additionally, the mGO shows satisfactory exfoliation within the epoxy with flake thicknesses between 5-6 nm leading to an average aspect ratio of ~163, while eGO displays flake thicknesses of ~20 nm leading to an average aspect ratio of 25. As such, despite the fact that both fillers lead to similar electrical conductivity values (> 10^{-8} S/cm), the mGO- filled epoxy shows percolation threshold 10 times smaller than that of eGO (0.53 vol.% and 5.3 vol.%, respectively). Moreover, mGO leads to nanocomposites with markedly higher thermal conductivity values compared with the systems containing eGO, a fact ascribed not only to the higher aspect ratio, but also to the promoted mGO/epoxy bonding.

The amine functionalisation of mGO, and its effect on the electrical and thermal performance of the respective epoxy nanocomposites are presented in Chapter 6. This surface treatment process was chosen in accordance to the presented literature review, where it was shown to represent the most efficient and least extensive method that resulted in substantially higher maximum electrical conductivity (~10^{-2} S/cm) [123] with the usage of GO derivatives. Thus, three different amine-terminated moieties were utilized: two bifunctional reagents of different lengths and a trifunctional one, in order to determine the optimal surfactant structure. The attachment of all three functionalisers onto the mGO surface was confirmed with the long bifunctional surfactant (d4000) being able to react at both ends. This resulted in looped chain configurations, increased amounts of secondary/tertiary amines and, thus, a minor T_g decrease (~1 ^oC), in contrast to both short surfactants that showed a T_g decrease of 4 ^oC. The long-chain surfactant showed enhanced characteristics in the case of electrical performance, since incorporation of the d4000/fGO into the epoxy resulted in a percolation threshold half that displayed by the mGO-, d230/fGO and t440/fGO-filled systems (0.26 vol.% instead of 0.53 vol.%). It was also revealed that the amino-functionalisation of mGO prevented re-stacking phenomena that occur at high filler contents in the mGO-filled samples, an effect that is more pronounced with the usage of the long surfactant, resulting in conductivity values increased by one order of magnitude. Nevertheless, the improvements in the maximum electrical conductivity that were achieved with amino-functionalization are considerably limited compared with the related literature mentioned above, which was ascribed to the usage of different precursor GO materials. Finally, it was shown that the thermal conductivity of the amine functionalised systems was slightly lower at low-to-medium filler contents compared to the mGO-filled systems, a phenomenon that was attributed to increased number of thermal interfaces and hindered heat propagation.

7.2 Future Directions

Based on the findings of Chapter 4, it is suggested that the GO/epoxy systems obtain stoichiometric balance by the addition of larger amounts of hardener prior to curing/post-curing, which could, presumably, result in further mechanical improvements. Alternatively, the crosslinking reactions between GO and anhydride-based epoxy systems could be investigated in depth, since such systems were shown in the literature [116] to display drastically more pronounced effects compared to the amine-based systems.

Possible future work regarding the findings of Chapter 5 would be further tailoring of the mGO oxygenation degree via minor modifications on the synthesis route, such as smaller amounts of CrO_3, prolonged duration of the oxidation process, elevated temperatures etc. Alternatively, the usage of other metal oxides as oxidants instead of CrO_3 could be investigated.

Possible future work regarding the findings of Chapter 6, would involve the functionalisation of GO, and eGO systems with the exact same functionalisers (d230, t440, d4000) and comparison with the respective fGO systems that resulted from the mGO precursor. In this way, the effect of the amount and the position of the surfactant molecules on the graphitic surfaces would be investigated.

Overall, it was shown in the literature review that the maximum achieved conductivity of epoxy resins filled with GO (and often EG) derivative systems is, often, mediocre (~10^{-8} – 10^{-7} S/cm). It should be taken into account that this effect might not be totally attributable to the filler's intrinsic properties. The prolonged time that the epoxy matrix needs to solidify during curing might be a reason for the platelets to re-agglomerate due to precipitation. Thus, future studies should compare the effect of a specific filler (e.g. mGO) on various resins that require different curing durations, or even different kinds of matrices, such as thermoplastics that solidify drastically faster upon processing.

7.3 Conclusions

This study served to offer a view of the advantages, and also disadvantages each one of the investigated graphitic surface chemistries result. Answers to specific research questions that emerged from the related literature were also provided. It was shown that when particular parameters concerning surface chemistry, are properly tailored, the usage of graphene-based materials as epoxy resin fillers can be a promising material solution with industrial applicability.

It was made clear that the GO-epoxy bonding varies under different circumstances; GO consumes the hardener's amines during curing, while homopolymerization/etherification effects are triggered during post-curing at higher than 100 ^{o}C. This could potentially give guidelines for targeted reaction and attachment of specific groups onto the GO surface. However, GO is particularly ineffective in terms of electrical and thermal property enhancements. The mGO which is moderately decorated both basally and peripherally via a single-step, high yield, method could potentially embody an alternative choice to the existing commercial graphene-based products. Upon comparison with the commercial product considered here (eGO), the mGO resulted in ten (10) times smaller required filler content to achieve electrical percolation (0.53 vol.%). Moreover, the maximum thermal conductivity achieved with mGO (threefold increase) could not be achieved even with the usage of double the eGO filler content. Furthermore, mGO could represent an alternative precursor for studies considering further surface treatment of graphene-based materials with moderate oxygen/surfactant content. Indeed, functionalisation of mGO with amine-terminated molecules furtherly improved the percolation threshold to twenty (20) times smaller than that of the commercial eGO (0.26 vol.%). Moreover, knowledge was established on the electrical and thermal performance of graphene-based materials treated with molecules of various chemical structures, since the surfactants exhibiting long linear structures were shown to be optimal for electrical conductivity, while none of the amine reagents furtherly increased the thermal conductivity.

Therefore, the enhanced properties at considerably low filler contents that the mGO-based systems exhibit compared to the commercially available alternatives could be proved of major scientific and industrial importance, especially by considering the simplicity and high yield of the associated synthesis methods. It is the author's strong belief that research focus on structure/property relations of graphene-epoxy composites, such as the ones described in this study, will potentially lead to high performance polymer nanocomposites with prominent roles in sectors such as sustainable energy and engineering.

Appendix A Manufacturing Methods of Polymer Nanocomposites

As mentioned above, the incorporation of nanometric sized fillers, especially 2D materials, requires high standards in terms of dispersion due to their tendency to agglomerate. An effective mixing process should be applied in order to homogenize the particles inside the polymer matrix, thus, several methods have been suggested [24, 51, 168, 169]. It is also worth mentioning that the simplicity and the environmental impact of the process is a crucial factor, especially in the case of industrial applicability. Most of the techniques described in the literature fall within these generic methods:

- Melt compounding
- Solvent mixing
- In situ polymerization

Melt compounding is considered as the most efficient, straight forward and cost-effective method [24], as it does not require any special or advanced polymer technology, only the already existing processing techniques (e.g. extrusion, injection or compression moulding). The only factors to consider are the optimum mixing conditions for a specific polymer, such as the temperature. The procedure is described by mixing with regular compounding equipment, such as extruders, kneading mixers, blenders etc, depending also on the viscosity of the polymer melt [168]. Since these methods apply only for thermoplastic materials and the polymer matrix used for this study is thermosetting (epoxy resin) we will not focus further on the details of these methods.

The solvent method (Figure A.1) is a common procedure, especially for intercalating layered fillers in polymer or pre-polymer solutions [24]. It can be applied both to thermoplastic and thermosetting polymers. The filler is first dispersed in an appropriate organic solvent and then mixed with the polymer, which is also dissolved in an appropriate solvent.

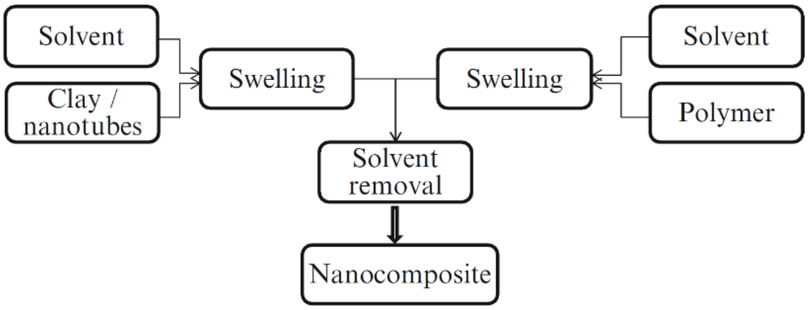

Figure A.1 Solvent method scheme for nanocomposite preparation, reproduced from [24].

When in organic solvents, the nanoparticles are generally stabilized (at least temporarily) by steric effects and the disaggregation occurs with stirring or sonication, with the latter being more efficient [170]. When polar particles are concerned, distilled water can also be used as a solvent, however it is often avoided due to difficulties in removal. Upon mixing, the polymer chains intercalate and displace the solvent between the filler layers. After the solvent is removed, the intercalated configuration still remains, resulting in satisfactorily dispersed nano-inclusions. This mixing procedure could leave residual molecules inside the material and thus, the solvent must be extracted fully. Solvent removal can be done either by heating or cooling (freeze-drying) both accompanied by vacuum degassing. This method can result in fine disaggregation, as shown earlier, but its industrial applicability is limited, due to the usage of the environmentally unfriendly, and also costly, organic solvents.

The in-situ processes are the simplest and most commonly used methods for preparing thermoset-based nanocomposites. In these methods, the nanoparticles, are added and dispersed inside the monomer solution (liquid phase) prior to the polymerization step, as shown in Figure A.2.

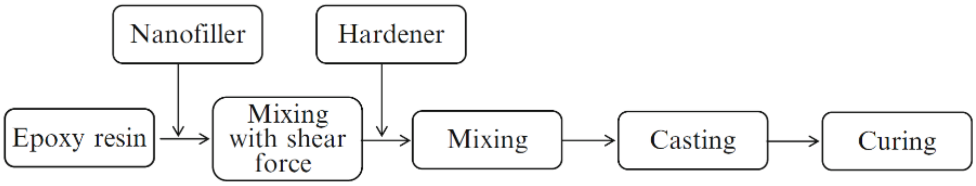

Figure A.2 In situ preparation scheme for nanocomposite preparation, reproduced from [24].

These processes, are usually considered poorer in terms of dispersion/distribution, compared with the solvent methods, as shown earlier. However, they include devices that can be scaled up for mass production, making them easier to apply. The composite viscosity determines the applied dispersing technology, as low viscosity resins could be processed with simple dissolver stirrers and/or sonication under ambient or elevated temperatures. Devices generating higher speed mixing conditions (thus increased shear forces), like planetary mixers can also be used or combined with any of the abovementioned techniques, as shown in Figure A.3. This method's basic principle is spinning the sample holder (rotation) and the mixing arm (revolution) towards different directions and can also be applied for higher viscosity polymers.

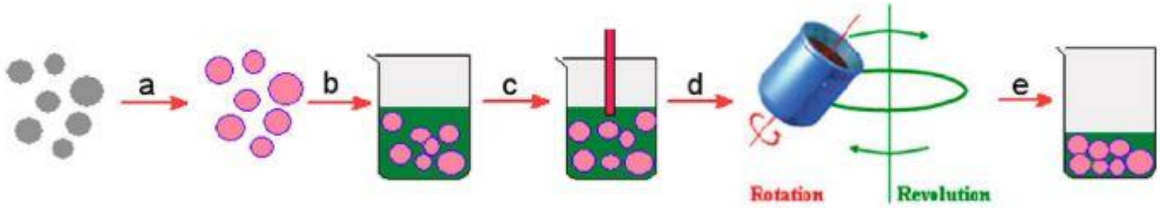

Figure A.3 Preparation procedure followed by [171], including (a) surface treatment, (b) suspension into resin/hardener mixture, (c) sonication and (d) planetary mixing. Image reproduced from [171].

Other methods based-upon various mixing devices can be used, such as the three roll-milling (3RM) which has been reported lately to be quite efficient in homogenizing nanoparticles inside a liquid phase [172]. The fundamental principle of this device is based on the combination of the crushing forces of its rollers and the high shearing forces resulting from the different roller rotation speeds. Preparation methods of specific composite geometries have also been used, with promising results. The electrospinning method [173], can be used to prepare fibre-shaped composites while the spin-coating method [174] is used to prepare thin films. Furthermore, methods of particle orienting have been used. An externally applied field is utilized to align or orient the particles in specific patterns prior or during the polymerization step. For example, Kim et al. [175] managed this by placing the uncured suspension between paralleled electrodes and applying AC electric field. By altering the shape of the electrodes, the particle orientation was tailored.

Finally, it has to be mentioned that since the applied processing methods may vary between thermoset and thermoplastic based polymer nanocomposites, direct comparison of those should not be straight forward even if they were filled with the same filler. Comparison on the respective properties of such systems should be done with respect to the processing method. As an example, a simple moulding method, (usually applied for thermosets) will result in poorer thermal conductivity values compared to a pressing method (usually applied for thermoplastics) [20], as shown in Figure A.4.

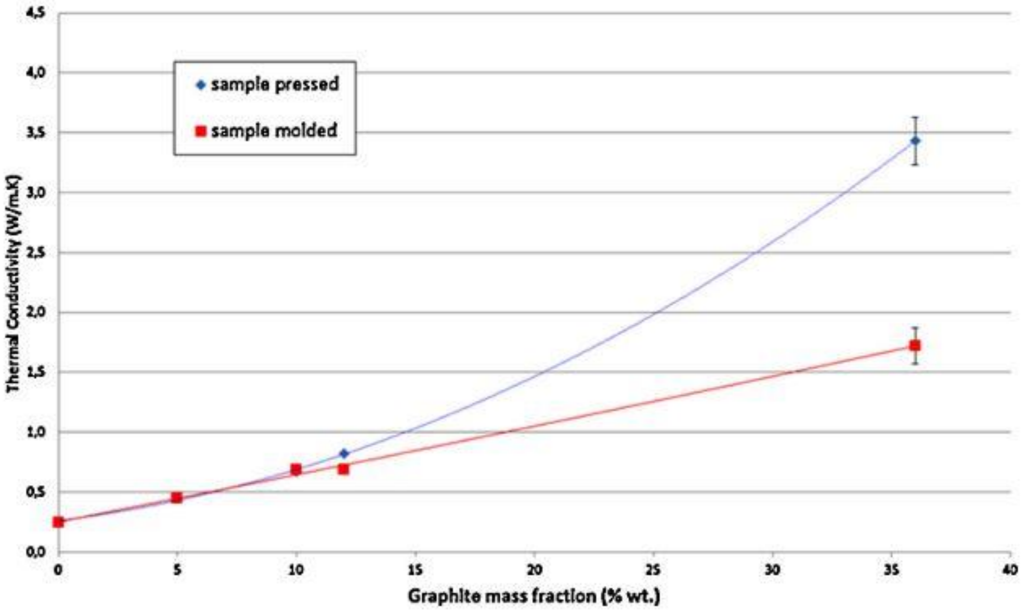

Figure A.4 Thermal conductivity dependency between moulded and pressed samples. Image reproduced from [20].

Appendix B Epoxy Resin Crosslinking & Stoichiometry

Epoxy resins have been used as adhesives, coatings, and structural materials since the 1940s [176]. Their low cost and low weight combined with high design versatility, good insulation, mechanical properties and resistance to chemicals make epoxy resins strong candidates for various applications such as insulation of power transformers or coils, bushings [162, 177], as well as structural components such as the ones described in Chapter 1. As thermoset polymers, epoxy resins form a macromolecular network through chemical cross-linking upon which, the system becomes *"set"* meaning that it cannot flow any more, transforming from liquid to solid state [154]. The prepolymer constituents are often called "epoxy monomer" and "hardener" and the process with which the resin is cross-linked is called "curing". During curing, the constituents are mixed together (usually at elevated temperatures) which triggers reactions that form molecular chains and increase the viscosity of the mixture. As the process continues the molecular chains grow and branch, eventually linking with each other, forming an infinite amorphous network [154, 177], as shown in Figure B.1.

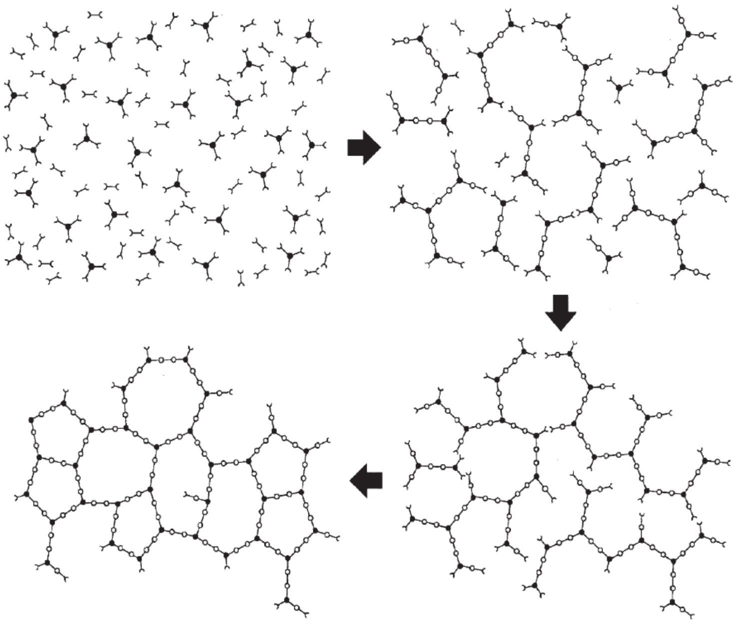

Figure B.1 Typical illustration of thermoset curing process over time, reproduced from [154].

From a chemical point of view the prepolymer constituents consist of reactive end-groups, namely epoxides (oxiranes) and often amines as shown in Figure B.2. Predominantly, cross-linking occurs by epoxide ring opening through reaction with the hardener's primary amine groups, which display two hydrogens available for bonding.

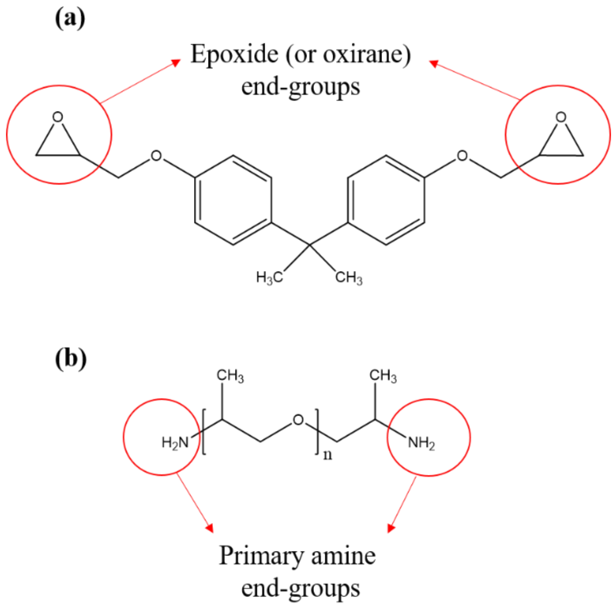

Figure B.2 Typical illustration of: (a) epoxy monomer and (b) hardener molecules.

The outcome of the crosslinking reactions is the consumption of one of the hardener's hydrogen (turning it into secondary amine, with one hydrogen available) and the epoxy's oxirane, with the consequent formation of chain structures containing pendent hydroxyl side-groups (see Figure B.3a and b). As the reaction proceeds, some groups remain unreacted due to the increased viscosity of the system and the consequent low molecular mobility, as stated above. This phenomenon is termed vitrification [154] and is usually addressed by elevating the curing temperature (i.e. post-curing) [178]. Subsequently, at high enough temperatures (usually above 100 ^{o}C), unreacted epoxide groups can react with the hydroxyl groups identified above and not exclusively with amine groups [179]. In this way, more highly crosslinked macromolecular chains are formed, containing an ether linkage and a hydroxyl group (etherification or homo-polymerization of epoxy) [179], as portrayed in Figure B.3c. In any case, small amounts of unreacted oxirane or amine molecules could be expected to exist even after post-curing.

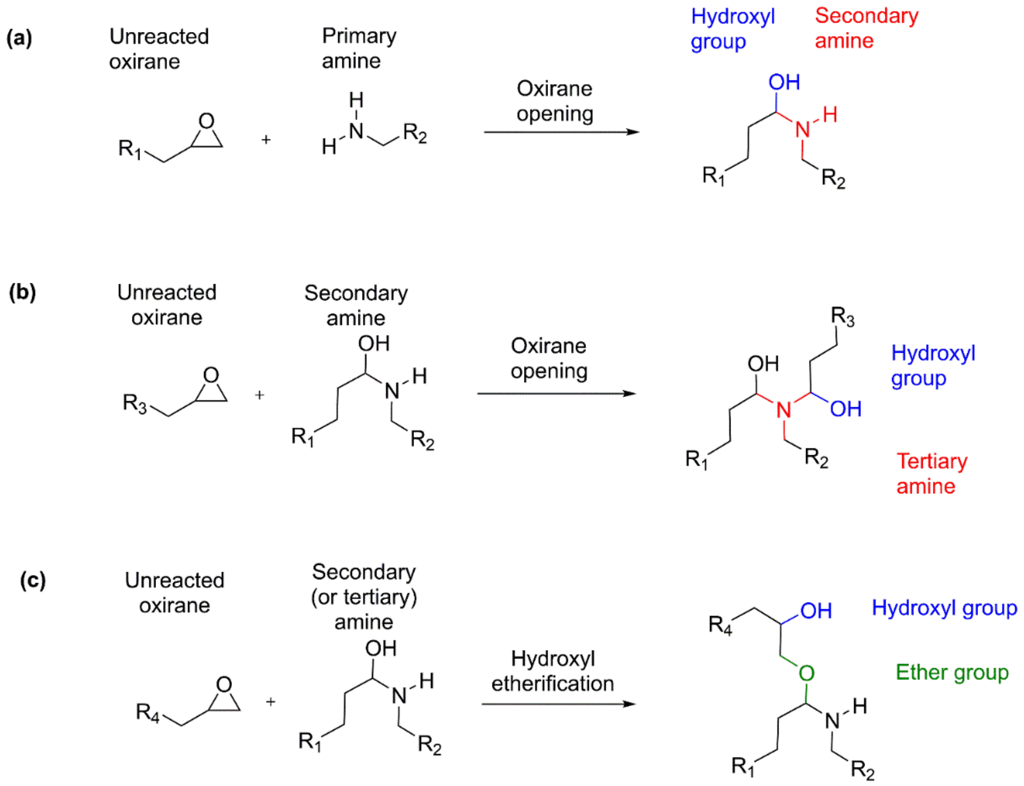

Figure B.3 Epoxy crosslinking processes during curing (a, b) and post-curing (b, c).

As every other polymer, epoxy resins display a glass transition temperature (T_g). The T_g is crucial from a practical point of view; for many applications, it determines the highest operational temperature, since above this temperature the mechanical performance of the system is drastically deteriorated. In general, every epoxy formation displays a specific stoichiometric ratio (given either in mass or volume) between the monomer and the hardener that dictates the maximum achievable T_g. Further addition of any of the constituents results in altered stoichiometry, thus decreased T_g as shown in Figure B.a. More specifically, further addition of epoxy monomer results in excess of epoxides (Figure B.b) and further addition of hardener results in excess amines (Figure B.d).

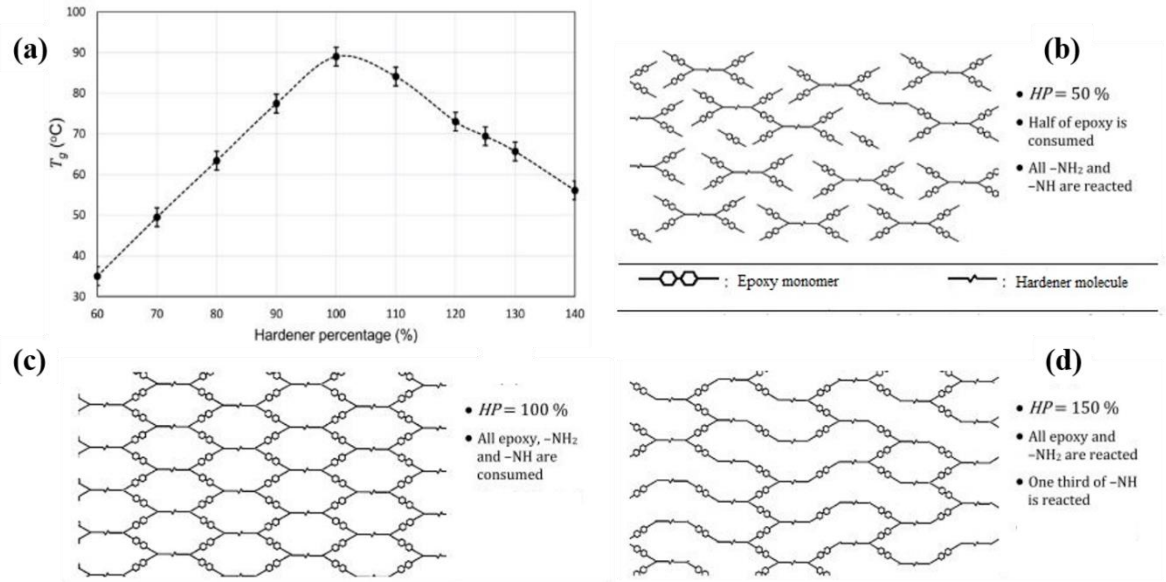

Figure B.4 (a) Dependency of T_g on the hardener content, where a percentage of 100% represents the stoichiometric ratio. Illustration of the molecular network displaying: (b) excess epoxy monomer, (c) stoichiometric balance, (d) excess hardener. Images adapted from [180].

The main focus in a mid-IR spectrum concerns the wavelength regions, ~3400 cm^{-1}, 1180-1010 cm^{-1} and 915-830 cm^{-1}, which are associated with hydroxyl, ether and epoxide groups respectively. Figure B.5 shows the evolution of the associated peaks during crosslinking from a liquid mixture. It can be seen that as the reaction propagates the epoxide-related bands become weaker (in absorbance) while the hydroxyl (-OH) and ether (-O-) become more pronounced.

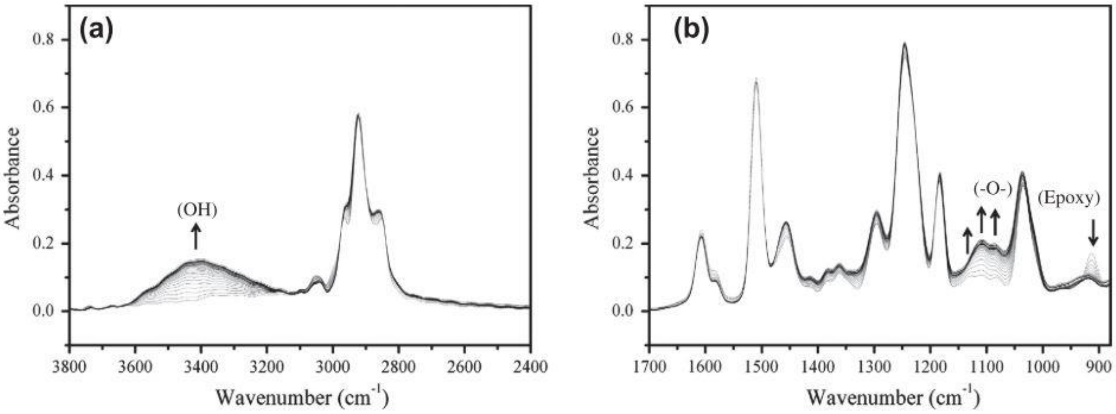

Figure B.5 Evolution of mid-IR spectrum during the crosslinking of an epoxy resin in the: (a) 3800–2400 cm^{-1} and (b) 1700–850 cm^{-1} regions. Images reproduced from [181].

During the curing process the secondary relaxations reveal notable alterations, related to the respective chemical reactions occurring inside the material [155]. For example, during curing, the β- relaxation signal becomes more pronounced and considerably shifts to lower frequencies (or higher temperatures) due to the propagation of crosslinking density and thus limited mobility of the respective dipoles. On the contrary, the γ- relaxation signal remains at similarly high frequency since the respective dipoles' size remains the same, but its intensity reduces as a result of their continuous consumption [155]. A representative example can be found in Figure B.6 where the intensity of the β- relaxation weakens with the addition of excessive epoxy monomer, thus the formation of less cross-links inside the system.

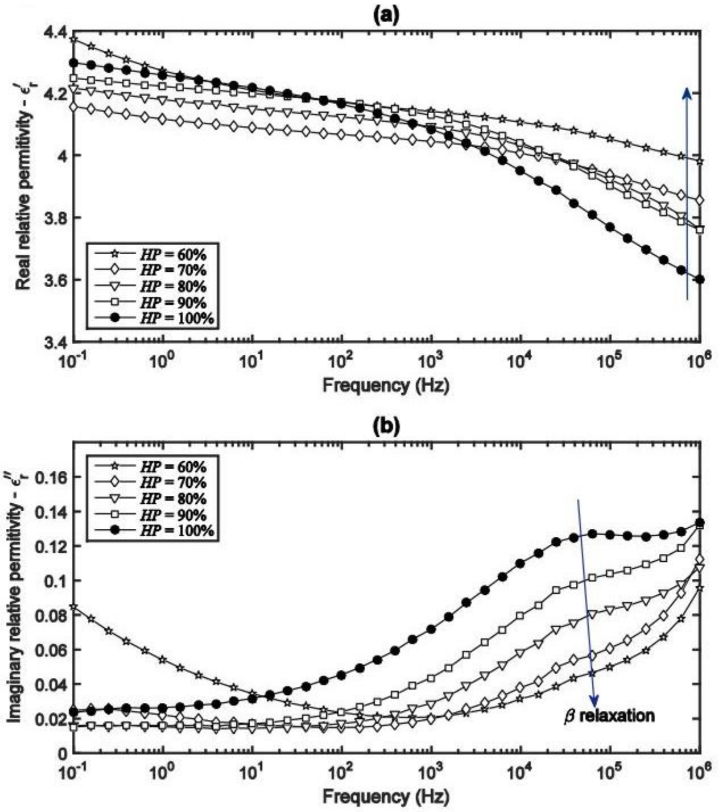

Figure B.6 Dielectric spectra showing the frequency dependency of the (a) real and (b) imaginary parts of the complex relative permittivity of epoxy with different amounts of hardener. Images reproduced from [180].

The utilization of fillers in epoxy matrices could potentially lead to major alterations of the stoichiometry, depending on the respective nanoparticle surface chemistry. This behaviour is consistently aligned with the above-mentioned phenomena that emerge from the nanometric size of the particles, such as the formation of large interaction surfaces. Thus, incorporation of surface functionalized nanoparticles into epoxy might reveal interesting filler – matrix interactions, however from a practical point of view, it should be considered and designed carefully, especially when material development for specific applications is intended.

Appendix C Characterization of Graphene-based Materials

Figure C.1a shows a quantitative Raman spectrum of a graphitic sample. Four characteristic bands can be seen, namely D, G, D′ and 2D. The G band is associated with the in-phase vibrations of the sp^2 carbon lattice [182, 183], while the D and D′ bands are associated with the extent of disorder, such as sp^3 hybridization, impurities or lattice imperfections usually located at the graphitic edges [146, 184]. The G and D mode motions of carbon atoms are presented in Figure C.1b; the D mode motion (also called breathing mode) is not possible in perfect graphite and can only be activated in the presence of defects [185]. The 2D band is associated with the highly ordered stacking sequence of crystalline graphitic layers [146]. It should be noted that the intensity and shape of the bands and especially the D band is highly dependent on the laser used to obtain the spectra [146, 185], so direct comparison of results found in the literature should be considered carefully, unless similar laser excitation was used. Nevertheless, the peak intensities and shapes are also affected by structural divergences such as the ones obtained by the oxidation of graphite described above. As such the Raman spectrum of the precursor graphite is usually dominated by vibrations of the sp^2 carbon atoms (sharp and intense G band) but could also contain lattice defects, which are evinced by the presence of the D and the (lower intensity) D′ band, as shown in Figure C.1c.

All of the oxidation methods described above result in pronounced D bands and broadened G bands (Figure C.1c) indicating decreased size of the in-plane sp^2 domains through sp^3 bonding [98] of the attached oxygen groups. It is noteworthy that the G band broadening conceals the weak D′ band which usually is not visible in the case of GO systems, giving rise to the so-called apparent G peak (or G_{app}, or most of the times just G band). Recently, an alternative interpretation of the effect considered the contribution of D′ band on the broadening and the location of the G band by deconvolution [186]. However, such an approach needs further investigation since various fitting artifacts, such as the D′ band shifting towards *lower* wavenumbers, than the G band remain unclear [186]. Furthermore, the 2D band appears to be eliminated (or be very broadened) which is associated with the heavily disrupted stacking order induced by the inherent structural imperfections [98]. Characterization of such spectra is done by peak analysis. For example formation of new sp^3 carbon atoms in the graphite lattice causes the G band to shift to *higher* wavenumbers [98], as well as display increased full width at half maximum (FWHM) values, as can be seen in Figure C.1d [98]. Further evaluation of the degree of structural disorder can be done by monitoring the intensity ratio between the D and G bands ($I_{(D)}/I_{(G)}$), or between the 2D and G bands (($I_{(2D)}/I_{(G)}$) [98]. For this, either the peak height-, or peak area- ratios are used [185]. In either case, the $I_{(D)}/I_{(G)}$ and $I_{(2D)}/I_{(G)}$ values might display discrepancies, as shown in Figure C.1e, which leads to the conclusion that while Raman spectroscopy offers crucial structural information, it does not necessarily provide straightforward indications of the chemical aspect of the oxidation degree.

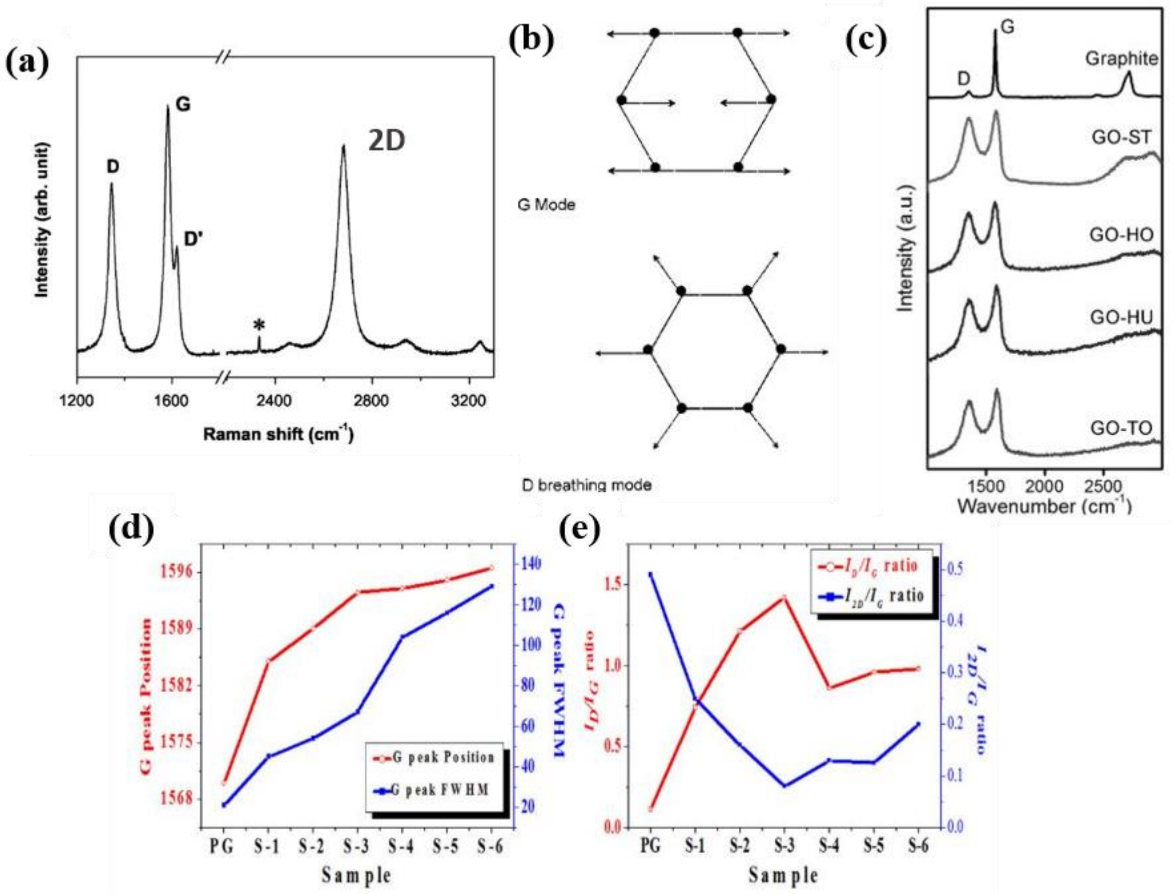

Figure C.1 (a) Main Raman characteristic bands of graphite [146]. Motions of carbon atoms in G and D modes [185]. (c) Raman spectra of GO prepared with Staudenmaier (GO-ST), Hofmann (GO-HO), Hummers (GO-HU), Tour (GO-TO) methods, as well as their precursor graphite [91]. (d) Dependence of G band position and FWHM and (e) dependence of ($I_{(D)}/I_{(G)}$) and $I_{(D)}/_{(G)}$ ratios with respect to oxidation level, with respect to oxidation level (S-1, S-2, etc. is the increasing amount of $KMnO_4$) [98]. Images reproduced from the respective references.

Figure C.2a shows the XPS spectra of GO prepared with various methods and the precursor graphite, from which it is apparent that the oxygen related peak (O1s) intensity aligns with the oxidation degree of each system. The relative peak areas give information on the respective elemental ratios, such that graphite would show very large C/O values while GO usually displays C/O ratios around 2-4. In the case of rGO typical C/O values are around ~7.5 [102], and can be improved up to 12 [106], while GNP usually display higher values (>13), with the oxygen content being limited typically around ~7% [135] or lower [187]. Under certain circumstances the electrochemical exfoliation mentioned earlier results in C/O values of 5, describing the product as mildly oxidized GO [104]. Typically, the permanganate methods (Hummers and Tour) provide higher extent of oxidation compared to the chlorate methods (Staudenmaier and Hofmann) [91]. As described earlier, Tour's method appears to result in the highest oxygen content among every other method. On the contrary, as shown earlier, the Raman spectroscopy of the same samples (Figure C.1b) showed very similar structural characteristics, without readily distinguishing between each other.

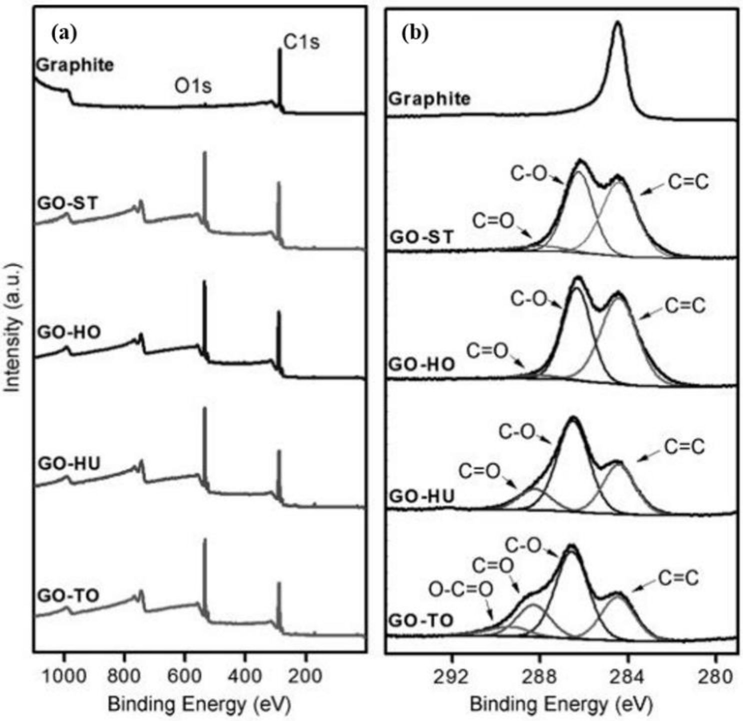

Figure C.2 XPS (a) survey and (b) C1s deconvolution spectra of GO prepared with Staudenmaier (GO-ST), Hofmann (GO-HO), Hummers (GO-HU), Tour (GO-TO) methods, as well as their precursor graphite. Image reproduced from [91].

Deconvolution of the C1s spectra (Figure C.2b) reveals constituent peaks representing different carbon bonds, such as: C-O bonds from hydroxyls or epoxides, C=O and O=C-O bonds from carboxyl groups. XPS spectra reveal that the permanganate methods provide higher extent of C-O bonds but also increased edge oxidation compared to the chlorate methods which is elaborated by the pronounced C=O and O-C=O peaks.

Furthermore, structural characteristics can also be monitored with XPS, as distinction between sp^2 and sp^3 hybridized carbon is possible. For example, Li et al. [70] thermally treated GNP to remove oxygen which was evaluated as diminished O1s peak (Figure C.3a and b) as well as weakened oxygen-related constituent peaks in the C1s spectrum (Figure C.3c and d). However, the peak associated with sp^3 hydrocarbon-based defects such as anthracene [166], was shown to remain present even after oxygen removal [70].

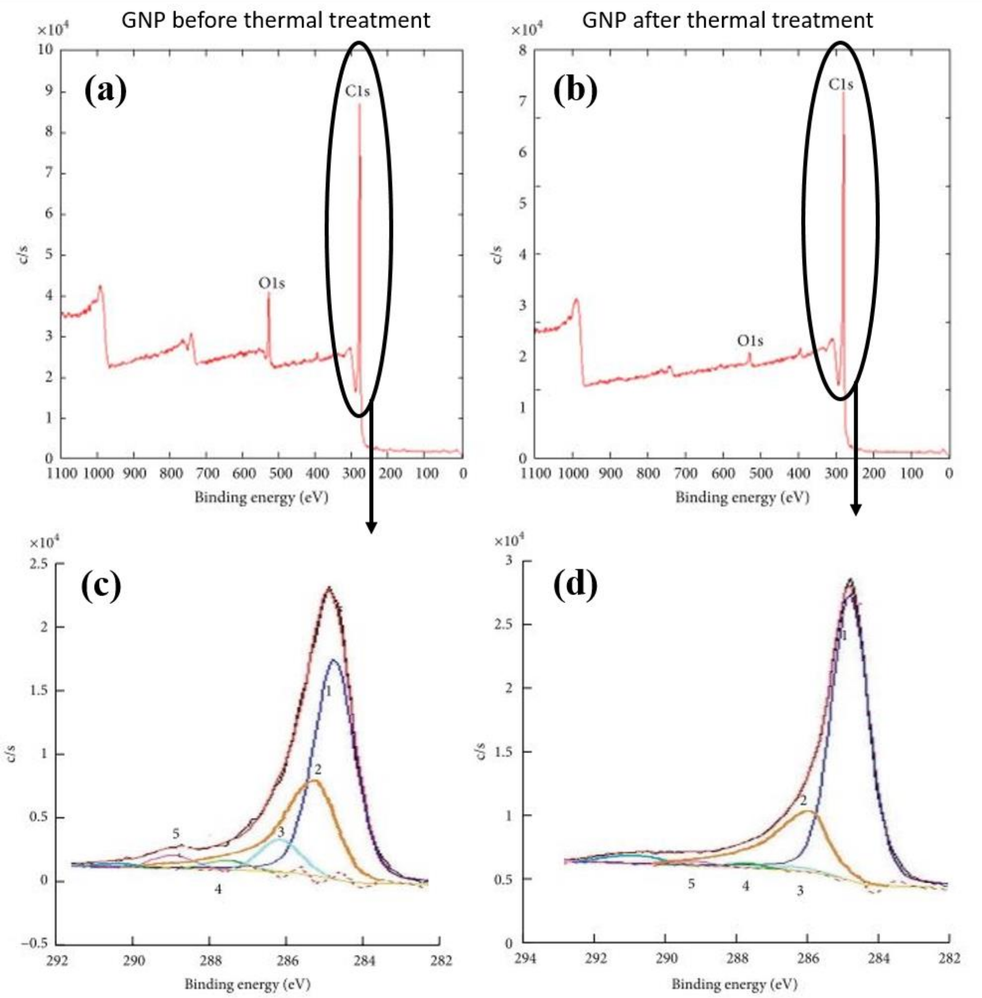

Figure C.3 XPS survey scans of GNP (a) before and (b) after thermal reduction, as well as deconvolution of the respective C1s peaks (c) and (d). Peak numbers correspond to: 1) sp^2 carbon, 2) sp^3 carbon, 3) C-O, 4) C=O and 5) O-C=O. Images adapted from [70].

A few examples concerning TGA characterization of graphene-based materials can be found in Figure C.4. Regarding GO (Figure C.4a), any mass loss in the low temperatures is associated with release of adsorbed water [81, 96], since water molecules can be hydrogen bonded with the GO hydrophilic groups. The mass loss around 150-300 ^{o}C indicates the existence of labile oxygen-based groups with production of CO, CO_2 and steam [148]. Subsequently, a further monotonic decrease in mass until the end of the measurement can be seen, which can be attributed to the removal of more stable oxygen-based groups [100]. Therefore, monitoring the intensity of each of the described decomposition mechanisms gives useful information on the composition of the system. For example, chemical reduction followed by heating at 100 ^{o}C (denoted as partially reduced graphene in Figure C.4a) results in the same decomposition mechanisms with GO, albeit smaller mass losses due to the reduced oxygen content of the system. Further thermal reduction at 250 °C for 2 h under nitrogen atmosphere resulted in a product (denoted fully reduced graphene in Figure C.4a) with much weaker thermal decomposition [125], indicating the existence of residual stable oxygen groups. The TGA plot of GNP before any thermal reduction can be seen in Figure C.4b, displaying similar decomposition characteristics to the fully reduced graphene, shown before, while further thermal treatment (550 °C) reduces the mass loss even more [70]. The minimal high temperature residue in this case is due to the measurement being done under air and not any inert gas, as in the other plots shown.

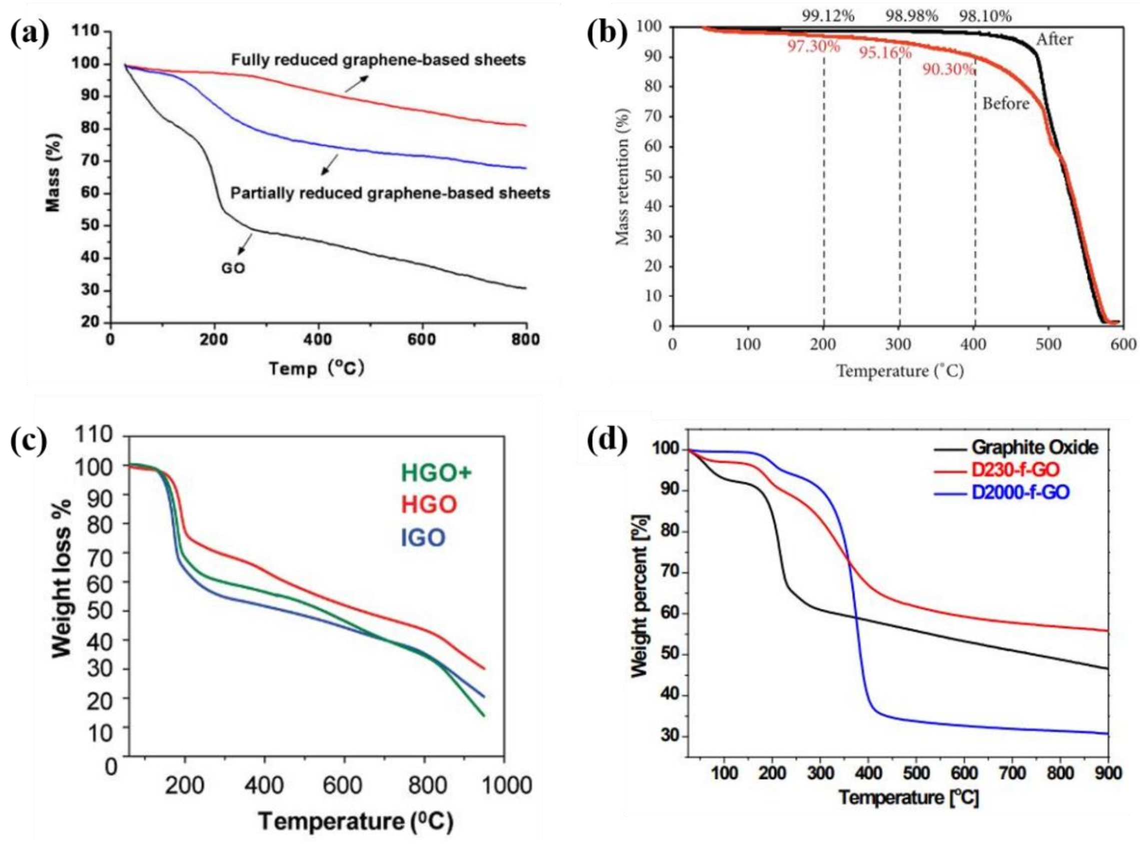

Figure C.4 TGA plots of: (a) GO, partially (chemical reduction and heating at 100 °C) and fully reduced GO (thermal reduction at 250 °C for 2 h under nitrogen atmosphere) done in nitrogen atmosphere [125], (b) GNP before and after thermal reduction, done in air atmosphere [70], (c) GO prepared with Hummers (HGO) modified Hummers with additional $KMnO_4$ (HGO+) and Tour (IGO) methods, done in nitrogen atmosphere [100], and (d) GO and fGO functionalized with short (D230-f-GO) and long (D2000-f-GO) amino-molecules done in nitrogen atmosphere [120] Images reproduced from the respective references.

Moreover, oxygen content differences induced by the oxidation process can be efficiently observed as seen in Figure C.4c, where GO prepared by the Hummers method (HGO) displays lower oxygen functionality than that prepared with additional $KMnO_4$ (denoted as HGO+), while GO prepared with Tour’s method (denoted as IGO) appears to be the mostly oxygenated one [100], aligning with the XPS spectra shown earlier. Finally, TGA has been proven very useful in evaluating the surface chemistry of fGO systems like the ones presented in Figure C.4d. More specifically, GO was functionalized with two different amine molecules [120], each of which decomposes at different temperatures, compared to the residual unreacted oxygen-based groups originating on the GO surface, making them easily distinguishable from the functionalization-related molecules.

List of References

1. Thostenson ET, Li C, Chou TW (2005) Nanocomposites in context. Compos Sci Technol 65:491–516. https://doi.org/10.1016/j.compscitech.2004.11.003

2. Paul DR, Robeson LM (2008) Polymer nanotechnology: Nanocomposites. Polymer (Guildf) 49:3187–3204. https://doi.org/10.1016/j.polymer.2008.04.017

3. Hornyak GL, Patrissi CJ, Oberhauser EB, et al (1997) Effective medium theory characterization of Au/Ag nanoalloy-porous alumina composites. Nanostructured Mater 9:571–574. https://doi.org/10.1016/S0965-9773(97)00127-X

4. Srinavasan S (1994) Wootz crucible steel: a newly discovered production site in South India. Pap from Inst Archaeol 5:49–59. https://doi.org/10.5334/pia.60

5. Verhoeven JD, Pendray AH, Dauksch WE (1998) The key role of impurities in ancient damascus steel blades. Jom 50:58–64. https://doi.org/10.1007/s11837-998-0419-y

6. Reibold M, Paufler P, Levin AA, et al (2006) Materials: Carbon nanotubes in an ancient Damascus sabre. Nature 444:286. https://doi.org/10.1038/444286a

7. Koenig JL (1999) Spectroscopy of polymers. Elsevier

8. Bak CL, Faria da Silva F (2016) High voltage AC underground cable systems for power transmission – A review of the Danish experience, part 1. Electr Power Syst Res 140:984–994. https://doi.org/10.1016/J.EPSR.2016.05.034

9. Jager K-M, Lindbom L (2005) The continuing evolution of semiconductor materials for power cable applications. IEEE Electr Insul Mag 21:20–34. https://doi.org/10.1109/MEI.2005.1389267

10. Gupta T (2017) Carbon: The black, the gray and the transparent

11. Mishnaevsky L, Branner K, Petersen HN, et al (2017) Materials for wind turbine blades: An overview. Materials (Basel) 10:1–24. https://doi.org/10.3390/ma10111285

12. Candela Garolera A, Madsen SF, Nissim M, et al (2016) Lightning Damage to Wind Turbine Blades From Wind Farms in the U.S. IEEE Trans Power Deliv 31:1043–1049. https://doi.org/10.1109/TPWRD.2014.2370682

13. Hirano Y, Katsumata S, Iwahori Y, Todoroki A (2010) Artificial lightning testing on graphite/epoxy composite laminate. Compos Part A Appl Sci Manuf 41:1461–1470. https://doi.org/10.1016/j.compositesa.2010.06.008

14. Ogasawara T, Hirano Y, Yoshimura A (2010) Coupled thermal-electrical analysis for carbon fiber/epoxy composites exposed to simulated lightning current. Compos Part A Appl Sci Manuf 41:973–981. https://doi.org/10.1016/j.compositesa.2010.04.001

15. Liu Y, Zwingmann B, Schlaich M (2015) Carbon fiber reinforced polymer for cable structures-a review. Polymers (Basel) 7:2078–2099. https://doi.org/10.3390/polym7101501

16. Gojny FH, Wichmann MHG, Fiedler B, et al (2006) Evaluation and identification of electrical and thermal conduction mechanisms in carbon nanotube/epoxy composites. Polymer (Guildf) 47:2036–2045. https://doi.org/10.1016/j.polymer.2006.01.029

17. Senis EC, Golosnoy IO, Dulieu-Barton JM, Thomsen OT (2019) Enhancement of the electrical and thermal properties of unidirectional carbon fibre/epoxy laminates through the addition of graphene oxide. J Mater Sci 54:8955–8970. https://doi.org/10.1007/s10853-019-03522-8

18. Pavlidou S, Papaspyrides CD (2008) A review on polymer-layered silicate nanocomposites. Prog Polym Sci 33:1119–1198. https://doi.org/10.1016/j.progpolymsci.2008.07.008

19. Yeon J, Gyeong Y&, Choi M (1999) Percolation Behavior of Conductor-Insulator Composites with Varying Aspect Ratio of Conductive Fiber

20. Burger N, Laachachi A, Ferriol M, et al (2016) Review of thermal conductivity in composites: Mechanisms, parameters and theory. Prog Polym Sci 61:1–28. https://doi.org/10.1016/j.progpolymsci.2016.05.001

21. Galpaya DGD, Fernando JFS, Rintoul L, et al (2015) The effect of graphene oxide and its oxidized debris on the cure chemistry and interphase structure of epoxy nanocomposites. Polymer (Guildf) 71:122–134. https://doi.org/10.1016/j.polymer.2015.06.054

22. Raccichini R, Varzi A, Passerini S, Scrosati B (2015) The role of graphene for electrochemical energy storage. Nat Mater 14:271–279. https://doi.org/10.1038/nmat4170

23. Dearmitt C, Rothon R (2002) Fillers and surface treatment. Plast Addit Compd 4:12–14

24. Bellucci F, Fabiani D, Montanari GC, Testa L (2010) The Processing of Nanocomposites. In: Dielectric Polymer Nanocomposites. Springer US, Boston, MA, pp 31–64

25. Liu L, Qi Z, Zhu X (1999) Studies on nylon 6/clay nanocomposites by melt-intercalation process. J Appl Polym Sci 71:1133–1138. https://doi.org/10.1002/(SICI)1097-4628(19990214)71:7<1133::AID-APP11>3.0.CO;2-N

26. Xiong J, Liu Y, Yang X, Wang X Thermal and mechanical properties of polyurethane/montmorillonite nanocomposites based on a novel reactive modifier. https://doi.org/10.1016/j.polymdegradstab.2004.07.001

27. Bharadwaj RK, Mehrabi AR, Hamilton C, et al Structure±property relationships in cross-linked polyester±clay nanocomposites

28. Atif R, Shyha I, Inam F (2016) Mechanical, thermal, and electrical properties of graphene-epoxy nanocomposites-A review. Polymers (Basel) 8:. https://doi.org/10.3390/polym8080281

29. Giannelis EP (1996) Polymer-Layered Silicate Nanocomposites. Adv Mater 8:29–35. https://doi.org/10.1016/B978-0-12-374396-1.00058-1

30. Chung DDL (2004) Electrical applications of carbon materials. J Mater Sci 39:2645–2661. https://doi.org/10.1023/B:JMSC.0000021439.18202.ea

31. Lux F (1993) Models proposed to explain the electrical conductivity of mixtures made of conductive and insulating materials. J Mater Sci 28:285–301. https://doi.org/10.1007/BF00357799

32. McLachlan DS (1986) Equations for the conductivity of macroscopic mixtures. J Phys C Solid State Phys 19:1339–1354. https://doi.org/10.1088/0022-3719/19/9/007

33. Kirkpatrick S (1973) Percolation and Conduction. Rev Mod Phys 45:574–588. https://doi.org/10.1103/RevModPhys.45.574

34. Stankovich S, Dikin DA, Dommett GHB, et al (2006) Graphene-based composite materials. Nature 442:282–286. https://doi.org/10.1038/nature04969

35. Yang X, Hu J, Chen S, He J (2016) Understanding the Percolation Characteristics of Nonlinear Composite Dielectrics. Sci Rep 6:1–11. https://doi.org/10.1038/srep30597

36. Gonon P, Boudefel A (2006) Electrical properties of epoxy/silver nanocomposites. J Appl Phys 99:. https://doi.org/10.1063/1.2163978

37. McLachlan DS, Chiteme C, Park C, et al (2005) AC and DC percolative conductivity of single wall carbon nanotube polymer composites. J Polym Sci Part B Polym Phys 43:3273–3287. https://doi.org/10.1002/polb.20597

38. Nan C-W, Shen Y, Ma J (2010) Physical Properties of Composites Near Percolation. Annu Rev Mater Res 40:131–151. https://doi.org/10.1146/annurev-matsci-070909-104529

39. Sang-Ha Hwang, Young-Bin Park KHY and DSB (2011) Smart materials and structures based on carbon nanotube composites. In: Carbon Nanotubes - Synthesis, Characterization, Applications. InTech

40. Shrivastava NK, Khatua BB (2011) Development of electrical conductivity with minimum possible percolation threshold in multi-wall carbon nanotube/polystyrene composites. Carbon N Y 49:4571–4579. https://doi.org/10.1016/j.carbon.2011.06.070

41. Aliev AE, Lima MH, Silverman EM, Baughman RH (2010) Thermal conductivity of multi-walled carbon nanotube sheets: Radiation losses and quenching of phonon modes. Nanotechnology 21:35709–35720. https://doi.org/10.1088/0957-4484/21/3/035709

42. Debelak B, Lafdi K (2007) Use of exfoliated graphite filler to enhance polymer physical properties. Carbon N Y 45:1727–1734. https://doi.org/10.1016/j.carbon.2007.05.010

43. Kim HS, Jang J-U, Yu J, Kim SY (2015) Thermal conductivity of polymer composites based on the length of multi-walled carbon nanotubes. Compos Part B Eng 79:505–512. https://doi.org/10.1016/j.compositesb.2015.05.012

44. Zhang P, Li Q, Xuan Y (2014) Thermal contact resistance of epoxy composites incorporated with nano-copper particles and the multi-walled carbon nanotubes. Compos Part A Appl Sci Manuf 57:1–7. https://doi.org/10.1016/j.compositesa.2013.10.022

45. Park JG, Cheng Q, Lu J, et al (2012) Thermal conductivity of MWCNT/epoxy composites: The effects of length, alignment and functionalization. Carbon N Y 50:2083–2090. https://doi.org/10.1016/j.carbon.2011.12.046

46. Li J, Ma PC, Chow WS, et al (2007) Correlations between percolation threshold, dispersion state, and aspect ratio of carbon nanotubes. Adv Funct Mater 17:3207–3215. https://doi.org/10.1002/adfm.200700065

47. Nan C-W, Liu G, Lin Y, Li M (2004) Interface effect on thermal conductivity of carbon nanotube composites. Appl Phys Lett 85:3549–3551. https://doi.org/10.1063/1.1808874

48. McNamara AJ, Joshi Y, Zhang ZM (2012) Characterization of nanostructured thermal interface materials - A review. In: International Journal of Thermal Sciences. pp 2–11

49. Kim KK, Kim SM, Lee YH (2014) A New Horizon for Hexagonal Boron Nitride Film. J Korean Phys Soc 64:1605–1616. https://doi.org/10.3938/jkps.64.1605

50. Andritsch T, Fabiani D (2013) Nanodielectrics — Examples of Preparation and Microstructure. 24 IEEE Electr Insul Mag 29:21–25

51. Chiu CW, Huang TK, Wang YC, et al (2014) Intercalation strategies in clay/polymer hybrids. Prog Polym Sci 39:443–485. https://doi.org/10.1016/j.progpolymsci.2013.07.002

52. Alexandre M, Dubois P (2000) Polymer-layered silicate nanocomposites: Preparation, properties and uses of a new class of materials. Mater Sci Eng R Reports 28:1–63. https://doi.org/10.1016/S0927-796X(00)00012-7

53. Giannelis E (1996) Polymer layered silicate nanocomposites. Adv Mater 8:29–35. https://doi.org/10.1002/adma.19960080104

54. Potts JR, Dreyer DR, Bielawski CW, Ruoff RS (2011) Graphene-based polymer nanocomposites. Polymer (Guildf) 52:5–25. https://doi.org/10.1016/j.polymer.2010.11.042

55. Fréchette MF, Vijh A, Utracki L, et al (2010) Nanodielectrics: A panacea for solving all electrical insulation problems? In: Proceedings of the 2010 IEEE International Conference on Solid Dielectrics, ICSD 2010. pp 1–29

56. Yang L, Watts DJ (2005) Particle surface characteristics may play an important role in phytotoxicity of alumina nanoparticles. Toxicol Lett. https://doi.org/10.1016/j.toxlet.2005.03.003

57. Baroli B, Ennas MG, Loffredo F, et al (2007) Penetration of metallic nanoparticles in human full-thickness skin. J Invest Dermatol 127:1701–1712. https://doi.org/10.1038/sj.jid.5700733

58. Jani PU, McCarthy DE, Florence AT (1994) Titanium dioxide (rutile) particle uptake from the rat GI tract and translocation to systemic organs after oral administration. Int J Pharm 105:157–168. https://doi.org/10.1016/0378-5173(94)90461-8

59. Hwang CY (1983) Size and shape of airborne asbestos fibres in mines and mills. Br J Ind Med 40:273–9

60. Erdely A, Dahm M, Chen BT, et al (2013) Carbon nanotube dosimetry: From workplace exposure assessment to inhalation toxicology. Part Fibre Toxicol 10:1–14. https://doi.org/10.1186/1743-8977-10-53

61. Ou L, Song B, Liang H, et al (2016) Toxicity of graphene-family nanoparticles: A general review of the origins and mechanisms. Part Fibre Toxicol 13:. https://doi.org/10.1186/s12989-016-0168-y

62. Hirsch A (2010) The era of carbon allotropes. Nat Mater 9:868–871. https://doi.org/10.1038/nmat2885

63. Falcao EHL, Wudl F (2007) Carbon allotropes: beyond graphite and diamond. J Chem Technol Biotechnol 82:524–531. https://doi.org/10.1002/jctb

64. El-Tantawy F, Kamada K, Ohnabe H (2002) In situ network structure, electrical and thermal properties of conductive epoxy resin-carbon black composites for electrical heater applications. Mater Lett 56:112–126. https://doi.org/10.1016/S0167-577X(02)00401-9

65. Fan Z, Zheng C, Wei T, et al (2009) Effect of carbon black on electrical property of graphite nanoplatelets/epoxy resin composites. Polym Eng Sci 49:2041–2045. https://doi.org/10.1002/pen.21445

66. Yu A, Ramesh P, Sun X, et al (2008) Enhanced thermal conductivity in a hybrid graphite nanoplatelet - Carbon nanotube filler for epoxy composites. Adv Mater 20:4740–4744. https://doi.org/10.1002/adma.200800401

67. Sengupta R, Bhattacharya M, Bandyopadhyay S, Bhowmick AK (2011) A review on the mechanical and electrical properties of graphite and modified graphite reinforced polymer composites. Prog Polym Sci 36:638–670. https://doi.org/10.1016/j.progpolymsci.2010.11.003

68. Yasmin A, Luo JJ, Daniel IM (2006) Processing of expanded graphite reinforced polymer nanocomposites. Compos Sci Technol 66:1179–1186. https://doi.org/10.1016/j.compscitech.2005.10.014

69. Celzard A, Marêché JF, Furdin G (2002) Surface area of compressed expanded graphite. Carbon N Y 40:2713–2718. https://doi.org/10.1016/S0008-6223(02)00183-5

70. Li X, Biswas S, Drzal LT (2013) High temperature vacuum annealing and hydrogenation modification of exfoliated graphite nanoplatelets. J Eng (United States) 2013:. https://doi.org/10.1155/2013/638576

71. D. Hoang T, Joonkyu P, Sang A H, et al (2011) Electrical and Thermal Conductivities of Stycast 1266 Epoxy/Graphite Composites. J Korean Phys Soc 59:2760–2764. https://doi.org/10.3938/jkps.59.2760

72. Novoselov KS, Geim AK, Morozov S V, et al (2004) Electric field in atomically thin carbon films. Science (80-) 306:666–669. https://doi.org/10.1126/science.1102896

73. Geim A, Novoselov K (2007) The Rise of Graphene. Nat Mater 6:183–191. https://doi.org/doi:10.1038/nmat1849

74. Geim AK (2009) Graphene: Status and prospects. Science (80-.). 324:1530–1534

75. Young RJ, Kinloch IA, Gong L, Novoselov KS (2012) The mechanics of graphene nanocomposites: A review. Compos Sci Technol 72:1459–1476. https://doi.org/10.1016/j.compscitech.2012.05.005

76. Jang BZ, Zhamu A (2008) Processing of nanographene platelets (NGPs) and NGP nanocomposites: A review. J Mater Sci 43:5092–5101. https://doi.org/10.1007/s10853-008-2755-2

77. Dreyer DR, Todd AD, Bielawski CW (2014) Harnessing the chemistry of graphene oxide. Chem Soc Rev 43:5288–5301. https://doi.org/10.1039/c4cs00060a

78. Dikin DA, Stankovich S, Zimney EJ, et al (2007) Preparation and characterization of graphene oxide paper. Nature 448:457–460. https://doi.org/10.1038/nature06016

79. Lerf A, He H, Forster M, Klinowski J (1998) Structure of Graphite Oxide Revisited. J Phys Chem B 102:4477–4482. https://doi.org/10.1021/jp9731821

80. Park S, Ruoff RS (2009) Chemical methods for the production of graphenes. Nat Nanotechnol 4:217–224. https://doi.org/10.1038/nnano.2009.58

81. Paredes JI, Villar-Rodil S, Martínez-Alonso A, Tascón JMD (2008) Graphene oxide dispersions in organic solvents. Langmuir 24:10560–10564. https://doi.org/10.1021/la801744a

82. Bhattacharya M (2016) Polymer nanocomposites-A comparison between carbon nanotubes, graphene, and clay as nanofillers. Materials (Basel). 9:1–35

83. Li Z, Young RJ, Wang R, et al (2013) The role of functional groups on graphene oxide in epoxy nanocomposites. Polymer (Guildf) 54:5821–5829. https://doi.org/10.1016/j.polymer.2013.08.026

84. Li Z, Chu J, Yang C, et al (2018) Effect of functional groups on the agglomeration of graphene in nanocomposites. Compos Sci Technol 163:116–122. https://doi.org/10.1016/j.compscitech.2018.05.016

85. Stankovich S, Dikin DA, Piner RD, et al (2007) Synthesis of graphene-based nanosheets via chemical reduction of exfoliated graphite oxide. Carbon N Y 45:1558–1565. https://doi.org/10.1016/j.carbon.2007.02.034

86. Mu X, Wu X, Zhang T, et al (2014) Thermal transport in graphene oxide--from ballistic extreme to amorphous limit. Sci Rep 4:3909. https://doi.org/10.1038/srep03909

87. Pei S, Cheng H-M (2012) The reduction of graphene oxide. Carbon N Y 50:3210–3228. https://doi.org/10.1016/j.carbon.2011.11.010

88. Ma J, Meng Q, Zaman I, et al (2014) Development of polymer composites using modified, high-structural integrity graphene platelets. Compos Sci Technol 91:82–90. https://doi.org/10.1016/j.compscitech.2013.11.017

89. Miller SG, Heimann PJ, Barlow JP, Allred RE (2007) Physical Properties of Exfoliated Graphite Nanocomposites By Variation of Graphite Surface Functionality. In: 52nd International SAMPE Symposium and Exhibition. Baltimore, MD

90. Pu X, Zhang H Bin, Li X, et al (2014) Thermally conductive and electrically insulating epoxy nanocomposites with silica-coated graphene. RSC Adv 4:15297–15303. https://doi.org/10.1039/c4ra00518j

91. Chua CK, Sofer Z, Pumera M (2012) Graphite oxides: Effects of permanganate and chlorate oxidants on the oxygen composition. Chem - A Eur J 18:13453–13459. https://doi.org/10.1002/chem.201202320

92. Brodie BC (1859) On the Atomic Weight of Graphite. Philos Trans R Soc London 149:249–259. https://doi.org/10.1098/rstl.1859.0013

93. Staudenmaier L (1898) Verfahren zur darstellung der graphitsäure. Berichte der Dtsch Chem Gesellschaft 31:1481–1487. https://doi.org/10.1002/cber.18980310237

94. Hofmann U, König E (1937) Untersuchungen über Graphitoxyd. Zeitschrift für Anorg und Allg Chemie 234:311–336. https://doi.org/10.1002/zaac.19372340405

95. Hummers WS, Offeman RE (1958) Preparation of graphitic oxide. J Am Chem Soc 80:1339–1339

96. Chen J, Yao B, Li C, Shi G (2013) An improved Hummers method for eco-friendly synthesis of graphene oxide. Carbon N Y 64:225–229. https://doi.org/10.1016/j.carbon.2013.07.055

97. Shen L, Zhang L, Wang K, et al (2018) Analysis of oxidation degree of graphite oxide and chemical structure of corresponding reduced graphite oxide by selecting different-sized original graphite. RSC Adv 8:17209–17217. https://doi.org/10.1039/c8ra01486h

98. Krishnamoorthy K, Veerapandian M, Yun K, Kim SJ (2013) The chemical and structural analysis of graphene oxide with different degrees of oxidation. Carbon N Y 53:38–49. https://doi.org/10.1016/j.carbon.2012.10.013

99. Guerrero-Contreras J, Caballero-Briones F (2015) Graphene oxide powders with different oxidation degree, prepared by synthesis variations of the Hummers method. Mater Chem Phys 153:209–220. https://doi.org/10.1016/j.matchemphys.2015.01.005

100. Marcano DC, Kosynkin D V., Berlin JM, et al (2010) Improved synthesis of graphene oxide. ACS Nano 4:4806–4814. https://doi.org/10.1021/nn1006368

101. Higginbotham AL, Kosynkin D V., Sinitskii A, et al (2010) Lower-defect graphene oxide nanoribbons from multiwalled carbon nanotubes. ACS Nano 4:2059–2069. https://doi.org/10.1021/nn100118m

102. Dutta D, Ganda ANF, Chih JK, et al (2018) Revisiting graphene-polymer nanocomposite for enhancing anticorrosion performance: A new insight into interface chemistry and diffusion model. Nanoscale 10:12612–12624. https://doi.org/10.1039/c8nr03261k

103. Su CY, Lu AY, Xu Y, et al (2011) High-quality thin graphene films from fast electrochemical exfoliation. ACS Nano 5:2332–2339. https://doi.org/10.1021/nn200025p

104. Vasilieva FD, Kapitonov AN, Yakimchuk EA, et al (2018) Mildly oxidized graphene oxide suspension for printing technologies. Mater Res Express 5:65608. https://doi.org/10.1088/2053-1591/aacb58

105. Chen CH, Yang SW, Chuang MC, et al (2015) Towards the continuous production of high crystallinity graphene via electrochemical exfoliation with molecular in situ encapsulation. Nanoscale 7:15362–15373. https://doi.org/10.1039/c5nr03669k

106. Papageorgiou DG, Kinloch IA, Young RJ (2017) Mechanical properties of graphene and graphene-based nanocomposites. Prog Mater Sci 90:75–127. https://doi.org/10.1016/j.pmatsci.2017.07.004

107. Wang X, Jin J, Song M (2013) An investigation of the mechanism of graphene toughening epoxy. Carbon N Y 65:324–333. https://doi.org/10.1016/j.carbon.2013.08.032

108. Park YT, Qian Y, Chan C, et al (2015) Epoxy toughening with low graphene loading. Adv Funct Mater 25:575–585. https://doi.org/10.1002/adfm.201402553

109. Wan Y, Tang L, Gong L, et al (2013) Grafting of epoxy chains onto graphene oxide for epoxy composites with improved mechanical and thermal properties. Carbon N Y 69:467–480. https://doi.org/10.1016/j.carbon.2013.12.050

110. Silva LCO, Silva GG, Ajayan PM, Soares BG (2015) Long-term behavior of epoxy/graphene-based composites determined by dynamic mechanical analysis. J Mater Sci 50:6407–6419. https://doi.org/10.1007/s10853-015-9193-8

111. Zaman I, Phan TT, Kuan HC, et al (2011) Epoxy/graphene platelets nanocomposites with two levels of interface strength. Polymer (Guildf) 52:1603–1611. https://doi.org/10.1016/j.polymer.2011.02.003

112. Tang X, Zhou Y, Peng M (2016) Green Preparation of Epoxy/Graphene Oxide Nanocomposites Using a Glycidylamine Epoxy Resin as the Surface Modifier and Phase Transfer Agent of Graphene Oxide. ACS Appl Mater Interfaces 8:1854–1866. https://doi.org/10.1021/acsami.5b09830

113. Wang R, Zhuo D, Weng Z, et al (2015) A novel nanosilica/graphene oxide hybrid and its flame retarding epoxy resin with simultaneously improved mechanical, thermal conductivity, and dielectric properties. J Mater Chem A 3:9826–9836. https://doi.org/10.1039/c5ta00722d

114. Zhou T, Nagao S, Sugahara T, et al (2015) Facile identification of the critical content of multi-layer graphene oxide for epoxy composite with optimal thermal properties. RSC Adv 5:20376–20385. https://doi.org/10.1039/c4ra15881d

115. Galpaya D, Wang M, Yan C, et al (2013) Fabrication and characterisation of graphene oxide-epoxy nanocomposite. Fourth Int. Conf. Smart Mater. Nanotechnol. Eng. 8793

116. Kopsidas S, Rocha VG, Taylor AC, et al (2017) A facile way to produce epoxy nanocomposites having excellent thermal conductivity with low contents of reduced graphene oxide. J Mater Sci 52:7323–7344. https://doi.org/10.1007/s10853-017-0969-x

117. Bao C, Guo Y, Song L, et al (2011) In situ preparation of functionalized graphene oxide/epoxy nanocomposites with effective reinforcements. J Mater Chem 21:13290–13298. https://doi.org/10.1039/c1jm11434d

118. Liu F, Wu L, Song Y, et al (2015) Effect of molecular chain length on the properties of amine-functionalized graphene oxide nanosheets/epoxy resins nanocomposites. RSC Adv 5:45987–45995. https://doi.org/10.1039/c5ra02013a

119. Sharmila TKB, Nair AB, Abraham BT, et al (2014) Microwave exfoliated reduced graphene oxide epoxy nanocomposites for high performance applications. Polymer (Guildf) 55:3614–3627. https://doi.org/10.1016/j.polymer.2014.05.032

120. Guan LZ, Wan YJ, Gong LX, et al (2014) Toward effective and tunable interphases in graphene oxide/epoxy composites by grafting different chain lengths of polyetheramine onto graphene oxide. J Mater Chem A 2:15058–15069. https://doi.org/10.1039/c4ta02429j

121. Mancinelli P, Heid TF, Fabiani D, et al (2013) Electrical conductivity of graphene-based epoxy nanodielectrics. Annu Rep - Conf Electr Insul Dielectr Phenomena, CEIDP 772–775. https://doi.org/10.1109/CEIDP.2013.6748282

122. Kim J, Im H, Kim J, Kim J (2012) Thermal and electrical conductivity of Al(OH)3 covered graphene oxide nanosheet/epoxy composites. J Mater Sci 47:1418–1426. https://doi.org/10.1007/s10853-011-5922-9

123. Tang G, Jiang ZG, Li X, et al (2014) Simultaneous functionalization and reduction of graphene oxide with polyetheramine and its electrically conductive epoxy nanocomposites. Chinese J Polym Sci (English Ed 32:975–985. https://doi.org/10.1007/s10118-014-1488-8

124. Hsiao MC, Ma CCM, Chiang JC, et al (2013) Thermally conductive and electrically insulating epoxy nanocomposites with thermally reduced graphene oxide-silica hybrid nanosheets. Nanoscale 5:5863–5871. https://doi.org/10.1039/c3nr01471a

125. Liang J, Wang Y, Huang Y, et al (2009) Electromagnetic interference shielding of graphene/epoxy composites. Carbon N Y 47:922–925. https://doi.org/10.1016/j.carbon.2008.12.038

126. Jović N, Dudić D, Montone A, et al (2008) Temperature dependence of the electrical conductivity of epoxy/expanded graphite nanosheet composites. Scr Mater 58:846–849. https://doi.org/10.1016/j.scriptamat.2007.12.041

127. Celzard A, McRae E, Marêché JF, et al (1996) Composites based on micron-sized exfoliated graphite particles: Electrical conduction, critical exponents and anisotropy. J Phys Chem Solids 57:715–718. https://doi.org/10.1016/0022-3697(95)00337-1

128. Zheng C, Fan Z, Wei T, Luo G (2009) Temperature dependence of the conductivity behavior of graphite nanoplatelet-filled epoxy resin composites. J Appl Polym Sci 113:1515–1519. https://doi.org/10.1002/app.30009

129. Jia W, Tchoudakov R, Narkis M, Siegmann A (2005) Performance of expanded graphite and expanded milled-graphite fillers in thermosetting resins. Polym Compos 26:526–533. https://doi.org/10.1002/pc.20123

130. Li J, Sham ML, Kim JK, Marom G (2007) Morphology and properties of UV/ozone treated graphite nanoplatelet/epoxy nanocomposites. Compos Sci Technol 67:296–305. https://doi.org/10.1016/j.compscitech.2006.08.009

131. Monti M, Rallini M, Puglia D, et al (2013) Morphology and electrical properties of graphene-epoxy nanocomposites obtained by different solvent assisted processing methods. Compos Part A Appl Sci Manuf 46:166–172. https://doi.org/10.1016/j.compositesa.2012.11.005

132. Chandrasekaran S, Seidel C, Schulte K (2013) Preparation and characterization of graphite nano-platelet (GNP)/epoxy nano-composite: Mechanical, electrical and thermal properties. Eur Polym J 49:3878–3888. https://doi.org/10.1016/j.eurpolymj.2013.10.008

133. Wajid AS, Tanvir Ahmed HS, Das S, et al (2013) High-performance pristine graphene/epoxy composites with enhanced mechanical and electrical properties. Macromol Mater Eng 298:339–347. https://doi.org/10.1002/mame.201200043

134. Ghaleb ZA, Mariatti M, Ariff ZM (2014) Properties of graphene nanopowder and multi-walled carbon nanotube-filled epoxy thin-film nanocomposites for electronic applications: The effect of sonication time and filler loading. Compos Part A Appl Sci Manuf 58:77–83. https://doi.org/10.1016/j.compositesa.2013.12.002

135. Wu S, Ladani RB, Zhang J, et al (2015) Aligning multilayer graphene flakes with an external electric field to improve multifunctional properties of epoxy nanocomposites. Carbon N Y 94:607–618. https://doi.org/10.1016/j.carbon.2015.07.026

136. Zaman I, Kuan H-C, Dai J, et al From carbon nanotubes and silicate layers to graphene platelets for polymer nanocomposites †. https://doi.org/10.1039/c2nr30837a

137. Kim J, Kim J, Yim BS, Kim JM (2012) The effects of functionalized graphene nanosheets on the thermal and mechanical properties of epoxy composites for anisotropic conductive adhesives (ACAs). Microelectron Reliab 52:595–602. https://doi.org/10.1016/j.microrel.2011.11.002

138. Chatterjee S, Wang JW, Kuo WS, et al (2012) Mechanical reinforcement and thermal conductivity in expanded graphene nanoplatelets reinforced epoxy composites. Chem Phys Lett 531:6–10. https://doi.org/10.1016/j.cplett.2012.02.006

139. Gu J, Yang X, Lv Z, et al (2016) Functionalized graphite nanoplatelets/epoxy resin nanocomposites with high thermal conductivity. Int J Heat Mass Transf 92:15–22. https://doi.org/10.1016/j.ijheatmasstransfer.2015.08.081

140. Skowroński JM, Jurewicz K (1991) Anodic oxidation of CrO3-graphite intercalation compounds in sulfuric acid. Synth Met 40:161–172. https://doi.org/10.1016/0379-6779(91)91772-3

141. Mittal J, Konno H, Inagaki M (1998) Synthesis of graphite intercalation compounds with CrVI compounds using CrO3 and HCl at room temperature. Synth Met 96:103–108. https://doi.org/http://dx.doi.org/10.1016/S0379-6779(98)00070-8

142. Ebert LB, Huggins RA, Brauman JI (1974) The nature of the chromium trioxide intercalation in graphite. Carbon N Y 12:199–208. https://doi.org/10.1016/0008-6223(74)90026-8

143. Tang G, Jiang ZG, Li X, et al (2014) Electrically conductive rubbery epoxy/diamine-functionalized graphene nanocomposites with improved mechanical properties. Compos Part B Eng 67:564–570. https://doi.org/10.1016/j.compositesb.2014.08.013

144. Mancinelli P, Heid TF, Fabiani D, et al (2013) Thermal in situ reduction of graphene oxide in epoxy-based nanodielectrics: Influence on dielectric properties. In: Annual Report - Conference on Electrical Insulation and Dielectric Phenomena, CEIDP. pp 768–771

145. Fang M, Zhang Z, Li J, et al (2010) Constructing hierarchically structured interphases for strong and tough epoxy nanocomposites by amine-rich graphene surfaces. J Mater Chem 20:9635–9643. https://doi.org/10.1039/c0jm01620a

146. Pimenta MA, Dresselhaus G, Dresselhaus MS, et al (2007) Studying disorder in graphite-based systems by Raman spectroscopy. Phys Chem Chem Phys 9:1276–1291. https://doi.org/10.1039/b613962k

147. Prime RB, Bair HE, Vyazovkin S, et al (2009) Thermogravimetric analysis (TGA). In: Thermal analysis of Polymers: Fundamentals and Applications. pp 241–317

148. Eigler S, Dotzer C, Hirsch A, et al (2012) Formation and decomposition of CO2intercalated graphene oxide. Chem Mater 24:1276–1282. https://doi.org/10.1021/cm203223z

149. González-González M, Cabanelas JC, Baselga J (2012) Applications of FTIR on Epoxy Resins – Identification, Monitoring the Curing Process, Phase Separation and Water Uptake. In: Infrared Spectroscopy - Materials Science, Engineering and Technology. pp 261–284

150. Nikolic G, Zlatkovic S, Cakic M, et al (2010) Fast fourier transform IR characterization of epoxy GY systems crosslinked with aliphatic and cycloaliphatic EH polyamine adducts. Sensors 10:684–696. https://doi.org/10.3390/s100100684

151. Chike KE, Myrick ML, Lyon RE, Angel SM (1993) Raman and near-infrared studies of an epoxy resin. Appl Spectrosc 47:1631–1635. https://doi.org/10.1366/0003702934334714

152. Saeedi IA, Vaughan AS, Andritsch T (2019) Functional design of epoxy-based networks: tailoring advanced dielectrics for next-generation energy systems. J Phys D Appl Phys 52:205301. https://doi.org/10.1088/1361-6463/ab09be

153. Menczel JD, Judovits L, Prime RB, et al Differential Scanning Calorimetry (DSC). In: Thermal Analysis of Polymers. John Wiley & Sons, Inc., Hoboken, NJ, USA, pp 7–239

154. Menczel JD, Bair HE, Reading M, et al (2009) Thermal Analysis of Polymers. John Wiley & Sons, Inc., Hoboken, NJ, USA

155. Vassilikou-Dova A, Kalogeras IM (2008) Dielectric Analysis (DEA). In: Thermal Analysis of Polymers: Fundamentals and Applications. John Wiley, New Jersey, pp 497–613

156. Schönhals A, Kremer F (2003) Theory of Dielectric Relaxation. In: Broadband Dielectric Spectroscopy. Springer, Berlin, Heidelberg, pp 1–33

157. Psarras GC (2010) Conductivity and dielectric characterization of polymer nanocomposites. In: Polymer Nanocomposites: Physical Properties and Applications. Woodhead Publishing Limited, Cambridge, pp 31–69

158. Ganguly A, Sharma S, Papakonstantinou P, Hamilton J (2011) Probing the Thermal Deoxygenation of Graphene Oxide Using High-Resolution In Situ X-ray-Based Spectroscopies. J Phys Chem C 115:17009–17019

159. Pantea D, Darmstadt H, Kaliaguine S, Roy C (2003) Electrical conductivity of conductive carbon blacks: Influence of surface chemistry and topology. Appl Surf Sci 217:181–193. https://doi.org/10.1016/S0169-4332(03)00550-6

160. Fothergill JC (2010) Electrical Properties. In: Dielectric Polymer Nanocomposites. Springer, Troy, NY, USA, pp 197–228

161. Vryonis O, Anastassopoulos DL, Vradis AA, Psarras GC (2016) Dielectric response and molecular dynamics in epoxy-BaSrTiO3 nanocomposites: Effect of nanofiller loading. Polymer (Guildf) 95:82–90. https://doi.org/10.1016/j.polymer.2016.04.050

162. Singha S, Thomas M (2008) Dielectric properties of epoxy nanocomposites. IEEE Trans Dielectr Electr Insul 15:12–23. https://doi.org/10.1109/T-DEI.2008.4446732

163. Mancinelli P, Fabiani D, Saccani A, et al (2013) Preparation and dielectric behavior of epoxy resin containing graphene oxide. In: Proceedings of IEEE International Conference on Solid Dielectrics, ICSD. pp 915–918

164. Bernard S, Beyssac O, Benzerara K, et al (2010) XANES, Raman and XRD study of anthracene-based cokes and saccharose-based chars submitted to high-temperature pyrolysis. Carbon N Y 48:2506–2516. https://doi.org/10.1016/j.carbon.2010.03.024

165. Bo Z, Shuai X, Mao S, et al (2014) Green preparation of reduced graphene oxide for sensing and energy storage applications. Sci Rep 4:. https://doi.org/10.1038/srep04684

166. Estrade-Szwarckopf H (2004) XPS photoemission in carbonaceous materials: A “defect” peak beside the graphitic asymmetric peak. Carbon N Y 42:1713–1721. https://doi.org/10.1016/j.carbon.2004.03.005

167. Zeng C, Tang Z, Guo B, Zhang L (2012) Supramolecular ionic liquid based on graphene oxide. Phys Chem Chem Phys. https://doi.org/10.1039/c2cp40517b

168. Hanemann T, Szabó DV (2010) Polymer-nanoparticle composites: From synthesis to modern applications

169. Krishnamoorti R (2007) Strategies for dispersing nanoparticles in polymers. MRS Bull 32:341–347. https://doi.org/10.1557/mrs2007.233

170. Nguyen VS, Rouxel D, Vincent B (2014) Dispersion of nanoparticles: From organic solvents to polymer solutions. Ultrason Sonochem 21:149–153. https://doi.org/10.1016/j.ultsonch.2013.07.015

171. Huang X, Iizuka T, Jiang P, et al (2012) Role of interface on the thermal conductivity of highly filled dielectric epoxy/AlN composites. J Phys Chem C 116:13629–13639. https://doi.org/10.1021/jp3026545

172. Raza MA, Westwood AVK, Brown AP, Stirling C (2012) Texture, transport and mechanical properties of graphite nanoplatelet/silicone composites produced by three roll mill. Compos Sci Technol 72:467–475. https://doi.org/10.1016/J.COMPSCITECH.2011.12.010

173. Bian S, Jayaram S, Cherney E a. (2012) Electrospinning as a new method of preparing nanofilled silicone rubber composites. IEEE Trans Dielectr Electr Insul 19:777–785. https://doi.org/10.1109/TDEI.2012.6215080

174. Sahu N, Parija B, Panigrahi S (2009) Fundamental understanding and modeling of spin coating process: A review. Indian J Phys 83:493–502. https://doi.org/10.1007/s12648-009-0009-z

175. Kim G (2005) Thermo-physical responses of polymeric composites tailored by electric field. Compos Sci Technol 65:1728–1735. https://doi.org/10.1016/J.COMPSCITECH.2005.02.013

176. Kaufman HS (1970) Handbook of epoxy resins. Henry Lee and Kris Neville. John Wiley & Sons, Inc.

177. Nguyen V, Vaughan A, Lewin P, Krivda A (2015) The effect of resin stoichiometry and nanoparticle addition on epoxy/silica nanodielectrics. IEEE Trans Dielectr Electr Insul 22:895–905. https://doi.org/10.1109/TDEI.2015.7076790

178. Gillham JK (1986) Formation and properties of thermosetting and high Tg polymeric materials. Polym Eng Sci 26:1429–1433. https://doi.org/10.1002/pen.760262012

179. Nakka JS, Jansen KMB, Ernst LJ (2013) Tailoring the viscoelasticity of epoxy thermosets. J Appl Polym Sci 128:3794–3806. https://doi.org/10.1002/app.38435

180. Alhabill FN, Ayoob R, Andritsch T, Vaughan AS (2017) Effect of resin/hardener stoichiometry on electrical behavior of epoxy networks. IEEE Trans Dielectr Electr Insul 24:3739–3749. https://doi.org/10.1109/TDEI.2017.006828

181. Yamasaki H, Morita S (2014) Identification of the epoxy curing mechanism under isothermal conditions by thermal analysis and infrared spectroscopy. J Mol Struct 1069:164–170. https://doi.org/10.1016/j.molstruc.2014.01.037

182. Esmaeili A, Entezari MH (2014) Facile and fast synthesis of graphene oxide nanosheets via bath ultrasonic irradiation. J Colloid Interface Sci 432:19–25. https://doi.org/10.1016/j.jcis.2014.06.055

183. Tuinstra F, Koenig JL (1970) Raman Spectrum of Graphite. J Chem Phys 53:1126–1130. https://doi.org/10.1063/1.1674108

184. Venugopal G, Jung M-H, Suemitsu M, Kim S-J (2011) Fabrication of nanoscale three-dimensional graphite stacked-junctions by focused-ion-beam and observation of anomalous transport characteristics. Carbon N Y 49:2766–2772. https://doi.org/10.1016/j.carbon.2011.03.003

185. Ferrari AC, Robertson J (2000) Interpretation of Raman spectra of disordered and amorphous carbon. Phys Rev B 61:95–107

186. King AAK, Davies BR, Noorbehesht N, et al (2016) A new raman metric for the characterisation of graphene oxide and its derivatives. Sci Rep 6:. https://doi.org/10.1038/srep19491

187. Wang Y, Yu J, Dai W, et al (2015) Enhanced Thermal and Electrical Properties of Epoxy Composites Reinforced With Graphene Nanoplatelets. Polym Compos 36:556–565. https://doi.org/10.1002/pc.22972

Dissemination

- 4-Day Summer School on Dielectric Interfaces, 9-13 September 2018, Bertinoro, Italy
  Organized by: IEEE Dielectrics and Electrical Insulation Society
- International Conference on Dielectrics (ICD), 1-5 July 2018, Budapest, Hungary.
  Poster participation: *"Solvent Mixing and Its Effect on Epoxy Resin Filled with Graphene Oxide"*
- UHVnet Colloquium, 15-16 January 2018, Winchester, UK
  Poster Participation: *"Epoxy Resin/Graphene Oxide nanocomposites:*
  Optimising exfoliation parameters"
- Conference on Electrical Insulation & Dielectric Phenomena (CEIDP), 22-15 October 2017, Fort Worth, Texas, US.
  Poster participation: *"On the effect of solvent method processing on epoxy resin systems: A molecular dynamics study"*
- International Conference on Lightning & Static Electricity (ICOLSE), 13-15 September 2017, Nagoya, Japan.
  Oral presentation: *"Graphene Oxide - Epoxy Resin Nanocomposites:*
  A Potential Candidate for Improving Lightning Protection Systems of Wind Turbine Carbon Fibre Sparcaps"
- Wind Energy Science Conference (WESC), 26-29 June 2017, Copenhagen, Denmark.
  Oral presentation: *"Improved Lightning Protection Concepts*
  Increasing the electrical conductivity of epoxy resin: Isotropic CFRP WT spars"
- Conference on Electrical Insulation & Dielectric Phenomena (CEIDP), 16-19 October 2016, Toronto, Canada.
  Poster participation: "*Improved Lightning Protection of Carbon Fiber Reinforced Polymer Wind Turbine Blades: Epoxy/Graphene Oxide Nanocomposites"*